Development of Transparent Soil Testing using Planar Laser Induced Fluorescence in the Study of Internal Erosion of Filters in Embankment Dams

---

A Thesis

Submitted in partial fulfillment of the requirements of the degree

of

Master of Science in Engineering Geology

at the

University of Canterbury

by

Robert Peter Hunter

UNIVERSITY OF CANTERBURY

2012

Frontispiece

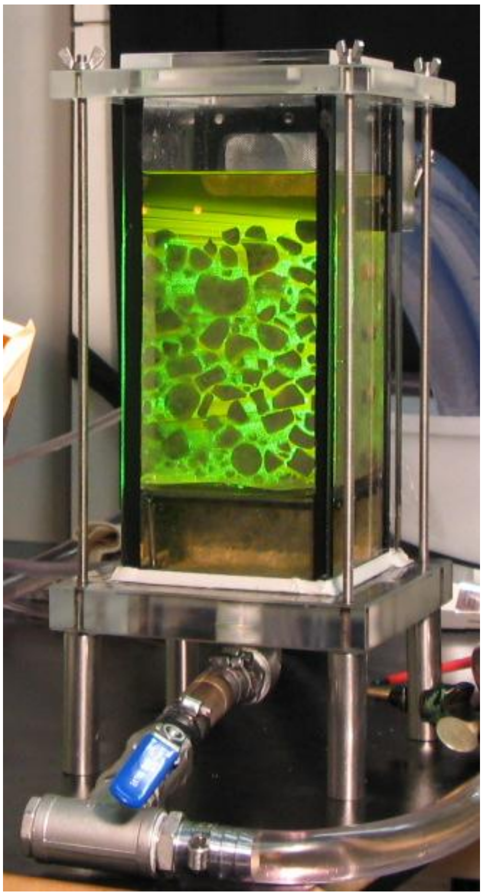

‘Seeing Is Believing’ – An Idiom, first recorded in 1639

Abstract

A new ‘transparent soil permeameter’ has been developed to study the mechanisms occurring during internal erosion in filter materials for embankment dams. Internal erosion or suffusion is the process where fine particles are removed from a matrix of coarse grains by seepage of water, and which ultimately leads to instabilities within the soil. The laboratory-based experiments in this thesis utilises a novel approach where up-scaled glass particles are used in place of soil particles, and optically matched oil is used in place of water. Rhodamine dye in the oil allows the fluid to fluoresce brightly when a sheet of laser light is shone through the sample, while the glass particles appear as dark shadows within the plane of the laser sheet. This technique is known as Planar Laser Induced Fluorescence (PLIF) and enables a two-dimensional "slice" or plane of particles and fluid to be viewed inside the permeameter, away from the permeameter walls. During a test, fluid is passed through the solid matrix in upward flow, with the flow rate (therefore hydraulic gradient) being increased in stages until internal erosion or bulk movement of the entire assembly develops and progresses. A high speed camera captures images of the two-dimensional plane over the duration of a test, which are then analysed using Image Pro and ImageJ processing software. Until now, the fundamental mechanisms that lead to internal erosion have been rather speculative, as there has been no way to physically observe the processes behind the initiation and continued movement of particles.

This visualisation experiment allows internal erosion mechanisms to be studied away from permeameter walls where boundary effects do not occur. The technique was validated by confirming Darcy’s (1856) law of laminar flow, and Terzaghi’s (1925) theoretical critical hydraulic gradient for an upward flow through materials with no top stress. Results of replicated materials tested by Skempton and Brogan (1994) and Fannin and Moffat (2006) also confirm this methodology to be valid by way of material behaviour, permeability and the alpha factor (Skempton & Brogan 1994). An assessment to predict the stability of soils was carried out using the Kenney and Lau (1985), Kezdi (1979), Burenkova (1993), Wan and Fell (2008) and Istomina (1957) approaches, with the Kenny and Lau and Kezdi methods proving to be the most robust across the particle size distributions tested. In the tests, unstable materials showed a migration of fine grains under hydraulic gradients as low as $i_c = 0.25$, while stable materials showed little movement of particles, and eventually failed by heave. Image processing using Image Pro and ImageJ were successful in producing quantitative results, however with further enhancements to the test equipment and methodology, these could be improved upon.

The testing technique developed in this thesis has proven to be successful in the study of internal erosion of filter materials. The technique proves that optically matched glass and oil can behave similarly to soil and water materials as used in previous laboratory testing, and that the PLIF technique and image capturing has merit in understanding the mechanisms occurring during internal erosion processes.

Acknowledgements

I would like to express sincere appreciation to my senior supervisor, Dr. Elisabeth Bowman, Senior Lecturer and UCSA Postgraduate Supervisor of the Year (2011) at the University of Canterbury, for ongoing support, collaboration, motivation and enthusiasm throughout the challenges of this thesis. Also to my Co-supervisor, Senior Lecturer, Mr David Bell also of the University of Canterbury, for sparking a passion for Engineering Geology and support throughout the Engineering Geology Post-Graduate course. A big thank you to Ian Sheppard, Kevin Wines and Siale Faitotonu, technical staff at the University of Canterbury, for helping with the design and construction of the apparatus, and for solving ongoing technical problems.

I would like to thank the AusIMM and the NZGS for financially supporting this research, and also to NZSOLD for providing funding for the purchase of Image Pro software, which was a huge benefit to the processing and output of results in this thesis.

I was lucky enough to meet PhD candidate Kaley Crawford-Flett and Dr. R. Jonathan Fannin of the University of British Columbia, who share an interest in internal erosion, and provided valuable collaboration and motivation during this research, thank you both for the support.

To my Mum and Dad, Jenny and Peter, thank you for all the ongoing encouragement, support and motivation, I'm very fortunate to have such a close relationship with you both. I'm also lucky enough to have a lovely partner, Juliette, a special thanks for making every day a pleasure and providing encouragement when needed. Also, a big thank you to all my other family and friends for making life enjoyable and providing ongoing support throughout my University career. And finally, thanks to Countdown for keeping their shelves stocked full of Dilmah tea, this thesis would not have been completed without it.

Table of Contents

Frontispiece……………………………………………………………………………………………I

Abstract……………………………………………………………………………………………II

Acknowledgements……………………………………………………………………………………III

Table of contents……………………………………………………………………………………IV

List of figures………………………………………………………………………………………V

List of tables………………………………………………………………………………………VI

Notation……………………………………………………………………………………………VII

Chapter 1: Introduction 1

1.1 Motivation.. 1

1.2 Objectives.. 2

Chapter 2: Filter materials for embankment dams 5

2.1 Embankment Dams: Overview.. 5

2.2 Embankment dam failures.. 6

2.3 Basic requirements of filters in embankment dams.. 8

2.4 Flow conditions acting on filters.. 10

2.5 Internal erosion.. 10

2.5.1 Erosion properties of soil 12

2.5.2 Suffusion 13

2.5.3 Suffosion 14

2.6 Self Filtration.. 15

2.7 Clogging.. 16

2.8 Arching and Bridging.. 16

2.9 Piping.....17
2.9.1 Backward Erosion.....18
2.9.2 Concentrated leak erosion.....18
2.9.3 Stages and Development of Piping Failure.....19
2.10 Filter design criteria and methods for evaluation of filter performance.....23
2.11 Synthesis.....31
Chapter 3: Previously employed testing apparatus and methods for modelling internal erosion 33
3.1 Bertram (1940).....33
3.2 Karpoff (1955).....34
3.3 Vaughan and Soares (1982).....35
3.4 Hillis and Truscott (1983).....35
3.5 Sherard et al. (1984a).....36
3.6 Sherard et al. (1984b).....38
3.7 Kenny and Lau (1985, 1986).....40
3.8 Sherard and Dunnigan (1985, 1989).....42
3.9 Lafleur, Mlynarek and Rollin (1989).....44
3.10 Burenkova (1993).....46
3.11 Okita and Nishigaki (1993).....47
3.12 Skempton and Brogan (1994).....48
3.13 Tomlinson and Vaid (2000).....51
3.14 Foster and Fell (2001a).....52
3.15 Garner and Sobkowicz (2002).....55
3.16 Wan and Fell (2002, 2004a, b) and Wan (2006).....57
3.17 Fannin and Moffat (2006).....58
3.18 Moffat and Fannin (2006).....60
3.19 Synthesis.....62
Chapter 4: Development of apparatus and testing methodology.....63

4.1 Introduction 63
4.2 Background and aims 63
4.3 Visualisation technique 64
4.3.1 Requirements for transparency 64
4.3.2 Fluorescence 65
4.3.3 Planar Laser Induced Fluorescence (PLIF) 67
4.4 Adopted technique 68
4.4.1 Light source and optics 68
4.4.2 Image Acquisition 70
4.5 Materials 71
4.5.1 Solid, fluid and dye properties 71
4.5.2 Permeability and scaling of the particles 73
4.5.3 Preparation of particles 77
4.6 Placing Sample 82
4.7 Permeameter Apparatus 83
4.7.1 Permeameter Issues 87
4.8 Oil supply and control system 89
4.8.1 Constant Head Tank Issues 90
4.8.2 Rotameter Issues 92
4.9 Particle Size Distribution (PSD) selection 93
4.9.1 Coarser Fraction and Finer Fraction Tests 93
4.9.2 G22FF and G40FF Tests 94
4.9.3 Skempton and Brogan (1994) Replications: GS&B-A, GS&B-B and GS&B-D 97
4.9.4 S&B-Hybrid 100
4.9.5 Fannin and Moffat (2006) Replication: GF&M-G4C 101
4.9.6 Long Tail Moraine Till Replication 102
4.10 PSD Analyses 104

4.11 Testing Procedure 104
4.11.1 Static conditions 104
4.11.2 Dynamic condition 105
4.12 Image analysis using Image Pro and ImageJ software 105
4.13 Synthesis 107
Chapter 5: Results from PSD analysis and physical testing 109
5.1 Introduction 109
5.2 Uniform PSD Tests 109
5.2.1 G100CF Test 109
5.2.2 G100FF Tests 113
5.2.2.1 G100FF - loose test 114
5.2.2.2 G100FF - compact test 116
5.3 G22FF and G40FF Tests 116
5.3.1 G22FF Test 119
5.3.2 G40FF Tests 123
5.3.3 UBC 22% and 40% finer fraction tests 126
5.4 Skempton and Brogan (1994) Replications 128
5.4.1 GS&B-A 130
5.4.2 GS&B-B 134
5.4.3 GS&B-D 138
5.5 Skempton and Brogan Hybrid 141
5.6 Fannin and Moffat (2006) Replication 150
5.7 Long Tail Test 155
5.8 Results from preliminary testing – pipe formation 159
5.9 Synthesis 159
Chapter 6: Image analysis using Image-Pro and ImageJ 161
6.1 Pre-test vs. Post-test comparisons 161

- 6.2 Assessment of particle orientation 164
- 6.3 ‘Phase’ Analysis 168
- 6.4 Synthesis 172

Chapter 7: Analysis and Discussion 173

- 7.1 G100CF Test 173
- 7.2 G100FF Tests 174
- 7.3 G22FF-2 Test 174
- 7.4 G40FF Tests 175
- 7.5 UBC 22FF, 40FF and 100FF Tests 176
- 7.6 GS&B-A Test 177
- 7.7 GS&B-B Test 180
- 7.8 GS&B-D 183
- 7.9 GS&B-Hybrid Test 185
- 7.10 GF&M-G4C Test 185
- 7.11 Glass Long Tail Test 187
- 7.12 Other results from preliminary testing – pipe formation 188
- 7.13 Discussion of PSD analysis 188
- 7.14 Limitations and Improvements in Apparatus and Procedure 191
- 7.15 Discussion of Image Analysis 196

Chapter 8: Conclusions and Recommendations 197

- 8.1 Conclusions on stability analyses: 197
- 8.2 Laboratory tests have led to the following conclusions: 197
- 8.3 Image processing using Image Pro and ImageJ software led to the following conclusions: 198
- 8.4 To improve the quality of results, the following are recommended: 198

Bibliography 199

Appendix 203

Appendix A – Cargille data sheet on Immersion Liquid 5095 203
Video Appendix A – GFM-G4C (see attached CD) 204
Video Appendix B – Pipe formation (see attached CD) 204

List of Figures

Figure 2.1: Example of an embankment dam showing the various zones: 1 – central core; 2A and 2B are both downstream filters, and 2C is an upstream filter; 3B – shoulder fill (Fell et al. 2005)........ 5

Figure 2.2: Dam zoning categories (Foster et al., 2000). 6

Figure 2.3: Time after construction of incidents of piping through the embankment (Foster et al., 2000). 8

Figure 2.4: Flow perpendicular (left) and parallel (right) to filter/base interface (Bakker, et al., 1987 in ICOLD (1994)). 10

Figure 2.5: An example of a gap graded soil where the fine grains (light) are present in the pore space (white) of the coarse grains (dark). With the introduction of flow, the fine particles become mobile when the upward flow forces exceed the frictional and gravitational forces of the grain (Rosenbrand 2011).. 11

Figure 2.6: Conceptual approach showing overlapping and interacting adverse conditions and internal erosion mechanisms (Garner & Fannin 2010).. 12

Figure 2.7: Descriptors for erosion rates of soil (Wan (2006) in Fell et al. (2008))............................. 12

Figure 2.8: Representative erosion rate index ($\tilde{\imath}_{HET}$) versus soil classification for non dispersive soils based on Wan and Fell (2002) in Fell et al. (2008)... 13

Figure 2.9: Classification of broadly graded soils as described by Lafleur et al. (1989). 14

Figure 2.10: Grading envelopes of some broadly graded soils which did not self filter (Sherard 1979). 16

Figure 2.11: Two dimensional schematic arrangement of simple arches in a statically compacted specimen (Mahmood & Mitchell 1974). 17

Figure 2.12: Arching phenomenon at contact surface of filter and base, upward flow (USACE 1953). 17

Figure 2.13: Conceptual erosion boundaries of filter test behaviour, Foster and Fell (2001b)........... 20

Figure 2.14: Models for the development of failure by piping (Foster & Fell 1999) in Cyganiewicz et al. (2008). 21

Figure 2.15: Stages of development of piping failure (Foster et al., 2000). 22

Figure 2.16: Event Tree (Cyganiewicz et al. 2008) 22

Figure 2.17: Original Terzaghi (1922) specifications for grain sizes of material for filters. The Left-hand shaded area encloses all grain-size curves for material to be protected; right-hand area indicates range within which curves for filter material must lie (Terzaghi et al. 1996). 24

Figure 2.18: Terzaghi criteria based on relationship between d_{85} of base to D_{15} of the filter materials, from Terzaghi et al. (1996). 24

Figure 2.19: Method to evaluate the potential for grading instability (Kenney & Lau 1985). 26

Figure 2.20: Example of a split curve showing the original gradation and the finer and coarser fraction, used in the calculation of $(D'_{15}/d'_{85})_{max}$ according to Kezdi (1979). 27

Figure 2.21: Synthesis of the Kenney and Lau (1985) and Kezdi (1979) criteria. NG, narrowly graded, WG, well graded (Li & Fannin 2008). 28

Figure 2.22: Evaluation of piping processes in soils according to test results (Burenkova 1993). 29

Figure 2.23: Contours of probability of internal instability for silt-sand-gravel soils and clay-silt-sand-gravel soils of limited clay content and plasticity (Wan & Fell 2008). 30

Figure 2.24: Alternative method for assessing internal instability of broadly graded silt-sand-gravel soils (Wan & Fell 2008). 30

Figure 3.1: Design of Bertram's Filter Test Apparatus (Bertram 1940) 34

Figure 3.2 (left): Drum Permeameter (Hillis & Truscott 1983) and; 36

Figure 3.3 (right): Timber Flume (Hillis & Truscott 1983). 36

Figure 3.4: Filter test apparatus used by Sherard et al. (1984a). 37

Figure 3.5: High Pressure “Slot” Test Apparatus (Sherard et al. 1984b). 39

Figure 3.6: High pressure “Slurry” Test Apparatus (Sherard et al. 1984b). 40

Figure 3.7: Test arrangement using 245 mm diameter seepage cell (Kenney & Lau 1985). 41

Figure 3.8: Test arrangement using 580 mm diameter seepage cell (Kenny and Lau, 1985). 41

Figure 3.9: No Erosion Filter Test Details – No Scale (Sherard & Dunnigan 1985). 43

Figure 3.10: Permeameter for Screen Tests (Lafleur et al. 1989). 45

Figure 3.11: Filter test apparatus for compatibility tests (Lafleur 1984). 46

Figure 3.12: State of no clogging (Okita & Nishigaki 1993). 47

Figure 3.13: State of clogging (Okita & Nishigaki 1993)....48

Figure 3.14: Process of self-filtration (Okita & Nishigaki 1993)....48

Figure 3.15: Skempton and Brogans' upward flow test apparatus (Skempton & Brogan 1994)....51

Figure 3.16: Schematic diagram of the test layout (Tomlinson & Vaid 2000)....52

Figure 3.17: Schematic design of the permeameter (Tomlinson & Vaid 2000)....52

Figure 3.18: CEF Test Apparatus (Foster & Fell 2001a)....54

Figure 3.19: Summary results of statistical analysis and proposed criteria of no-erosion boundary of filter tests for assessment of filters of existing embankment dams (Foster & Fell 2001a)....54

Figure 3.20: Conceptual erosion boundaries of filter test behaviour (Foster & Fell 2001a)....55

Figure 3.21: The large scale permeameter used by Garner and Sobkowicz (2002)....56

Figure 3.22: Schematic diagram of hole erosion test assembly (Wan & Fell 2004b)....58

Figure 3.23: Schematic diagram of the slot erosion test assembly (Wan & Fell 2004b)....58

Figure 3.24: Configuration of Permeameter used by Fannin and Moffat (2006)....60

Figure 3.25: Large Permeameter cell commissioned by Moffat and Fannin (2006)....61

Figure 4.1: An example of the PLIF configuration used in the study of laboratory debris flows by Sanvitali (2010)....64

Figure 4.2: Example of refractive index matching materials (the rod is resting on the bottom of the beaker) (Sanvitali 2010)....65

Figure 4.3: a) Diagram of singlet energy levels of a molecule, including superimposed vibrational and rotational energy levels. b) Example of excitation and fluorescent emission, E = energy difference between the origin and destination energy levels during excitations and emission of light h = Planck's constant; c = the speed of light; λ = the wavelength of the absorbed or emitted light. The energy of the light is inversely proportional to the wavelength of the light (E = hc/λ) that is, shorter-wavelength light is higher energy than longer-wavelength light (Amersham Biosciences Technical Note #57 in Sanvitali (2010))....67

Figure 4.4: Powell Lens (Sanvitali 2010)....68

Figure 4.5: Line of laser light generated, projected onto a wall in a dark room....69

Figure 4.6: Laser line generator system (OZ Optics in Sanvitali (2010))....69

Figure 4.7: a) Fibre optic cable coupling to the line generator, or Powell lens; b) Lased light generator and coupling to the fibre optic cable. 69

Figure 4.8: MotionPro Y4 camera for capturing images. Note the light filter over the lens. 70

Figure 4.9: Internal transmittance of the employed optical filter at reference thickness d (mm) = 3 (Schott data sheet in Sanvitali (2010). 71

Figure 4.10: Refractive index as function of wavelength for Duran glass (Schott private communication) and hydrocarbon oil 5095 (Cargille data sheet) in Sanvitali (2010). 72

Figure 4.11: Absorption and emission spectra of Nile Red in the hydrocarbon oil. The concentration of the sample is 5mg/l (Sanvitali 2010). 73

Figure 4.12: Transparent Soil Permeameter encasing Borosilicate glass 'soil' and hydrocarbon oil fluid (illuminated by laser sheet). 73

Figure 4.13: Zones of laminar and turbulent flows (Taylor (1948) cited by Sanvitali (2010)). 75

Figure 4.14: Example of PSD for Skempton and Brogan (1994) soil sample A and equivalent Glass PSD. Also shown is the limiting glass particle size (in red) for the transparent soil permeameter. 77

Figure 4.15: Rods and tubes used for the production of the solid grains (Sanvitali 2010). 78

Figure 4.16: Steel slabs used for crushing the glass tubing to make fine particles. 78

Figure 4.17: Bench machine used for producing larger particles by cutting the glass rods. 79

Figure 4.18: Coarse glass particles used as transparent solid (Sanvitali 2010). 79

Figure 4.19: Fine glass particles used as transparent solid (Sanvitali 2010). 80

Figure 4.20: Glass particles being washed in methylated spirits bath. Particles are then poured into water before rinsing through a sieve. 81

Figure 4.21: Clean glass particles are sieved and separated into like particles sizes, ready for the creation of a different PSD. 81

Figure 4.22: a) oil is added to the glass PSD and then; b) the glass particle-oil mixtures are placed into vacuum desiccators. 82

Figure 4.23: A teaspoon is used to scoop the saturated and de-aired glass particles out of prepared PSD mixture, and into the permeameter, which has a layer of oil to keep particles saturated. 83

Figure 4.24: Schematic sketch of proposed apparatus. 84

Figure 4.25: As built dimensions of the 'transparent soil permeameter'. 85

Figure 4.26: a) steel frame support; b) steel mesh with PVC seal and; c) mesh over frame as set up inside permeameter......87

Figure 4.27: a) Original apparatus before modification – note 2x 15 mm Ø outlet ports and; b) Apparatus after modifications - note increase in port to 40 mm Ø, a total of 5 piezometer ports, additional silicon sealant around base. 88

Figure 4.28: a) Outlet ports prior to steel mesh installation and; b) Outlet ports with steel mesh installed......88

Figure 4.29: a) Test specimen resting on mesh directly over diffusment particles (notice the uplifting mesh and undulations; b) test specimen resting on mesh, supported by steel frame and sealed with PVC tube. Also note increase from 3 to 5 piezo ports. 89

Figure 4.30: Davies and Onga Pump used to pump oil into header tank. 90

Figure 4.31: Outlet pipes returning oil back into reservoir......90

Figure 4.32: Original wall mounting system for header tank. 91

Figure 4.33: Oil control system: a) Bench with attached hand winch, header tank and piezometer tubes; b) header tank with height scale; c) hand winch to control head. 92

Figure 4.34: Rotameter calibrations in a selection of preliminary tests......93

Figure 4.35: G100CF and G100FF PSD curves. 94

Figure 4.36: Bimodal granular material: volumes and porosity as a function of the proportion of fines in a constant total weight of grains (Skempton & Brogan 1994). 96

Figure 4.37: G22FF and G40FF PSDs. 96

Figure 4.38: Skempton and Brogan PSDs (Skempton & Brogan 1994). 98

Figure 4.39: Skempton and Brogan (1994) specimen parameters for tested soils. 98

Figure 4.40: PSD of Skempton and Brogan (1994) soil sample 'A' and the GS&B-A replication......99

Figure 4.41: PSD of Skempton and Brogan (1994) soil sample 'B' and the GS&B-B replication......99

Figure 4.42: PSD of Skempton and Brogan (1994) soil sample 'D' and the GS&B-D replication. 100

Figure 4.43: S&B-Hybrid PSD......101

Figure 4.44: Specimen parameters for the Fannin and Moffat (2006) G4-C sample......101

Figure 4.45: GF&M-G4C replication of Fannin and Moffat (2006) G4-C sample. 102

Figure 4.46: Wolds Till Lining material, design grading range (Benson 2011) 103

Figure 4.47: PSD of Glass Long Tail and 'prototype' soil PSD, in which the glass PSD is modelling. . 104

Figure 4.48: Selection of an intensity range that will 'highlight' the 'open void space' (in red), to create the 'mask', also shown. 106

Figure 4.49: Example of selecting a threshold, or intensity range, to 'highlight' (in red) the coarser fraction, in this case. 106

Figure 5.1: Burenkova (1993) plot for predicting stability of G100CF and G100FF. 110

Figure 5.2: Wan and Fell (2008) approach to stability analysis for the G100FF and G100CF materials. 111

Figure 5.3a-b: Pre test slices of the G100CF sample: a) 1 cm and; b) 2 cm from front wall. 112

Figure 5.4: Average hydraulic gradient vs. flow velocity (corrected) in the G100CF test 113

Figure 5.5: Pre-test Image of G100FF - loose sample. 114

Figure 5.6: Average hydraulic gradient vs. flow velocity (corrected) for the G100FF - loose test. ... 115

Figure 5.7: 'Fluidised' G100FF - loose sample. Note lighter areas where surges of oil are flowing, therefore having a lower density of particles. 115

Figure 5.8: Average hydraulic gradient vs. flow velocity (corrected) for the uniform G100FF - compact test. 116

Figure 5.9: Kenney and Lau (1985) method for stability analysis on G22FF and G40FF samples. Also shown on graph is the Kezdi (1979) boundary for stability. 117

Figure 5.10: Burenkova (1993) plot for predicting stability of G22FF and G40FF. 118

Figure 5.11: Wan and Fell (2008) approach to stability analysis for G22FF and G40FF tests. 118

Figure 5.12a-d: Slices through the G22FF-2 sample prior to testing commenced. Images a-d are from 1 cm, 2 cm, 3 cm and 4 cm from the front of the apparatus respectively. 120

Figure 5.13: Average hydraulic gradient vs. flow velocity in the G22FF-2 test. 121

Figure 5.14a-b: Changes in the G22FF-2 sample between i_{av} = 0 (a) to 0.152 (b). White circles showing some of the areas with minor change. 122

Figure 5.15a-b: At i_{av} = 0.238 there is a washout of fines (outlined in white circles) mainly along the right hand glass wall, before particles stabilise again. a) shows the G22FF-2 sample just before the onset, and b) 170 seconds later. 122

Figure 5.16: Post G22FF-2 test slices at a) 1 cm; b) 2 cm; c) 3 cm and d) 4 cm. 123

Figure 5.17a-d: Pre-test slices of G40FF-2 sample at a) 5 mm; b) 10 mm; c) 15 mm and; d) 20 mm from front wall. 124

Figure 5.18: Average hydraulic gradient vs. flow velocity (corrected) in G40FF-2 test - failure within sample. 125

Figure 5.19: Average hydraulic gradient vs. flow velocity (corrected) in G40FF-3 - failure along glass wall. 126

Figure 5.20: Kenney and Lau (1985) diagrams for GS&B-A, GS&B-B and GS&B-D materials. 128

Figure 5.21: Burenkova (1993) plot showing predicted stability of GS&B-A, GS&B-B and GS&B-D materials. 129

Figure 5.22: Wan and Fell (2008) approach to stability analysis for GS&B-A, GS&B-B and GS&B-D materials. 129

Figure 5.23a-c: Pre test slices of sample GS&B-A at a) 1 cm; b) 2 cm and; c) 3 cm from front of apparatus. 131

Figure 5.24: Average hydraulic gradient vs. flow velocity for GS&B–A. 132

Figure 5.25a-b: Change in particle structure of Glass S&B-A between a) i_{av} = 0 and; b) i_{av} = 0.153. Note some changes highlighted with white circles where fines have migrated away. 133

Figure 5.26a-b: Chances in particle structure of Glass S&B-A between a) i_{av} = 0.248 and; i_{av} =0.286. Note some changes highlighted with white circles. 133

Figure 5.27a-b: Change in particle structure of GS&B-A between a) i_{av} = 0.286 and; b) i_{av} = 0.381, with a selection of changes highlighted in white where fines have migrated away. 134

Figure 5.28: GS&B-B sample at beginning of test. 135

Figure 5.29: Average hydraulic gradient vs. flow velocity for GS&B-B. 136

Figure 5.30: Minor changes in material structure in GS&B-B between a) i_{av} = 0.1 and b) i_{av} = 0.157 (some changes highlighted in white circles). 136

Figure 5.31: Changes in GS&B-B between a) i_{av} = 0.229 and; b) i_{av} = 0.5. 137

Figure 5.32: GS&B-B between a) i_{av} = 0.621 and; b) i_{av} = 0.879. Note air bubbles in oil degrading image quality. 137

Figure 5.33: GS&B-B at i_{av} = 1.014 when the sample failed by ‘heave’. ‘Gap’ in material shows where upper portion of sample has heaved. 138

Figure 5.34: Average hydraulic gradient vs. flow velocity for GS&B–D. 139

Figure 5.35: GS&B-D at, a) i_{av} =0.5 and; b) i_{av} = 1.33 when 'heave' first observed. 140

Figure 5.36: GS&B-D at a) i_{av} = 1.54 and; b) i_{av} = 1.63. 141

Figure 5.37: PSD of GS&B-Hybrid. Also shown is a ‘prototype’ soil PSD, in which the glass PSD is modelling. 142

Figure 5.38: Kenny and Lau Analysis for GS&B-Hybrid. 142

Figure 5.39: Burenkova (1993) plot for predicting stability of GS&B-Hybrid. 143

Figure 5.40: Wan and Fell Analysis for GS&B-Hybrid. 143

Figure 5.41: Pre test slices of GS&B-Hybrid at a) 1 cm; b) 2 cm; c) 3 cm and; d) 4 cm from front of apparatus. 145

Figure 5.42: a) Calibration dots at 15 mm from front of permeameter, and; b) first test image, at 15 mm from front of permeameter. 146

Figure 5.43: Average hydraulic gradient vs. flow velocity for GS&B-Hybrid. 147

Figure 5.44: GS&B-Hybrid changes in structure between a) i_{av} = 0 and; b) i_{av} = 0.152. 147

Figure 5.45: GS&B-Hybrid changes in structure between a) i_{av} = 0.152 and; b) i_{av} = 0.19. 148

Figure 5.46: Change in particle structure of GS&B-Hybrid between a) i_{av} = 0.19 and; b) i_{av} =0.276.. 148

Figure 5.47: Change in structure of GS&B-Hybrid between a) i_{av} = 0.33 and; b) i_{av} = 0.6. Note washing out of fines. 149

Figure 5.48: Post-test slices of GS&B-Hybrid at a) 1 cm; b) 2 cm; c) 3 cm and; d) 4 cm from front of apparatus. 150

Figure 5.49: Kenney and Lau (1985) plot for GF&M-G4C. 151

Figure 5.50: Burenkova (1993) plot for predicting stability of GF&M-G4C. 152

Figure 5.51: Wan and Fell approach to stability analysis for GF&M-G4C. 152

Figure 5.52: Average hydraulic gradient vs. flow velocity for GF&M-G4C. 154

Figure 5.53: GF&M-G4C at a) i_{av} = 0 and; b) i_{av} = 0.5. 154

Figure 5.54: GF&M-G4C at a) i_{av} = 0.58 and; b) i_{av} = 0.72. 155

Figure 5.55: Kenney and Lau (1985) analysis for Glass Long Tail specimen. 156

Figure 5.56: Burenkova (1993) plot for stability analysis of Glass Long Tail. 156

Figure 5.57: Wan and Fell (2008) approach to stability analysis for Glass Long Tail specimen. 157

Figure 5.58: Average hydraulic gradient vs. flow velocity for Glass Long Tail test. 158

Figure 5.59: Glass Long Tail test at, a) i_{av} = 0 and; b) i_{av} = 0.143. 158

Figure 6.1: An example of 'masks' created from a) an unprocessed image, to highlight; b) the coarser fraction (in white), and; c) open void space (in white). 162

Figure 6.2: Image processing in ImageJ for GS&B-Hybrid, pretest 1 cm, showing a) unprocessed slice; b) image with pseudo flatfield filter; c) coarser fraction mask, and; d) particle outlines, with boundary particles excluded. 165

Figure 6.3: Rose diagrams showing long axis particle orientation for 1 cm slices of GS&B-Hybrid for a) pre-test and; b) post-test. '0' points towards the vertical. 166

Figure 6.4: Rose diagrams showing long axis particle orientation for 2 cm slices of GS&B-Hybrid for a) pre-test and; b) post-test. '0' points towards the vertical. 167

Figure 6.5: Rose diagrams showing long axis particle orientation for 3 cm slices of GS&B-Hybrid for a) pre-test and; b) post-test. '0' points towards the vertical. 167

Figure 6.6: Rose diagrams showing long axis particle orientation for 5 cm slices of GS&B-Hybrid for a) pre-test and; b) post-test. '0' points towards the vertical. 168

Figure 6.7: GS&B-Hybrid test results showing 6 phases. 169

Figure 6.8: a) Original image; b) Right hand half of image for processing; c) Division of sections 1-3. 170

Figure 6.9: Example of applying a mask to images in order to calculate the 'open void' area. 170

Figure 6.10: Area occupied by 'open voids', as a percentage of frame area for sections 1, 2 and 3 across 6 phases in the GS&B-Hybrid test. 172

Figure 7.1: Test results from S&B-A (Skempton & Brogan 1994). 178

Figure 7.2: GS&B-A PSD and a scaled PSD of Skempton and Brogan (1994) 'A' (Scaled S&B-A) showing D_{15} values 179

Figure 7.3: Test results from S&B-B (Skempton & Brogan 1994). 183

Figure 7.4: Test results from S&B-C (Skempton & Brogan 1994). 184

Figure 7.5: Light-particle interaction between laser sheet and glass particles of varying sizes. 195

List of Tables

Table 3.1: Recommended criteria with conservative safety factor for impervious soil groups. Compiled from Sherard and Dunnigan (1985). 44

Table 4.1: Solid and fluid properties (Sanvitali 2010). 72

Table 5.1: Summary PSD analysis for G100CF. 111

Table 5.2: Summary PSD analysis for G100FF. 114

Table 5.3: Summary PSD analysis and theoretical critical hydraulic gradient values for G22FF and G40FF materials. 119

Table 5.4: UBC vs. UC summary test data for GB22-0, GB22-50, GB22-100 and G22FF tests. 127

Table 5.5: UBC vs. UC summary test data for G40FF tests. 127

Table 5.6: UBC vs. UC summary test data for 100%FF and G100FF tests. 127

Table 5.7: Summary PSD analysis and theoretical critical hydraulic gradient for GS&B-A, GS&B-B and GS&B-D materials. 130

Table 5.8: Void ratio and porosity of GS&B-A, GS&B-B and GS&B-B materials. 130

Table 5.9: Summary of PSD Analysis for GS&B-Hybrid. 144

Table 5.10: Summary of PSD analysis for GF&M-G4C. 153

Table 5.11: Summary PSD analysis for Glass Long Tail specimen. 157

Table 6.1: Calculated and measured parameters from image processing of GS&B-Hybrid. 162

Table 6.2: Calculations of void ratio and porosity using pre-test slice images for GS&B-Hybrid. 164

Table 6.3: Area of open voids as a percentage of frame area, across sections 1, 2 and 3, in GS&B-Hybrid test. 171

Table 7.1: Comparison of properties between Skempton and Brogan (1994) samples and GS&B samples. 178

Table 7.2: Comparison of properties between F&MG4-C and GF&M-G4C samples. 187

Table 7.3: Comparison of methods for evaluating stability of each PSD. The observed stability of the tested material is noted in brackets below the named specimen, while the coloured boxes show the

predicted stability. Green shaded boxes = stable, orange = boundary between stability and instability (transition zone), and red = unstable. 190

Notation

A	cross sectional area (m^2)
C_H	Hazen empirical coefficient
$C_{k\text{-}c}$	Kozeny-Carmen empirical coefficient
C_e	proportionality constant (coefficient of soil erosion) (s/m)
C_u	uniformity coefficient = (D_{60}/D_{10})
D	grain size (mm)
$(D'_{15}/d'_{85})_{max}$	maximum grain size ratio between coarser fraction and finer fraction, after the PSD has been split, following the Kezdi (1979) analysis
$(D'_{15}/d'_{85})_{min}$	minimum grain size ratio between coarser fraction and finer fraction, after the PSD has been split, following the Kezdi (1979) analysis
D_{15}	grain size of the filter material where 15% by weight is finer (mm)
$D_{15}^{'}$	grain size of the coarser fraction where 15% by weight is finer (mm)
d_{15}	grain size of the base soil where 15% by weight is finer (mm)
$d_{15}^{'}$	grain size of the finer fraction where 15% by weight is finer (mm)
$d_{85}^{'}$	grain size of the finer fraction where 85% by weight is finer (mm)
d_{SF}	characteristic diameter of base particles capable of initiating self-filtration
D_{10}	particle size for which 10% of the soil is finer (cm)
D_{eff}	effective diameter
e	void ratio

ε	extinction coefficient
F	mass fraction smaller than particle diameter, D
f_i	fraction of particles between sizes D_{li} and D_{si}
g	gravitational acceleration ($m.s^{-2}$)
H	a particle size between D and 4D
i	hydraulic gradient
I	erosion rate index
$\tilde{\imath}_{HET}$	hole erosion index
i_{av}	average hydraulic gradient
i_c	theoretical critical hydraulic gradient
i_{cr}	critical hydraulic gradient observed in test
k	Darcy’s permeability ($m.s^{-1}$)
n	porosity
PSD	particle size distribution
Q	quantity of flow measures (mm^3)
R_t	temperature correction factor for viscosity
S*	critical content of fines
S_0	specific surface area per unit volume of particles (1/cm)
t	time elapsed (s)

v	velocity (ms^{-1})
σ_{vm}	mean vertical effective stress
α	‘alpha’ reduction factor
σ'_f	effective stress of finer particles
ρ	specific gravity
ϕ	quantum yield
γ	unit weight of permeant
γ'	average effective stress
$\gamma'z$	average effective stress across a section at depth, z
γ_w	unit weight of water

Chapter 1: Introduction

1.1 Motivation

Embankment dams are required to retain their structural integrity if they are to be cost effective and safe for the environment and people surrounding them. Seepage through dams can lead to seepage erosion, including the process of suffusion (where fine grains move through a matrix of coarse grains with no change in volume), which can be attributed to over half of the historical embankment dam failures (Foster et al. 2000). An increasing amount of work is being targeted towards issues around the field of suffusion, especially following the occurrence of multiple sinkholes in the WAC Bennet Dam (Moffat & Fannin 2006) and other similar events elsewhere. The majority of recent laboratory based work has aimed at gaining quantitative empirical data by which criteria for the initiation of suffusion can be applied: Sherard and Dunnigan (1985, 1989), Lafleur et al. (1989), Burenkova (1993), Skempton and Brogan (1994), Foster (1999), Tomlinson and Vaid (2000), Foster and Fell (2001a), Garner and Sobkowicz (2002), Wan and Fell (2002), Fannin and Moffat (2006), Moffat and Fannin (2006), Moffat and Fannin (2006), Wan and Fell (2004a, 2008). 'Filters' in zoned embankment dams have the job of protecting adjacent soils from the loss of particles, or internal erosion, while allowing sufficient flow in which to relieve pore water pressure through the dam. In this thesis, a new approach to study the mechanisms of internal erosion is developed.

An apparatus for testing filter materials will typically consist of a clear cylindrical tube in which a base, and/or filter specimen is placed. Measurements of water flow through the specimen, hydraulic gradient, and visual observations about the top and sides of the test materials are typically made, while in some cases the tested material will undergo a grain size analysis, or dissection for visual observations. One major constraint to this style of testing is that one can only visually see the outside of the test material during a test. Unfortunately, observations made from the walls of rigid permeameters may not be representative of that occurring inside the test material, due to inhomogeneities in the soil structure that are often present at the sidewalls. To truly understand mechanisms occurring within a soil during internal erosion processes, an ideal method would allow one to 'see' inside the soil material as internal erosion processes develop.

To the best of the author's knowledge, the only attempt made to apply internal visualisation to the laboratory study of suffusion, was undertaken by Rosenbrand (2011) who used tracer particles within a soil, then applied particle image velocimetry (PIV), particle tracking (PT) and image subtraction (IS) computer techniques to study suffusion behaviour. This research aimed to apply spatial and temporal resolution that is lacking in outflow experiments, as noted by Baumann and Werth (2004). Despite the success of this technique, it does not solve the problem of being able study internal erosion deep within the soil. In order to achieve this aim of 'seeing' inside a soil, a slightly novel technique was proposed.

In the study of model debris flows, Sanvitali (2010) used a visualisation method involving glass and oil as a substitute to soil and water. Using these materials and a process known as Planar Laser Induced Fluorescence (PLIF), the dynamic condition occurring inside model debris flow was successfully studied, using GeoPIV software for image analysis.

1.2 Objectives

The objective of this research was to commission and trial an apparatus that could induce internal erosion using glass and oil mixtures, while capturing images from within the test material. A literature review of filters in embankment dams including their design criteria was undertaken, as well as a review of current testing apparatuses, to help form a basis for the design of this experiment. An experimental setup then was designed that allowed a test specimen to be placed into a 'transparent soil permeameter' and a flow induced until internal erosion mechanisms initiated. Using PLIF, fluorescent dye within the oil fluoresced under illumination by a sheet of laser light. Glass particles of a replicated soil do not fluoresce, thereby appearing as dark outlines within the bright background. To counteract the effects of using a higher viscosity fluid, the glass particles were scaled up accordingly, which also helped in visualisation as particles were increased in size. Using a camera, images of the illuminated slice within the 'soil' were captured, which were able to be viewed as a sequence for qualitative analysis, or analysed using Image Pro and ImageJ software.

Once a working apparatus had been commissioned, the primary aim was to validate the use of glass-oil mixtures for the study of internal erosion processes. To do this, a number of tests were performed to assess flow behaviour through 'soils' of equal particle size of typical filters to validate, a) Darcy's law for laminar flow (Darcy 1856) and, b) Terzaghi's predicted critical hydraulic gradient (Terzaghi 1925). Assuming that these simple laws were valid, soil materials previously tested by other authors, namely Skempton and Brogan (1994) and Fannin and Moffat (2006), were replicated and tested to assess how the artificial glass-oil mixtures compared to soil-water materials.

In summary, the objectives of this research were to:

- Commission a permeameter and accompanying control system that will allow glass and oil filter replications to be tested with the ability to initiate internal erosion through the specimen.
- Carry out tests using the ‘transparent soil permeameter’ and make an assessment as to the validity of this methodology by comparing results to those already published.
- Use image sequences from inside the ‘soil’ to make an examination of the mechanisms occurring inside the material.
- Use Image Pro and ImageJ software to create qualitative and quantitative outputs from the collected test images.

Chapter 2: Filter materials for embankment dams

This chapter outlines the purpose and importance of filters in embankment dams. It describes the mechanisms acting on filters during stability and instability, and different design criteria that have been developed for predicting behaviour of filter materials. Finally, methods to evaluate filter performance are considered.

2.1 Embankment Dams: Overview

Evidence of engineering and construction of dams and canals has been dated as far back as 2000 BC. Some examples include the Marib dam in Yemen where construction began around 750 BC and took 100 years to complete, consisting of a 4 metre high embankment and stone sluices for regulation control; a rock and earthfill dam in what is now Syria, constructed around 1300 BC and is still in use today; and numerous low dams built by Romans, including the famous Cornalbo earth dam in southern Spain, which had a height of 24 metres and a length of 185 meters (ICOLD 2008). It is also interesting to note that embankment dams (consisting of earth, rock and earth-rock combinations) represent about 75% of all dams in the world (ICOLD 2008). Today, embankment dams are typically constructed for hydroelectric power generation, irrigation storage water and municipal water supply.

Engineered embankment dams generally consist of a number of zones including a central 'impermeable' core, shoulder fill material providing strength to the dam, and filters to channel seepage flow and relieve pore water pressures within the dam (Figure 2.1). The stability of a dam is also enhanced when the downstream slope is kept free from seepage, which filters aim to achieve, resulting in stable, unsaturated compacted fill on the downstream shoulder (Thomas 1976).

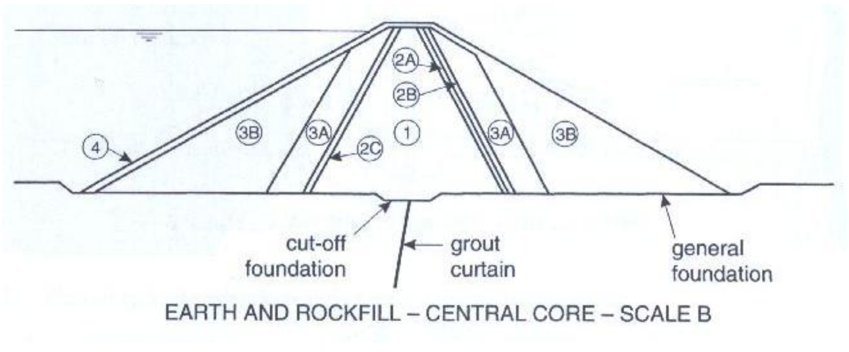

Figure 2.1: Example of an embankment dam showing the various zones: 1 – central core; 2A and 2B are both downstream filters, and 2C is an upstream filter; 3B – shoulder fill (Fell et al. 2005).

2.2 Embankment dam failures

There are many cases where earth and earth-rock dams have been unsuccessful in containing storage water. There are a number of modes of failure which can be generally categorised into three groups: overtopping and appurtenant; piping; and slides. Foster et al. (2000) summarised embankment dam incidents on 11,192 reported cases from around the world, dating back to pre 1900 and up until 1986. This number does not include Chinese or Japanese dams prior to 1930. The research by Foster et al. (2000) mainly focused on incidents relating to internal erosion and slope instability and was part of a greater research project to study methods for estimating the probability of failure of embankment dams for use in quantitative risk assessment (QRA). Selected statistics relating to incidents involving internal erosion are summarised from Foster et al. (2000) below. In addition, embankment dam zoning categories according to Foster et al. (2000) are shown in Figure 2.2.

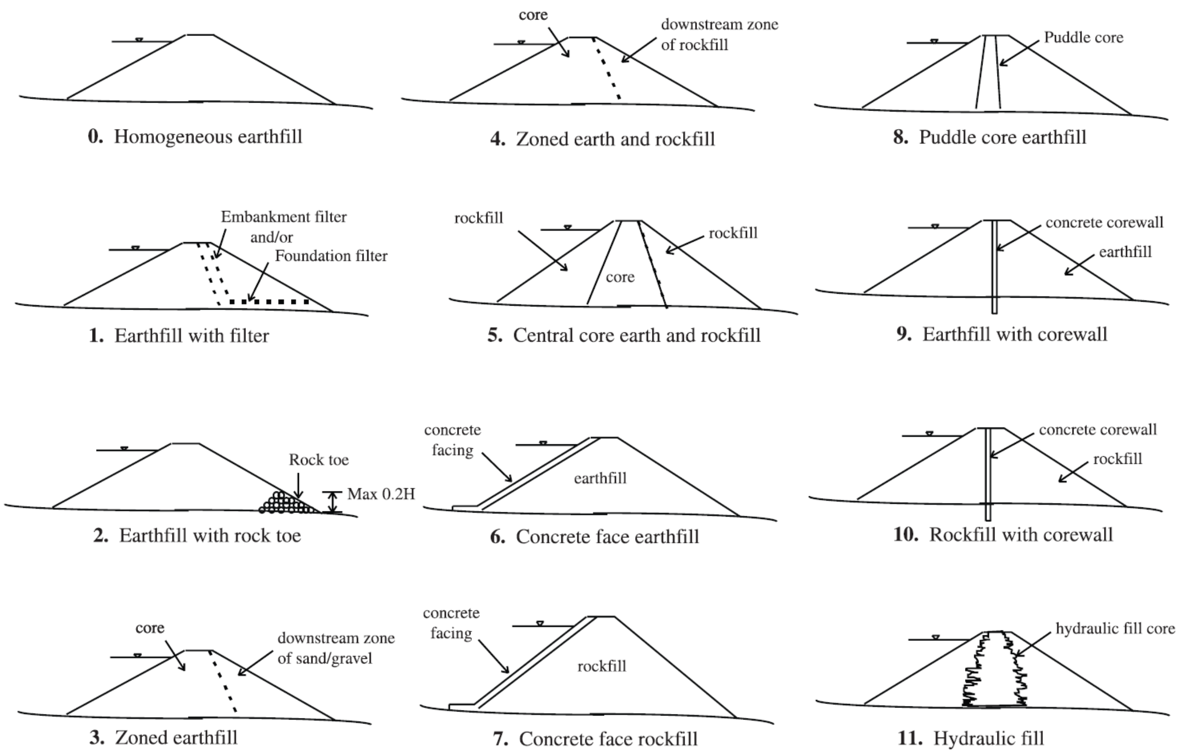

Figure 2.2: Dam zoning categories (Foster et al., 2000).

The study of internal erosion through embankment dams is important for environmental, protection of human and animal life, and financial reasons. Furthermore, there are a significant number of embankment dams worldwide (where the category of 'rockfill dams', may be comprised of zoned earth and rockfill dams, central core earth and rockfill dams, concrete face rockfill dams, or rockfill with corewall dams), accounting for 21% of all dams worldwide.

From the 11,192 dams in the study by Foster et al. (2000), 136 or 1.2% 'failed'. Failure modes included flood overtopping (46), gate-spillway failure (16), piping through the embankment (39), piping through the foundation (19), piping from the embankment into the foundation (2), slope instability, and earthquake-liquefaction induced failures (2), while there were also some failures of unknown mode (8). In addition, approximately half of all failures in large dams involved piping, slope instability or an earthquake, of which piping failures accounted for about half of these. To further elaborate, piping through the embankment is two times higher than piping through the foundation, and is 20 times higher than piping from the embankment into the foundation. It is therefore evident that piping, and therefore internal erosion, is an important process to understand when considering the long lasting stability of embankment dams.

Interestingly, Foster et al. (2000) found that homogeneous dams have the highest frequency of failure, being nearly five times higher than the average for all dams combined. Dams of earthfill with rock toe, concrete face earthfill and puddle core earthfill dams make up 80% of failure cases, while only making up 25% of the population. The causes of many failures studied were found to be due to piping around conduits that passed through the dam, piping through poorly compacted fill materials, and piping through dispersive fill materials. From the dams that failed due to piping, earthfill dams with a rock toe had one of the highest frequencies of failure. In these cases, failure and accidents were attributed to outlet conduits passing through the dam, piping of the fill materials into coarse rockfill materials, or piping through cracks which formed through the dam over irregularities in the foundation or steep abutments.

In contrast to types of dams that have suffered the majority of failures, zoned earthfill dams have a relatively low probability of failure. However, where zoned earthfill dams have suffered failures, it is interesting to note that in four of the seven failed dams, there was no embankment filter which allowed the core to erode into the downstream rockfill. Furthermore, from the 21 piping accidents in central core and rockfill dams, 15 of these involved piping in materials of broadly graded core materials of glacial origin into coarse or segregated filters. It is evident from Foster et al. (2000) that dams with core materials of glacial origin have experienced more piping accidents than those built from other materials. Furthermore, as could be expected, dams that had poor compaction of core materials experienced higher than average accidents, while those with good compaction experienced lower than average accidents.

When comparing accidents to failures, it was concluded that the relatively high amount of accidents compared to the lower amount of failures is reflective of the slow movements involved, and that warnings are usually given to indicate slope instability problems. Therefore, remedial actions or drawing down the reservoir level are usually possible.

As shown in Figure 2.3, the frequency of piping failures in dams is significantly higher upon first filling and in the early stages of the dam's life. However, there is also a tendency for piping incidents to increase in older dams. Piping and mechanisms causing internal erosion are discussed later in this Chapter.

Figure 2.3: Time after construction of incidents of piping through the embankment (Foster et al., 2000).

2.3 Basic requirements of filters in embankment dams

There are two fundamental functions that are required by filters in earth, earth-rock, and rockfill embankment dams. These are:

1) Retention function: Also referred to as the stability criterion, this function requires that the filter must prevent the migration of soil particles from the adjacent filter, foundation or fill materials. Therefore, the filter must be capable of preventing the migration of finer-grained impervious fill or foundation material.
2) Permeability function: This function requires that the filter must be able to accept seepage flows from adjacent foundation or fill materials, or that coarse filters must be able to accept the flows from adjacent upstream fine filters without the build-up of excess hydrostatic pressure. Specifications as to adequate permeability ratios have been prescribed, and it is

commonly quoted that adjacent filter materials should be at least 25 times greater than adjacent materials. Further variations as to this value are summarised later in Chapter 2.

For the above functions to be achieved, an ideal filter or filter zone must adhere to the following, as listed by ICOLD (1994):

1) Not segregate: Avoiding segregation may be the most important criterion in creating a successful filter. The filter gradation material must remain sufficiently uniform during processing, handling, placing, spreading and compaction, especially between the interfaces of adjacent materials.
2) Not change in gradation: The prescribed gradation must not only be maintained during processing, handling, placing, spreading and compaction, but also with time, hence must not degrade due to freeze thaw or seepage flow. To achieve this, particles must be hard and durable, and not be susceptible to degradation due to slaking, weathering, or other mechanisms. If a gradation is not maintained, the retention and permeability criteria may be compromised. To check materials after construction, samples should be tested and compared against the original prescription.
3) Have no apparent or real cohesion: The materials used should not have the ability to cement as a result of chemical, physical or biological action. The filter must remain cohesionless to avoid cracking, even if an adjacent material has itself cracked.
4) Have internal stability: The coarser fraction of the filter material, with respect to its own finer fraction, must meet the retention criterion. For broadly graded materials, segregation during handling and placement is more likely, therefore internal stability can become a problem. In this thesis, issues surrounding internal stability or instability form the primary focus.
5) Have sufficient discharge capacity: Seepage entering the system should be conveyed safely and readily with little head loss, therefore filter systems need to be designed with ample discharge capacity. The design of these systems should consider the worst case scenario, which might occur from a cracked core, hydraulic fracturing or core segregation. It may be difficult to achieve a design that accounts for the retention criteria and sufficient discharge capacity, so either a large single zone or a filter with a free draining zone may be required.
6) Have the ability to control and seal a concentrated leak: Leaks through the core must be sealed in the event that they form. Tests have been developed to test the ability of filters in achieving this (Hillis and Truscott (1983); Sherard et al. (1984b); Sherard and Dunnigan (1985); Sherard and Dunnigan (1989); Foster and Fell (2001b)).

2.4 Flow conditions acting on filters

Two basic flow conditions can exist between a base material and filter, as shown in Figure 2.4.

1) Perpendicular flow: Flow in this direction may exist in a number of locations including the contacts between upstream or downstream core and fine filters, coarse and fine filters, or between up or downstream contacts between foundation soils and blankets with filter layers (Figure 2.4).
2) Parallel flow: Parallel flow may occur between contacts with bedding filters and base material, between slope protection and base soils, or at the contacts between coarse and fine filters (Figure 2.4).

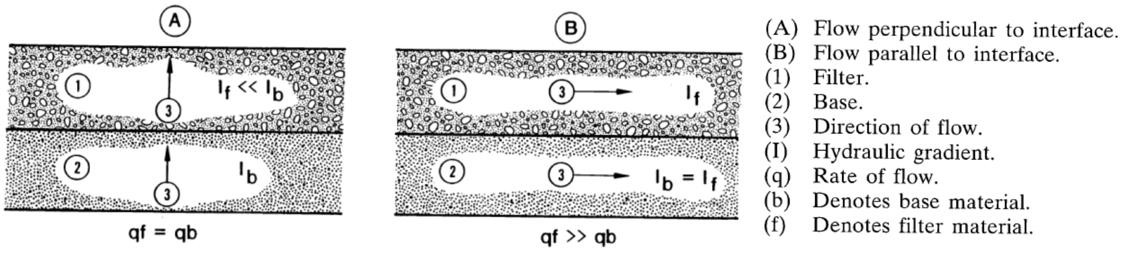

Figure 2.4: Flow perpendicular (left) and parallel (right) to filter/base interface (Bakker, et al., 1987 in ICOLD (1994)).

2.5 Internal erosion

'Internal erosion' in basic terms refers to the migration of particles initiated by the erosive forces of water along pre-existing flow paths such as cracks in cohesive material or voids in a cohesionless soil structure (Richards & Reddy 2007), creating the condition of 'internal instability'. Fell et al. (2005) describe internal instability as an inability of the coarser fraction of a soil to prevent migration of its finer fraction as a result of seepage flow. In contrast, 'internal stability' of a particle size distribution (PSD) is defined by Kenney and Lau (1985) as 'the ability of a granular material to prevent loss of its own small particles due to disturbing agents such as seepage and vibration'. The idea of a 'perfect filter' was suggested by Vaughan and Soares (1982), and is defined as a filter that will retain the smallest particles that could arise during erosion.

The basic requirement required for a particle to become mobile is that the frictional drag force must be greater than the forces holding the particle within the soil, so that the grain can detach from its parent material, as shown in Figure 2.5. Resisting forces are dependent upon the cohesion, the interlocking effect and the weight of the soil particles. When the critical force or local velocity is surpassed, the particle will move along a path that is predetermined by the internal structure of the layer (if the void space allows). Initially, it is the finest grains that are mobile and move within the interior of the layer. These grains may then stop after travelling a certain distance, or be washed out of the layer. If grains are stopped within the layer, then there is no change in the overall solid volume, only redistribution within the layer (suffusion). In the ‘zone of accumulation’ there will be a reduction in porosity and permeability, whereas there will be an increase in porosity and permeability in the ‘zone of removal’. As a result of this structural change, flow will be concentrated in the zones of increased permeability, therefore increasing the forces acting on larger particles, which may in turn result in their mobility. If particles moving along a flow path are able to leave the layer, then the overall total solid volume will be decreased (suffosion), while porosity and permeability will increase (Kovacs 1981).

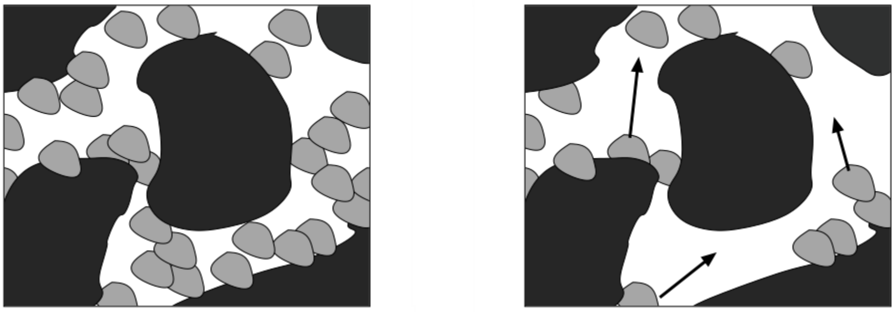

The soil without seepage flow. The pore space is not entirely filled by the fine grains.

Seepage flow mobilises fine grains (particle transport is indicated by arrows).

Figure 2.5: An example of a gap graded soil where the fine grains (light) are present in the pore space (white) of the coarse grains (dark). With the introduction of flow, the fine particles become mobile when the upward flow forces exceed the frictional and gravitational forces of the grain (Rosenbrand 2011).

Internal erosion will only occur if all the required conditions for initiation and progression are met, as shown in Figure 2.6. Garner and Fannin (2010) describe these as:

a) Material susceptibility (inability to resist internal erosion);
b) Critical hydraulic load (seepage velocities and hydraulic gradients);
c) Critical stress conditions (arching and low stresses).

According to their conceptual approach, the form and extent of the internal erosion process is determined by the combined influence of weakness, being material susceptibility, critical hydraulic gradient load and the critical stress.

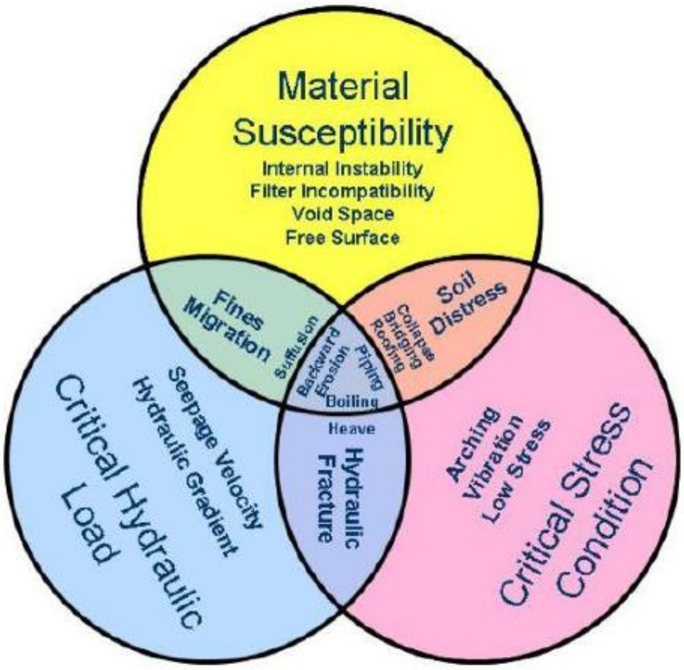

Figure 2.6: Conceptual approach showing overlapping and interacting adverse conditions and internal erosion mechanisms (Garner & Fannin 2010).

2.5.1 Erosion properties of soil

Fell et al. (2008) note that Wan (2006) and Fell and Wan (2004), Wan and Fell (2004a) developed the Hole Erosion Test (HET) to measure the erosion properties of soils used in embankment dams. In these tests, the erosion rate is expressed in the form of an Erosion Rate Index, I. Furthermore, the representative erosion rate index, $\tilde{I}_{HET}$ is defined as the hole erosion index I_{HET} for soils compacted to a density of 95% of maximum dry density at optimum moisture content. Soils were classified into 6 groups according to their $\tilde{I}_{HET}$ as shown in Figure 2.7. Additionally, Figure 2.8 was developed from testing data to give a first approximation to the likely $\tilde{I}_{HET}$ for different classifications of non-dispersive soils.

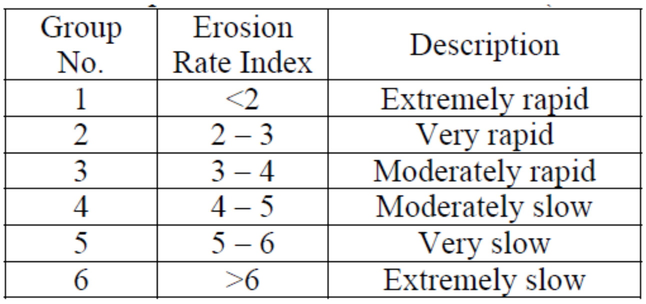

Group No.	Erosion Rate Index	Description
1	<2	Extremely rapid
2	2 – 3	Very rapid
3	3 – 4	Moderately rapid
4	4 – 5	Moderately slow
5	5 – 6	Very slow
6	>6	Extremely slow

Figure 2.7: Descriptors for erosion rates of soil (Wan (2006) in Fell et al. (2008)).

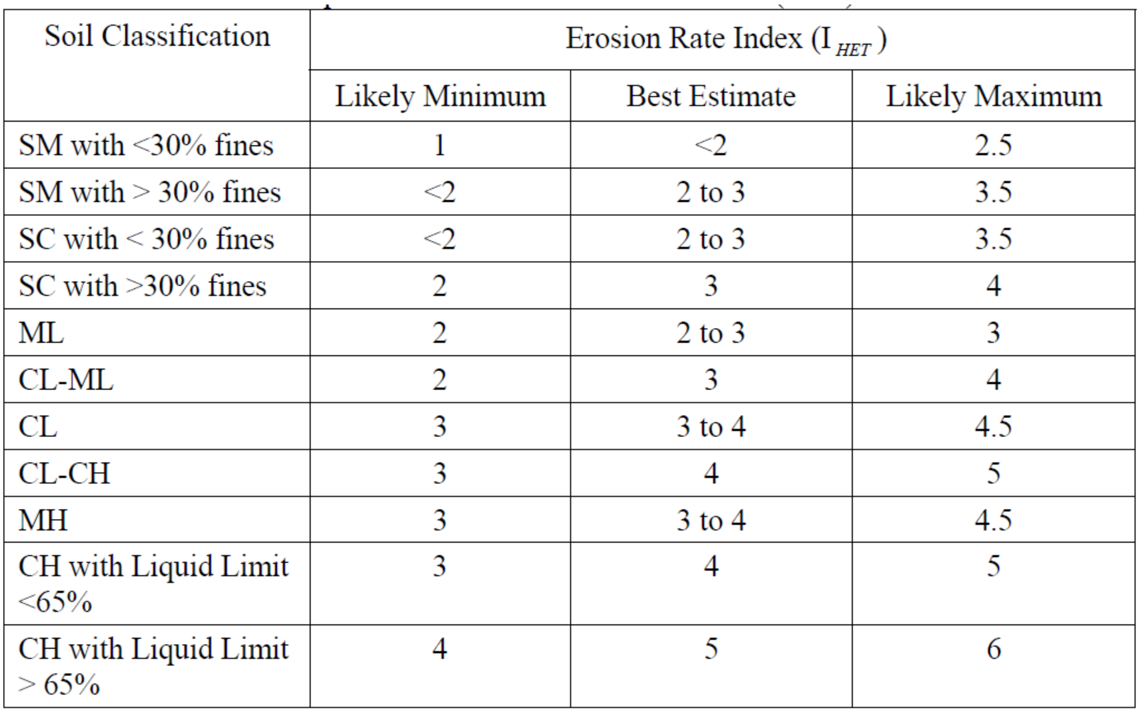

Soil Classification	Erosion Rate Index (I_{HET})		
	Likely Minimum	Best Estimate	Likely Maximum
SM with <30% fines	1	<2	2.5
SM with > 30% fines	<2	2 to 3	3.5
SC with < 30% fines	<2	2 to 3	3.5
SC with >30% fines	2	3	4
ML	2	2 to 3	3
CL-ML	2	3	4
CL	3	3 to 4	4.5
CL-CH	3	4	5
MH	3	3 to 4	4.5
CH with Liquid Limit <65%	3	4	5
CH with Liquid Limit > 65%	4	5	6

Figure 2.8: Representative erosion rate index ($\tilde{I}_{HET}$) versus soil classification for non dispersive soils based on Wan and Fell (2002) in Fell et al. (2008).

2.5.2 Suffusion

Bonelli and Marot (2008) note that Pavlov introduced the term ‘suffusion’ in 1898. ‘Suffusion’ is described by Moffat et al. (2011, p. 399) as when “the finer fraction of an internally unstable soil moves within the coarser fraction without any loss of matrix integrity or change in volume”. This process is also described as ‘internal suffusion’ by Kovacs (1981, p.350) as the “redistribution of fine grains within the layer [so that] the solid layer is not changed, only the local permeability is altered.” This phenomenon has been described as being “relatively benign behaviour within the core or filter of a dam” by Garner and Sobkowicz (2002). Kovacs (1981) also describes the term ‘external suffusion’ as the “scouring of fine grains when the volume of the matrix is reduced, accompanied by an increase in permeability, while the stability of the skeleton composed of the coarse grains is unaffected”. This term ‘suffusion’ is not to be confused with suffosion, described later in this Chapter.

For suffusion to occur, there are three criteria that need to be satisfied, as summarised by Wan and Fell (2004a) below. They note that the first two criteria are ‘geometrical’ criteria, and are related to the grain-size distribution of the soil, while the third is a ‘hydraulic’ criterion and is related to the hydraulic forces that cause the movement of fine soil particles.

1. The size of the soil particles must be smaller than the size of the constrictions between the coarser particles, which form the primary fabric of the soil;
2. The amount of the fine soil particles must be less than that which is enough to fill the voids of the primary fabric (if there are more than enough fine soil particles for void filling, the coarser particles will be ‘floating’ in the matrix of the fine soil particles, so that a primary fabric comprising of mainly coarser particles will not exist);
3. The velocity of flow through the soil matrix must be high enough to move the loose soil particles through the constrictions between the larger soil particles.

Materials that are typically susceptible to suffusion are widely or gap graded soils, as shown in Figure 2.9. Lafleur et al. (1989) classifies broadly graded soils into three categories, such that linear soils are typically stable, while gap graded soils and soils with upwardly concave shapes are typically unstable. In the most developed instance, suffusion can result in the entire fine grained volume being ‘washed out’, leaving a coarse grained skeleton.

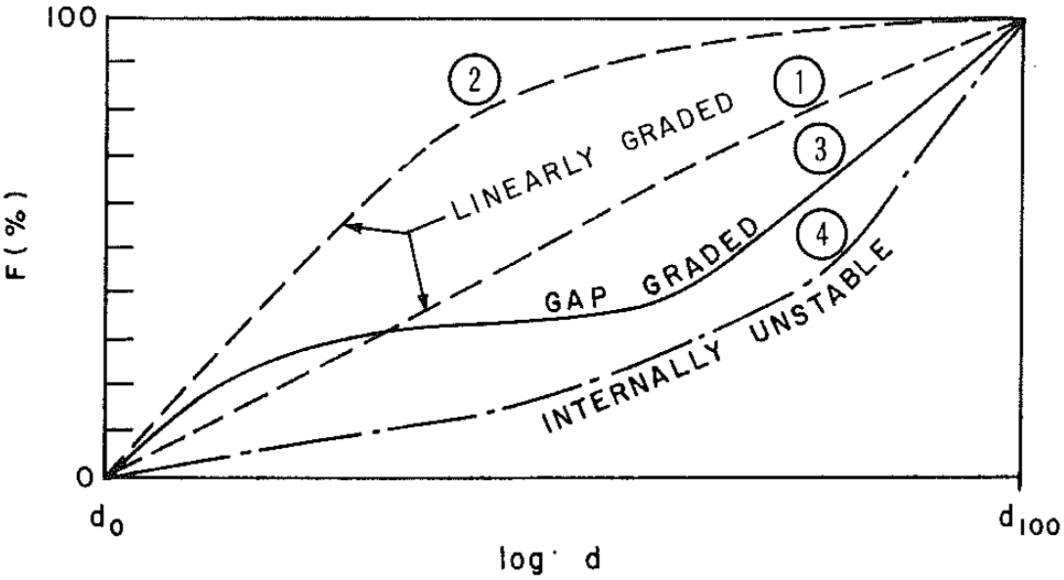

Figure 2.9: Classification of broadly graded soils as described by Lafleur et al. (1989).

2.5.3 Suffosion

In Richards and Reddy’s critical appraisal of piping phenomena in earth dams (2007), they note how the term ‘suffosion’ was coined by a series of East European researchers. The term describes the gradual migration of fine materials through a coarse matrix and results in a reduction in the total volume, eventually leading to failure. The process can lead to a loose framework and high seepage flows that can collapse the soil skeleton, as opposed to ‘external suffusion’ where the skeleton is unaffected (Kovacs 1981). In addition, Chapuis (1992, p. 711) describes suffosion as “the transport of small particles from a soil, which leaves large openings between the particles”. Burenkova (1993, p. 357) describes further details to the definition, whereby ‘inner suffosion’ takes place “when fine particles are transported in the soil structure under the action of constant or pulsating seepage flow” (suffusion), and ‘outer suffosion’ with the “transportation of fine fractions totally out of the soil in question” (suffosion). Suffosion has been described as a slow process in comparison to piping along concentrated leaks. One of the main differences between suffusion and suffosion is that suffosion involves particle movements that could be considered more permanently damaging and pose the potential for unsafe behaviour within the core or filter of a dam (Garner & Sobkowicz 2002). This is due to the increase in void ratio and permeability, which results in the instability of the soil structure (Burenkova 1993).

2.6 Self Filtration

This mechanism is one of particle re-distribution leading to particle stability (particles migration stops) at the base soil-filter interface. It can occur when the coarser particles are floating in a matrix of finer particles, such as with broadly graded soils. As water percolates through the soil, particles smaller than the opening size of the filter voids will be carried from the core material into the filter. Settlement of the soil will occur as a result of this particle washout. As medium sized particles are washed into the filter, they become trapped by the coarse soil particles as they come into contact with one another. These retained medium sized particles then in turn prevent erosion of, or filtrate, finer particles, which in turn filtrate even finer particles. This process will continue until no more particles can migrate. The area within the filter where the self filtration mechanism occurs, is commonly coined the ‘self filtration zone’. Kezdi (1979) and Sherard (1979) both formulated a method in parallel, in which self filtration can be evaluated. This is done by splitting the grading curve and the fine and coarse fractions are checked for compatibility. Figure 2.10 shows a grading envelope in which Sherard (1979) found materials that did not self filter. These tend to be broadly graded soils which are also susceptible to suffusion. Lafleur et al. (1989) described this self filtration mechanism, and developed a laboratory test to assess the model. They found that for broadly graded soils, the self-filtration process is mainly related to the coefficient of broadness, defined as O_F'/d_o, where O_F' is the actual opening size of voids and d_o is the smallest grain size, and to the profile of the particle size distribution (PSD).

As shown by Kezdi (1979) and Sherard (1979), self filtering can be evaluated based on an assessment of geometric particle mechanics and an analytical approach that considers particle parameters such as particle size. Kenney et al. (1985) used an analytical and experimental approach to present the idea of 'controlling constriction sizes'. This approach is not one of self filtering, but is similar in that it evaluates the maximum possible size of particle, D_c*, that can be transported through a filter of specific thickness.

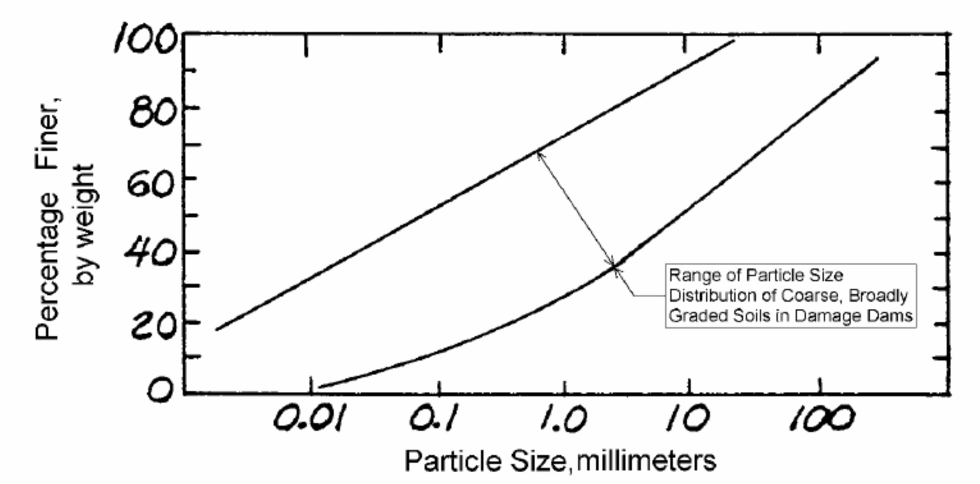

Figure 2.10: Grading envelopes of some broadly graded soils which did not self filter (Sherard 1979).

2.7 Clogging

The performance of a filter is governed by the permeability and the stability of materials, as described by the Terzaghi (1939) filter criterion. The permeability criterion allows pore pressures to be relieved by transmitting seepage water through the voids of the soil network. If for instance, enough particles are transported into the filter and become trapped by the filter particles themselves, then the void space in the original filter material is reduced. If enough of these void spaces are filled with soil particles, then the filter's permeability or ability to transmit seepage water is greatly reduced. This condition is known as 'clogging'. Okita and Nishigaki (1993) performed tests to assess different clogging states, and their results are discussed in Chapter 3.

2.8 Arching and Bridging

The mechanism of arching, also known as bridging, is best described by a yielding mass of soil particles transferring its bearing pressure onto adjoining, stationary particles (Mahmood & Mitchell 1974). Figure 2.11 shows an example of simple two dimensional arches. In this situation, the soil is said to 'arch' over the yielding part of the support, with the arch being maintained by shearing stresses in the soil, and the yielding particles behind the arch creating a zone of 'free material' in which no inter-granular stresses exist. In a base soil-filter situation, arching will typically occur at the interface, however may also occur within a uniform matrix. The diagram in Figure 2.12 represents an upward flow direction where the ‘free material’ is supported by the arching particles. However, in a downward flow situation, arching may still occur, but the free material will fall into or through the filter material, creating a void space behind the arch (USACE 1953). In the situation where vibration is applied, the arch may breakdown causing a redistribution of base and filter particles, which in turn leads to ‘suffusion’. In the situation of an upward flow, the free material present may hinder the flow of material to some extent until a new arch forms (USACE 1953).

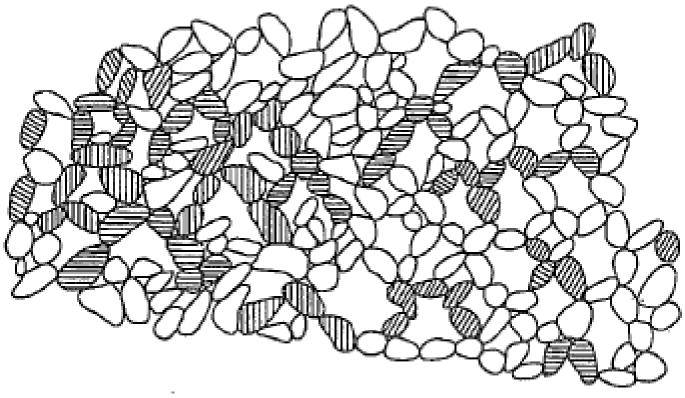

Figure 2.11: Two dimensional schematic arrangement of simple arches in a statically compacted specimen (Mahmood & Mitchell 1974).

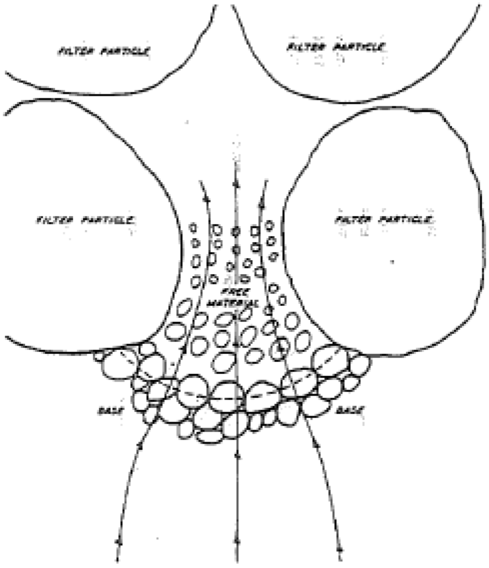

Figure 2.12: Arching phenomenon at contact surface of filter and base, upward flow (USACE 1953).

2.9 Piping

Piping is a result of coarse grains moving near the surface to form a channel of high permeability within a layer, also known as ‘interface erosion’ (Regazzoni & Marot 2011) which occurs in cracks or concentrated leaks. The channel has an opening at the surface where grains are expelled creating a 'boiling' effect. Charles (2001) *in* Garner and Sobkowicz (2002, p. 1) describes piping as a process that "starts at the exit point of seepage and in which a continuous passage or pipe is developed in the soil by backward erosion". Sherard et al. (1963) note that most of the serious trouble from piping results from 'backward erosion' of concentrated leaks which gradually enlarge the seepage channel, until complete failure of the dam occurs, in the worst case scenario. In some instances such as those in sandy gravels, piping of fines may occur while the gravel component remains practically undisturbed. Skempton and Brogan (1994) coined this as 'segregation piping' and in their testing, note that in unstable materials migration and strong piping of fines was occurring at about one third to one fifth of the theoretical critical gradient. The critical hydraulic gradient is generally the average hydraulic gradient across the test specimen where mechanisms of internal erosion first initiate, and for upward flow tests with no top stress, can be calculated using a Terzaghi (1925) equation, defined in Chapter 4.

2.9.1 Backward Erosion

'Backward erosion' has been described by a number of authors including Terzaghi (1939), Sherard et al. (1963) and others. This process occurs as soil particles are progressively dislodged from the soil matrix as intergranular water seepage creates tractive forces in the direction of a free unfiltered surface. For example, free unfiltered surfaces may be the ground surface of a soil foundation, the downstream face of a homogeneous embankment, or a coarse rockfill zone immediately downstream from the fine-grained core (Cyganiewicz et al. 2008). For particles to become mobilised, tractive forces must be greater than the shear resistance of grains and weight of the soil particles. The term 'backward erosion' is coined due to the backward progression in which particles become detached and migrate away from the discharge point and towards the reservoir until a continuous pipe is formed. This backward progression occurs as the erosive forces are greatest where the flow concentrates at exit points. As particles are removed, the magnitude of erosive forces amplifies as the concentration of flow is increased. It is also widely recognised that if heave occurs, backward erosion is likely to initiate (Cyganiewicz et al. 2008).

2.9.2 Concentrated leak erosion

Cracks may form within an embankment due to differential settlement, desiccation, freezing and thawing, or by hydraulic fracture (Fell et al. 2005). When this occurs the concentration of flow causes the walls of the crack to erode, or scour. Concentrated leaks may also occur in continuous, permeable zones that contain coarse and/or poorly compacted materials which form interconnecting void systems.

2.9.3 Stages and Development of Piping Failure

Generally, the occurrence of piping failure can be broken down into four stages: initiation, continuation, progression and breach/failure (Foster & Fell 1999). These are briefly outlined below, and shown in Figure 2.13 to Figure 2.15.

1) *Initiation:* Initiation is the trigger which allows piping to begin. It may occur due to flaws in the soil materials, which may result from poor compaction and settlement, from leakage on the downstream side of the core or foundation, or from a concentrated leak through the core. The root cause may relate back to poor compaction of materials leading to settlement and hence cracks or flaws, or may be related to natural forces, such as earthquakes, which could also create cracking, slope instability and/or settlement.
2) *Continuation:* Continuation is the phase which is governed by the relationship between particle size distribution of the base soil (the central core of the dam) and the filter materials. This interaction will determine whether erosion will continue, or will cease. Foster and Fell (1999, 2001) and Foster (1999) defined four levels of security, being ‘No Erosion’, ‘Some Erosion’, ‘Excessive Erosion’ and ‘Continuing Erosion’ (Figure 2.13).
3) *Progression:* In the process of internal erosion, progression is where hydraulic stresses within the eroding soil may or may not lead to the enlargement of the pipe. During this phase, pore pressures and seepage will increase. Several factors govern whether a pipe will enlarge, and if so, its rate of enlargement, as well as whether the pipe will collapse. These factors are based on the type of soil, its strength, cohesion (which is typically none) and water seepage rates. Pipe progression may be limited by upstream zones which limit the flow of water, and may also be limited by low permeability zones throughout the embankment.
4) *Breach:* Breach or failure, is the final phase of internal erosion, and may occur due to one of four phenomena. Fell et al. (2008) lists these, noted below, in the order of their observed frequency.
    i. Gross enlargement of the pipe (which may result in the development of a sinkhole between the pipe and crest of the embankment).
    ii. Slope instability of the downstream slope, i.e. slides and slumping.
    iii. Unravelling of the downstream face.

iv. Overtopping (as a result of settlement of the crest due to suffosion and/or due to the development of a sinkhole, as described above).

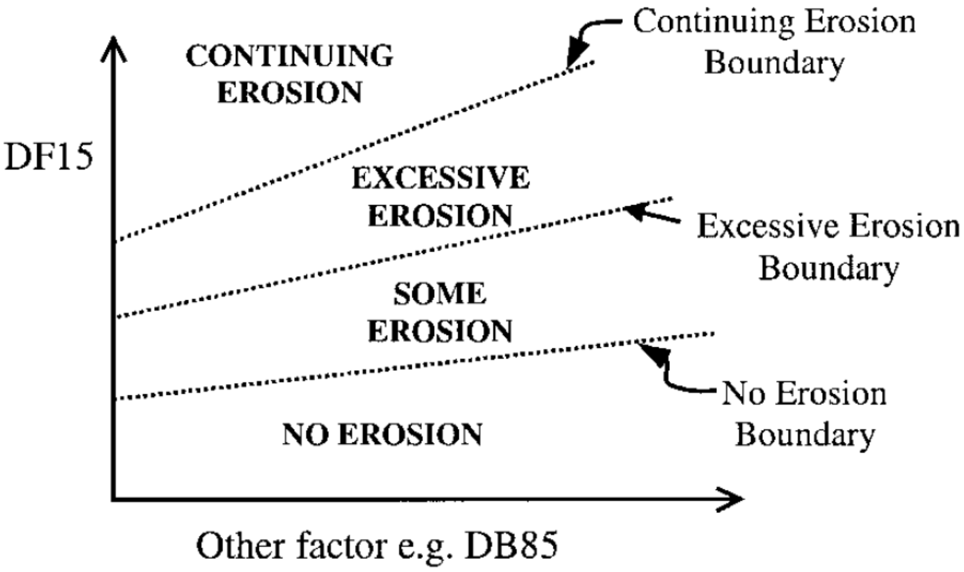

Figure 2.13: Conceptual erosion boundaries of filter test behaviour, Foster and Fell (2001b).

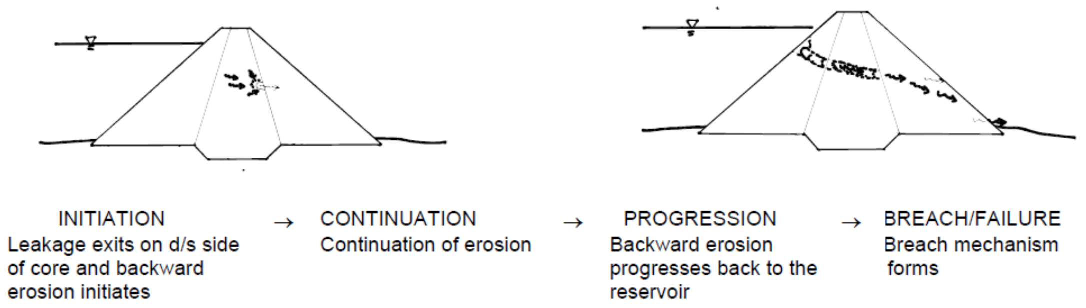

(A) PIPING IN THE EMBANKMENT INITIATED BY BACKWARD EROSION

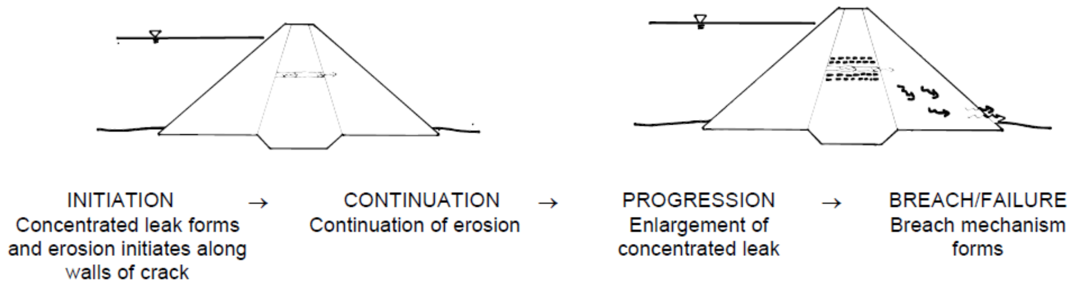

(B) PIPING IN THE EMBANKMENT INITIATED BY EROSION IN A CONCENTRATED LEAK

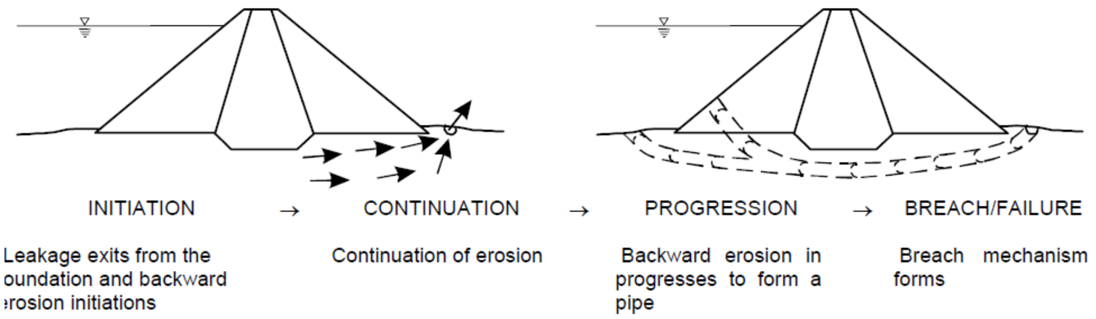

(C) PIPING IN THE FOUNDATION INITIATED BY BACKWARD EROSION

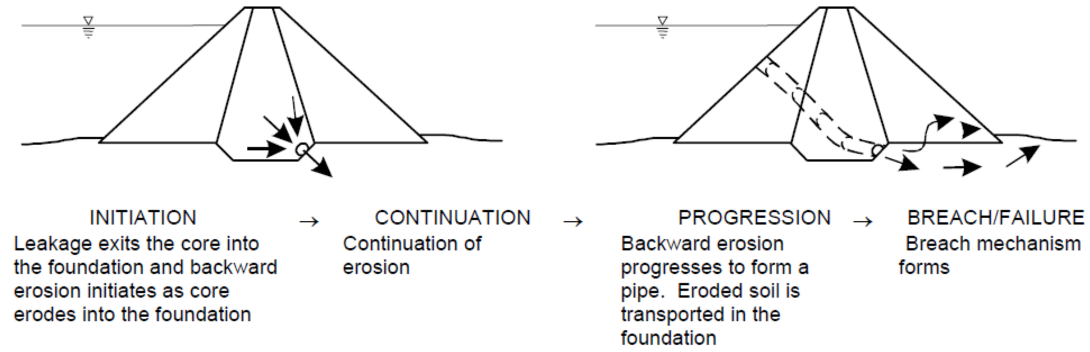

(D) PIPING FROM THE EMBANKMENT TO FOUNDATION INITIATED BY BACKWARD EROSION

Figure 2.14: Models for the development of failure by piping (Foster & Fell 1999) in Cyganiewicz et al. (2008).

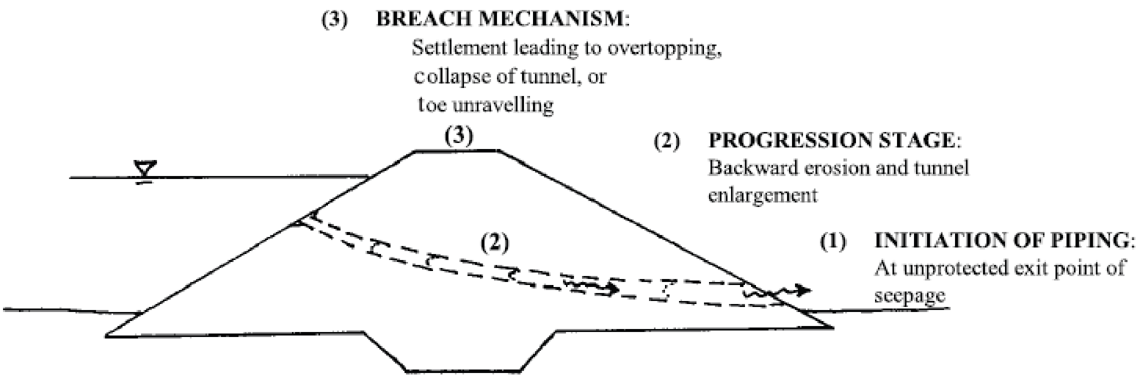

Figure 2.15: Stages of development of piping failure (Foster et al., 2000).

↳Reservoir Rises

↳Initiation – Flaw exists (1) (2)

↳Initiation – Erosion starts

↳Continuation – Unfiltered or inadequately filtered exit exists (consider: no erosion/some erosion/excessive erosion/continuing erosion)

↳Progression – Roof forms to support a pipe

↳Progression – Upstream zone fails to fill crack

↳Progression – Upstream zone fails to limit flows

↳Intervention fails

↳Dam breaches (consider all likely breach mechanisms)

↳Consequences occur

(1) A 'flaw" is a crack or poorly compacted zone in which a concentrated leak may form.

(2) For Backward Erosion Piping (BEP) no flaw is required but a continuous zone of cohesionless soil in the embankment or foundation is required.

Figure 2.16: Event Tree (Cyganiewicz et al. 2008)

2.10 Filter design criteria and methods for evaluation of filter performance

The first specifications, or filter criteria came from Terzaghi (1922) and were written in German, and then in English (Terzaghi 1939). Based on testing, experience and reason, Terzaghi proposed two criteria, originally designed as technical advice on control of seepage beneath concrete weirs and soils of zoned earthfill dams (Fannin 2008):

1) $D_{15}/d_{85} < 4$ Soil retention criterion
2) $D_{15}/d_{15} > 4$ Permeability criterion

These criteria compare a ratio of particle size between the filter (D_{15} - the particle size where 15% by weight is finer) and the base material (d_{85} or d_{15} - the particle size where 85% or 15% by weight is finer respectively), which is typically the dam core or another filter directly upstream of the filter in question.

The filter coefficient of 4 was likely established based on the diameter of a sphere that can fit into voids created by the arrangement of spheres in a dense and loose state (Kezdi 1979). These two criteria have formed a sound basis for filter design, and particularly in reference to the D_{15}/d_{85} ratio, are generally regarded as providing a conservative design standard today. An example of a base material to be protected and the required filter PSD according to Terzaghi (1922) is shown in Figure 2.17. However, following laboratory testing of soils by numerous authors, an increasing pool of data has led to Terzaghi et al. (1996) relaxing the soil retention criteria to $D_{15}/d_{85} < 5$, as shown in Figure 2.18. Terzaghi et al. (1996) note that if one filter is not capable of fulfilling these retention and permeability criteria, then a series of filters may be required. These assemblages are known as 'graded filters'.

Since these criteria were proposed, many laboratory testing methods have been developed to assess the performance of various material compositions and to verify these rules. In such tests, Bertram (1940) found the minimum ratio of D_{15}/d_{85} to be 6, Sherard et al. (1984a, 1984b) found the value $D_{15}/d_{85} \leq 5$ to be conservative, Okita and Nishigaki (1993) found that there was no base soil loss when $D_{15}/d_{85} \leq 7$, and Tomlinson and Vaid (2000) could not induce piping when $D_{15}/d_{85} < 8$. Lafleur et al. (1989) suggests that the Terzaghi (1922) criterion has a factor of safety of approximately two.

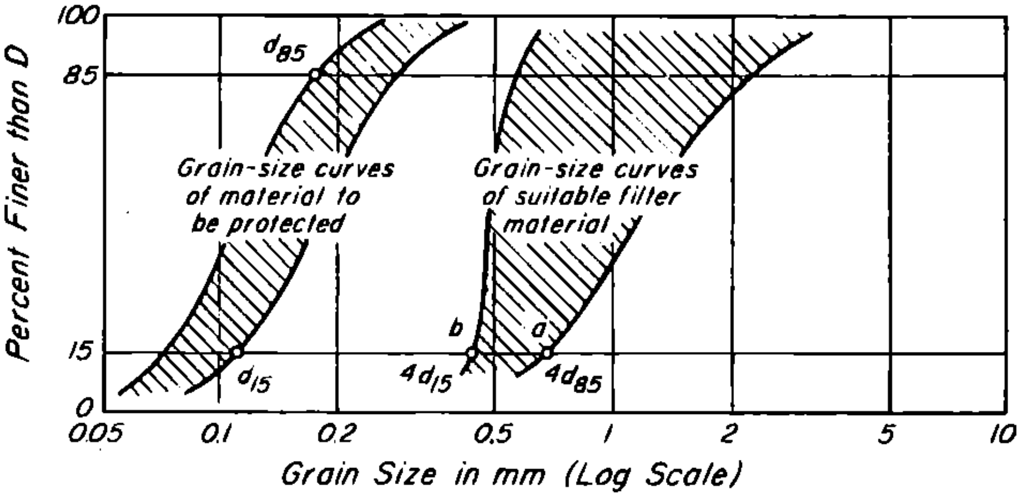

Figure 2.17: Original Terzaghi (1922) specifications for grain sizes of material for filters. The Left-hand shaded area encloses all grain-size curves for material to be protected; right-hand area indicates range within which curves for filter material must lie (Terzaghi et al. 1996).

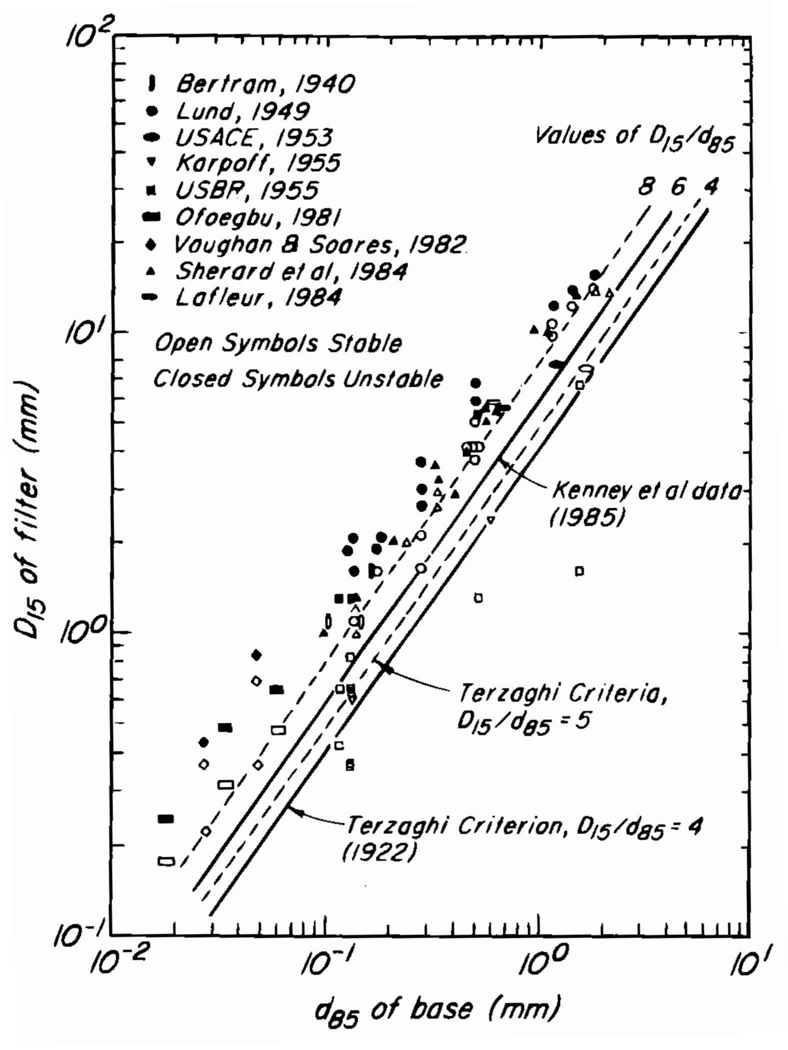

Figure 2.18: Terzaghi criteria based on relationship between d_{85} of base to D_{15} of the filter materials, from Terzaghi et al. (1996).

In Karpoff (1955), ratios of D_{50}/d_{50} and D_{15}/d_{15} were proposed, giving values for natural, subrounded materials, filters with graded materials and values for crushed angular rock, however according to Sherard et al. (1984a) these ratios are not founded on sound theoretical or experimental basis, and have since been abandoned. Furthermore, Sherard et al. (1984a) suggest that particles of crushed rock can be used in place of rounded alluvial particles for filters, and the same criterion can be used for their design.

Experience has shown that the shape of a grading curve has a significant part to play in the stability or instability of a filter material, with linear PSDs generally being internally stable, while broadly graded and gap-graded materials being internally unstable. Terzaghi et al. (1996) notes that filter materials should not be broadly or gap-graded. Considering this, Kenny (1985) proposed a method to evaluate the grading stability based on the shape of the PSD, applicable to concave upward and bi-modal PSDs. This method calculates a series of ratios of (H/F), where H corresponds to a particle size between particle diameter D and 4D, and F corresponds to the 'mass fraction smaller than' a particle diameter, D (Figure 2.19). The size interval of 4D was chosen because the size of predominant constrictions in the void network of a filter is approximately equal to one quarter the size of particles making up the filter, meaning particles of size D can pass through a filter composed of particles of size 4D or larger. The suggested boundary between stable and unstable grading curves was originally defined as $H = 1.3F$, for the portion of gradation up to $F = 0.2$ for widely graded soils, and $F = 0.3$ for narrowly graded soils. After a discussion of the data by Milligan (1986), Kenney and Lau (1986) changed the boundary to $H = 1.0F$, or $H/F = 1.0$.

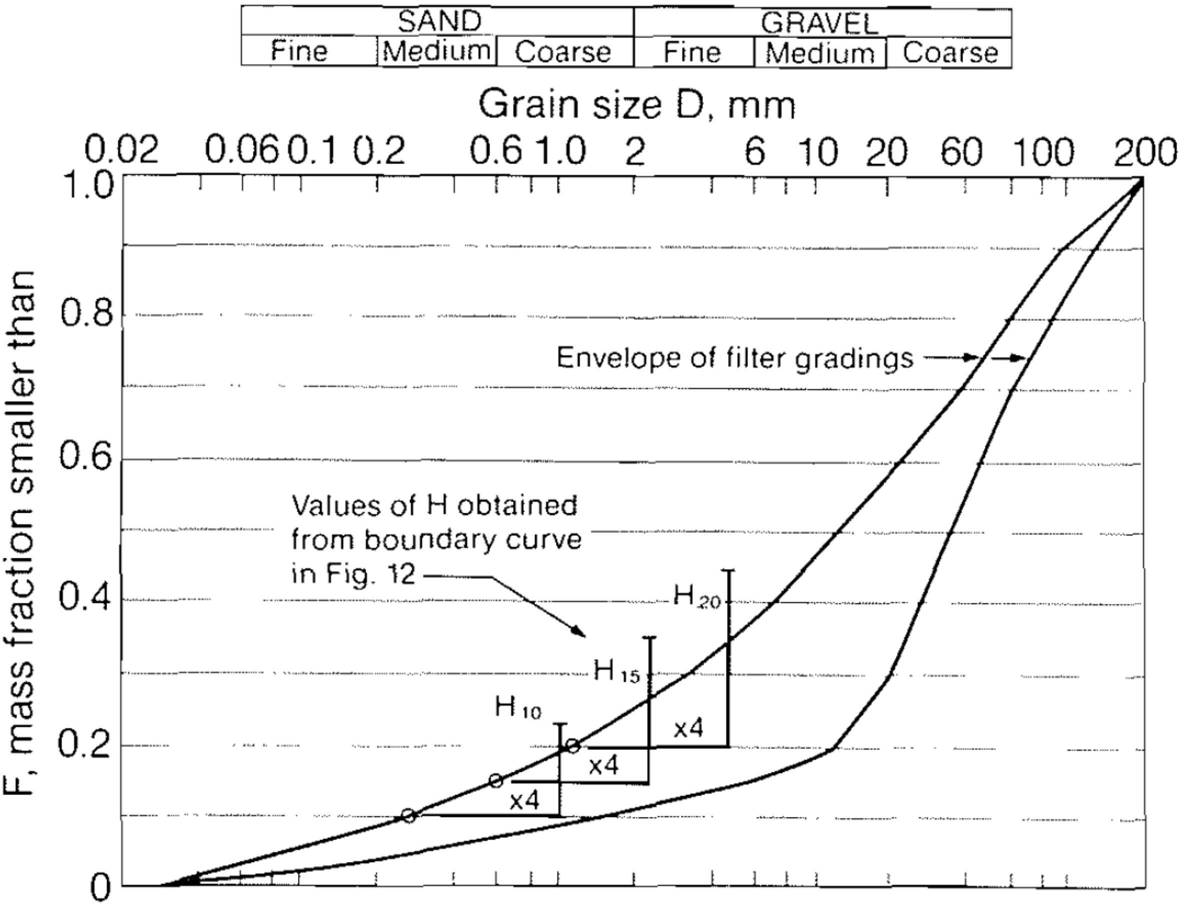

Figure 2.19: Method to evaluate the potential for grading instability (Kenney & Lau 1985).

Assuming the theory and criterion advocated by (Terzaghi 1922), where a soil retention ratio $D_{15}/d_{85} < 4$ between a base soil and filter material is suggested, Kezdi (1979) and Sherard (1979) both presented a method independently to investigate self-filtering, where a PSD is split into a coarse fraction and a fine fraction at a point on the curve, each of which must satisfy the limiting criterion $D'_{15}/d'_{85} < 4$. The filter PSD can be split at a range of points on the curve, and a $(D'_{15}/d'_{85})_{max}$ determined. An example of a split curve is shown in Figure 2.20 (this method is reported by Kovacs (1981) to have been developed in 1969 by Kezdi). Li and Fannin (2008) note that De Mello (1975) independently makes reference to this approach as a "simple check to unacceptable skip grading with respect to internal erosion". This method is also supported by Lowe (1988) to assess the ability of broadly graded and gap-graded materials to self-filter.

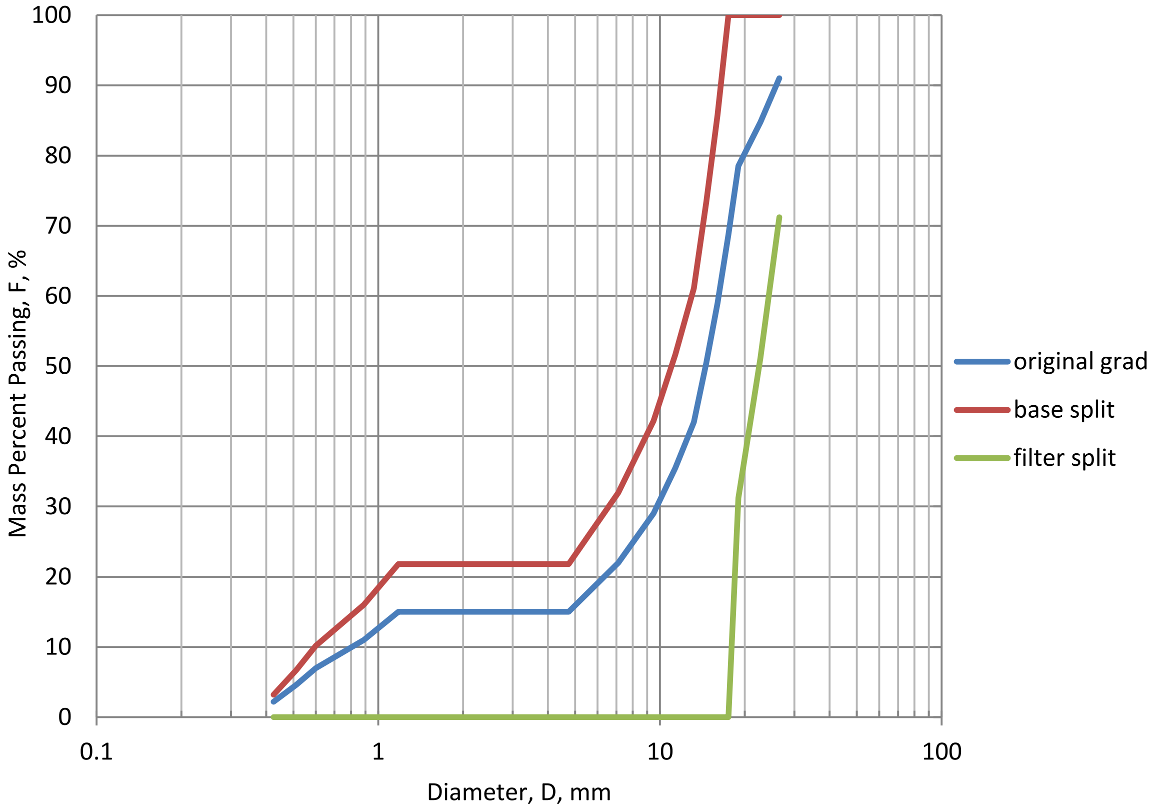

***Figure 2.20:** Example of a split curve showing the original gradation and the finer and coarser fraction, used in the calculation of $(D'_{15}/d'_{85})_{max}$ according to Kezdi (1979).*

Li and Fannin (2008) set out to compare the subtle differences between the Kenney and Lau (1985) and Kezdi (1979) methods using a database of 25 gap-graded soils and 32 widely graded soils. The Kenny and Lau criterion for instability can be described as “the slope is flatter than F% per four times change in grain size” while the Kezdi criterion for instability can be expressed as “the slope is flatter than 15% per four times change in grain size” as noted by Li and Fannin (2008, p. 1303). The plot in Figure 2.21 shows these criteria graphically with the areas where instability can be expected, and also the area where both Kenney and Lau (1985) and Kezdi (1979) predict instability.

From the evaluation of the two methods above, a number of conclusions were made. In the evaluation of gap-graded soils, the Kezdi (1979) method proved more successful in distinguishing between stable and unstable soils. On the other hand, in distinguishing widely graded soils, the Kenney and Lau (1985) approach proved more successful. Finally, comparing the filter ratio (D'_{15}/d'_{85}), Li and Fannin (2008)found the method to be more conservative for F < 15%, and the stability index $(H/F)_{min}$ from the Kenney and Lau (1985) method to be more conservative for F > 15%.

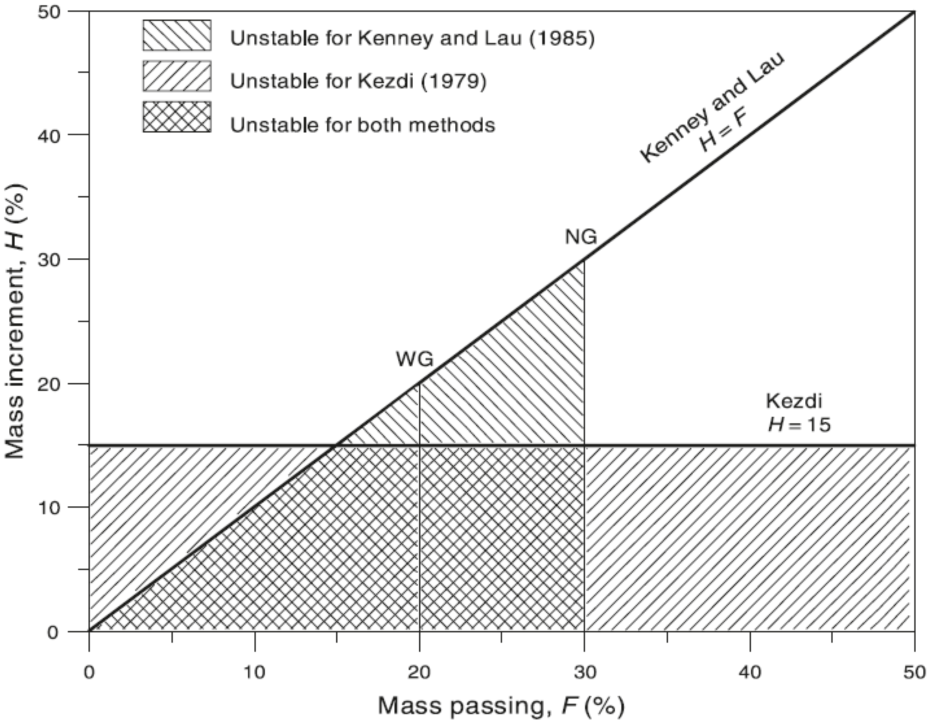

Figure 2.21: Synthesis of the Kenney and Lau (1985) and Kezdi (1979) criteria. NG, narrowly graded, WG, well graded (Li & Fannin 2008).

Following upward and downward seepage tests on 22 granular materials, Burenkova (1993) proposed an in-equation to predict the suffosiveness of widely graded soils, in terms of the D_{90}, D_{60}, and D_{15} grain sizes. The equation;

$$0.76\log(h'') + 1 < h' < 1.86\, log(h'') + 1. \qquad (2.1)$$

represents an area named Zone II in Figure 2.22, where soils that fall within the boundaries are deemed non-suffosive. Three other zones were identified, where zones I and III are zones of suffosive compositions and zone IV is a zone of artificial soil. Rönnqvist (2010) described a validation exercise carried out by Li (2008), finding the Burenkova (1993) method for filter evaluation to be slightly conservative, while Wan and Fell (2004a) conclude its prediction to be satisfactory.

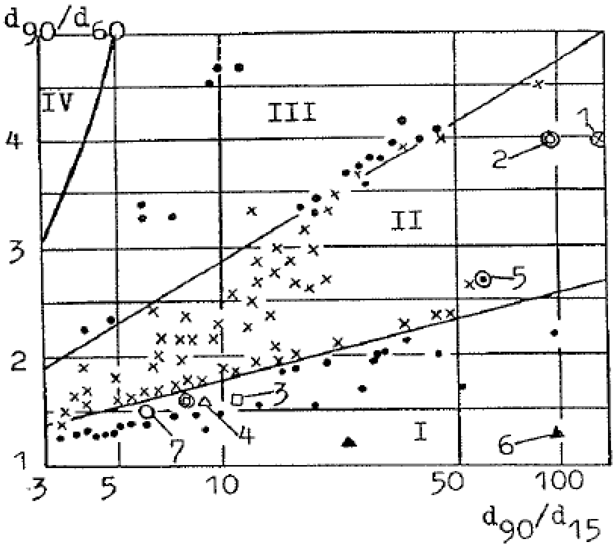

Figure 2.22: Evaluation of piping processes in soils according to test results (Burenkova 1993).

Based on testing of 20 soils, combined with pooled data from Kenney et al. (1983, 1984), Kenney and Lau (1984, 1985), Lafleur et al. (1989), Burenkova (1993), Skempton and Brogan (1994) and Chapuis et al. (1996), Wan and Fell (2008) first applied contours of equal probability of internal erosion to the Burenkova (1993) d_{90}/d_{60} and d_{90}/d_{15} plot in Figure 2.23, as a modified Burenkova method for broadly graded and gap-graded soils. However, this method does not give a clear cut boundary between internally unstable and stable soils. An alternative method was then proposed for broadly graded soils. Based on experience using the modified Burenkova method, Wan and Fell (2008) determined that soils with a steep slope on the coarse fraction, and a shallow slope on the finer fraction were likely to be internally unstable. Trials found that these gradations could be represented by d_{90}/d_{60} and d_{20}/d_5. Figure 2.24 plots these values and defines two boundaries to predict the soils where the likelihood of internal instability is low, and another to define an area where soils are highly likely to be internally unstable. It is important to note that this method is not able to identify the internal instability of gap-graded soils (Wan & Fell 2008).

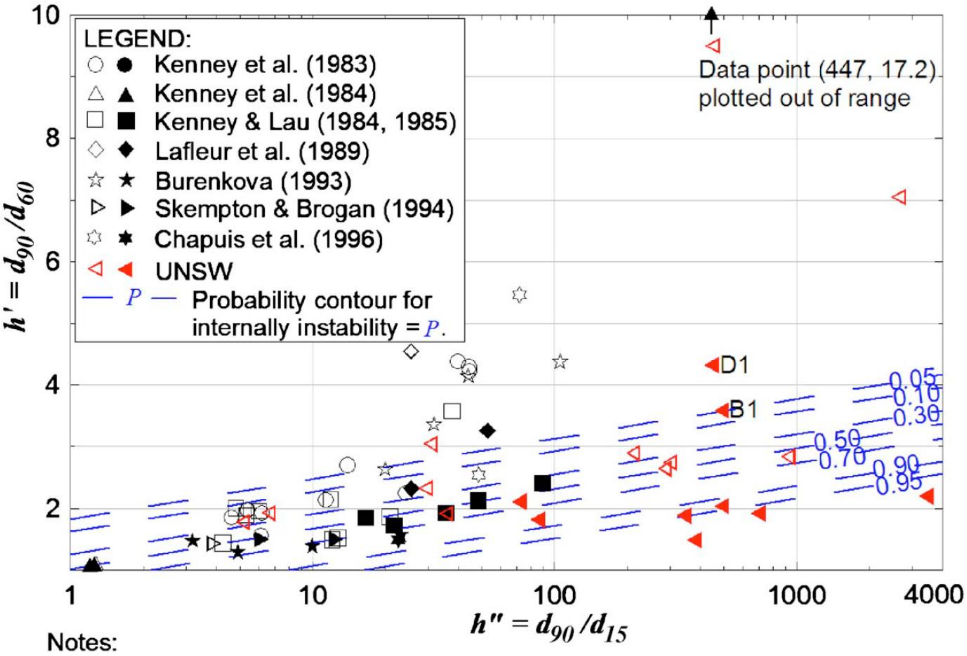

Notes:
1. Hollow symbol represents internally stable sample.
2. Solid symbol represents internally unstable sample.
3. UNSW samples B1 and D1 not used in logistic regression.

Figure 2.23: Contours of probability of internal instability for silt-sand-gravel soils and clay-silt-sand-gravel soils of limited clay content and plasticity (Wan & Fell 2008).

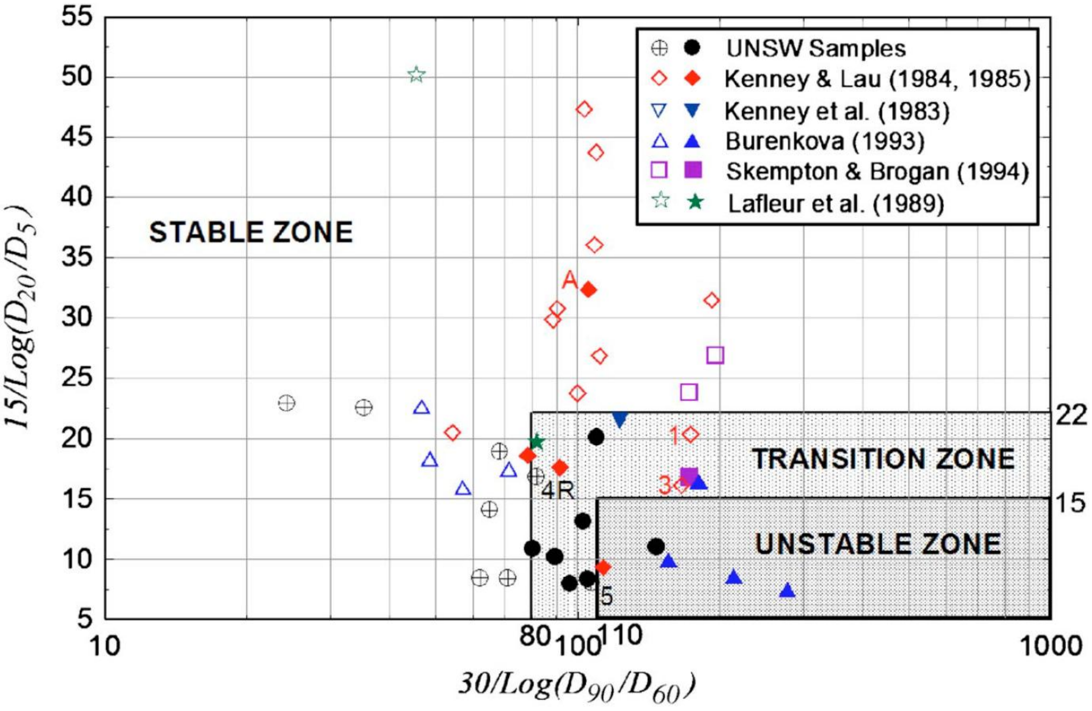

Notes:
1. Hollow symbol represents internally stable sample.
2. Solid symbol represents internally unstable sample.

Figure 2.24: Alternative method for assessing internal instability of broadly graded silt-sand-gravel soils (Wan & Fell 2008).

In Kovacs (1981, p. 352), the authors note that Hazen's (1892) uniformity coefficient ($C_u = D_{60}/D_{10}$) can predict geometrical condition of suffusion, based on writings from Istomina (1957). The classifications state that:

- There is no suffusion if $C_u \leq 10$
- Transition condition $10 \leq C_u \leq 20$
- Suffusion is liable if $C_u \geq 20$.

Laboratory experiments with sandy gravels by Cistin (1955) *in* Kovacs (1981), found that no grain movements occurred if the uniformity coefficient was smaller than 8 or 10, very high hydraulic gradients were required to produce suffusion in the transition zone, and when $C_u > 25$, fine grains started to move readily under small hydraulic gradients, which supports the Istomina (1957) criterion. The C_u value is commonly reported in laboratory tests for testing of filter materials.

Many other criteria have been proposed that do not relate to internal erosion issues, some of which are described by Thomas (1976), USBR (1987), Locke and Intraratna (1999) and Vaughan and Soares (1982). These criteria prescribe recommendations for more specific soil types and for examples of construction techniques.

2.11 Synthesis

- Dams with filters have a relatively low probability of failure;
- Filter design requirements include retention and permeability functions with generally accepted and conservative values specified by Terzaghi (1922), being $D_{15}/d_{85} < 4$ and $D_{15}/d_{15} > 4$ for retention and permeability respectively;
- Internal erosion requires conditions of material susceptibility, critical hydraulic load and critical hydraulic stress to initiate and progress;
- Mechanisms during internal erosion may include suffusion, suffosion, self filtration, clogging, arching and bridging, piping and backward erosion;
- Several methods have been developed for evaluating the performance of filter materials including those by Terzaghi (1922), Kenney and Lau (1985), Kezdi (1979), Burenkova (1993) and Kovacs (1981).

Chapter 3: Previously employed testing apparatus and methods for modelling internal erosion

Numerous laboratory testing apparatuses and methods have been designed and utilised since the early 1940's to evaluate the compatibility of materials in embankment dams. Such methods have typically involved packing filter and/or base soil materials into tubes through which water is then allowed to seep. The response of the particles to the seepage is then monitored, and judgements made as to the suitability of the filter material. This chapter describes a selection of testing apparatuses and methods that have been utilised to assess the stability or instability of filter and/or core materials for embankment dams. Principal findings following each piece of research are summarised. This review forms the basis for the methodology and design of the transparent soil permeameter, described in Chapter 4.

3.1 Bertram (1940)

Bertram's testing apparatus (Bertram 1940) is shown in Figure 3.1, and consisted of a Lucite tube with 2 inch (5.1 cm) diameter and 6 inch (15.2 cm) length, used as a permeameter. Tests were carried out to verify soil retention criteria proposed by Terzaghi (1939). Filter and base materials of natural sands, Ottawa sand and quartz sand were compacted to 70% Standard Proctor and each measured approximately 6 cm in thickness. Most tests were downward flow tests, however a few selected cases were upward flowing, and lasted either 2 hours (for hydraulic gradient, i = 18 to 20) or 4 hours (for i = 6 to 8). The transportation of base material into the filter material was determined through pre test and post test comparisons of the base material through a sieve analysis. Visible movement of particles was found to initiate very quickly and cease after three to five minutes.

Principal Findings

- Importance of using distilled de-aired water so the permeability of the soil is not affected.
- Minimum critical ratio for stability was $D_{15}/d_{85} = 6$, acceptable for tests with hydraulic gradients between 6 to 20.
- D_{15}/d_{85} independent of shape of soil particles.

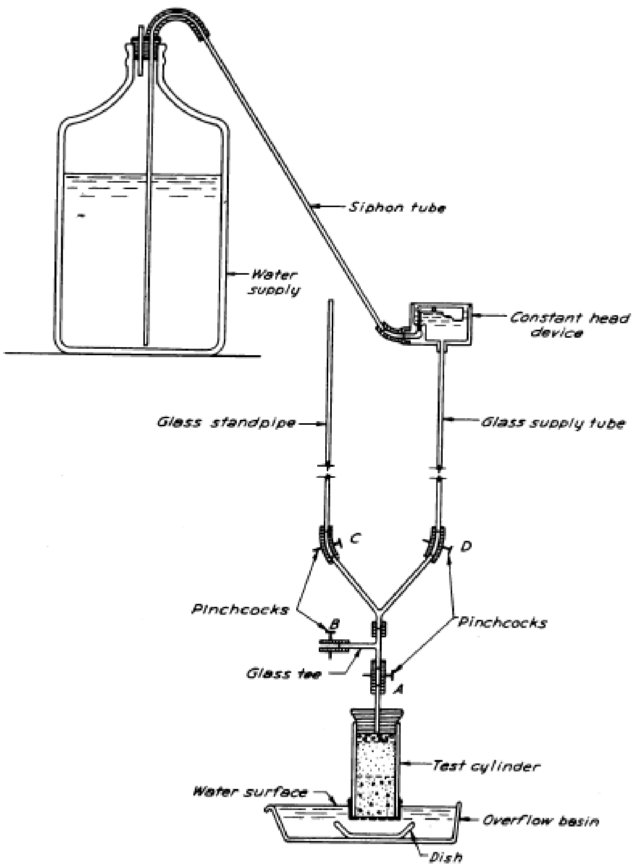

Figure 3.1: Design of Bertram's Filter Test Apparatus (Bertram 1940)

3.2 Karpoff (1955)

Karpoff (1955) conducted a series of experiments using an apparatus of several transparent, plastic cylinders 8 inches (20.3 cm) high and 8 inches (20.3 cm) in diameter, of which several were bolted together. Layers of different gradations of natural rock particles, then later crushed rock and subrounded base and filter material, were compacted into the cylinder using about half of the standard compactive effort recommended by the Bureau of Reclamation (Karpoff 1955). The cylinder was connected to a water supply with hydraulic heads of between 2 and 30 feet (0.61 to 9.1 m) which were subjected to the sample.

Principal Findings

- For natural, subrounded materials $D_{50}/d_{50} = 5$ to 10.
- Testing on filters with graded materials $D_{50}/d_{50} = 12$ to 58.
- For crushed rock $D_{50}/d_{50} = 9$ to 30 and, $D_{15}/d_{15} = 6$ to 18.

3.3 Vaughan and Soares (1982)

Vaughan and Soares (1982) ran laboratory tests using a 50 mm diameter by 450 mm long vertical clear acrylic tube containing a 75 mm high compacted, presaturated filter which rested on coarse material. Water was then introduced and the permeability was measured. Flocculated clay was then introduced in a dilute suspension with water while the flow rate was monitored, and water re-circulated. A successful test was defined as having an outflow with no clay particles in the water.

Principal Findings

- Suggested that permeability is the main parameter in filter performance, given that permeability is a direct function of pore size.
- Filters should be cohesionless in order to avoid cracking.
- Upon the formation of a crack in a dam, the eroded material may segregate with coarser particles being deposited in the crack. The process of self-filtering to plug the crack cannot be relied on.
- The proposed concept of a 'perfect filter' is conservative and describes the ability of a filter to retain the smallest particles arising during erosion. If flocculation occurs then the smallest particle is that of a clay floc.

3.4 Hillis and Truscott (1983)

A series of large scale tests were carried out on core and filter materials used in the four Magot Dams in the Philippines, which were completed in late 1982 (Hillis & Truscott 1983). The tests involved a 580 mm diameter permeameter developed by converting an oil drum (Figure 3.2), and also a large timber flume (Figure 3.3). Since the location of the dams lie within a seismically active zone, tests were carried out using both intact and cracked core materials, simulating cracking caused by ground shaking. The drum was equipped with a swivel so that both vertical and horizontal tests could be carried out, both with a 5 meter head. The performance of this filter test was determined on the visual inspection during the test, visual and numerical evaluations of the total solids content of the outflow water, and the time taken to reach constant outflow.

Principal Findings

- The tests carried out by these authors were successful in evaluating base and filter material combinations against cracking.
- Using adequate filter materials, cracks through base materials would fill and be almost undetectable, apart from a small depression at the surface.

- Using base materials with even a small amount of cohesion, the size of the cohesive arch that developed was much greater than then gap occurring between particles in a conventionally designed filter. Therefore, Hillis and Truscott (1983) suggest that commonly used filter criteria are too conservative for the core material of the Magot Dams.

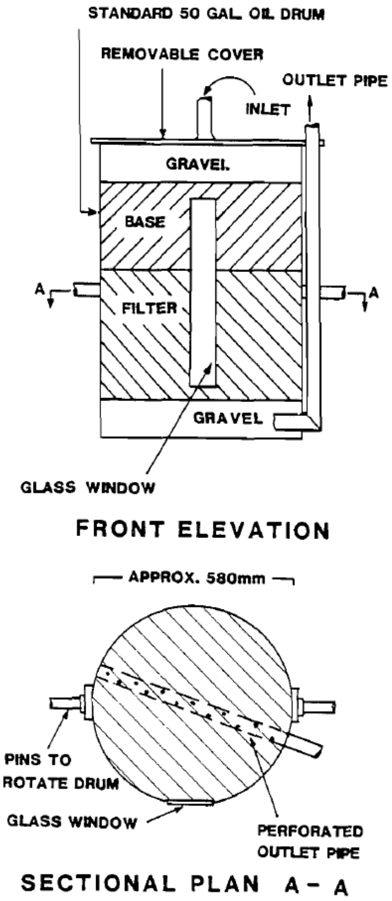

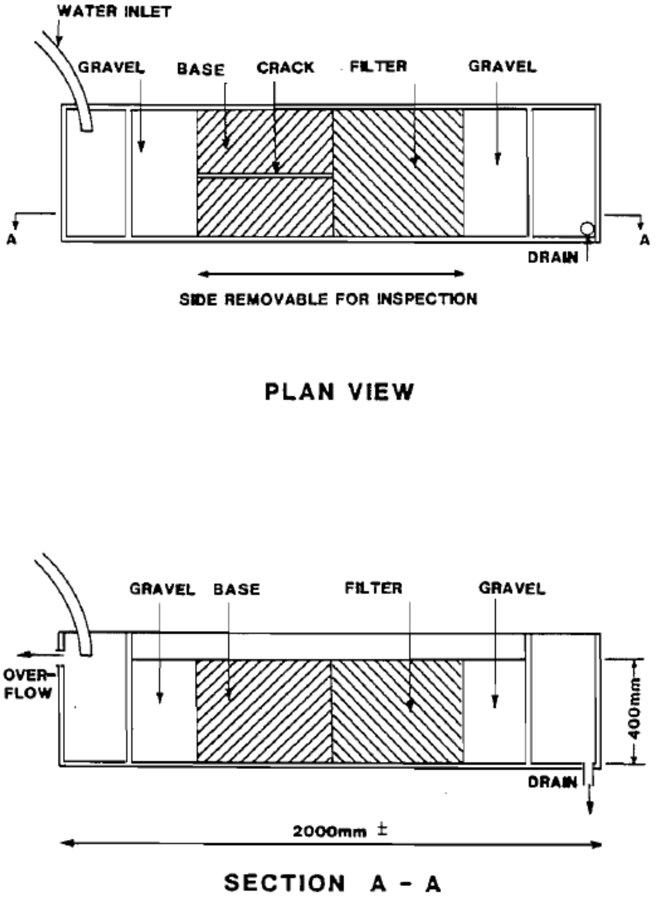

Figure 3.2 (left): Drum Permeameter (Hillis & Truscott 1983) and;

Figure 3.3 (right): Timber Flume (Hillis & Truscott 1983).

3.5 Sherard et al. (1984a)

Sherard et al. (1984a) carried out research to improve the understanding of fundamental properties and behaviour of filters, using the test apparatus shown in Figure 3.4. The permeameter was packed with the filter material, which was uniform coarse sand, uniform gravel or well graded sandy gravel, and then the base soil of uniform fine, medium or coarse sand was packed on top. The test samples were 10 cm in diameter, and had a length between 5 and 10 cm (base soil) and 12.5 cm to 17 cm (filter material). Pressurised water was fed into the top of the apparatus to create a downward flow for the duration of the 5-10 minute test. If little or no sand had passed through the filter specimen after the initial 5-10 minutes, then the apparatus was moved onto a shaking table for 60 seconds with the water still flowing in one last attempt to cause instability. The authors judged the tests and categorised them into 'successful', 'failure' or 'borderline' results, depending on the quantity of base material that migrated through the filter.

Principal Findings

- The filter design criteria, $D_{15}/d_{85} \leq 5$ is conservative, however for filters with D_{15} larger than 1 mm it should serve as the main criterion. Filters with a D_{15} smaller than 1 mm, the authors refer to Sherard et al. (1984b), which is outlined in Chapter 3.6, below.
- Filter criteria based on D_{50}/d_{50} and D_{15}/d_{15} ratios are not founded on sound theoretical or experimental basis and should be abandoned.
- PSD curves do not have to be of similar shape to base soil curve.
- Angular particles of crushed rock can be used in place of rounded alluvial particles for filters, and the same criterion can be used for their design.

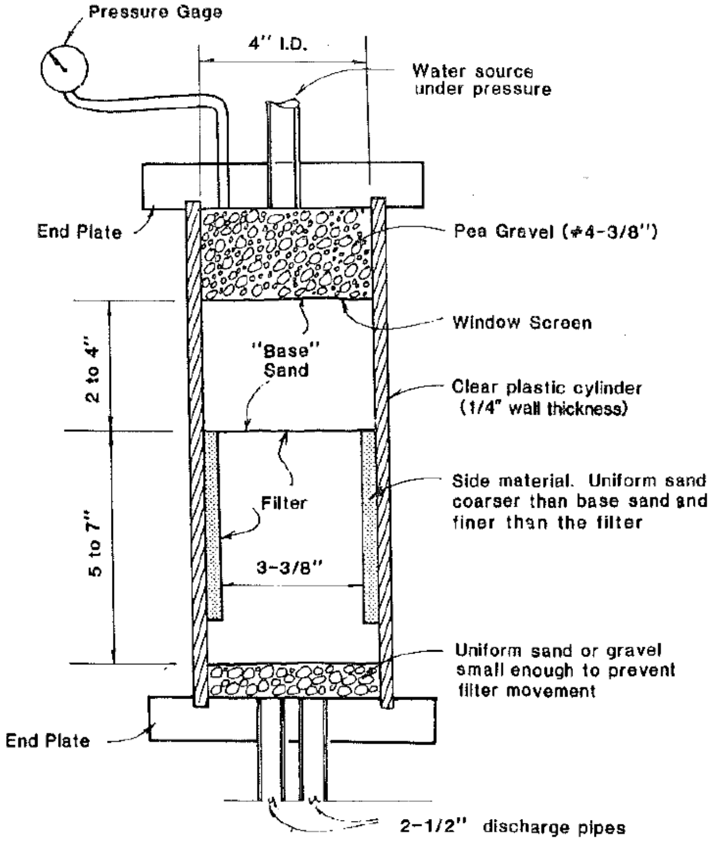

Figure 3.4: Filter test apparatus used by Sherard et al. (1984a).

3.6 Sherard et al. (1984b)

Sherard et al. (1984b) investigated the design criteria required to protect silts and clays that are commonly used in embankment dams. In doing so, they carried out the three variations in the testing procedure. This included conventional filter tests, slot tests and slurry tests, as described below.

Conventional tests (described in Sherard et al. (1984a)) (Figure 3.4) were carried out using sand and sandy gravel filters with clay and silt base specimens 30-60 mm thick. Water pressure was increased in increments of 0.5 kg/cm^2 (49 kPa) until a concentrated leak of coloured water formed. If the eroded material sealed the filter face and the leak was stopped then the filter was deemed ‘successful’, whereas if the eroded material was carried through the filter without sealing then the filter was ‘unsuccessful’.

The slot test was a horizontal flow test in which a small slot (13 mm x 2 mm) was located in the base soil to simulate a concentrated leak. The test apparatus is shown in Figure 3.5. In the tests described in Sherard et al. (1984b), the base soil was 16.5 cm thick and the filter 10 cm thick. Water was allowed to flow into slot in the base specimen with 4 kg/cm^2 (392 kPa) pressure, and through the filter. The advantages of this test were that the concentrated leak was always located in the centre of the base specimen, a longer base specimen could be used in comparison to the conventional test, and the slot for the initial channel for the leak always had the same dimensions. In a successful test the flow rate would rapidly decrease and the water would become clearer until the concentrated leak would seal, or would stabilise at a very small constant flow. In unsuccessful tests, the surge of dirty water would continue with no reduction in flow rate, and the test would be stopped after only a few minutes. An open hole through an unsuccessful tests was commonly 10 – 15 mm in diameter or larger. In carrying out the slot test the authors found that the water eroded the base specimen to its basic particle size, and hence the filter voids were not being plugged and sealed by small pieces of intact compacted clay larger than the 1.0 mm sand size. For this reason, the slurry test was developed.

The slurry test apparatus is shown in Figure 3.6. The filter was placed and compacted as in the slot test, however in place of the compacted base specimen a base slurry mixture was poured in having water content 2.5 times the liquid limit. Water was poured on top, filling the cylinder, before the water valve was opened with a 4 kg/cm^2 pressure. In a successful test the slurry abruptly settled a few millimetres and then stopped, with only a small amount of cloudy water emerging over about 2 minutes, whereas in an unsuccessful test, the slurry was forced through the filter in 2 or 3 seconds and the upper filter surface was left clean.

Principal Findings

- For sandy silts and clays: $D_{15}/d_{85} \leq 5$ is conservative and reasonable for silts and clays with a significant sand component (d_{85} of 0.1-0.5 mm).
- For fine grained clays (d_{85} of 0.03-0.10 mm), sand of gravelly sand filters with D_{15} not exceeding about 0.5 mm are reasonable and conservative.
- For fine grained silts of low cohesion and without significant sand content (d_{85} of 0.03-0.10 mm) and low plasticity, sand or gravelly sand filters with average D_{15} not exceeding 0.3 mm are conservative.
- For exceptionally fine soils such as clays and silts with d_{85} less than about 0.02 mm (not very common in nature), filters with an average D_{15} of 0.2 mm or smaller are conservative.

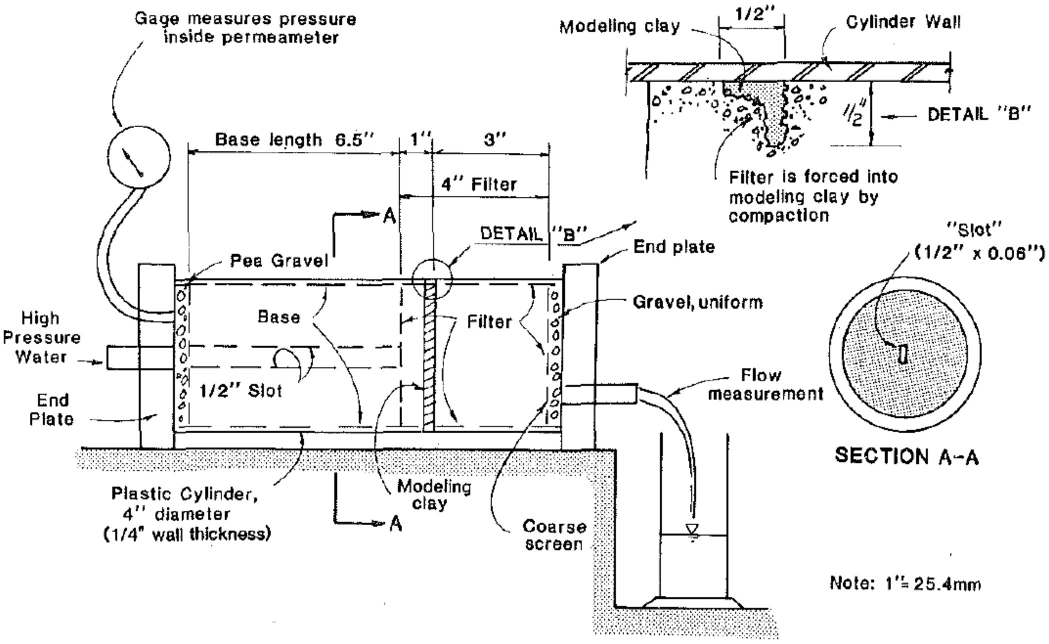

Figure 3.5: High Pressure "Slot" Test Apparatus (Sherard et al. 1984b).

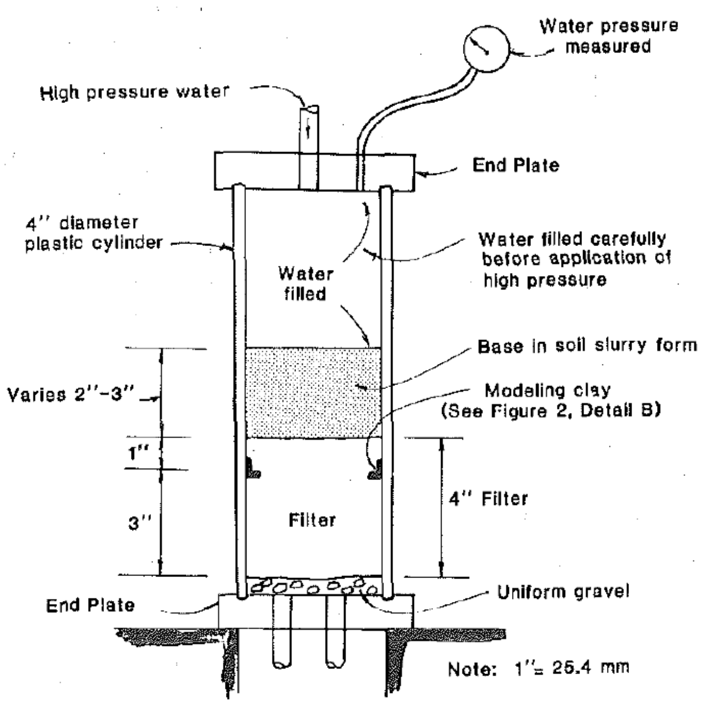

Figure 3.6: High pressure "Slurry" Test Apparatus (Sherard et al. 1984b).

3.7 Kenny and Lau (1985, 1986)

In Kenney and Lau (1985), a study was carried out on the effect of disturbing forces such as seepage and vibration. Two constant head tests were performed using seepage cells which housed base soil specimens of 245 mm diameter (450 mm length) and 580 mm diameter (860 mm length) shown in Figure 3.7 and Figure 3.8. Throughout the tests a light vibration was applied, and was found to have a significant influence on some of the soils, while the top surface was stressed with a 10 kPa perforated plate.

Principal Findings

- Results from tests allowed authors to propose a method in which to evaluate grading instability, based on the shape of the grain size curve (applicable to concave upwards and bimodal grain-size distributions). This method was outlined in Chapter 2.

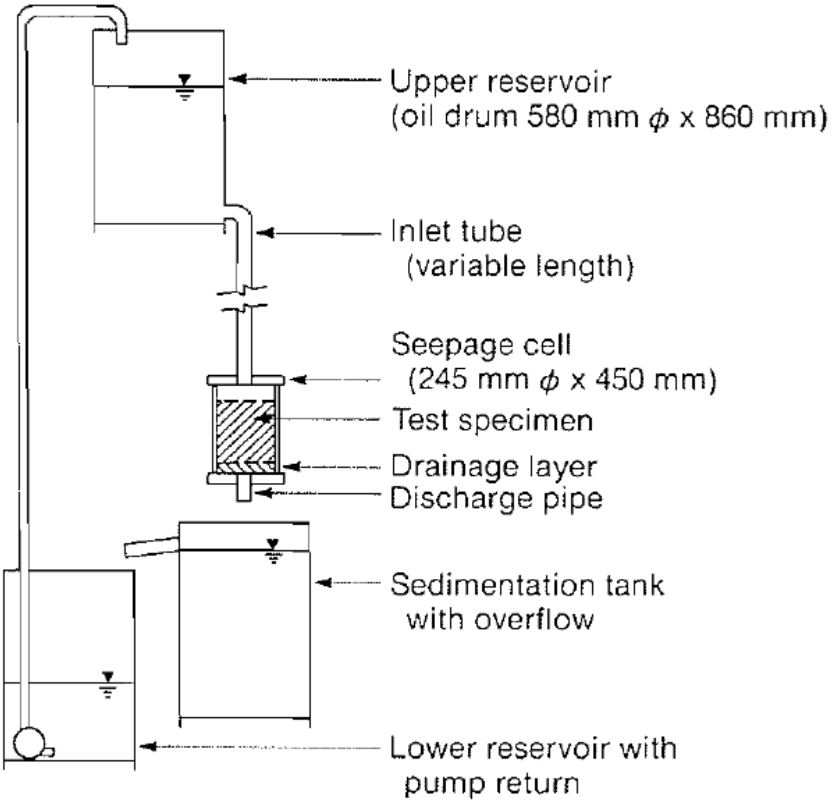

Figure 3.7: Test arrangement using 245 mm diameter seepage cell (Kenney & Lau 1985).

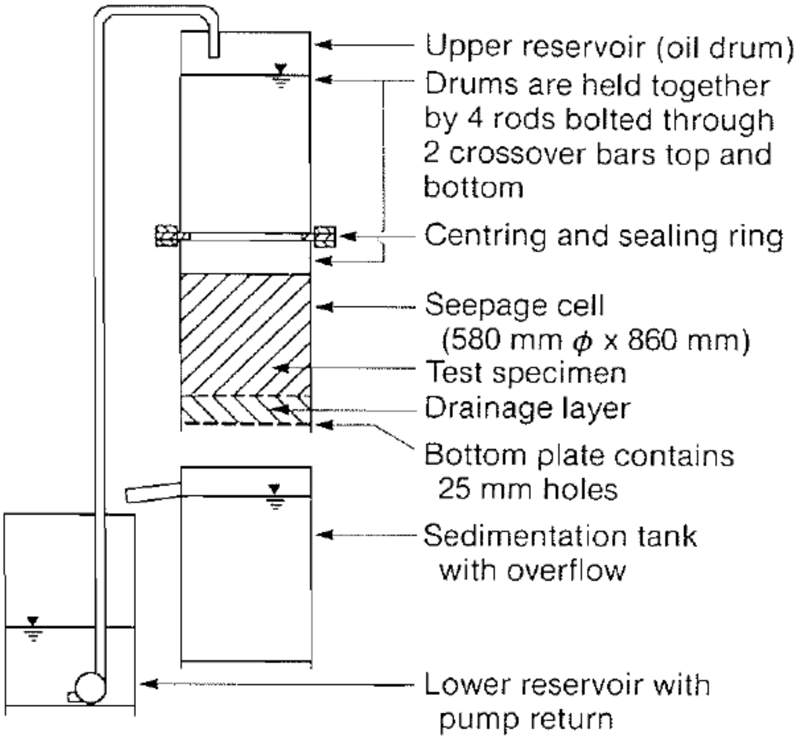

Figure 3.8: Test arrangement using 580 mm diameter seepage cell (Kenny and Lau, 1985).

3.8 Sherard and Dunnigan (1985, 1989)

Prior to Sherard and Dunnigan (1985) it was thought that the central core was the most important element in a dam, and that the dam would remain safe so long as no cracks or other concentrated leaks formed. However, as Sherard and Dunnigan (1985) noted, concentrated leaks were commonly found to form in well designed and constructed dams, and hence it became clear that the most important element in a dam was the filter downstream from the core.

Following on from previous filter test development in Sherard et al. (1984a, b) the authors designed another filter test, named the ‘No Erosion Filter Test’ (NEF-Test) with its apparatus shown in Figure 3.9. This downward flow test involved water flowing through a hole in the base specimen under about 4 kg/cm^2 (392 kPa) pressure for 5-10 minutes, and measuring the water quantity and observing its turbidity (colour). The apparatus was then dismantled and observations made on the erosion of the base specimen.

In Sherard and Dunnigan (1989) further research was published following extensive testing on 28 different base samples and 4 filters. In addition, Ramos and Locke (2000) provide a detailed procedure for implementing the NEF-test including apparatus construction, filter and base soil preparation and interpretation of results.

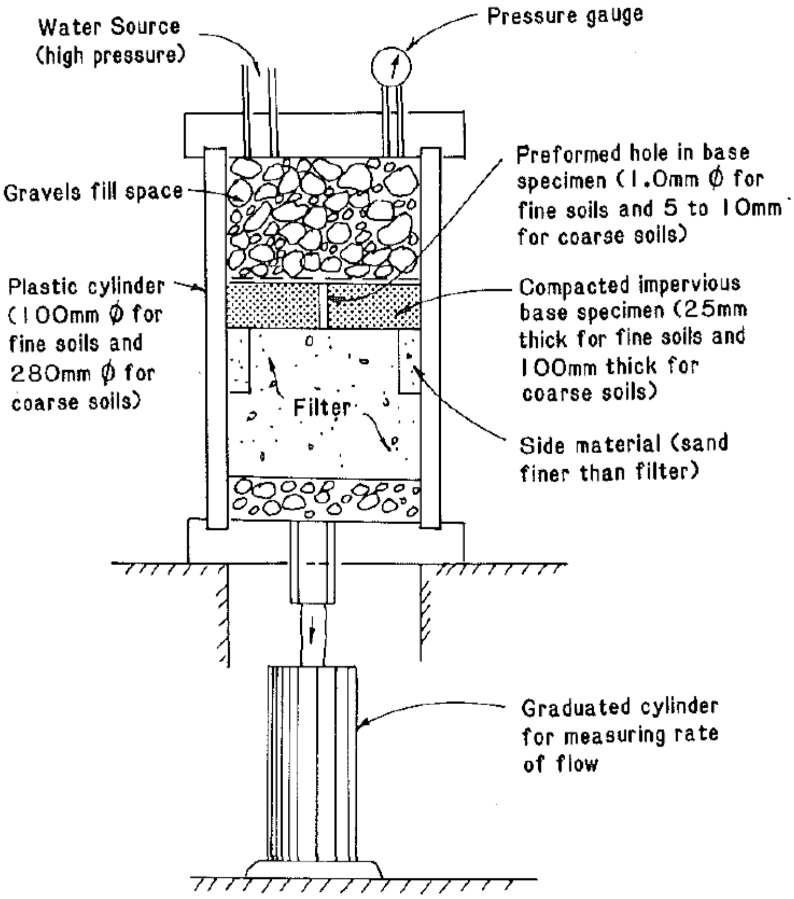

Figure 3.9: No Erosion Filter Test Details – No Scale (Sherard & Dunnigan 1985).

Principal Findings

- Four impervious soil groups are categorised and recommended criteria were given for each, shown in Table 3.1.
- The NEF test is the best available test for evaluating critical filters downstream of impervious cores in embankment dams.
- NEF-test was a worst case scenario of core material behaviour.
- Success or failure of a filter is independent of the hydraulic gradient.
- Water content and density of the core are not controlling factors in filter success.
- The main factor influencing success is the ratio of filter gradation to base gradation.

Table 3.1: Recommended criteria with conservative safety factor for impervious soil groups. Compiled from Sherard and Dunnigan (1985).

Impervious Soil Group	Description	Criteria
1	Fine Silts and Clays	For > 85% by weight particles finer than the No. 200 sieve (0.075mm): $D_{15} \leq 9\ d_{85}$
2	Sandy Silts and Clays, and Silty and Clayey Sands	For 40-85% by weight particles finer than the No. 200 sieve: $D_{15} \leq 0.7$mm
3	Sands and Sandy Gravels with Small Content of Fines	For < 15% by weight particles finer than the No. 200 sieve: $D_{15} \leq 4\ d_{85}$
4	Coarse impervious soils between groups 2 and 3	For 15-40% by weight particles finer than the No. 200 sieve.

3.9 Lafleur, Mlynarek and Rollin (1989)

Lafleur et al. (1989) recognised that the filtration mechanism of broadly graded soils is different from uniform soils. Therefore testing of cohesionless broadly graded soils was undertaken to quantify the potential migration of base particles, the self-filtration layer, and the quantity of particles carried away using glass ballotini beads. Laboratory testing consisted of two types of tests: 1) Screen Tests (apparatus shown in Figure 3.10) to estimate the size portion of base materials where particle migration occurs, and also to measure the quantity of soil particles lost during the self-filtration process; 2) Compatibility Tests (apparatus shown in Figure 3.11) using filters of increasing coarseness designed to determine the indicative diameter of soils where an insignificant loss of particles occurs. Laboratory procedures are published in Lafleur et al. (1986), and the self filtration mechanism is discussed in detail in Chapter 2.6.

Principal Findings

- The quantity of fines carried away and the thickness of the self filtration layer could be related to the gradation curve profile, and to the soil broadness coefficient.
- The tests overestimate the loss of particles and the height of the self-filtration zone due to: a) the smooth surface of glass ballotini beads (hence low surface friction) and; b) the vibrations which promote a downward movement of particles, which both discourage the formation of soil arches.
- The opening size of filters must be compared with an indicative base size that involve minimal particle migrations.

- For linearly graded soils, the minimum base size value is equal to the d_{50}, and the self filtration process will lead to equilibrium.
- For gap-graded soils, d_{SF} (characteristic diameter of base particles capable of initiating self-filtration) should correspond to the lower fraction of the gap, since coarser particles of these soils do not intervene in the self-filtration process.

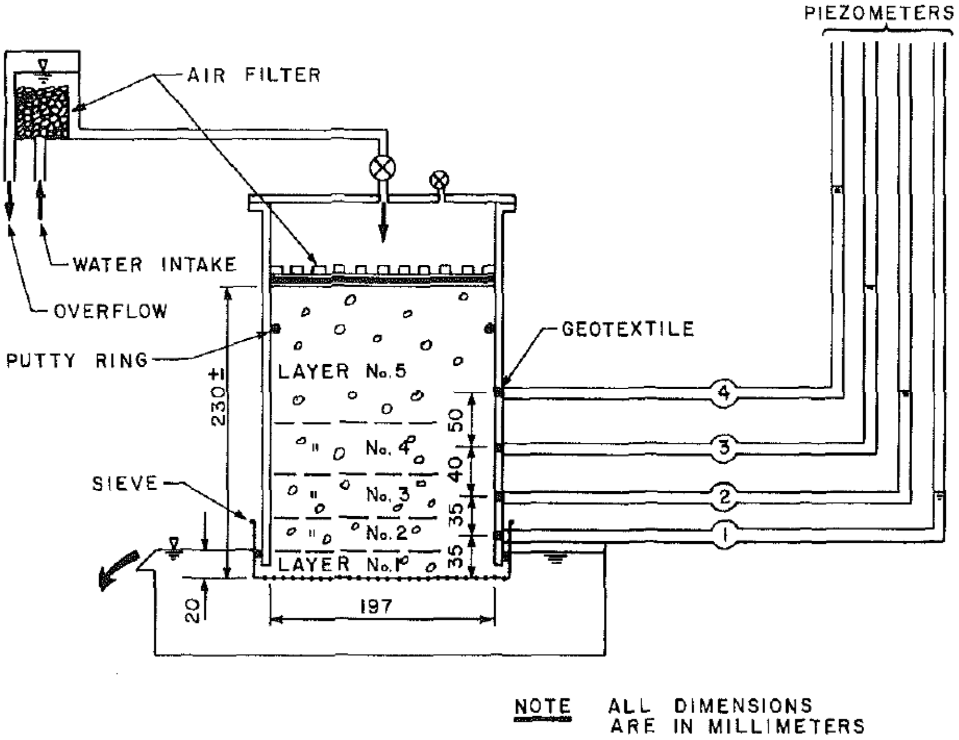

Figure 3.10: Permeameter for Screen Tests (Lafleur et al. 1989).

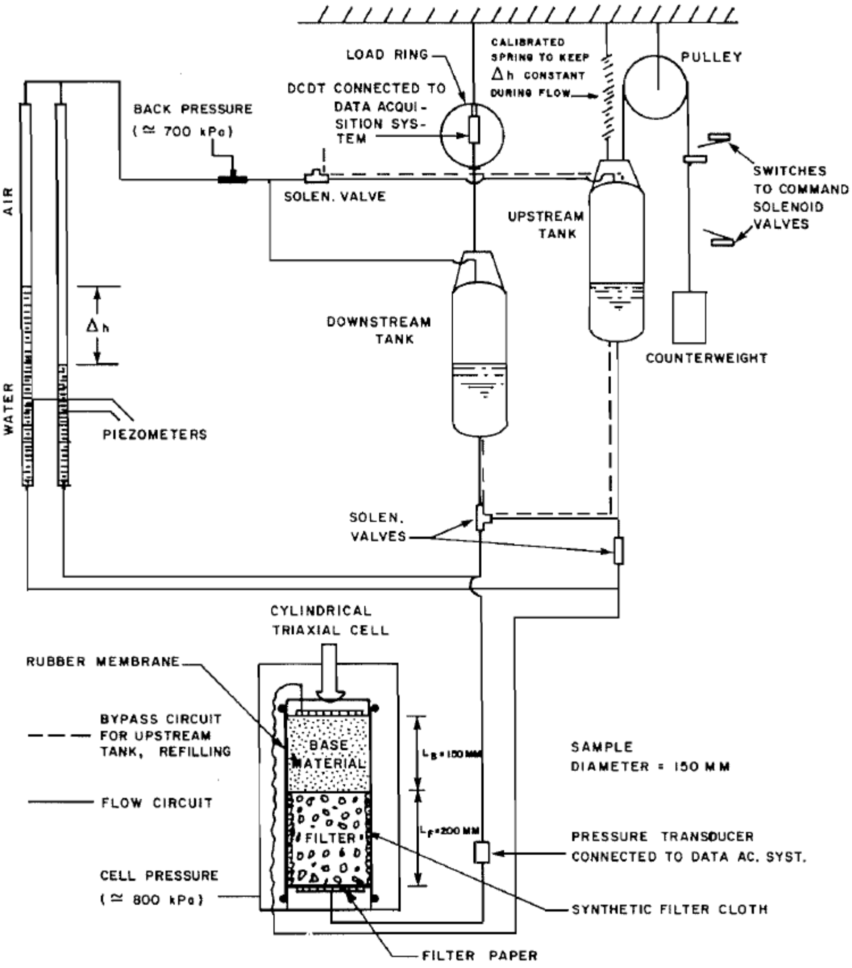

Figure 3.11: Filter test apparatus for compatibility tests (Lafleur 1984).

3.10 Burenkova (1993)

Burenkova (1993) carried out both upward and downward flow seepage tests on 22 granular materials. From the results, the non-uniform soils were divided into suffosive and non-suffosive groups. Few details were given about the testing device, apart from that it had ‘a number of piezometers and a trap for eroded sand’ (Burenkova 1993, p. 359).

Principal Findings

- A method was proposed to predict the suffosiveness of a soil in terms of D_{90}, D_{60} and D_{15} soil grain sizes, as described in Chapter 2.10.
- Non-suffosive soils can be described by the inequality:

$$0.76\log(h'') + 1 < h' < 1.86\, log(h'') + 1. \tag{3.1}$$

3.11 Okita and Nishigaki (1993)

Okita and Nishigaki (1993) carried out an investigation on the filtration processes, particularly clogging conditions, using a γ-ray density meter. Uniform silica sand of size No. 6 sieve (3.35 mm) was compacted into an acrylic cylinder equipped with four pressure sensors to measure the hydraulic gradient through the specimen. Water was pumped through the horizontal specimen with a pressure of 1.0 kgf/cm^2 (98 kPa), and flow rate was measured at an outlet at the same time as the density distribution, every three minutes.

Principal Findings

- The clogging state depended on the effective grain size ratio, D_{15F}/D_{85B} and the duration of the test.
- No base soil loss occurred when $D_{15}/d_{85} \leq 7$ (no clogging process) (Figure 3.12).
- Some fine particles intruded into the gravel filter to form a self-filtering zone and therefore protected the adjacent material from clogging when $7 < D_{15}/d_{85} \leq 10$ (self filter making process) (Figure 3.13).
- Clogging started to develop and build up boundlessly when $10 < D_{15}/d_{85}$ (filter clogging process) (Figure 3.14).

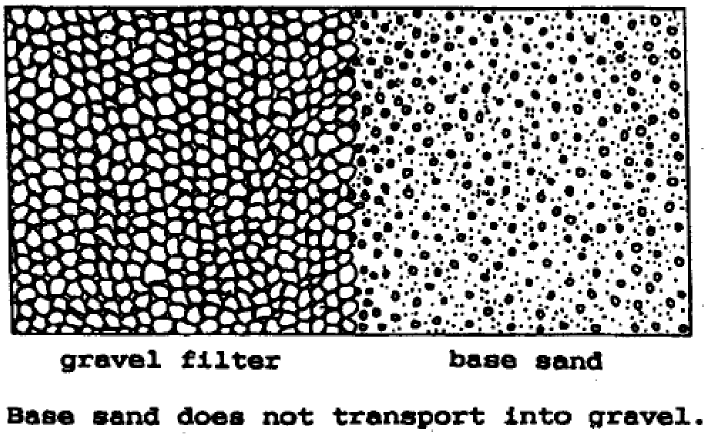

Figure 3.12: State of no clogging (Okita & Nishigaki 1993).

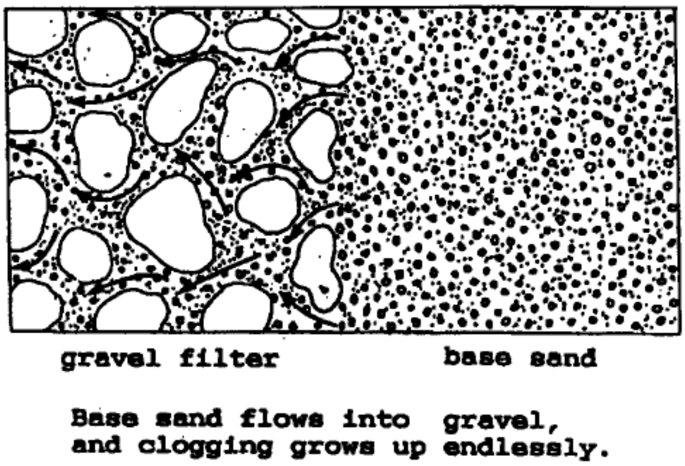

Figure 3.13: State of clogging (Okita & Nishigaki 1993).

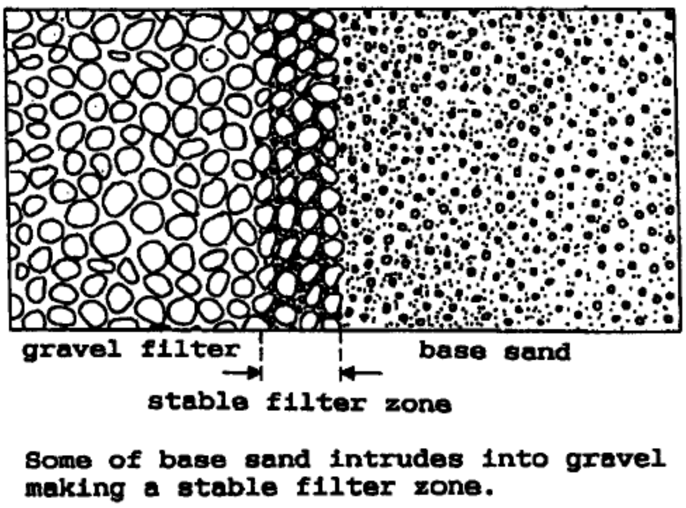

Figure 3.14: Process of self-filtration (Okita & Nishigaki 1993).

3.12 Skempton and Brogan (1994)

Piping tests on internally unstable sandy gravels were performed to compare the theoretical value of the critical hydraulic gradient at which piping occurs under an upward flow (according to Terzaghi (1925)) with the actual hydraulic gradient. The testing apparatus used on these stable and unstable materials consisted of a transparent 13.9 cm diameter cylinder in which a compacted filter specimen approximately 15.5 cm in length, rested on a screen which overlayed dispersing material, shown in Figure 3.15. Four standpipe piezometers measured the piezometric response as the upward flow of water was increased in small steps until either piping failure occurred, or the opening of a horizontal crack which would then work its way to the surface, typically yielding a large increase in flow. Each test had a duration of about 1.5 hours, and at the conclusion of the test washed out fines were collected, dried and weighed.

Skempton and Brogan (1994) found that in their internally unstable tests, laminar flow according to Darcy's law (1856) occurred until slightly before the critical hydraulic gradient, which occurred at values significantly lower than calculated using Terzaghi's equation (1925):

$$i_c = (1 - n)(1 - \rho) = \frac{\gamma'}{\gamma_w} \tag{3.2}$$

where n is the overall porosity of the material, ρ is the specific gravity of the grains, γ' is the submerged unit weight of the soil and γ_w is the unit weight of water.

The authors noted that the theory must be true that for piping to occur, the effective stress σ' is zero, therefore the pore pressure, u, is equal to the total vertical stress σ, as $\sigma' = \sigma - u$. The authors proposed that the most likely reason for the critical hydraulic gradient being reached prematurely is that in the most extreme circumstances, the overburden load is being carried entirely by the coarser fraction skeleton. This allows the finer particles to migrate away by conditions simply required to suffuse particles in horizontal flow when gravity plays little part. Skempton and Brogan (1994) coined this 'segregation piping'. Conversely, if the fine grains are initially carrying some proportion of the overburden load, then the effective stress on the finer particles (σ_f'), which is only a portion of the effective stress on the coarser particles (σ'), can be described by:

$$\sigma_f' = \alpha\gamma' z \tag{3.3}$$

where α is a reduction factor and $\gamma' z$ is the average effective stress across a section at depth z, which is also σ'. Therefore, the critical gradient for piping in the fine grains will be:

$$i_{cr} = \alpha\left(\frac{\gamma'}{\gamma_w}\right) \text{ or } i_{cr} = \alpha i_c \tag{3.4}$$

where i_{cr} is the critical hydraulic gradient observed in the test. This relationship describes that a larger α will yield a greater resistance to the onset of seepage-induced instability, as outlined by Li and Fannin (2012).

Results from the Skempton and Brogan (1994) 'A' sample showed that the $i_{cr} = 0.2$, while the $i_c = 1.09$, therefore giving a $\alpha = 0.18$. Implied by this is that the initial effective stress in the fine grained material in a no-flow condition is 18% of the average effective stress across the whole sample. Therefore, the fine grains are expected to pipe when the effective stress is reduced to zero by an upward flow (Skempton & Brogan 1994).

Skempton and Brogan (1994) also note was that in their ‘A’ sample, piezometer readings initially showed uniform hydraulic gradients from the top to the bottom of the material. Part way through the test a distinct discontinuity in recordings occurred, and was attributed to the presence of fines that had been washed out and were collecting at the surface of the sample. Skempton and Brogan (1994) ran successive tests with a sand filter overlying the main filter material in question, and then repeated these with an increase in the D_{15} from 0.60 to 0.86. In all tests they obtained similar results, therefore showing a significant proportion of the sand grains could migrate within the sample, when the exit from the upper surface was prevented. In their ‘C’ and ‘D’ samples which were internally stable, piping could only be induced when the theoretical hydraulic gradient, i_c, was reached.

Principal Findings

- Discrepancy between experimental (i_{cr}) and theoretical (i_c) values of critical hydraulic gradient can probably be explained by the greater overburden load being carried on a framework of gravel particles. Therefore, the finer fraction is under a smaller effective stress and hence is able to migrate away, typically occurring at critical hydraulic gradients approximately 1/3 to 1/5 of the theoretical hydraulic gradient in internally unstable materials.
- Piping occurs in internally stable materials when the effective stress is approaching zero, which for uniform sands, arises when the theoretical hydraulic gradient is reached (Terzaghi 1925). For internally unstable materials where only a portion of the effective stress is carried by the finer fraction, then $i_{cr} = \alpha i_c$.
- The stable to unstable boundary defined by Kenney and Lau (1985, 1986) was in agreement with their own.
- The stable to unstable boundary proposed by Kezdi (1979) was in agreement with their own, based on the filter ratio of the sand and gravel components.

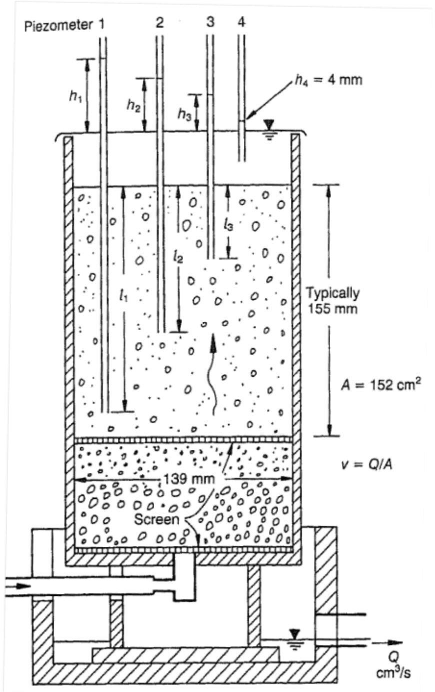

Figure 3.15: Skempton and Brogans' upward flow test apparatus (Skempton & Brogan 1994).

3.13 Tomlinson and Vaid (2000)

Tomlinson and Vaid (2000) carried out an experimental study to determine the critical gradient at which soil erodes through a filter by subjecting the materials to variable confining pressures inside a permeameter. The apparatus, shown in Figure 3.16 and Figure 3.17, enclosed a 10 cm diameter by 10 cm high soil-filter specimen which had a vertical stress of 50 to 400 kPa applied using a top loading platen. A downward flow of tap water through the sample generated a hydraulic gradient between 0 and 25, with test durations up to 4.5 hours. Granular materials used were spherical glass beads of known shape, surface texture, and uniform size to help promote consistency. Different values of D_{15}/d_{85} were tested over a range of confining stresses, hydraulic gradients, rate of increase and filter thicknesses.

Principal Findings

- For $D_{15}/d_{85} < 8$, no piping was induced, even with the maximum gradient applied.
- For $8 < D_{15}/d_{85} < 12$, piping occured, but only when the critical gradient was reached.
- For $D_{15}/d_{85} > 12$, piping occurred spontaneously under little gradient.
- Critical gradient required to induce piping decreased as D_{15}/d_{85} is increased.
- The D_{15}/d_{85} required to initiate critical gradient decreased with increasing confining pressure.

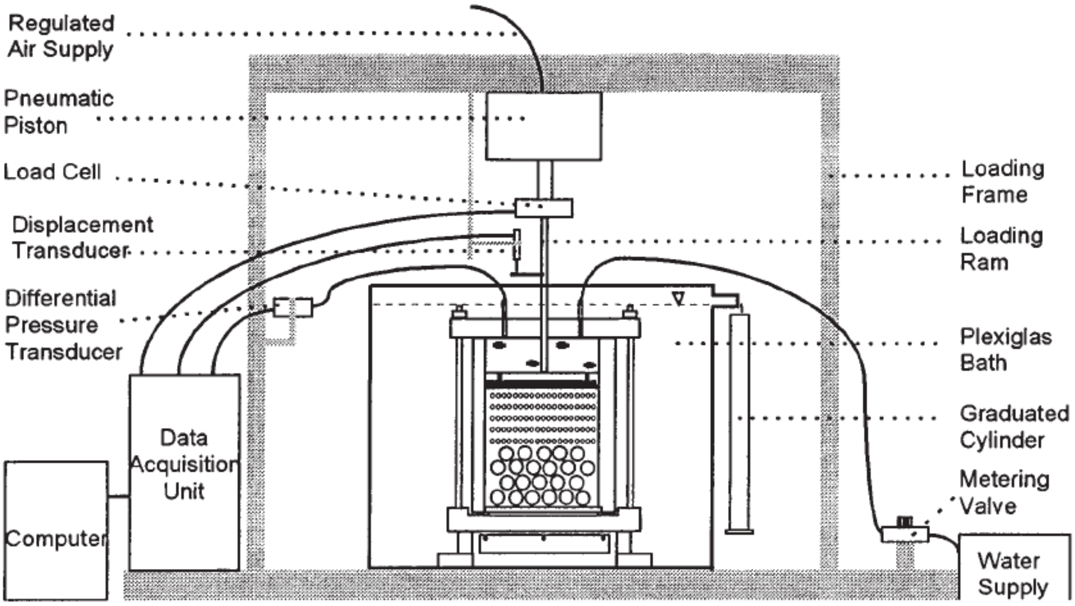

Figure 3.16: Schematic diagram of the test layout (Tomlinson & Vaid 2000).

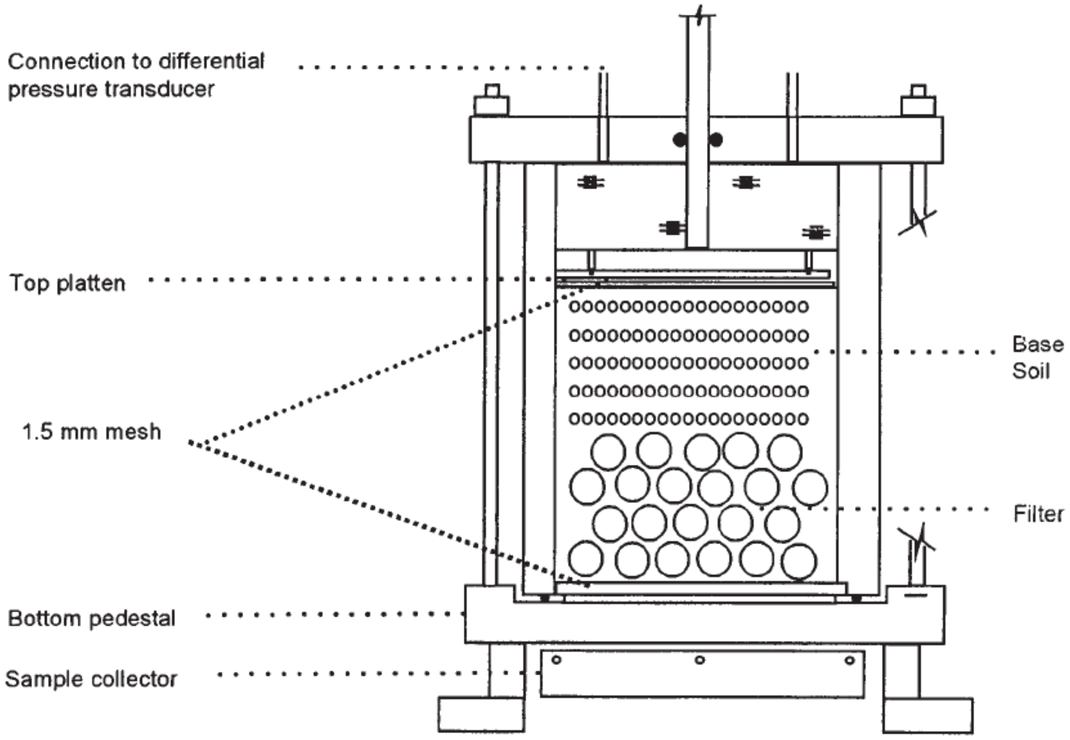

Figure 3.17: Schematic design of the permeameter (Tomlinson & Vaid 2000).

3.14 Foster and Fell (2001a)

Foster and Fell (2001a) presented the continuing-erosion filter (CEF) test to investigate the continuing-erosion boundaries for base soils with a fines content between 15-85%, and to identify the main factors that influence the erosion losses required to seal coarse filters. Testing procedures were similar to those of Sherard and Dunnigan (1989), however a few variations were introduced.

For example: 1) the water passing through the filter was collected, dried and weighed to determine the amount of base soil loss required to seal the filter; 2) progressively coarser filters were used until the filter was not sealed; and 3) thicker base specimens were used to allow for a greater erosion loss. The testing apparatus is shown in Figure 3.18.

Soils were split into 4 groups:

1. Soil group 1 (fines content 85-100%);
2. Soil group 2A (fines content 35-85%);
3. Soil group 3 (fines content <15%) and;
4. Soil group 4A (fines content 15-35%).

Design criteria from Sherard and Dunnigan (1989) are compared to “No-Erosion” boundary criteria proposed by Foster and Fell (2001a), in Figure 3.19.

Principal Findings

- For soil groups 2 and 4, the subdivision of fines content be changed to 35%, from 40%.
- Criteria were proposed for the no-erosion, excessive-erosion and continuing erosion boundaries, as shown in Figure 3.20.
- Filters coarser than the criteria recommended by Sherard and Dunnigan (1989) are capable of sealing concentrated leaks, but the authors do not recommend relaxing the design criteria.
- Recommend that the NEF-test be carried out to confirm the D_{15} for no erosion.

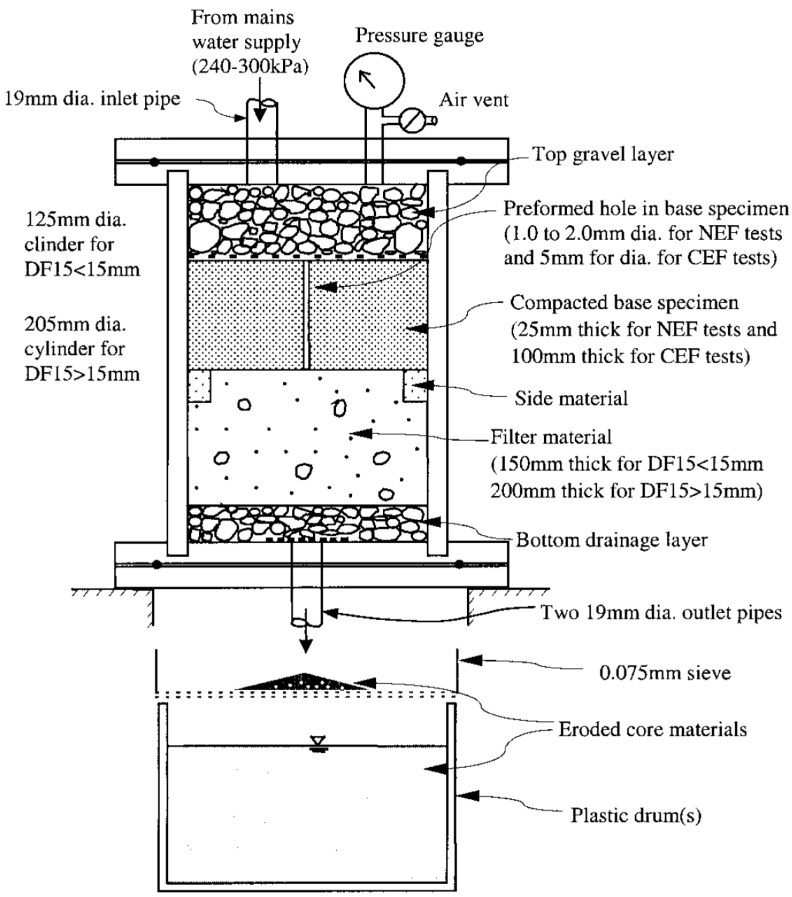

Figure 3.18: CEF Test Apparatus (Foster & Fell 2001a).

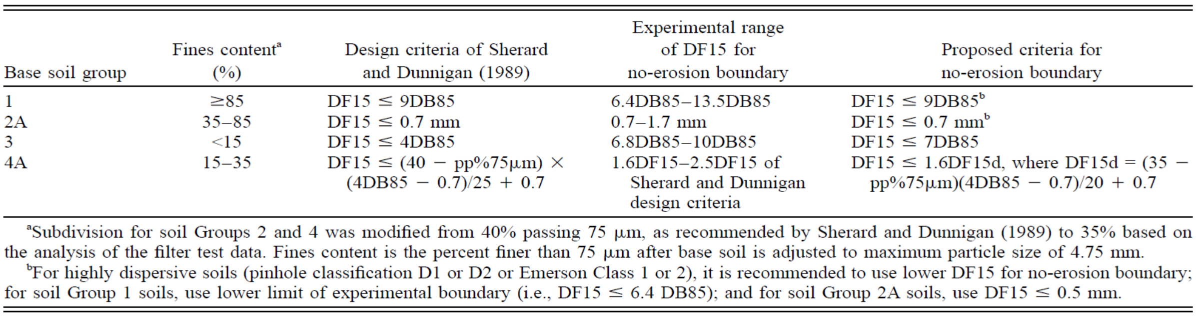

Base soil group	Fines content[a] (%)	Design criteria of Sherard and Dunnigan (1989)	Experimental range of DF15 for no-erosion boundary	Proposed criteria for no-erosion boundary
1	≥85	DF15 ≤ 9DB85	6.4DB85–13.5DB85	DF15 ≤ 9DB85[b]
2A	35–85	DF15 ≤ 0.7 mm	0.7–1.7 mm	DF15 ≤ 0.7 mm[b]
3	<15	DF15 ≤ 4DB85	6.8DB85–10DB85	DF15 ≤ 7DB85
4A	15–35	DF15 ≤ (40 − pp%75µm) × (4DB85 − 0.7)/25 + 0.7	1.6DF15–2.5DF15 of Sherard and Dunnigan design criteria	DF15 ≤ 1.6DF15d, where DF15d = (35 − pp%75µm)(4DB85 − 0.7)/20 + 0.7

[a] Subdivision for soil Groups 2 and 4 was modified from 40% passing 75 µm, as recommended by Sherard and Dunnigan (1989) to 35% based on the analysis of the filter test data. Fines content is the percent finer than 75 µm after base soil is adjusted to maximum particle size of 4.75 mm.

[b] For highly dispersive soils (pinhole classification D1 or D2 or Emerson Class 1 or 2), it is recommended to use lower DF15 for no-erosion boundary; for soil Group 1 soils, use lower limit of experimental boundary (i.e., DF15 ≤ 6.4 DB85); and for soil Group 2A soils, use DF15 ≤ 0.5 mm.

Figure 3.19: Summary results of statistical analysis and proposed criteria of no-erosion boundary of filter tests for assessment of filters of existing embankment dams (Foster & Fell 2001a).

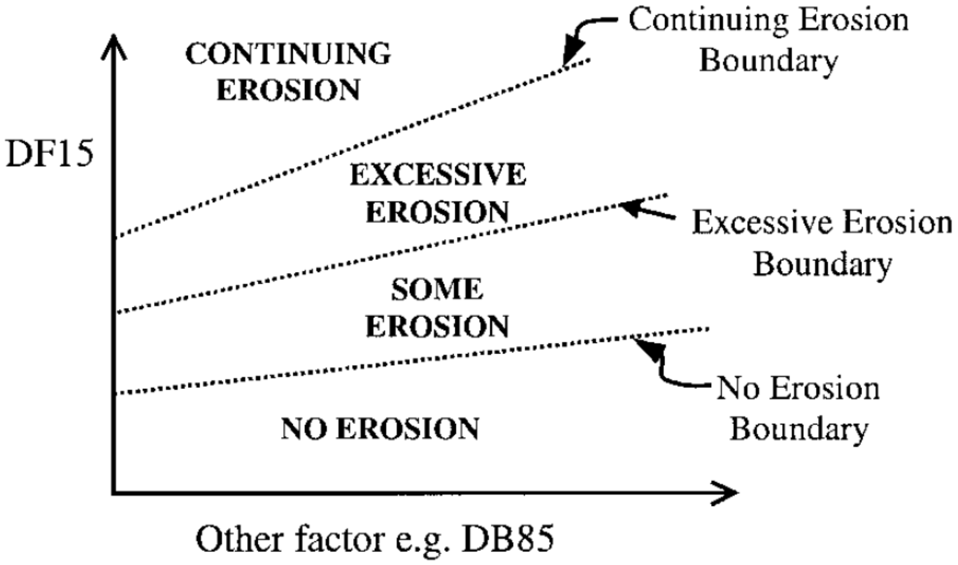

Figure 3.20: Conceptual erosion boundaries of filter test behaviour (Foster & Fell 2001a).

3.15 Garner and Sobkowicz (2002)

With mounting evidence to support the relationship between piping in dams and dykes and the presence of gap-graded materials, a large scale permeameter was developed to test the effects of gas exsolution, as described by Sobkowicz et al. (2000). Tests were carried out on soils with a gap-grading between the 30% and 40% passing, relating to medium to coarse sands. The permeameter (Figure 3.21) consisted of a 1 m long Lucite tube with diameter of 30.38 cm, in which water would flow from a de-aeration tank, upwards through the apparatus. Pore pressures were measured at seven, approximately equidistant, points using electronic piezometers, while a mounting frame holding the permeameter applied a 600 kPa seating load. The flow rate and pressure were controlled using valves and accumulators, and data from recording equipment was collected through a multiplexer and stored in data loggers.

In their tests, the base specimen was placed in fifteen 45 mm layers, to a height of 660 mm. The filter was then overlaid in six layers, of about 50 mm each, from 660 mm to 953 mm. Each layer was compacted at optimal soil moisture content to 100% Standard Proctor density. A seating load of 313 kPa was applied to the specimen and the sample was saturated with de-aired water. When water emerged from the top of the sample the seating load was gradually increased to 600 kPa, while the base pressure was increased to 50 kPa and the back pressure increased to 5 kPa.

In the first phase of the test, the hydraulic gradient was increased to determine if hydraulic gradient alone could trigger suffusion and/or suffosion. The hydraulic gradient was increased in small increments from April 6, 2001 to June 11, 2001. The second phase involved introducing 'gassy' water into the sample, achieved by bubbling air through the pressurised water reservoir. At the conclusion of the test, the specimen was frozen using frozen carbon dioxide and stored in a freezer. Computed Tomography (CT) scans on 50 horizontal slices were then taken for analysis of the suffusion and suffosion behaviour.

Principal Findings

- Suffusion can produce extremely low permeability, high gradient zones within internally unstable materials.
- Suffosion can occur in gap-graded materials that have a coarse fraction with widely dispersed particles.
- Suffosion can be triggered by the introduction of gassy water.
- The concept of self-healing in widely graded cores and filters may not apply to gap-graded soils that are vulnerable to suffosion.
- The Kenney and Lau (1985) internal stability criteria of H/F=1 possibly could extend to beyond F=20%.
- Additional research is required for fines migration in gap-graded materials.

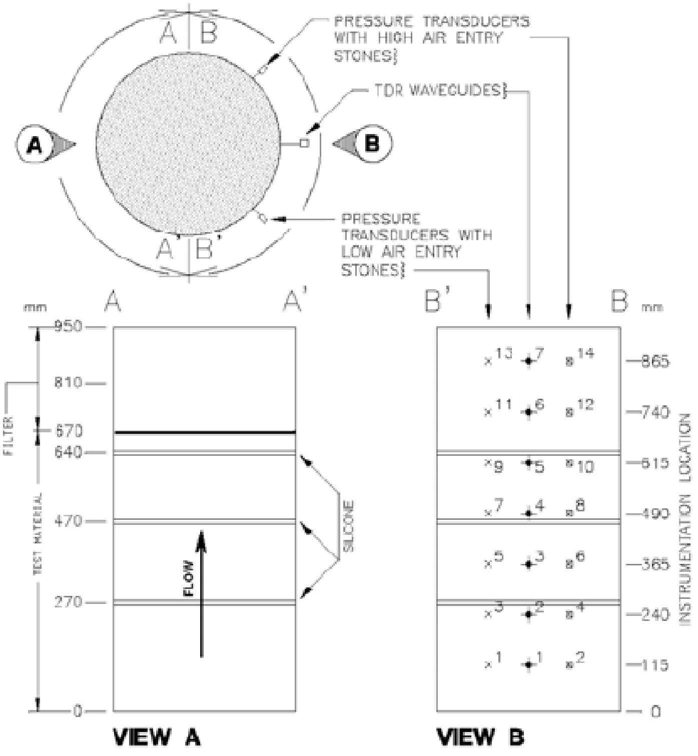

Figure 3.21: The large scale permeameter used by Garner and Sobkowicz (2002).

3.16 Wan and Fell (2002, 2004a, b) and Wan (2006)

Wan and Fell (2002, 2004 a, b) and Wan (2006) developed two tests to examine the erosion characteristics of soils passing through cracks in embankment dams. These tests called the ‘hole erosion test’ (HET) and the ‘slot erosion test’ (SET) are shown in Figure 3.22 and Figure 3.23 respectively, and were used to determine ‘the erosion rate index’ denoted by ‘*I*’. Values of *I* ranged from 0 to 6 and measure the rate of erosion given by:

$$I = -\log\left(C_e\right) \tag{3.5}$$

where C_e is a proportionality constant (coefficient of soil erosion) with the unit s/m. Small values imply a more rapidly erodible soil, while larger values imply a less rapidly erodible soil.

The HET has a soil specimen compacted inside a standard mould (used in standard compaction tests) which has a 6 mm-diameter hole drilled in a longitudinal direction. The flow rate is constantly measured throughout a test which allows for the indirect measurement of the diameter of the preformed hole. The SET is similar to the HET, however, a much larger soil specimen is compacted into a 0.15 m wide x 0.1 m deep x 1 m long box with a 2.2 mm wide x 10 mm deep x 1 m long slot formed along one surface of the soil sample. This slot is in contact with the Perspex pane and allows the width of the reformed slot to be measured at regular time intervals as it widens due to erosion. Equations allow the C_e, and hence *I* to be calculated.

Principal Findings

- Test results show that non-plastic and low plasticity soils erode extremely to moderately rapidly.
- The erosion rate index of soil is strongly influenced by the degree of compaction and water content. Specifically, a soil compacted to a higher dry density and to the wet side of the optimum water content will have a higher erosion rate index (higher erosion resistance).
- There is evidence that mineralogy can affect erosion rates, as samples with high iron oxide (hence, cementing properties) have low rates of erosion.
- Coarser grained soils have lower resistance to erosion compared to fine grained soils.

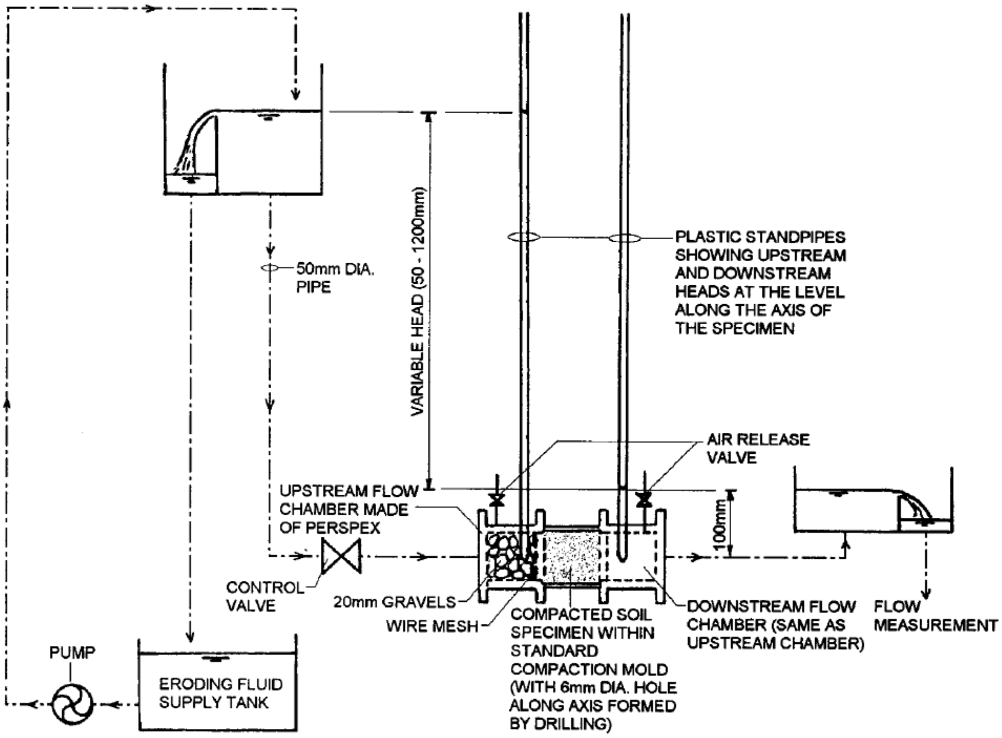

Figure 3.22: Schematic diagram of hole erosion test assembly (Wan & Fell 2004b).

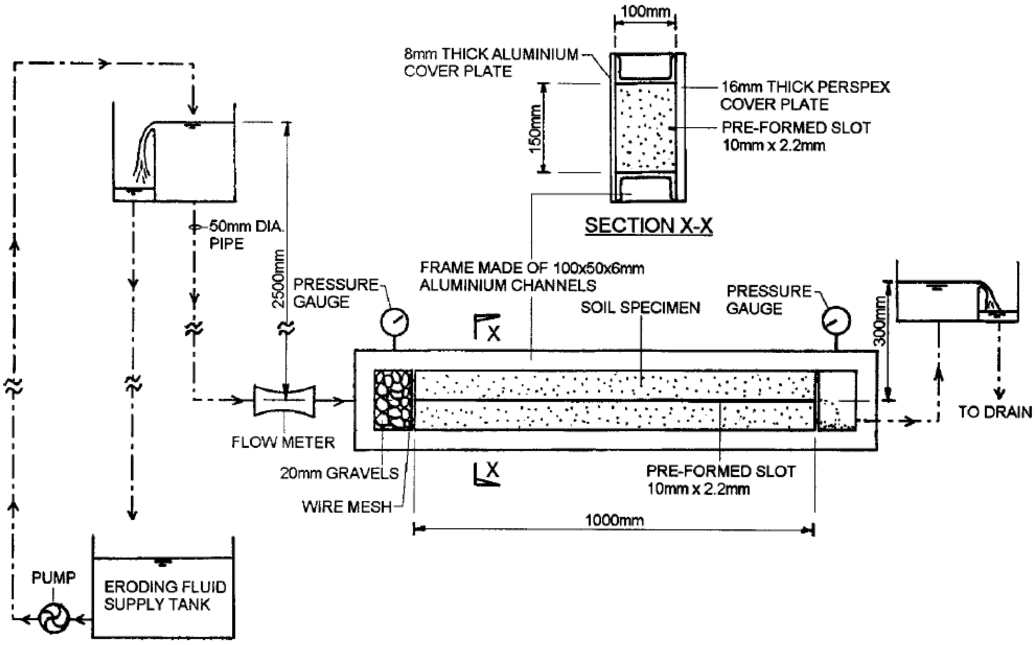

Figure 3.23: Schematic diagram of the slot erosion test assembly (Wan & Fell 2004b).

3.17 Fannin and Moffat (2006)

Fannin and Moffat (2006) constructed a rigid wall permeameter apparatus to test 5 soils, so that the Kezdi (1979) criterion could be evaluated. The apparatus was cylindrical and constructed of Plexiglas, with a 100 mm internal diameter, as shown in Figure 3.24. The specimen was reconstituted by slurry mixing under vacuum, then placed into the permeameter on a lower mesh screen using a spoon to create a saturated and homogeneous specimen. An upper mesh screen overlaid the specimen and a vertical stress of 25 kPa was applied using a perforated top plate. A downward flow of distilled, de-aired water at a temperature of about 20 °C was applied, controlled by the head height. Seven differential pressure transducers were mounted across the permeameter, and volumetric discharge was periodically measured. The washout of fines was collected at the bottom of the apparatus in a silicon hose, so the mass percentage of fines loss could be calculated. Flow through the specimen started at approximately i_{av} = 0.1 and was increased in stages up to 20, with each stage having a duration of 90 minutes. For samples that did not exhibit internal instability, a vibration of 1 Hz was applied using an air activated double acting hammer, mounted at the base of the permeameter. At the conclusion of the test the specimen was excavated in three equal layers and a grain size analysis was run on the top, middle and bottom sections.

Principal Findings

- The Kezdi (1979) criterion provides a conservative evaluation of the potential for internal instability in gap-graded soils, where unidirectional seepage occurs without vibration.
- The shape of the grain size curve governs the potential for instability, and may be quantified using the split gradation method attributed to Kezdi (1979) and evaluated with reference to the empirically derived limit of $D'_{15}/d'_{85} = 4$.
- Soils close to the limit $D'_{15}/d'_{85} = 4$ appear stable with seepage alone (no vibration).
- Soils with $D'_{15}/d'_{85} = 7$ exhibit internal instability at relatively low gradients.
- The ratio D'_{15}/d'_{85} where the onset of instability occurs with seepage alone appears consistent with the D_{15}/d_{85} ratio at which incompatibility of a uniform base soil and filter has been observed to occur (Fannin & Moffat 2006).

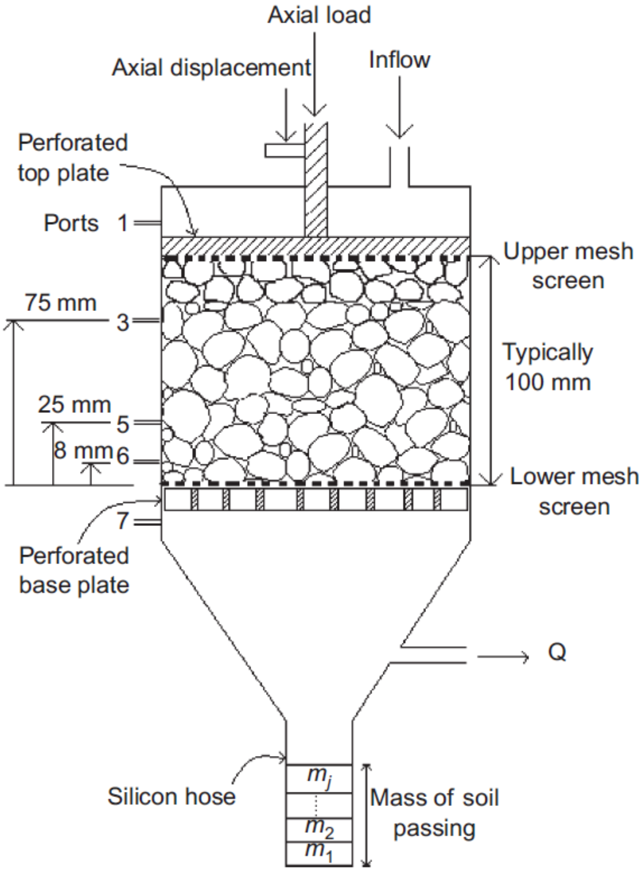

Figure 3.24: Configuration of Permeameter used by Fannin and Moffat (2006).

3.18 Moffat and Fannin (2006)

Following the occurrence of a sinkhole event in the W.A.C. Bennett Dam (Stewart & Garner 2002), Moffat and Fannin (2006) designed and commissioned a new large permeameter using experience gained by Garner and Sobkowicz (2002). The apparatus was then utilised for further testing in Moffat et al. (2011), Moffat and Fannin (2011) and is currently being used for further testing at the University of British Columbia (K Crawford-Flett 2011, pers. comm., 19.09.2011).

The apparatus shown in Figure 3.25 is a rigid wall acrylic permeameter that houses a specimen of 279 mm diameter and length of approximately 450 mm. Flow of filtered de-aired water through the sample can be either upward or downward and is controlled by adjusting the head height of the storage reservoir. An axial loading system can apply up to 350 kPa vertical effective stress. Seven total pressure transducers (TPR) and 6 differential pressure transducers (DPT) measure the hydraulic gradient and effective stress within the sample. A Linear Variable Differential Transducer (LVDT) mounted on the top of the specimen measures the axial displacement of the top loading plate. An automated system calculates the volumetric flow rate continuously by calculating the mass change in inlet verses outlet tank weight, over time.

In Moffat and Fannin (2006), a slurry deposition technique was used to reconstitute specimens, and involved placing the materials inside a vacuum chamber for 12 hours with frequent stirring to de-air the mixture. De-aired water was allowed into the permeameter to form a thin film covering the base mesh screen, before a large spoon was used to transfer the slurry mixture into the apparatus, while maintaining a thin film of water covering the placed material. Consolidation occurred upon axial loading of 5 kPa to 19 kPa increments to a maximum vertical effective stress of 350 kPa. Unidirectional seepage flow was then imposed on the specimen, and increased in increments of approximately $i_{av} = 1$ every 90 minutes, until failure occurred.

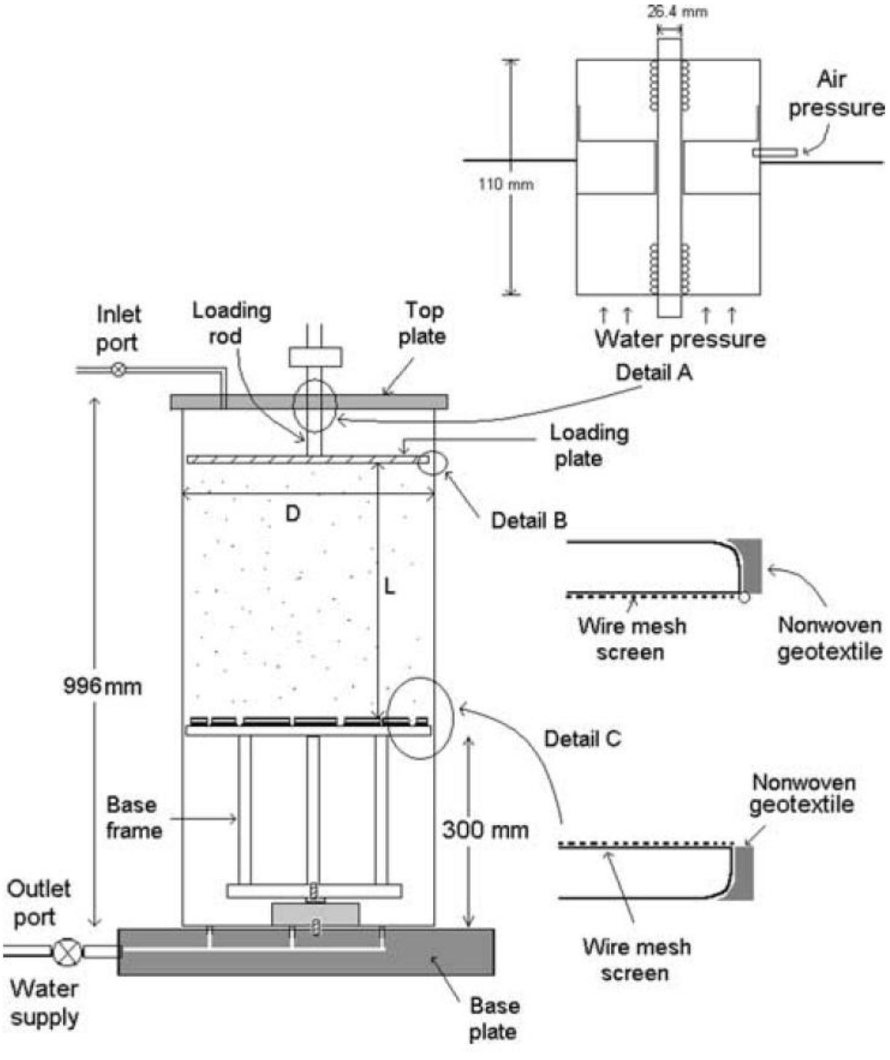

Figure 3.25: Large Permeameter cell commissioned by Moffat and Fannin (2006).

Principal Findings

- Measuring top and bottom axial load is integral to quantification of side-friction influence on the variation of effective stress along the specimen length.
- Using two arrays of pressure transducers is important in capturing the onset of failure, which is localised.
- The slurry deposition technique is satisfactory for reconstitution of a homogeneous saturated specimen of gap-graded material.
- There may be a relationship between effective stress and critical hydraulic gradient in triggering the onset of instability, which needs further investigation.

3.19 Synthesis

- Testing apparatuses typically involve either upward or downward flow of water through filter or base soil and filter materials that are packed in cylindrical tubes.
- Assessments can be made on the “success” of a filter material to resist the migration of soil particles by observations along transparent edges of the apparatus, the colour of out flowing water, the size of “holes” or “slots” that develop in base soils, the weight of eroded soil, or by carrying out a post-test sieve analysis to determine the change in PSD.
- Testing a range of PSDs and physical properties, like particle shape and compaction, under varying hydraulic gradients and confining pressures, helps to define more specific criteria for the design of adequate filter materials.

Chapter 4: Development of apparatus and testing methodology

4.1 Introduction

To study the mechanisms of internal erosion in filter materials a new technique has been employed, using glass particles and oil. Planar Laser Induced Fluorescence (PLIF) has proven successful in the study of model debris flows at the University of Canterbury (Sanvitali 2010) and the goal is to use this method to study internal erosion occurring in filter materials for embankment dams. The benefit in using this technique is that it allows a slice inside a 'soil' sample to be observed, whereas other test methods only allow for the outside edge to be seen through glass or Perspex walls. By examining an interior slice, the mechanisms of internal erosion can be examined without seeing edge effects that typically occur along the walls of rigid permeameters. For this testing to be carried out, a new 'transparent soil permeameter' needed to be designed and built, along with the development of a testing procedure. This chapter describes the development of the testing apparatus and testing methodology. It also outlines the particle size distributions (PSD) that were chosen for testing, and the methods for analysing each PSD in relation to its predicted stability.

4.2 Background and aims

The optical technique used in this experiment to 'see' the interior of the filter materials is known as Planar Laser Induced Fluorescence (PLIF), like that shown in Figure 4.1. In this experiment, glass particles are used in substitution for soil, and oil is used in substitution for water. In doing so, the glass particles are suitably up scaled to account for the fluid properties of the oil being different from water. This is beneficial in that particles are larger than those being replicated, and it therefore becomes easier to physically see particle interactions and changes inside the specimen. By seeing how the particles react and interact under various hydraulic gradients, packing (i.e. compacted or loose) and PSDs, it is hoped the mechanisms that occur during internal erosion will be better understood.

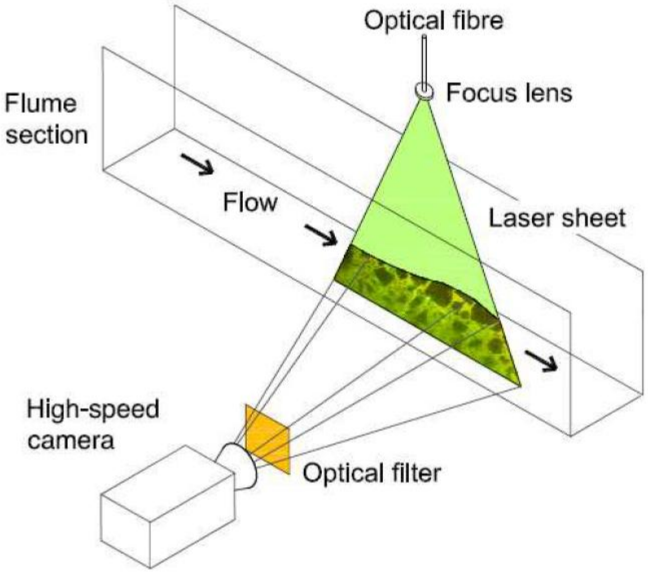

Figure 4.1: An example of the PLIF configuration used in the study of laboratory debris flows by Sanvitali (2010).

The aim of this project was to develop an apparatus and accompanying control system in which to employ the PLIF technique with glass and oil mixtures, so that the mechanisms of internal erosion could be studied. Once functioning, trial tests were carried out to validate the technique with already tested soil-water combinations. A method to analyse results was also investigated.

4.3 Visualisation technique

4.3.1 Requirements for transparency

In the discipline of optics, transparency is the physical property of allowing light to pass through an object, while the opposite property is known as opacity. A transparent material will transmit light through it, while an opaque material will not. Beams of light interact with materials in different ways depending on both the nature of the materials and the characteristics of the light (wavelength, frequency, energy etc.). The interaction of the light with the object can involve a combination of reflection, and transmittance with refraction. Examples of optically transparent materials are glass and distilled water, which allow most of the light to be transmitted through the material boundary, while a small portion of the light is reflected. The reflected light will have a change in direction due to the change in velocity it encounters between the two media. Numerous substances are selective in their absorption of white light frequencies, absorbing only certain portions of the visible spectrum and reflecting others. Frequencies of the spectrum that are not absorbed are either reflected back for us to see in the form of colour, or are transmitted through the medium.

The refractive index of a substance is the measure of the speed of light in that medium. It is defined as a ratio of the speed of light through a vacuum relative to that in the considered medium. Furthermore, it can be determined by the ratio of the sine of the angle of incidence of a ray of light entering a medium to the sine of the angle of refraction. It is possible to achieve optical transparency of a solid-liquid system by matching the refractive indices of their constituents, as shown in Figure 4.2. In this example a glass rod is resting in a refractively matched fluid, therefore making it transparent below the liquid line. In theory the mixture should be completely transparent, however in reality there are several factors that limit the depth to which light can penetrate, causing transparency degradation. A key weakness in practice is the ability to perfectly match the refractive indices of the fluid and solid media, which is made more difficult by the varying nature of the fluid with temperature and the presence of impurities. In addition, entrapped air bubbles in the solid-fluid mixture act as micro lenses that result in light rays to be mainly refracted and a little reflected, making the air bubbles semi-transparent.

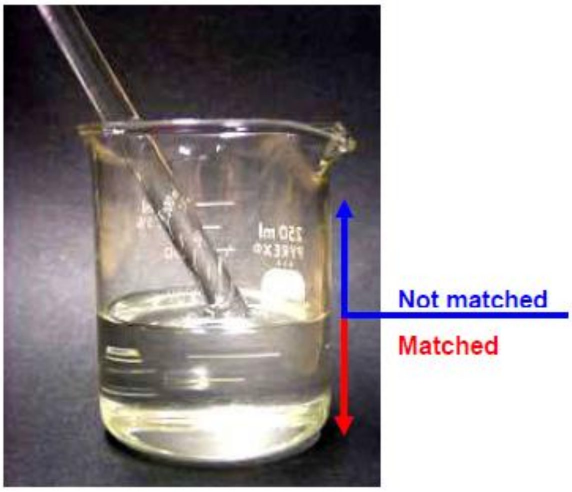

Figure 4.2: Example of refractive index matching materials (the rod is resting on the bottom of the beaker) (Sanvitali 2010).

4.3.2 Fluorescence

Fluorescence is the emission of light by a substance which has absorbed light of a different wavelength. The term stems from the mineral fluorite, which Sir George Stokes first found to emit red light upon illumination of ultraviolet light in 1952, although fluorescence is not limited to the fluorite mineral. Fluorochromes are the molecules in a mineral or substance that become fluorescent when appropriately excited. In an excited state the absorption of light energy boosts the electrons to a higher energy shell that is unstable. The excited state is brief in time where by the excited electron generally decays towards the lowest vibrational energy level, with lost energy being dissipated as heat. When the electron falls from the excited state to the previous state, light of a specific wavelength is emitted with photons possessing energy equal to the difference in energy between the ground and excited state. This energy difference determines the wavelength of the emitted light as shown in Figure 4.3. The spectrum of emitted light is always shifted to longer wavelengths (lower energy) compared to the absorbed spectrum. This difference in wavelength makes it possible to separate excitation light from emitted light by using optical filters. The difference in wavelength between the absorbed and emitted peaks of the fluorochrome is known as the 'Stokes Shift'. After an excitation pulse upon fluorochrome molecules, fluorescent emissions begin instantaneously and decay quickly. The time of the emissions are typically of a few nanoseconds, based on the half life of the fluorochromes in their excited state.

The brightness, or the intensity of light emitted from a fluorochrome is dependent on two properties:

- The ease in which the fluorochrome absorbs the excitation light (extinction coefficient);
- The efficiency in which it converts the absorbed light into emitted fluorescent light (quantum efficiency).

Therefore:

$$\text{Brightness} = \varepsilon\phi \tag{4.1}$$

where ϕ is the quantum yield, and is the ratio of the number of photons emitted compared to the number of photons absorbed. ε is the extinction coefficient and is the amount of a given wavelength that is absorbed by the fluorochrome.

Furthermore, besides the brightness function of a fluorochrome, the intensity of the emitted light is also dependent on the intensity and wavelength of the incident light, and the amount of fluorochrome present. The greater the light intensity used to illuminate the sample, the more the fluorochrome molecules are excited, resulting in a greater amount of photons being emitted. When using a light source such as a laser, the wavelength and intensity are able to be held constant, resulting in the number of photons emitted being proportional to the number of fluorochrome molecules present. Additionally, the fluorescence emission is largely affected by the localised environment surrounding the fluorochrome. For example, the solvent viscosity, ionic concentration, pH and hydrophobicity in the environment are variable that can all have profound effects on both the fluorescence intensity and the lifetime of the excited state (Sanvitali 2010).

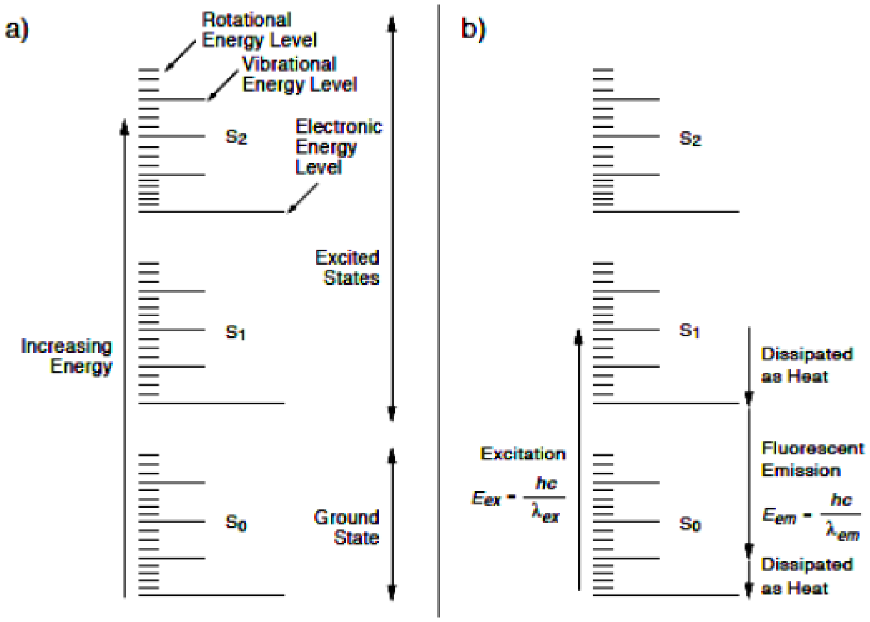

Figure 4.3: a) Diagram of singlet energy levels of a molecule, including superimposed vibrational and rotational energy levels. b) Example of excitation and fluorescent emission, E = energy difference between the origin and destination energy levels during excitations and emission of light h = Planck's constant; c = the speed of light; λ = the wavelength of the absorbed or emitted light. The energy of the light is inversely proportional to the wavelength of the light (E = hc/λ) that is, shorter-wavelength light is higher energy than longer-wavelength light (Amersham Biosciences Technical Note #57 in Sanvitali (2010)).

4.3.3 Planar Laser Induced Fluorescence (PLIF)

Planar Laser Induced Fluorescence (PLIF) is an optical technique that has been developed to characterise gas and liquid phase fluid flow situations. This technique can give both qualitative (visualisation) and quantitative measurements, including concentration, temperature, velocity and pressure. A laser source is used to produce a thin sheet of light that passes through the field of investigation. The investigated material can be either a homogeneous fluid to which a fluorescent dye has been added, or alternatively, it may contain some fluorescent particles used as tracers. The laser light enters the fluid and causes the fluorescent particles to become excited, as the light of specific wavelength is tuned to the fluorescent absorption waveband. After a few nanoseconds, a fraction of the absorbed photons are re-emitted with a modified spectral distribution, which differs between molecules. The light emitted is known as fluorescence, and is captured, typically using a camera. The amount of light that is captured by the camera is dependent on variables that include the concentration of fluorescent dye within the interrogated species, and the flow field conditions (e.g. temperature, pressure and mixture composition) (Sanvitali 2010).

4.4 Adopted technique

4.4.1 Light source and optics

The light source for the PLIF technique used here is generated by an 800 mW solid state green laser (MGL-H-532, Changchun New Industries) operating at 532 nm with as output of 800 mW. The laser beam is coupled into a fibre optic cable and then recollimated at the fibre output to be sent through a Powell lens (Figure 4.4), generating a vertical sheet of light (Figure 4.5). The fibre optic patchcord (cable) is a multimode fibre 25/125, meaning the fibre has a core size of 25 µm and a cladding diameter of 125 µm. The Powell lens produces a straight line of uniform intensity light output due to the aspherical curvature on its apex (Figure 4.4), and was selected over a cylindrical lens as they generate Gaussian beam profiles with hot-spot centre points and fading. Figure 4.6 and Figure 4.7 show the set up of the laser line generation system. Power losses in light intensity occur as the light passes through the fibre-optic cable and the fibre-optic connections. It is therefore critical that the light from the laser is coupled into the fibre correctly to minimise such losses. Following alignment of the fibre optic cable with the laser light, losses of energy at the end of the fibre optic cable were measured to be around 15-20%. The thickness of the laser sheet increases with distance from the lens and fans out at an angle of 60°. In these experiments the distance from the lens to the apparatus was approximately 290 mm, creating a laser sheet thickness of about 2 mm.

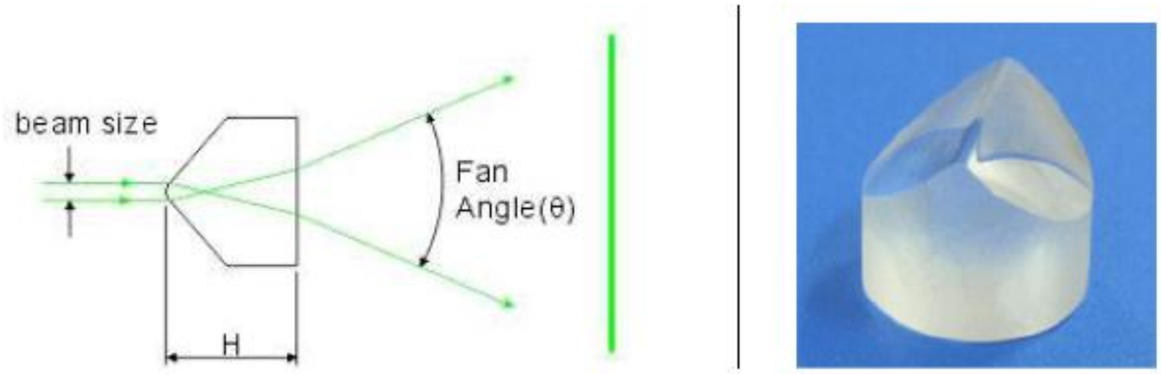

Figure 4.4: Powell Lens (Sanvitali 2010).

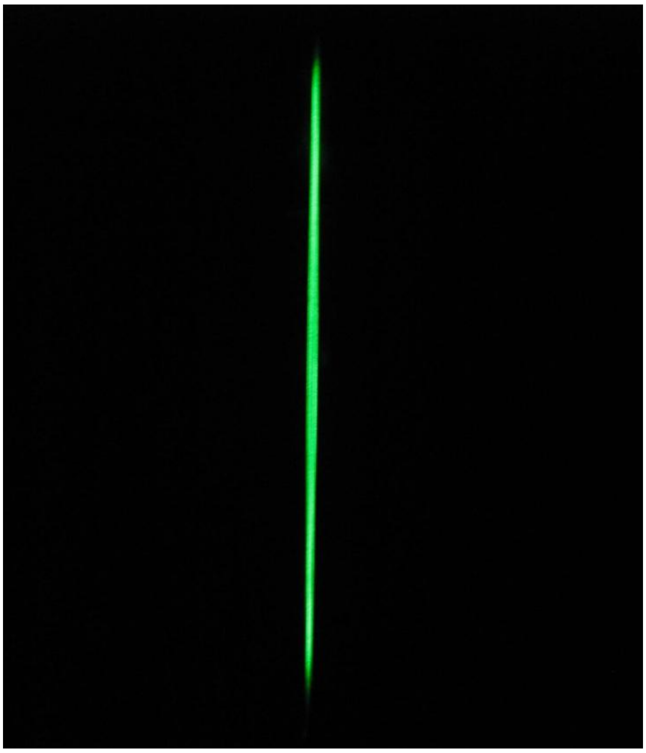

Figure 4.5: Line of laser light generated, projected onto a wall in a dark room.

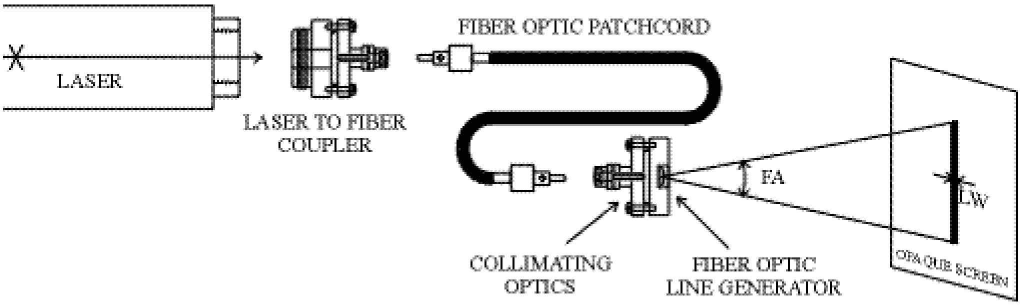

Figure 4.6: Laser line generator system (OZ Optics in Sanvitali (2010)).

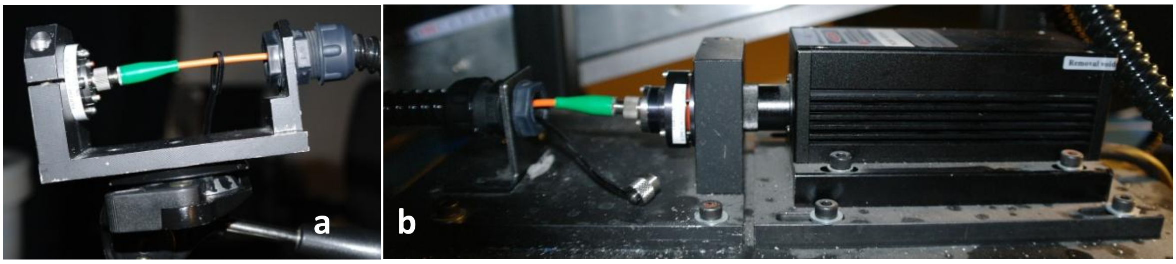

Figure 4.7: a) Fibre optic cable coupling to the line generator, or Powell lens; b) Lased light generator and coupling to the fibre optic cable.

4.4.2 Image Acquisition

A MotionPro Y4-S1 high speed camera (Figure 4.8) with a speed of 6000 frames per second (fps) at a resolution of 1024 x 1024 pixels was used to record the images. It used a CMOS – Polaris II 13.9 mm x 13.9 mm sensor with a 1.0 megapixel image size and 13.68 x 13.68 µm pixel size which could be controlled by a PC. The scan area could be adjusted to the area of interest in the permeameter device, and was dependent on the length of an extension tube used between the lens and camera (typically 5 mm or 10 mm). Frames were usually captured at the minimum frame rate of 10 fps, while not all of the frames were saved all of the time. In some tests, 1 fps was saved, while in others looking to gain a high resolution in image data, 10 or 20 fps were employed. A high-speed lens (Navitar, DO-5095) was used with the camera. It was a C-Mount, 1” format lens designed for 50 mm focal length, and was well suited for low light conditions. A long pass filter (Schott OG550) with a cut point at 550±6 nm was placed over the camera lens (Figure 4.8) to limit the imaging to the emission wavelengths of the fluorescent dye and to screen unwanted scattered light (the transmittance curve is shown in Figure 4.9).

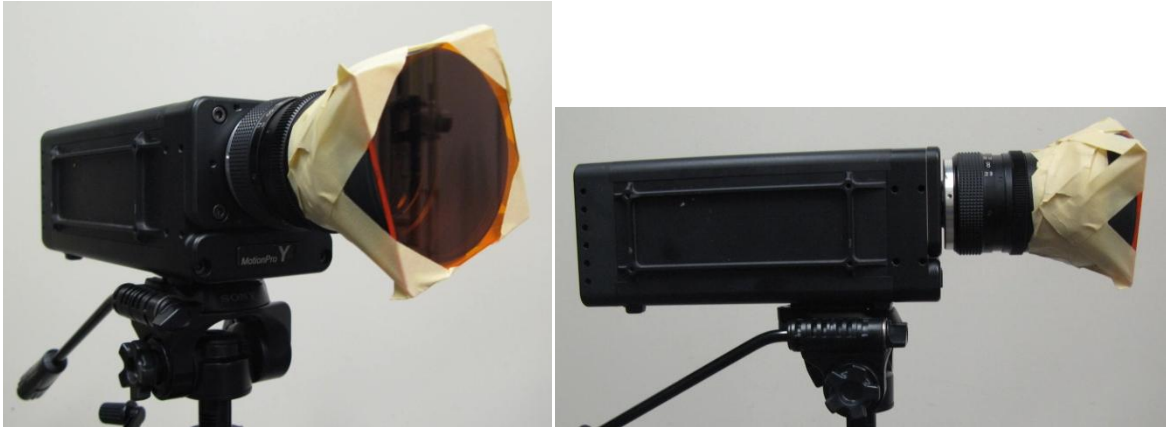

Figure 4.8: MotionPro Y4 camera for capturing images. Note the light filter over the lens.

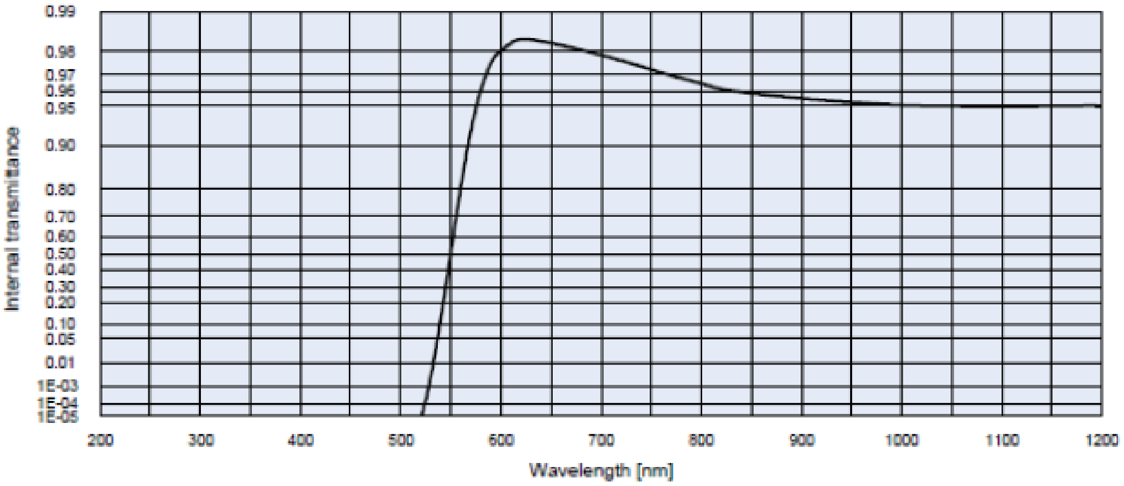

Figure 4.9: Internal transmittance of the employed optical filter at reference thickness d (mm) = 3 (Schott data sheet in Sanvitali (2010).

4.5 Materials

4.5.1 Solid, fluid and dye properties

In order for the chosen technique to be successful there needed to be an appropriate combination of particles and fluid. These materials must be optically matched, having a comparable refractive index, be economic, and be safe to work with.

The selected material to represent the solid particles was Borosilicate glass Duran (Schott Duran®), a commonly used glass with many chemical and engineering applications. Specifically, borosilicate glass has a low thermal expansion coefficient allowing it to be used at high temperatures, is chemically resistant, and has a relatively low refractive index in comparison with other glass. Borosilicate glass used in these experiments was bought in the form of rods, tubes and plates, which were then processed to make the desirable particles. For the fluid, synthetic hydrocarbon oil (Cargille Immersion Liquid code 5095) was used (Cargille data sheet in Appendix A). Both the oil and glass change refractive index with a change in wavelength and temperature, as Figure 4.10 shows for Duran glass at 21°C and for the oil at 25°C. Within a few degrees, temperature variations in the solid phase could generally be neglected as the temperature coefficient of refractive index (change in refractive index per °C) is usually significantly higher for the liquid than for solids. The index of refraction for the hydrocarbon oil was closely matched to the glass Duran at the dye emission wavelength and at a temperature of 23-24 °C. Optical and physical properties of the two solid and fluid materials are compared in Table 4.1.

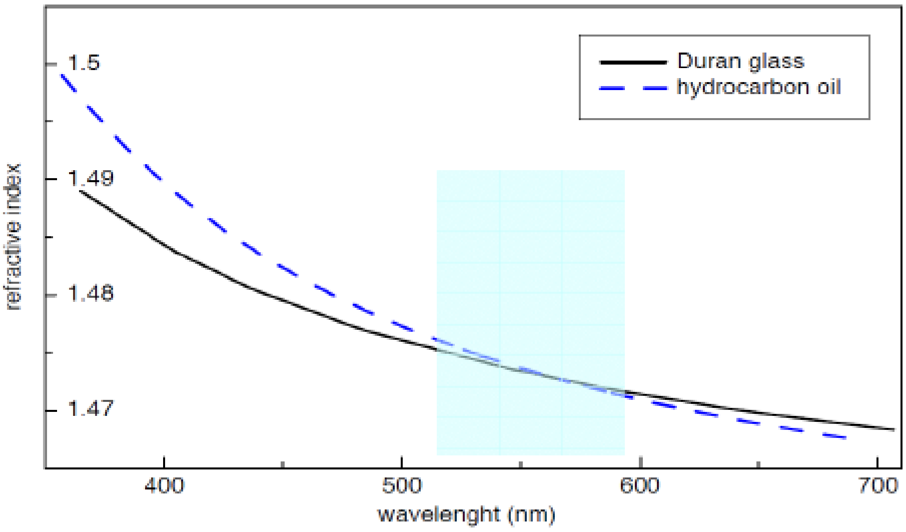

Figure 4.10: Refractive index as function of wavelength for Duran glass (Schott private communication) and hydrocarbon oil 5095 (Cargille data sheet) in Sanvitali (2010).

Table 4.1: Solid and fluid properties (Sanvitali 2010).

	Refractive index at 589.3 nm	Density at 25 ℃ (g/cm^3)	Kinematic viscosity at 25 ℃ (cSt)
Immersion oil	1.4715 (at 25 ℃)	0.846	16
Duran glass	1.4718 (at 21 ℃)	2.23	-

For a distinction to be made between the fluid and solid materials, Nile Red (Sigma-Aldrich) fluorescent dye was added to the oil. The dye is a neutral, hydrophobic and solvatochromic dye that in non-aqueous phase is strongly fluorescent.

Sanvitali (2010) investigated the absorption and emission spectra of the Nile Red dye in solution with the hydrocarbon oil. The results in Figure 4.11 show that the emission has red-shifted with respect to the emission wavelength of the laser (514 nm). Also noteworthy is that the fluorescent light emitted by the dye is similar to the band wavelength in which the refractive indices of the oil and Duran are very close together. This is important as non-matched conditions at the absorption wavelength causes scattering and distortion of the light of the laser sheet. This creates a distortion of particle images in this ill matched emission wavelength. No problems with distortion of the laser plane through the glass oil mixtures were experienced (Figure 4.12), and excessive brightness due to scattering of the light was eliminated using a long pass filter on the camera.

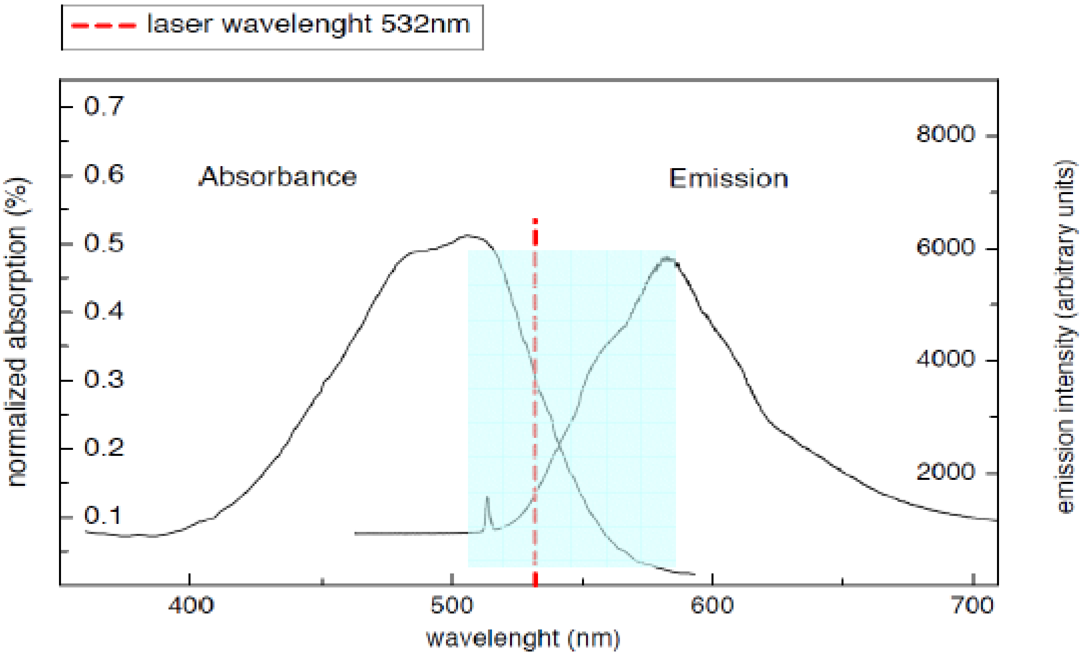

Figure 4.11: Absorption and emission spectra of Nile Red in the hydrocarbon oil. The concentration of the sample is 5mg/l (Sanvitali 2010).

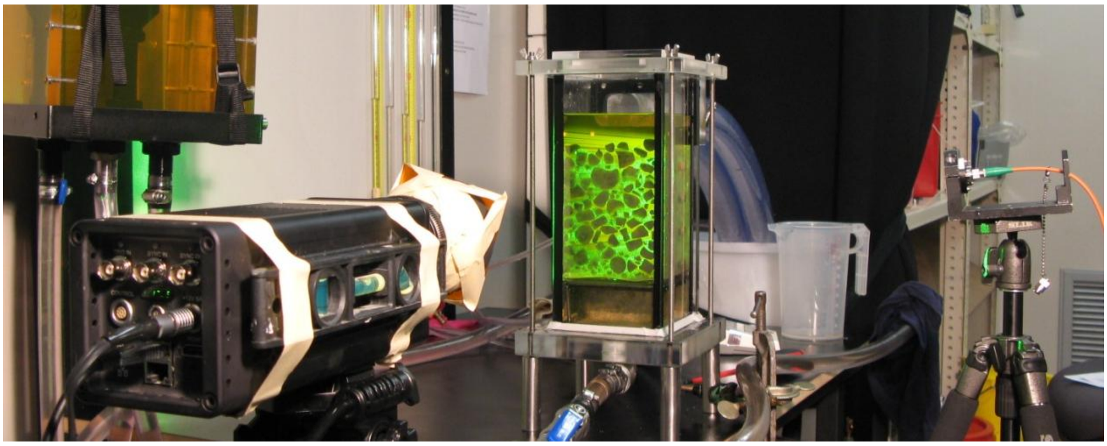

Figure 4.12: Transparent Soil Permeameter encasing Borosilicate glass 'soil' and hydrocarbon oil fluid (illuminated by laser sheet).

4.5.2 Permeability and scaling of the particles

The glass and oil materials used in these experiments have considerably different physical properties to those of real granular soil and water mixtures. Despite the relative densities of the particles and the fluid being reasonably similar compared to those in filter materials and water, the same is not true for the fluid viscosity. Because the fluid viscosity of hydrocarbons tends to be much higher than that of water, it is not possible to exactly match the properties of real soil and water. This is important to note as the fluid viscosity strongly affects the hydraulic behaviour of particle motion during internal erosion and re-stabilisation of particles. Therefore, to realistically model internal erosion behaviour of filter materials by creating hydraulic conditions that replicate those of soil and water mixtures, the soil particles need to be up-scaled compared to the prototype laboratory particle size distribution.

During flow through soil, fundamental hydraulics characterise two states of motion, being laminar or turbulent. Permeability, otherwise known as hydraulic conductivity, refers to the ease in which water can flow through a soil. Darcy (1856) experimentally proved that for laminar flow conditions in a saturated soil, flow discharge per unit time is directly proportional to the hydraulic gradient according to his law, which can be written as:

$$q = k.i.A \tag{4.2}$$

$$v = k.i \tag{4.3}$$

where A is the cross sectional area normal to the direction of flow, *k* is the coefficient of permeability and *i* is the hydraulic gradient.

Under laminar flow conditions where Darcy's law is valid, fluid particles travel along definite paths that never cross other particles. Conversely, turbulent flow occurs when fluid particles travel in irregular and twisting paths that cross and re-cross randomly, hence laminar flow laws are broken. Taylor (1948) shows the behaviour of fluid flow changing from laminar to turbulent in a discharge velocity vs. hydraulic gradient plot in Figure 4.13.

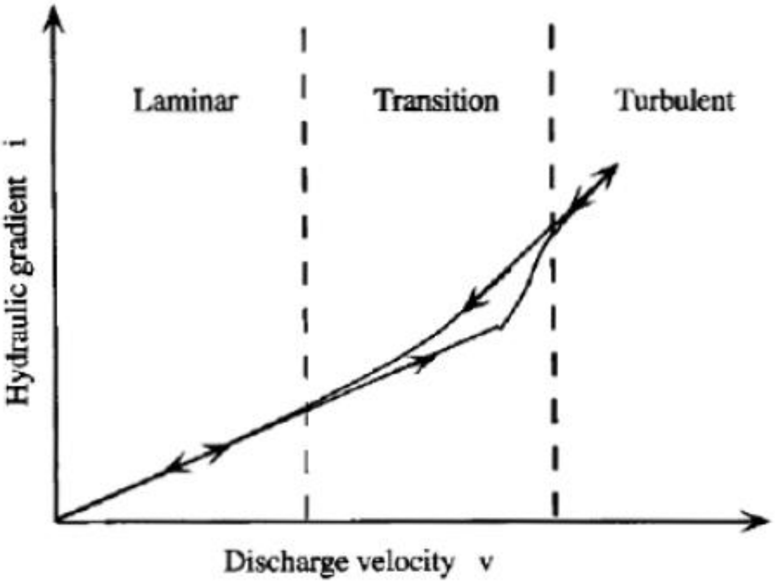

Figure 4.13: Zones of laminar and turbulent flows (Taylor (1948) cited by Sanvitali (2010)).

Because permeability is a function of pore space and hence particle size, permeability can be simply calculated by the Hazen (1892) equation for predicting permeabilities in saturated sand, by:

$$k = C_H . D_{10}^2 \tag{4.4}$$

where k = permeability (cm/s), C_H is the Hazen empirical coefficient and D_{10} is the particle size for which 10% of the soil is finer (cm). Using this equation, C_H is usually assumed to be 100, hence the main parameter affecting the permeability is D_{10}.

However, in using oil and glass materials, such a simple equation does not apply.

In her thesis, Sanvitali (2010) used the Kozeny-Carmen equation below, to determine the scaling factor of glass, when using the hydrocarbon oil:

$$k = \left(\frac{\gamma}{\mu}\right) . \left(\frac{1}{C_{k-c}}\right) . \left(\frac{1}{S_o^2}\right) \left[\frac{e^3}{1+e}\right] \tag{4.5}$$

where γ = unit weight of permeant; C_{k-c} = Kozeny-Carmen empirical coefficient; S_o = specific surface area per unit volume of particles (1/cm); e = void ratio.

In this equation, the coefficient $C_{k\text{-}c}$ takes into account the shape and tortuosity of the pores, which is typically a value of 5 for soils. The specific surface S_o for uniform spheres of diameter D is simply 6/D, however for a soil on non-uniform spheres, an effective diameter D_{eff} can be calculated from the PSD using the equation by Carrier (2003);

$$D_{eff} = \frac{100\%}{\sum(\frac{f_i}{D_{ave_i}})} \tag{4.6}$$

where f_i is the fraction of particles between two sizes (D_{li} and D_{si}) and D_{avei} is the average particle size between two sizes (= $D_{li}^{0.5}$. $D_{si}^{0.5}$), therefore allowing the specific surface to be found by S_0=6/D_{eff}. To further improve the accuracy of S_o, Sanvitali (2010) cites Loudon (1952) and Fair and Hatch (1933) who take into account the angularity of the individual particles by introducing a shape factor, SF:

$$S_o = \frac{SF}{D_{eff}} \tag{4.7}$$

where values between 6.0 and 8.4 for particles between rounded and angular are suggested by Fair and Hatch (1933), and Loudon (1952).

Sanvitali (2010) cites from Barr (2001) that the Kozeny-Carmen equation can describe the behaviour of cohesionless soil reasonably well, although is not suitable for clays. However, as pore sizes and velocities increase, turbulent flow and inertia must be taken into account when estimating permeabilities.

From this equation, the permeability is expected to be inversely proportional to the viscosity of the permeant. The kinematic viscosity of the hydrocarbon oil in these experiments is sixteen times greater than that of water, which significantly reduces the permeability in the glass-oil mixture compared to that in a soil-water mixture.

Using the Kozeny-Carmen equation, Sanvitali (2010) calculated that the glass particles were required to be scaled up by 4 times to account for the higher viscosity immersion oil compared to water with a lower viscosity. Constant head permeability tests were then carried out according to the ASTM D-2434 standard procedure, and found that the scaling gave laminar flow and a good agreement between observed and predicted permeability values, therefore validating the use of up-scaled glass particles and the hydrocarbon oil. As a benefit, smaller particles are made visible in captured images.

An example is shown in Figure 4.14, where the Skempton and Brogan (1994) soil sample A is plotted with the equivalent glass sample, with a shift to the right by four times the particle size. Due to constraints in the size of the apparatus, it is not feasible to use some of the larger glass particles that would be required. Particles larger than 26.5 mm in diameter were excluded from PSDs. Therefore, in recreating Skempton and Brogan (1994) sample A, the upper 9% tail of the curve is cut off. Scaled PSDs for each soil sample replication are shown in Chapter 4.9.3. It should be noted that using particles with a maximum diameter of 26.5 mm in a permeameter with a diameter of 100 mm means these tests do not meet ATSM (2006) standards. This issue is further discussed later in this Chapter.

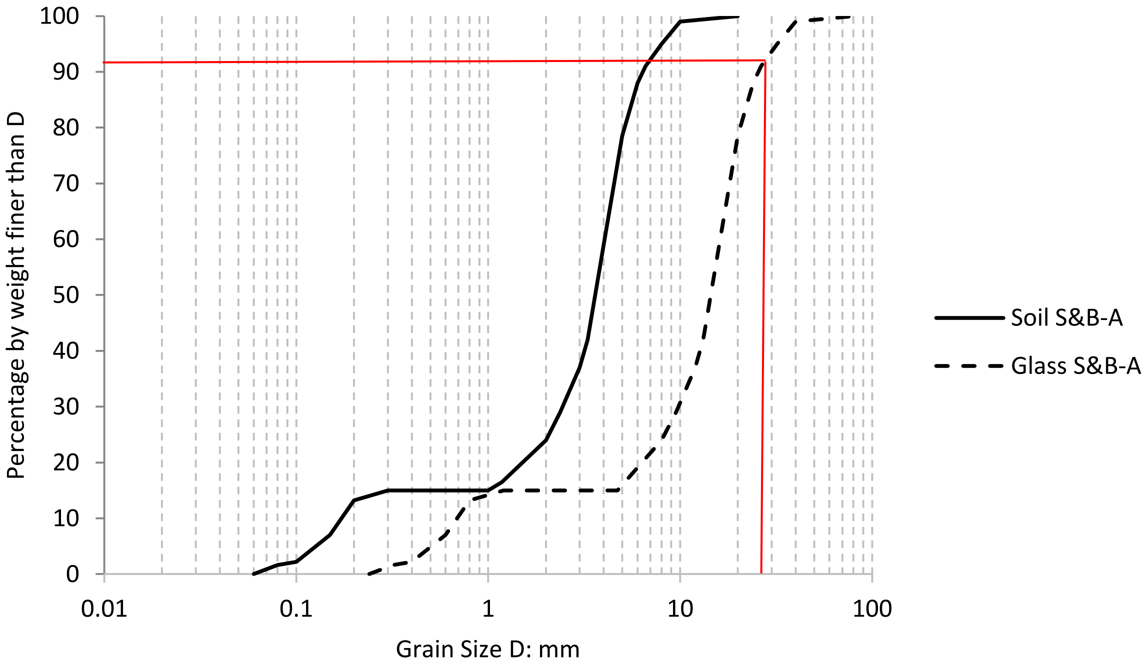

Figure 4.14: Example of PSD for Skempton and Brogan (1994) soil sample A and equivalent Glass PSD. Also shown is the limiting glass particle size (in red) for the transparent soil permeameter.

4.5.3 Preparation of particles

As randomly shaped particles of glass Duran are not commercially available, they had to be produced in the laboratory. Borosilicate rods with diameters between 4 mm and 30 mm and tubes with wall thicknesses ranging from 0.8 mm to 2.0 mm (Figure 4.15) were purchased from Schott manufacturers. A method was then employed to produce the particles ranging from 0.4 mm to 26.5 mm as required to fabricate the required PSDs. This initially involved crushing glass tubes with a hammer, and then if required, using a crusher to further reduce the particle size (Figure 4.16). The crusher was constructed of two steel slabs, with sides approximately 25 cm in length. Glass was placed on the lower plate, while the top plate was repeatedly dropped until particles of suitable size were formed. For the larger particle sizes, glass rods were used. These were initially sliced using a bench drill (Figure 4.17) with a flat head, and then shaped using a hammer to chip particles into the correct sizes and random shapes. These two processes formed the range of particle sizes required (Figure 4.18 and Figure 4.19), and were sieved to sort them into like sizes before being rinsed in water to remove dust, and then dried in an oven overnight.

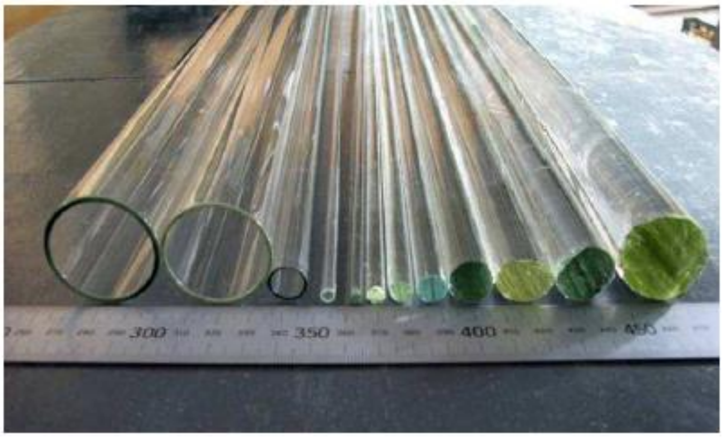

Figure 4.15: Rods and tubes used for the production of the solid grains (Sanvitali 2010).

Figure 4.16: Steel slabs used for crushing the glass tubing to make fine particles.

Figure 4.17: Bench machine used for producing larger particles by cutting the glass rods.

Figure 4.18: Coarse glass particles used as transparent solid (Sanvitali 2010).

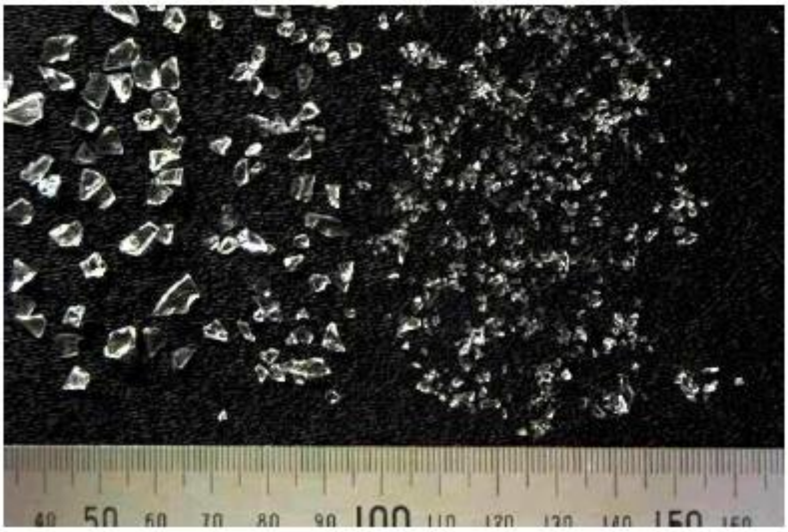

Figure 4.19: Fine glass particles used as transparent solid (Sanvitali 2010).

At the conclusion of each test, oil was drained from the apparatus and the oily particles were poured into a bowl. The oil needs to be separated from the particles prior to re-sieving and recycling in other tests to avoid particle clusters forming and affecting their ability to be sieved correctly. Furthermore, any impurities had to be removed from the grain surfaces, especially the smaller particles, in order to achieve a good transparency between the solid-fluid mixtures during experiments. To remove the oil from the glass, dirty particles were rinsed in methylated spirits (ethanol with 2% methanol). As the oil is partially soluble in this solvent, oil was removed from the grain surfaces where it would settle to the bottom of the container, as it has a higher density than the solvent. The oil could then be removed from the container using pipettes and syringes. After a few rinses the ability of methylated spirits in removing the oil from the glass reduced as it became saturated with oil, and needed replacing.

After two rinses in methylated spirits the particles were washed in water (Figure 4.20). The particles were then washed in hot soapy water, and rinsed in water once more, before being oven dried overnight. They were then sieved into like sizes using 600 µm, 1.18 mm, 2.36 mm, 4.75 mm, 9.5 mm, 13.2 mm, 19 mm and 26.5 mm sieve sizes. The particles would then undergo the cleaning process two more times, with the larger particles typically requiring less cleaning than the finer particles. Following this washing procedure, a visual inspection of the washed and sieved particles could be performed and any impurities on the glass removed using tweezers. A PSD for testing would then be created be weighing out the appropriate proportions of each particle size evenly across 3 or 4 separate bowls (Figure 4.21).

Figure 4.20: Glass particles being washed in methylated spirits bath. Particles are then poured into water before rinsing through a sieve.

Figure 4.21: Clean glass particles are sieved and separated into like particles sizes, ready for the creation of a different PSD.

Once a PSD was weighed out, immersion oil was poured into the bowls with the glass particles and gently stirred (Figure 4.22a). The bowls were then placed into a vacuum desiccator for 2-3 hours to de-air the sample (Figure 4.22b). Gentle stirring was required to release remaining air bubbles upon removal from the vacuum. The sample was then ready for placement into the permeameter.

Figure 4.22: a) oil is added to the glass PSD and then; b) the glass particle-oil mixtures are placed into vacuum desiccators.

4.6 Placing Sample

In order to dissipate the flow entering the permeameter so that an even flow traveled into the filter sample, a 50 mm high 'dispersing' filter material was placed at the bottom of the apparatus. In accordance with Falling Head/Constant Head Permeability Cell Procedures WF26010/20635 (Wykeham Farrance International Ltd, no date), the dispersing material was selected so that it was between 4 times the 15% size ($4D_{15}$) to 4 times the 85% size ($4D_{85}$) of the sample being tested. Once this material was placed in the apparatus, the oil control valves were opened, allowing oil to permeate to the top of the dispersing filter, before the valves were closed. A thin glass rod was used to stir air bubbles out of the oil, before a steel frame and steel gauze was placed over the dispersing filter, ready for the filter sample to be placed on top.

A variety of placement methods were trialled, with the 'slurry' technique proving most successful and reproducible. This method required that the glass particles were immersed in the de-aired oil, as described in the earlier section on glass particles preparation. The particles were gently stirred to generate an even particle size distribution, and then using a teaspoon with the head bent at 90 degrees, particles were scooped out and gently placed into the upper screen within the apparatus (Figure 4.23). Oil had been allowed into the apparatus so that the upper screen was just immersed with oil, in an attempt to keep the sample saturated while being placed. Attempts were made to create an even distribution of particles within the sample by being methodical in placement distribution. This method gave a 'loose' compaction, and care was taken not compact any part of the sample so that repeatability was possible.

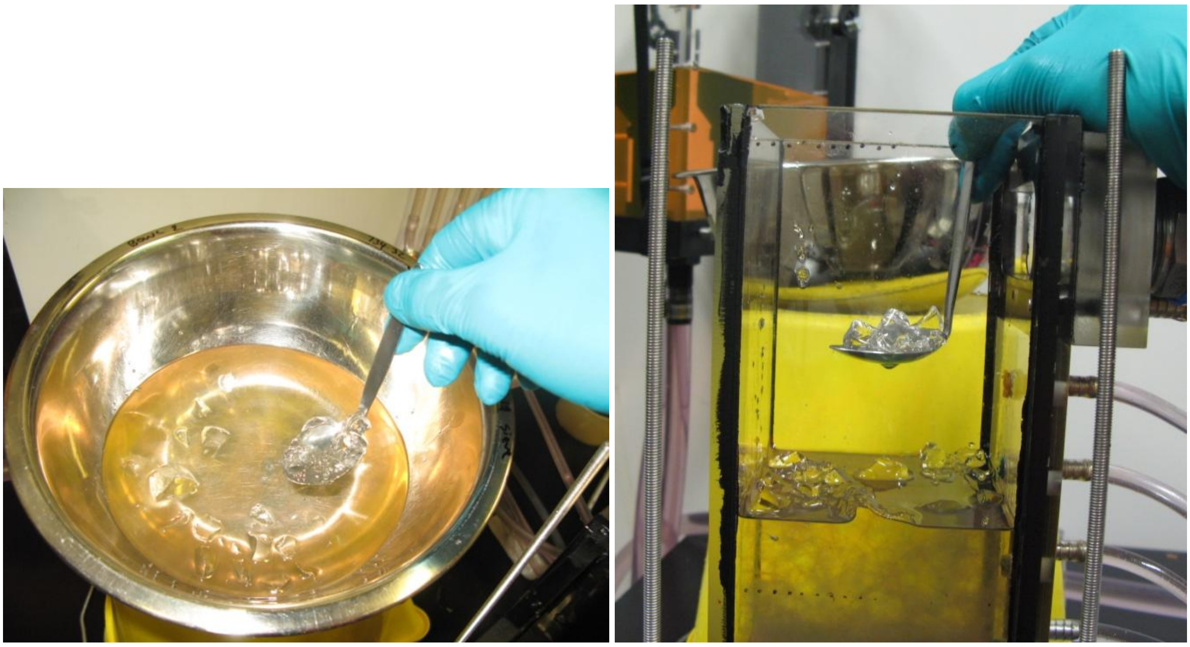

Figure 4.23: A teaspoon is used to scoop the saturated and de-aired glass particles out of prepared PSD mixture, and into the permeameter, which has a layer of oil to keep particles saturated.

Placement methods that did not work so well included a loose dry placement, loose partially saturated placement, compacted dry placement, and compacted partially saturated placement. Compaction was applied by tamping the sample at four different levels (approximately 30 mm lifts) as the sample was placed. The main issue with these placement techniques came from the amount of air bubbles in the sample. Air bubbles greatly reduce the image quality, and also the behaviour of particle interactions within the sample as the saturation is reduced. Therefore, these methods were rejected in favour of the slurry technique, described above.

4.7 Permeameter Apparatus

A new 'transparent soil permeameter' needed to be designed and built so that experimental tests could be trialled using PLIF. A range of testing apparatuses and methods for testing the susceptibility for internal erosion were researched, and have been presented in the literature review in Chapter 3. There were several requirements that the transparent soil apparatus needed to meet in order for successful testing to be achieved:

- Be of 'box' type construction to minimise refraction of incoming laser light and outgoing fluorescing oil (into the camera);
- Have a header tank in which a constant head could be applied to the soil;
- Be capable of transmitting an even upward flow of oil through the apparatus;
- Be capable of re-circulating oil through the apparatus for as long as a test may last;

- Have instrumentation to measure the flow of oil passing through the apparatus;
- Be able to adjust the head height easily so that changes to the flow of oil could occur;
- Have instrumentation to measure the hydraulic gradient throughout the sample;
- Have connection points and valves so the apparatus could be detached from the system for cleaning and changing the transparent soil;
- Be of appropriate size so that available oil, pump and header tank could cope with required flow conditions that needed to be replicated, and;
- Be of appropriate size to accommodate the limited amount of crushed glass.

Based on these requirements, the design of the apparatus was approximately based on that of the Skempton and Brogan (1994) apparatus for an upward flow test on soil-water PSD combinations. With the basic idea decided on, a preliminary sketch (Figure 4.24) was drawn up while other factors that were required for testing to be possible were worked through.

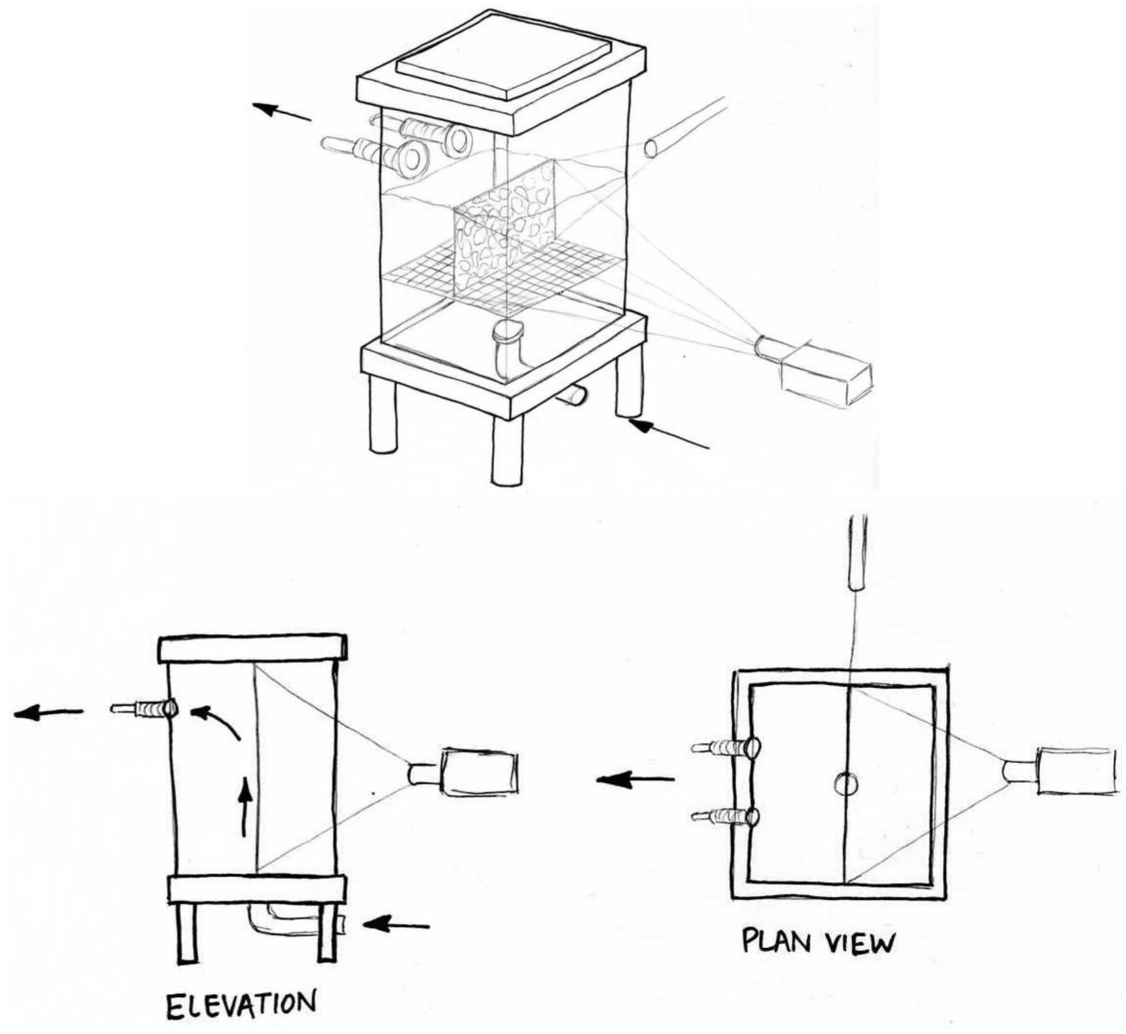

Figure 4.24: Schematic sketch of proposed apparatus.

Diagrams and images of the final design are shown in Figure 4.25. In contrast to other permeameters, this apparatus is a ‘box’ permeameter, as opposed to cylindrical permeameters which are typically utilised. Flat glass sides are required in this apparatus so that:

a) laser light entering the apparatus is not refracted into the test sample, and;

b) light captured by the camera (adjacent to laser light) is not refracted.

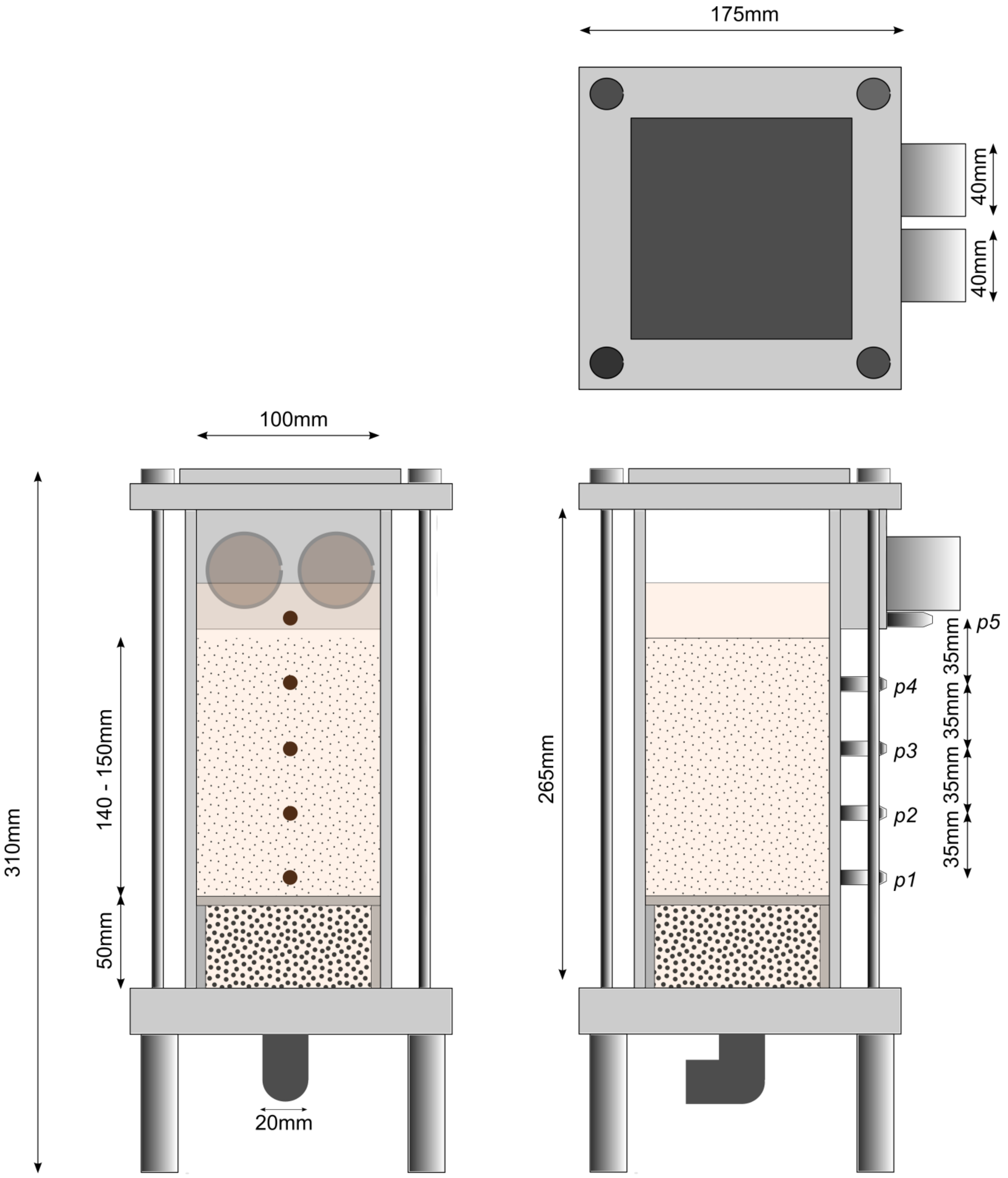

Figure 4.25: As built dimensions of the 'transparent soil permeameter'.

ATSM (2006) regulations for permeability tests state that the maximum particle size present in the permeameter should be:

1) 8-12 times smaller than the diameter of the permeameter;
2) not greater than 19 mm.

If the first rule was applied to this apparatus, the maximum particle size that might be expected, based on replicating previously reported filter materials, and considering the up-scaling by a factor of 4, glass particles may be required in sizes in excess of 50 mm Ø (breaking the second rule). Particles of this size would require an apparatus with diameter 600 mm, which is not feasible in these experiments due to: a) the volume of required glass; b) the volume of oil, and; c) the size of the pump and accompanying oil supply system, all of which exceed the resources and budget of this research project. Due to these constraints, the rules for maximum particle size were not abided by.

The apparatus has internal dimensions of 100 mm x 100 mm x 265 mm. A steel mesh (lower screen) covers the bottom of the apparatus to prevent particles falling down into the valves and hoses. A 50 mm high perforated steel frame (Figure 4.26a) sits at the bottom of the apparatus in which a fine steel mesh rests (upper screen). An 8 mm diameter PVC tube forms a border around the mesh (Figure 4.26b) so a seal is created against the glass sides and prevents preferential flow paths along the glass edge. Underneath the steel frame are particles passing the 9.5 mm or 4.75 mm sieve, which act to dissipate the oil flow from the inlet so that an even flow is obtained before it reaches the transparent soil sample overlying the steel frame and upper screen. The steel frame acts to support the overlying test sample, while the screen supports the test sample and stops particles falling down into the lower 'diffusing' material. The side of the permeameter with the outlet conduits and piezometer attachments is constructed from Perspex, while the remaining three sides are of the same glass Duran as the glass particles. Glass Duran is required for the sides in which the camera is orientated so refraction and distortion of images does not occur. Flow of oil is in an upwards direction, entering from a 20 mm Ø mesh covered inlet at the base and flowing out under gravity of two 40 mm Ø outlets. A Perspex lid prevents any impurities entering the permeameter. Oil is recycled, so upon leaving the permeameter returns to a storage bucket where it is then pumped up to a constant head tank. From here the fluid flows down through a rotameter and into the permeameter. Four or five piezometers measure hydraulic pressures (depending on sample height), which in turn are used to calculate hydraulic gradients across the transparent soil sample.

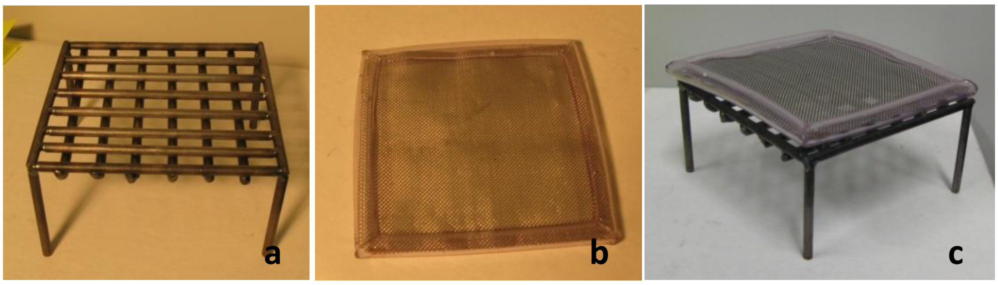

Figure 4.26: a) steel frame support; b) steel mesh with PVC seal and; c) mesh over frame as set up inside permeameter.

4.7.1 Permeameter Issues

As expected, ongoing modifications were required to achieve a fully functioning apparatus . This was related to: a) not having experience with permeameters for internal erosion testing and; b) dealing with an unfamiliar fluid. It was difficult to estimate the expected flow rates through the sample, and more so, the rate in which the oil was able to flow out of the apparatus unpressurised under gravity, especially because an unfamiliar fluid was being used (as opposed to water). Aspects that were modified throughout the implementation phase included:

- Increasing the size of the outlet ports so that sufficient oil could flow out of the apparatus under gravity (Figure 4.27 and Figure 4.28);
- Adding in an additional piezometric port above the initial three ports, and then later, another below the previous lowest to total 5 ports, so that better data could be obtained on average hydraulic gradients across the sample (Figure 4.29);
- Implementing steel mesh across the outlet to stop fine particles travelling into the oil reservoir (Figure 4.28);
- Creating a steel perforated frame to rest the upper steel screen upon, so that the test sample was evenly supported (Figure 4.26a);
- Installing a PVC ‘ring’ seal around the edge of the upper screen to create a seal between the lower diffusion material, and the upper test sample. This prevented finer test materials falling down the sides of the glass walls (Figure 4.26b);
- Addition of silicone sealant around the base of the apparatus and side walls to stop leaking (the apparatus needs to be pulled apart and ‘re-glued’ with new silicone from time to time as the oil used in testing is corrosive to silicon) (Figure 4.27).

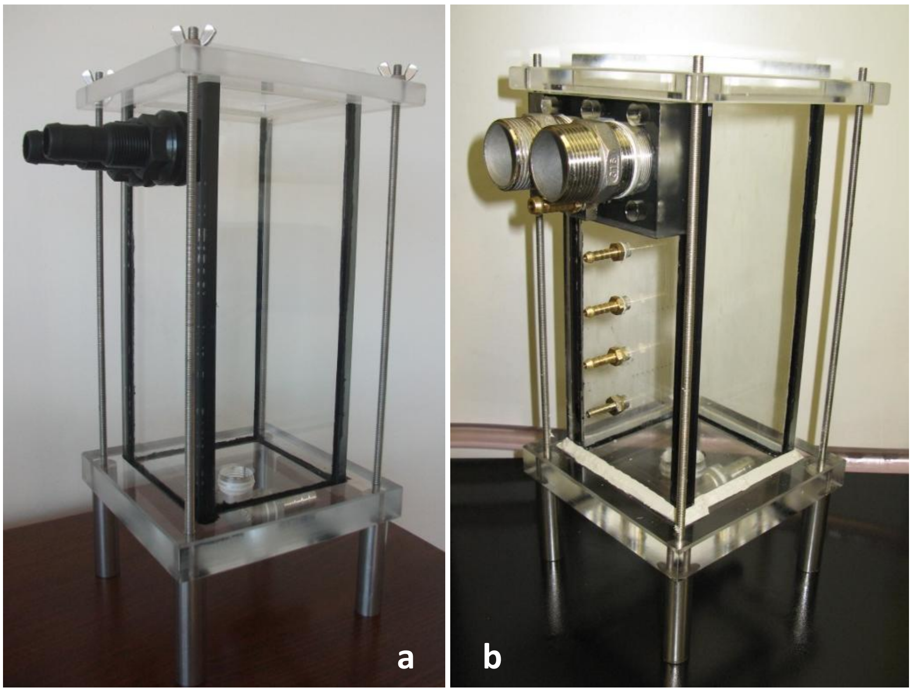

Figure 4.27: a) Original apparatus before modification – note 2x 15 mm Ø outlet ports and; b) Apparatus after modifications - note increase in port to 40 mm Ø, a total of 5 piezometer ports, additional silicon sealant around base.

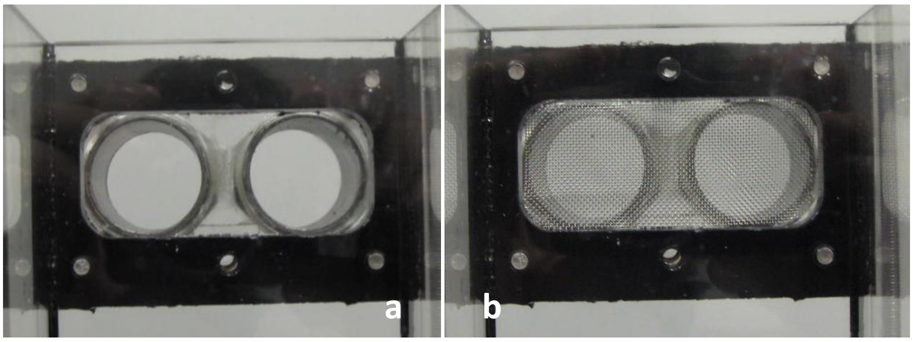

Figure 4.28: a) Outlet ports prior to steel mesh installation and; b) Outlet ports with steel mesh installed.

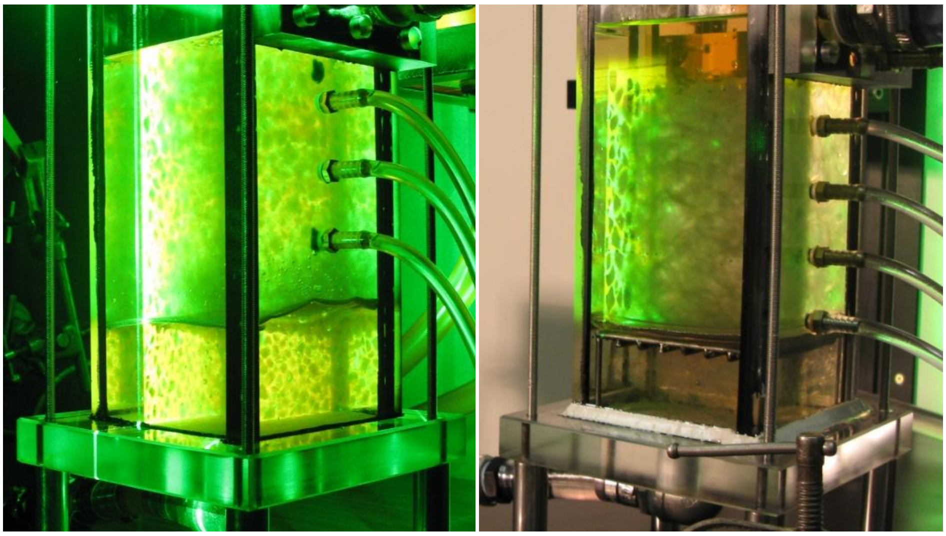

Figure 4.29: a) Test specimen resting on mesh directly over diffusment particles (notice the uplifting mesh and undulations; b) test specimen resting on mesh, supported by steel frame and sealed with PVC tube. Also note increase from 3 to 5 piezo ports.

4.8 Oil supply and control system

Approximately 15 litres of oil was pumped around the closed system using a Davies and Onga $K\frac{1}{6}$ Pump, capable of pumping approximately 60 litres of water per minute at a height of 5m. Oil was supplied to the pump from a reservoir which is controlled using a tap valve, and adjusted to maintain a constant head in the header tank. To control a constant head, an overflow cone inside the header tank allows excess oil to spill back down into the main reservoir. Oil from the header tank then flowed down through a rotameter before entering the permeameter. The rotameter selected in these experiments was a Metric 24K from Rotameter Manufacturing Co. Ltd, using a kaolinite float, giving flow rates up to 10 litres per minute for water. Care was taken to level the device as to allow the float to freely rotate and therefore give accurate results.

Once the experiment was set up, the oil then flowed through the permeameter under pressure, which was governed by the level of head. Oil then flowed out of the device under gravity via two 40 mm Ø hoses and back into the reservoir to be recycled (Figure 4.31). Besides these two outlet hoses from the permeameter, all hoses were clear PVC and 20 mm Ø. Several control valves were positioned in the system so each mechanism could be isolated. This allowed different sections to be removed for cleaning, or in the case of the permeameter, to be cleaned and repacked with a new PSD. The header tank and reservoir are frequently cleaned as impurities commonly build up on the bottom. Impurities normally found in the system were small pieces of silicon sealant which was used to seal the permeameter and header tank. It was found that the oil reacts with the silicone sealant so that over time, small pieces flaked away until a whole new seal was required.

Figure 4.30: Davies and Onga Pump used to pump oil into header tank.

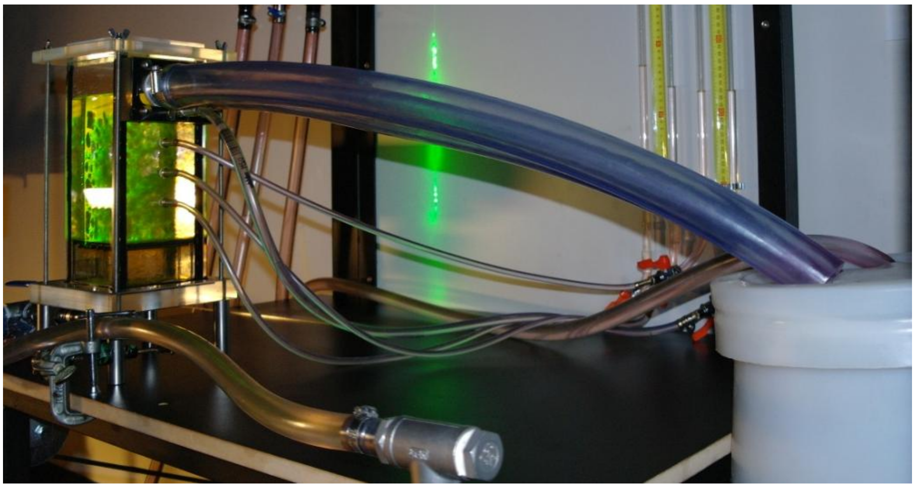

Figure 4.31: Outlet pipes returning oil back into reservoir.

4.8.1 Constant Head Tank Issues

Preliminary testing utilised a wall mounted constant head tank. In order to change the height of the tank, two people were required, one to lift or lower the tank, and another to fasten the tank to the wall mounted frame (Figure 4.32). It was quickly realised that this method was impractical as it: a) required two people; b) took too long to change the height during a test; c) was difficult to raise above shoulder height (some tests require greater head than this), and: d) posed a high risk to bumping the camera, apparatus and laser. For these reasons, a table to house the apparatus and control the head height was designed and built. The requirements of this apparatus were:

- Have a bench at a suitable height so that oil could flow out of the transparent soil apparatus (which rests on the bench) under gravity and back into the reservoir. The reservoir also required a height so oil could then flow under gravity into the pump which rested on the ground;

- Have a mounting system to hold the constant head tank;
- Have a system that could adjust the height of the header tank easily by one person;
- Have a measurement scale so the head height was known and could be replicated;
- Be able to secure the permeameter apparatus to the bench, and;
- Have space to mount the piezometers at an ergonomic position for easy recording.

The final design and construction of the bench and winch system are shown in Figure 4.33. To allow a single person to easily adjust the head height, a hand winch was installed. The winch allowed a strap to be shortened and lengthened as required so that the header tank was raised and lowered as required, by use of a pulley at the top of the high beam. Measuring the height of the header tank is achieved using a scale up the side of the pulley beam as shown in Figure 4.33.

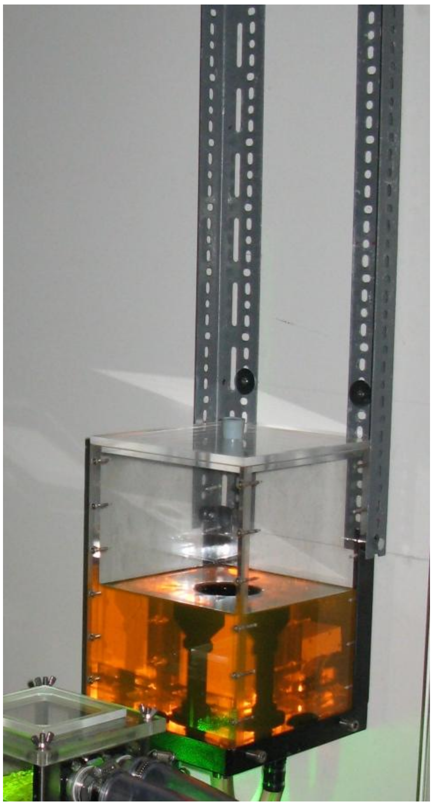

Figure 4.32: Original wall mounting system for header tank.

Figure 4.33: Oil control system: a) Bench with attached hand winch, header tank and piezometer tubes; b) header tank with height scale; c) hand winch to control head.

4.8.2 Rotameter Issues

In an attempt to measure the flow rate of the oil passing through the permeameter, the rotameter was installed so that the oil passes through the rotameter directly before it enters the permeameter. The rotameter came with a calibration curve, however was only applicable to the flow of water. A calibration of the rotameter therefore was carried out using the oil, while no particles were inside the apparatus. Oil flows were collected over time using a measuring cylinder and correlated to the rotameter value. A calibration curve was produced using the collected data, and was applied to some preliminary tests, before realising it did not appear to correlate to actual flows. From this point, flows were measured throughout preliminary tests to create calibration curves for a variety of tests. It became apparent that no curves were the same (Figure 4.34), possibly due to any number of the following:

- Temperature differences in the oil;
- PSD of the sample being tested;
- Density of the sample (loose vs. compact packing) creating resistance;

- Atmospheric pressure.

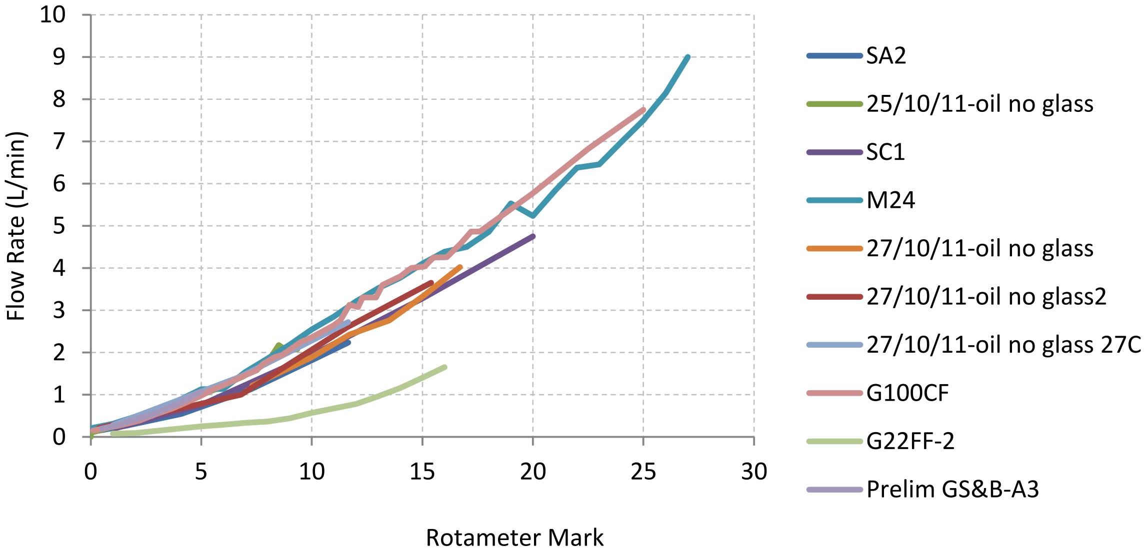

Figure 4.34: Rotameter calibrations in a selection of preliminary tests.

The current methodology during testing is to manually measure the flow of oil exiting the apparatus using a measuring cylinder, for each increment in head height. Sample collection occurs after 2-4 minutes of the head lift, as the flow rate stabilises, while rotameter values are recorded every minute. For every test, a calibration curve is created. Rotameter values that are taken between manual recordings can then be attributed to an estimated flow rate.

4.9 Particle Size Distribution (PSD) selection

4.9.1 Coarser Fraction and Finer Fraction Tests

Filter materials are made up of a coarser fraction and a finer fraction. To test the response of the oil-glass combination through the transparent soil permeameter, two tests were run using a representative coarser fraction (G100CF) and finer fraction (G100FF), each with a narrow range of particle sizes. Due to the high permeability and uniform particle size of the coarser fraction test, the sample was likely to be internally stable and was predicted to have a linear relationship between hydraulic gradient and flow velocity, if the glass and oil interact in a way that abides by Darcy's Law of laminar flow.

For the finer fraction test, the sample was much less permeable and so heave failure was predicted. In Terzaghi (1925) the classical theory is given where the critical upward hydraulic gradient i_c for sands is given by $i_c = (1 - \mathrm{n})(1 - \rho) = \gamma'/\gamma_w$ as outlined in Chapter 3. This equation suggests that the critical gradient will occur when the overburden stress of the grains is equal to the upward flow stress from the oil.

Using the graphs of i_{av} vs. v for valid Darcy's Las, the permeability can simply be calculated using:

$$k = \frac{v}{i} \tag{4.9}$$

The PSDs of G100CF and G100FF are shown in Figure 4.35.

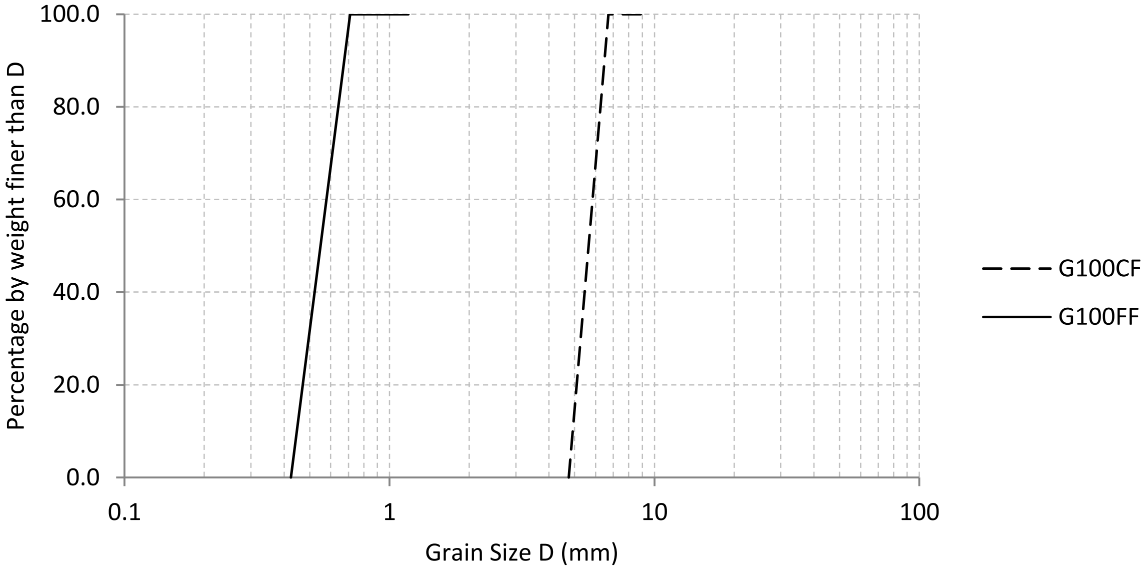

Figure 4.35: G100CF and G100FF PSD curves.

4.9.2 G22FF and G40FF Tests

Skempton and Brogan (1994) note that in gap graded soils there is a critical content of fines S* where the fines do not fill the voids in the coarse component. In this case, the soil is said to be 'clast supported', whereas if there is an excess of fines, the soil is said to be 'matrix supported'. This is determined by the equation:

$$\mathrm{S}* = \frac{\mathrm{A}}{1 + \mathrm{A}} \tag{4.10}$$

where

$$\mathrm{A} = \frac{\mathrm{n_c}(1 - \mathrm{n_f})}{1 - \mathrm{n_c}} \tag{4.11}$$

Inputting a range of n_c values, Figure 4.36 shows S*=27% is the separation between matrix and clast supported soils. Skempton and Brogan (1994) suggest that this value is unlikely to fall outside 24% for dense packing and 29% for loose packing. From the equation:

$$\mathrm{n_c} = \mathrm{n} + \mathrm{S_f}(1 - \mathrm{n}) \tag{4.12}$$

if the fines content S_f exceeds about 35%, then the coarse component is 'floating' within the finer fraction matrix.

Using this understanding of two basic differences in gap graded soils, two tests were devised using a PSD which is clast supported and another that is matrix supported. Since the placement technique in this testing is considered 'loose', a value of S*=22% for the finer fraction was chosen to be sure to be well below the theoretical threshold of 27%. For the matrix supported test, a finer fraction proportion of 40% was selected, well above the suggested maximum of 29% for loose packing. Both the glass 22% finer fraction and glass 40% finer fraction PSDs are shown in Figure 4.37, and are herein referred to as G22FF and G40FF respectively.

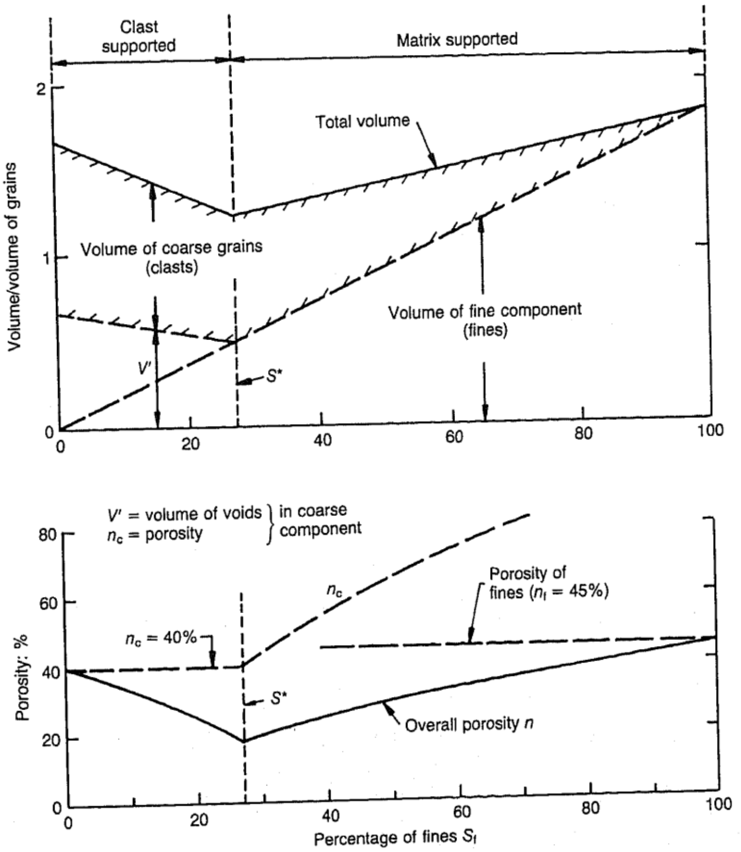

Figure 4.36: Bimodal granular material: volumes and porosity as a function of the proportion of fines in a constant total weight of grains (Skempton & Brogan 1994).

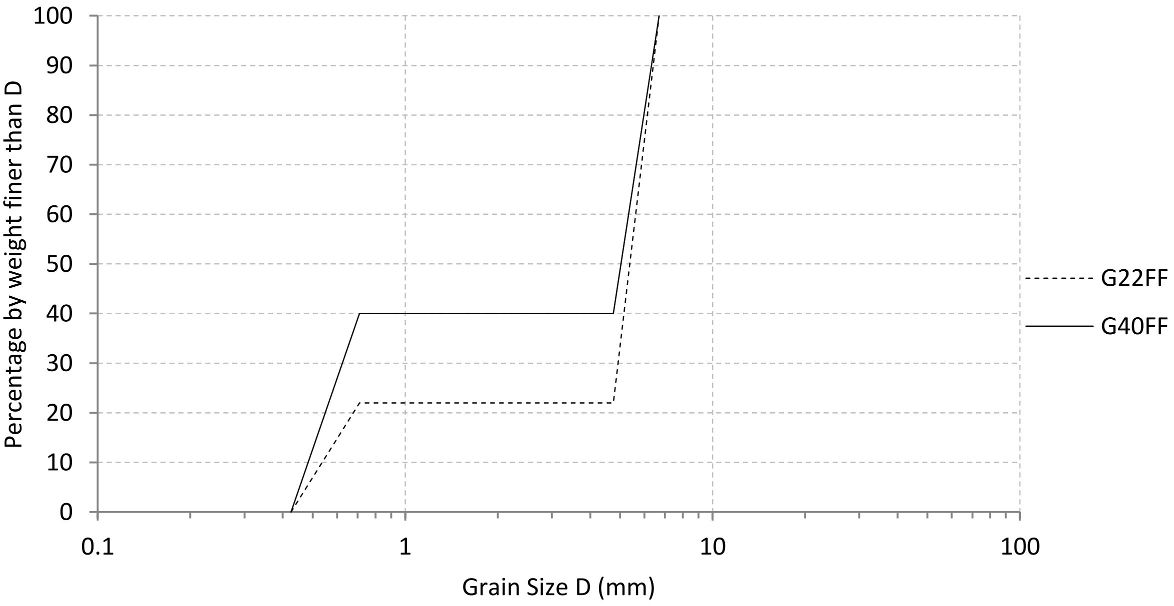

Figure 4.37: G22FF and G40FF PSDs.

4.9.3 Skempton and Brogan (1994) Replications: GS&B-A, GS&B-B and GS&B-D

The transparent soil permeameter has been modelled from Skempton and Brogan's (1994) soil permeameter and hence has a number of similarities. A selection of soil PSDs that Skempton and Brogan (1994) tested were replicated, as they provide results using a soil-water combination against which the glass-oil technique used in this study could be compared and validated.

Skempton and Brogan (1994) tested four different PSDs ranging in stability from 'unstable' to 'stable' Figure 4.38. Three PSDs were chosen to replicate here, being Skempton and Brogan (1994) samples A, B and D. Sample A was chosen as it is an 'unstable' gap graded material, sample B is on the boundary of 'stability' and 'instability', while sample D is classed as 'stable'. Testing these three materials of varying stabilities was beneficial for comparing results from these glass-oil tests, to those already tested using soil-water combinations. Physical parameters of the soils tested by Skempton and Brogan (1994) are shown in Figure 4.39.

Skempton and Brogan (1994) PSDs are shown in Figure 4.38, and show a range in particle size from 0 mm to 10 mm Ø, which when scaled for glass, corresponds to 0 mm to 40 mm Ø. Due to the limitations in size of the transparent soil permeameter, it was decided to have an upper limit of 26.5 mm in glass particle size, corresponding to a soil particle diameter of 6.63 mm. This corresponds to an upper limit of 91% of the original PSD. Additionally, as particles smaller than approximately 2 mm become difficult to individually differentiate in images (due to the thickness of the laser line), it was decided to apply a lower boundary. The lower boundary chosen was 0.4 mm, despite the particles between 0.4 mm to 2 mm being difficult to image process, they could still be physically seen during the test, and their presence is still required to contribute to the sample's stability or instability. Furthermore, particles smaller than 0.4 mm diameter size can easily become suspended in the oil, and therefore affect components of the recirculation system. Cutting the upper and lower tails off the samples changes the overall proportions of the sample being replicated. To mimic the Skempton and Brogan (1994) samples as closely as possible, their PSD curves were replicated and the upper and lower tails were simply excluded. This therefore resulted in the overall proportions of the 'as made' PSD being slightly stretched, however the proportions of each particle size in respect to each other should still remain the same. The curves in Figure 4.40, Figure 4.41 and Figure 4.42 show Skempton and Brogan (1994) PSDs, the scaled curve being replicated, and the replicated glass PSD. The glass replications have been named GS&B-A, GS&B-B and GS&B-D.

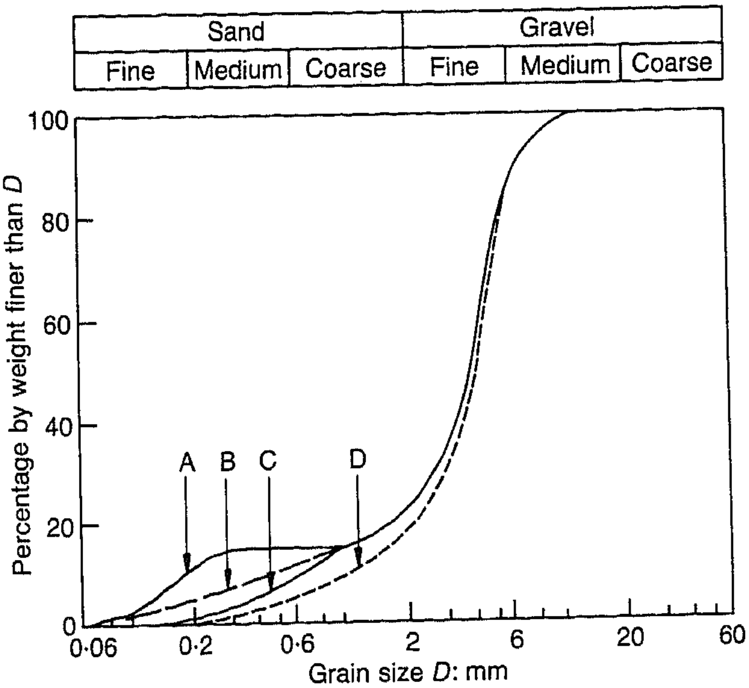

Figure 4.38: Skempton and Brogan PSDs (Skempton & Brogan 1994).

	A	B	C	D
Gravel component	85% G	85% G	85% G	90% G
Sand component	15% S1	15% S3	15% S2	10% S2
Porosity n : %	34	37	37·5	36·5
D_{15} : mm	0·60	0·90	0·98	1·6
C_u	24	10	7	4·5
Permeability k : cm/s	0·45	0·84	0·86	1·8
Filter ratio of components D'_{15}/d'_{85}	11	3·9	3·2	3·2
Stability index $(H/F)_{min}$	0·14	0·98	1·6	2·8
Critical gradient i_c in test	0·20	0·34	1·0	1·0

Figure 4.39: Skempton and Brogan (1994) specimen parameters for tested soils.

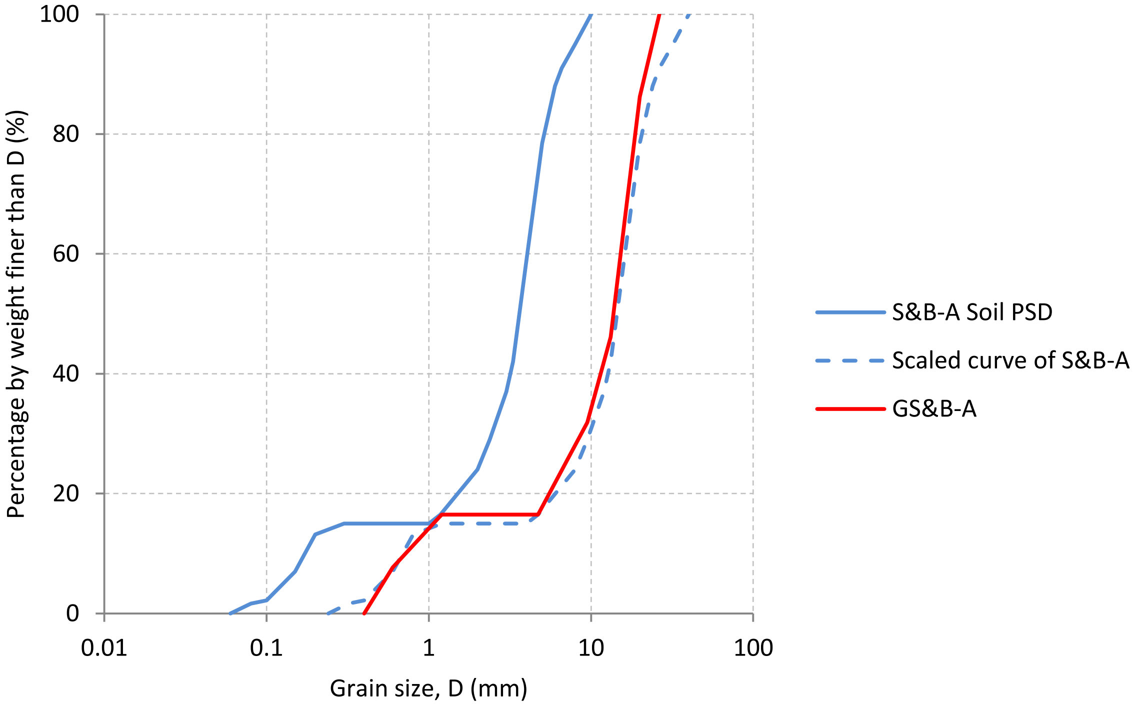

Figure 4.40: PSD of Skempton and Brogan (1994) soil sample 'A' and the GS&B-A replication.

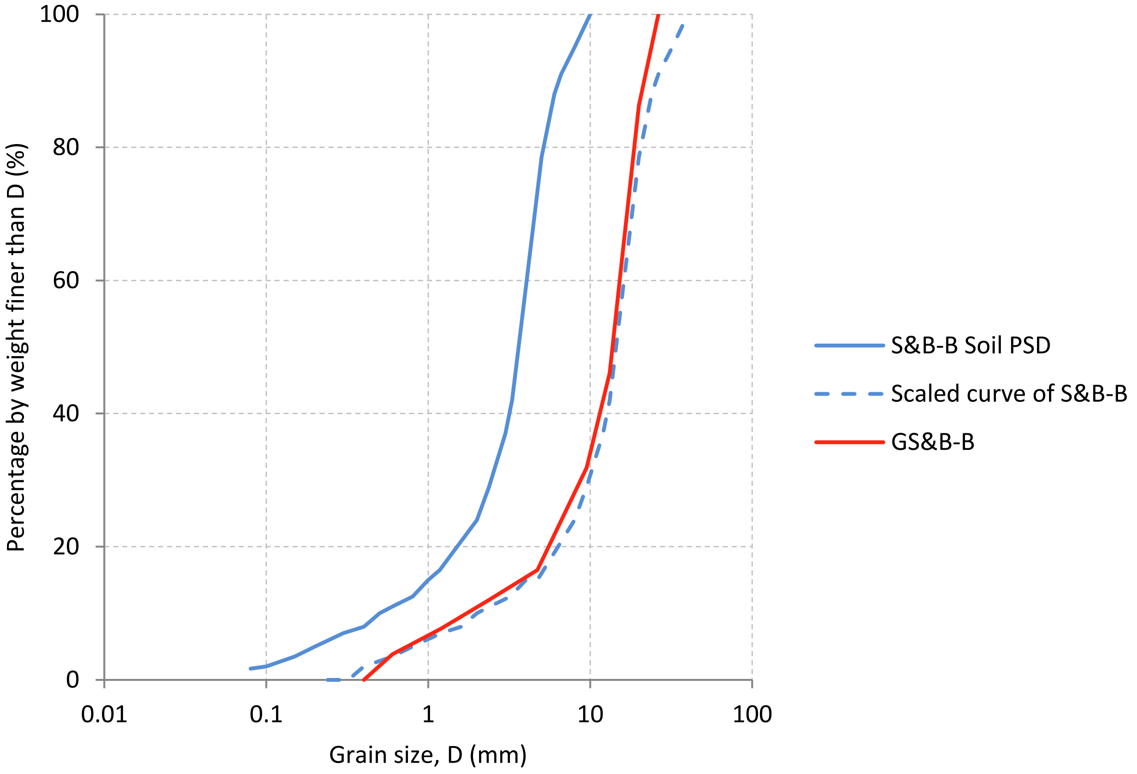

Figure 4.41: PSD of Skempton and Brogan (1994) soil sample 'B' and the GS&B-B replication.

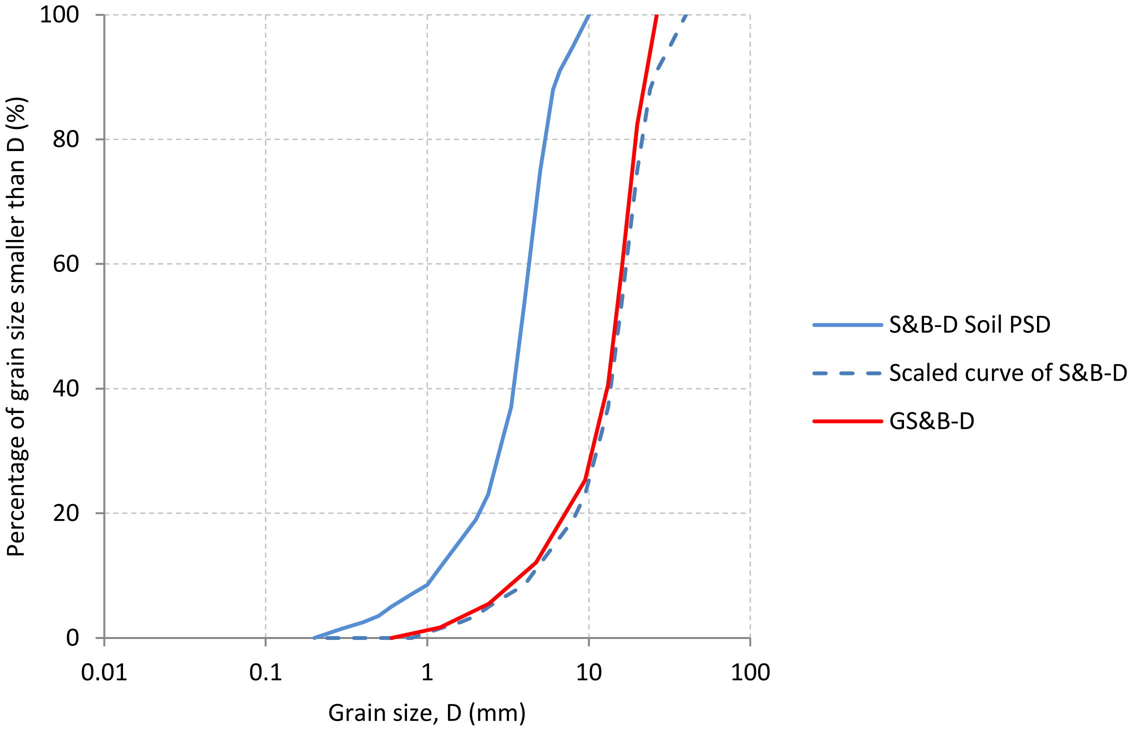

Figure 4.42: PSD of Skempton and Brogan (1994) soil sample 'D' and the GS&B-D replication.

4.9.4 S&B-Hybrid

The Skempton and Brogan ‘Hybrid’ specimen, herein named S&B-Hybrid, was produced following tests on GS&B-A and GS&B-B as a ‘hybrid’ or combination of the ‘A’ and ‘B’ PSDs. The aim of this sample was to compare how a slight change in the PSD affects the initiation of suffusion within the material. With GS&B-A having a distinct gap-grade, and GS&B-B having a ‘typical’ concave up PSD shape, GS&B-Hybrid has a ‘bimodal’ shape, as shown in Figure 4.43. This graph shows Skempton and Brogan (1994) ‘A’ and ‘B’ PSDs with the prototype ‘hybrid’ material. The ‘hybrid prototype’ was then scaled appropriately for testing in the transparent soil permeameter. The results from this test are described in Chapter 5, and discussed in Chapter 7.

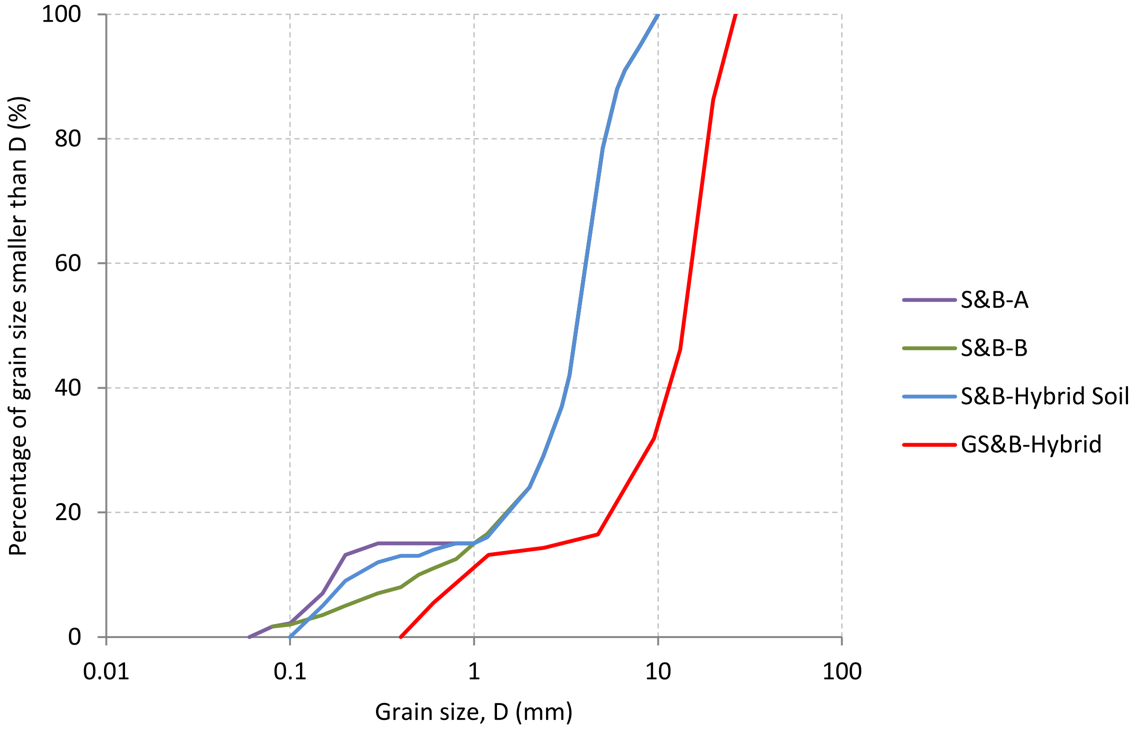

Figure 4.43: S&B-Hybrid PSD.

4.9.5 Fannin and Moffat (2006) Replication: GF&M-G4C

The Fannin and Moffat (2006) gap graded sample using spherical glass beads, named G4-C, was chosen for testing as it provides another example of a simple gap graded sample, to which test results from the transparent soil permeameter could be compared. The replicated glass PSD is referred to as GF&M-G4C herein. Soil specimen parameters of Fannin and Moffat (2006) G4-C are shown in Figure 4.44. The soil G4-C had a PSD that once scaled for glass and oil, did not require the exclusion of any particle sizes. The PSDs are shown in Figure 4.45.

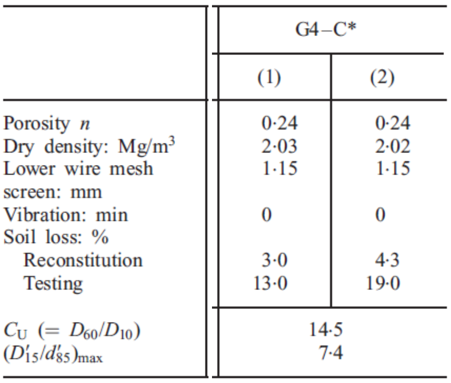

	G4–C*	
	(1)	(2)
Porosity n	0·24	0·24
Dry density: Mg/m^3	2·03	2·02
Lower wire mesh screen: mm	1·15	1·15
Vibration: min	0	0
Soil loss: %		
Reconstitution	3·0	4·3
Testing	13·0	19·0
C_U $(= D_{60}/D_{10})$	14·5	
$(D'_{15}/d'_{85})_{max}$	7·4	

Figure 4.44: Specimen parameters for the Fannin and Moffat (2006) G4-C sample.

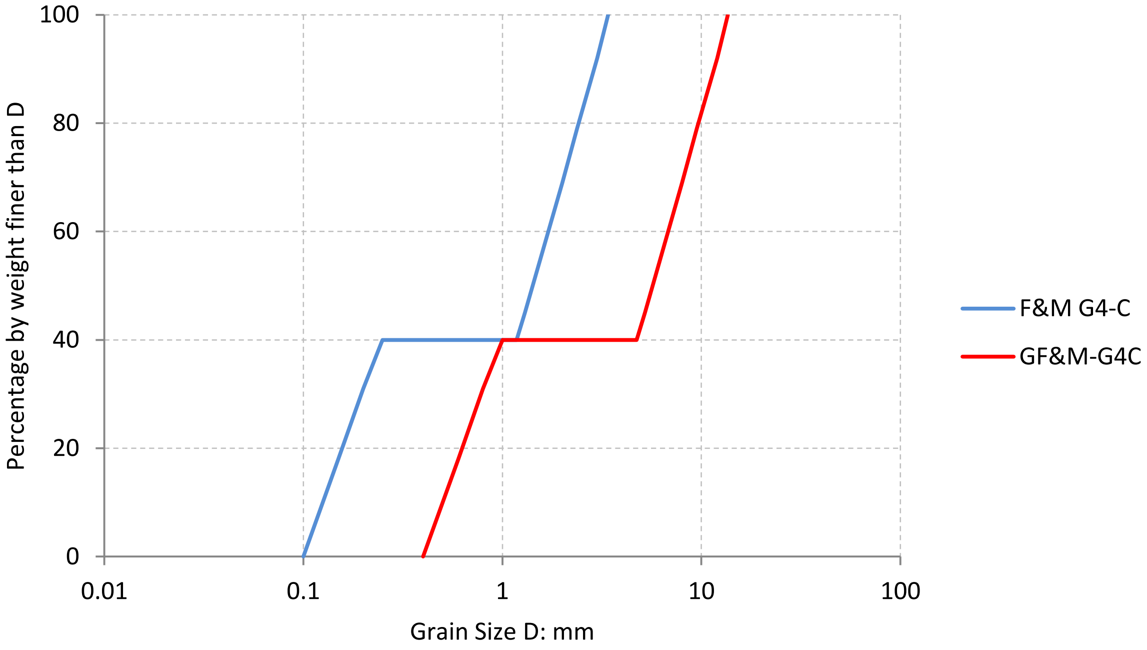

Figure 4.45: GF&M-G4C replication of Fannin and Moffat (2006) G4-C sample.

4.9.6 Long Tail Moraine Till Replication

In the mountainous areas of the Central South Island of New Zealand, soils are typically comprised of moraine till, and other like glacial deposits. In this area some of New Zealand's largest embankment dam and canal infrastructure projects are located, as part of the Waitaki Power Scheme. In this hydroelectric power network, there are multiple embankment dams and canals, including the Tekapo Canal. To relate some of this research back to some New Zealand soils that have been used, and may be used again for embankment projects, it was decided to attempt to test a moraine till, in particular the PSD used in the construction of the Tekapo Canal, named 'The Wolds' grading envelope (Figure 4.46). This grading envelope is of particular interest due to the seepage that has been observed at a localised point on the exterior of the banks since the canals first filling in 1977 (Benson 2011).

The Wolds grading envelope shows the PSD data from sieve analysis, but excludes hydrometer data. The grain size analysis of this material shows a range in particles sizes from ~0.075 mm to in excess of 100 mm, representing a widely graded material. Unfortunately, due to the size limitations of the transparent soil permeameter, this material could not be tested.

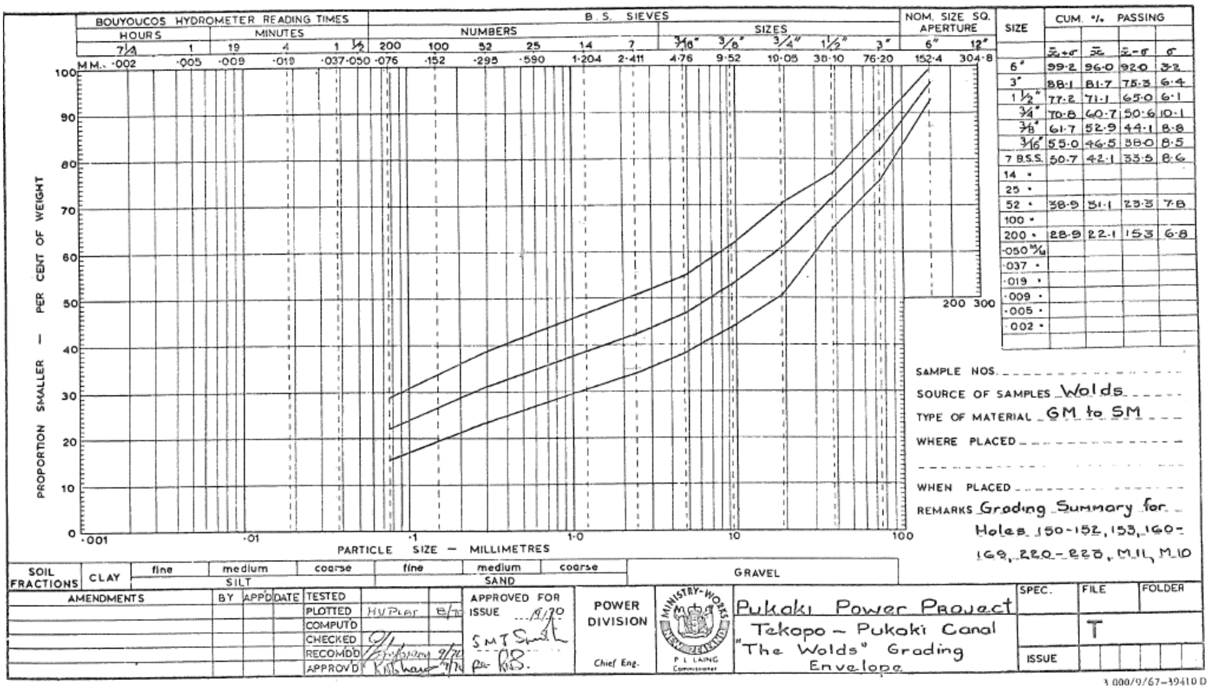

SIZE	CUM. % PASSING			
	$\bar{x}+\sigma$	$\bar{x}$	$\bar{x}-\sigma$	σ
6"	99·2	96·0	92·0	3·2
3"	88·1	81·7	75·3	6·4
1½"	77·2	71·1	65·0	6·1
¾"	70·8	60·7	50·6	10·1
⅜"	61·7	52·9	44·1	8·8
3/16"	55·0	46·5	38·0	8·5
7 B.S.S.	50·7	42·1	33·5	8·6
14 "				
25 "				
52 "	38·9	31·1	23·3	7·8
100 "				
200 "	28·9	22·1	15·3	6·8
·050 M/M				
·037 "				
·019 "				
·009 "				
·005 "				
·002 "				

SAMPLE NOS.
SOURCE OF SAMPLES Wolds
TYPE OF MATERIAL GM to SM
WHERE PLACED
WHEN PLACED
REMARKS Grading Summary for Holes 150-152, 153, 160-169, 220-223, M11, M10

AMENDMENTS | BY | APPD | DATE
TESTED
PLOTTED HVPlar 8/70
COMPUT'D
CHECKED
RECOMD'D 9/70
APPROV'D 9/70
APPROVED FOR ISSUE 9/70
POWER DIVISION
Chief Eng.
P. L. LAING Commissioner
Pukaki Power Project
Tekapo – Pukaki Canal
"The Wolds" Grading Envelope
SPEC. | FILE T | FOLDER
ISSUE
3 000/9/67—39410 D

Figure 4.46: Wolds Till Lining material, design grading range (Benson 2011)

However, given that some moraine tills typically have a 'long tail' PSD shape, a specimen was manufactured to represent a soil that might be found in a glacial landscape. The difficulty in manufacturing a PSD for this testing method is that the transparent soil permeameter has a reasonably narrow window for appropriate grain sizes, between 0.4 mm to 26.5 mm. However, using this 'window', the PSD for a 'long tailed moraine till' is shown in Figure 4.47 for the glass specimen, and for the representative soil material. This specimen is herein named 'Glass Long Tail'.

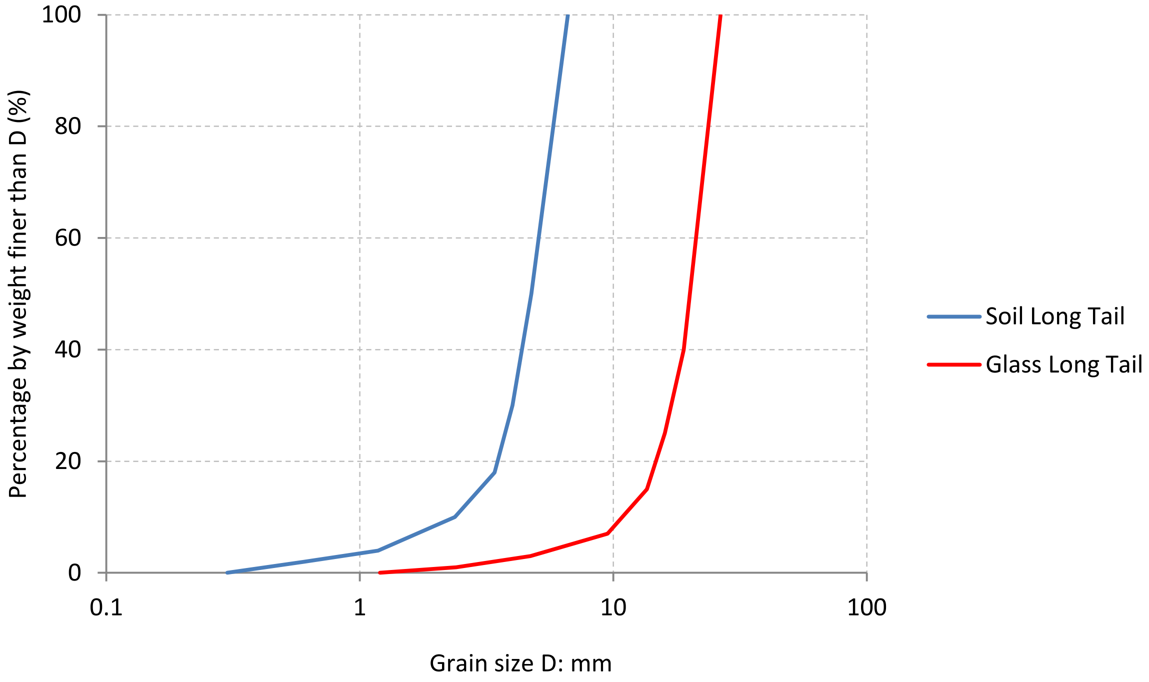

Figure 4.47: PSD of Glass Long Tail and 'prototype' soil PSD, in which the glass PSD is modelling.

4.10 PSD Analyses

Prior to testing of any sample, analysis on each PSD was undertaken. This included analyses by Kezdi (1979), Kenney and Lau (1985), Burenkova (1993), Wan and Fell (2008), and the uniformity coefficient ($C_u = D_{60}/D_{10}$) in which Istomina (1957) defines limits for suffusion. Each of these analyses are described in Chapter 2.10.

4.11 Testing Procedure

4.11.1 Static conditions

Prior to allowing oil to flow through the apparatus, static images were taken of the transparent soil sample. The 'sheet' of laser light was positioned so it intersected the side of the apparatus at 90° and aligned with the sample in question. This allowed for a 2-dimensional slice of the sample to be illuminated, in that the oil would fluoresce and the glass particles appeared as dark shadows. The camera was set up adjacent to the laser sheet so that was directed into the front of the apparatus. The camera's focus was adjusted so the illuminated slice became clear. The laser position was moved across the sample typically at 1 cm, 3 cm, 5 cm, 7 cm and 9 cm from the front of the apparatus, and images captured at each location (pre test slices). This process was repeated at the end of the dynamic test (post test slices), so that comparisons between pre and post test images could be made through various slices in the sample. Unfortunately it was not possible to re-position the laser in the exact same position before and after a test, so direct comparisons between the two images could not be accurately made.

4.11.2 Dynamic condition

The header tank was positioned so that upon opening the control valves the test specimen remained under static conditions. The head height was slowly raised in increments of 1 cm and left for a time until oil began to flow out of the apparatus at a consistent rate. Using a measuring cylinder, a sample of oil was collected for an amount of time, to calculate the flow rate. The piezometric heights at that flow rate were then recorded. At very low flows, the rotameter float would not rise, but when it did, the rotameter value was also recorded. In unison, the timing clock and camera capturing were initiated. From this point on, the piezometric levels and rotameter values were recorded approximately every minute. Using the change in piezometric values across the sample (ΔH) and the known distance between piezometric ports (L), the average hydraulic gradient (i_{av}) could be calculated by:

$$i_{\mathrm{av}} = \Delta\mathrm{H}/\mathrm{L} \tag{4.13}$$

After 6-8 minutes, the header tank was raised, typically 1-2 cm in the earlier part of the test, and up to 5 cm in the latter, and recording of data was continued. For every head increase, the flow was manually measured after a few minutes, once was stabilised. After another 6-8 minutes, the camera's memory became full and had to be downloaded, taking approximately 10-12 minutes. During that time the head height remained unchanged from the last lift. The flow was manually measured once again using the measuring cylinder, and piezometric and rotameter levels recorded. When all data had been downloaded, image capturing commenced and the head was raised. Notes were made throughout the test about interesting aspects, such as particle movements or significant changes in recorded data. This process was continued until the sample was deemed to have catastrophically 'failed' and violent piping or heave occurred. Post test slices were then captured, and control valves closed.

4.12 Image analysis using Image Pro and ImageJ software

As an example of how acquired images could be analysed, the GS&B-Hybrid test images were processed using a combination of Image Pro and ImageJ. Processing of the images began with the colour images being converted to 8-bit greyscale images. Filters were then applied to improve the image quality, and typically included sharpening (to create more defined boundaries between particles) and flattening. As laser light travelled through the permeameter it lost strength, due to interactions with particles causing reflection and refraction. As a result, the image was brighter on one side compared to the other, hence why a flattening filter helped to counterbalance this effect.

Using a colour, or shade threshold, certain parts of the image were 'highlighted' or separated from the background, for analysing. This separation is known as a 'mask'. For example, open voids (Figure 4.48) within the sample were calculated as they have a bright fluorescence, compared to an area of fine particles or a single coarse particle. Likewise, the portion of 'coarse' fraction was also highlighted, as it had a dark shade threshold, compared to the background image (Figure 4.49).

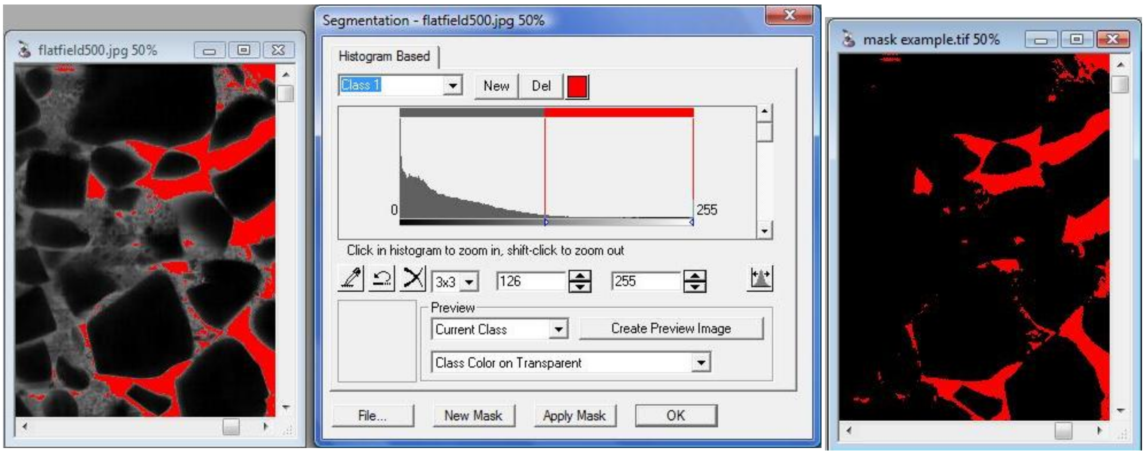

flatfield500.jpg 50%

Segmentation - flatfield500.jpg 50%

mask example.tif 50%

Class 1

Click in histogram to zoom in, shift-click to zoom out

3x3 126 255

Preview: Current Class

Class Color on Transparent

Figure 4.48: Selection of an intensity range that will 'highlight' the 'open void space' (in red), to create the 'mask', also shown.

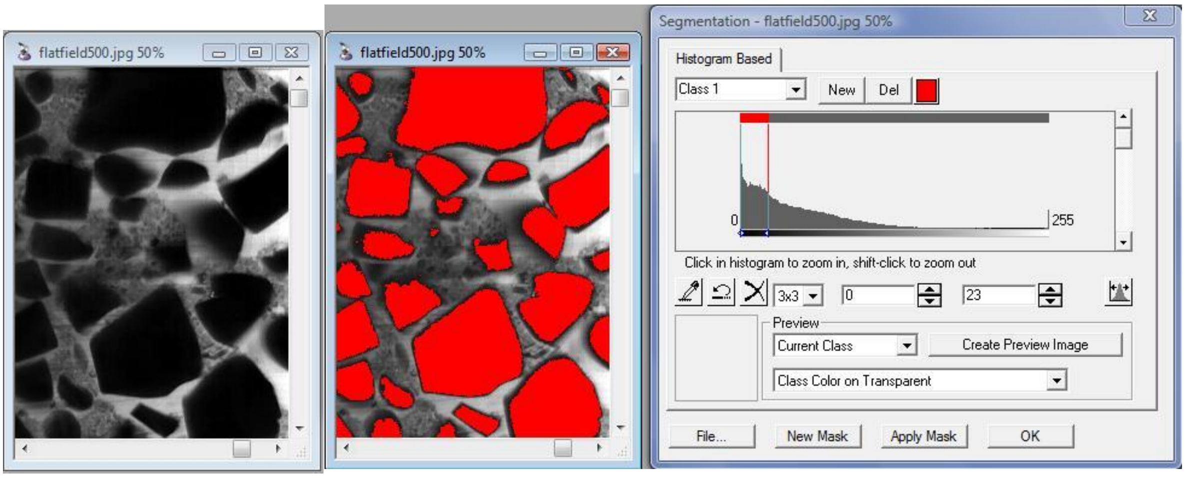

flatfield500.jpg 50%

flatfield500.jpg 50%

Segmentation - flatfield500.jpg 50%

Class 1

Click in histogram to zoom in, shift-click to zoom out

3x3 0 23

Preview: Current Class

Class Color on Transparent

Figure 4.49: Example of selecting a threshold, or intensity range, to 'highlight' (in red) the coarser fraction, in this case.

Once an image had a mask, a wide range of data was be exported, including particle angle, aspect ratio, diameter, perimeter and area, naming only a small selection of variables that can be selected.

This data was then used to calculate the area of coarse particles, open voids and the finer fraction, for a range of pre-test, post-test and test slices.

Chapter 6 presents comparisons in pre-test vs. post-test data, as well as changes that occur at various points of interest throughout the test duration. Pre and post test data were gathered from 4 slices within the sample to determine an average coarse particle area, open void volume and finer fraction volume. Comparing this data can quantify changes that have occurred within the specimen from the start to the conclusion of the test.

Using pre-test data, the void ratio and porosity were calculated and compared with measured values, which were obtained from measuring the sample weight and volume. The primary aim of this exercise was to assess whether the void ratio can be accurately estimated by image analysis.

ImageJ can present similar data as described above, however in this instance, the software was primarily used for the creation of Rose diagrams. Like in Image Pro, filtering and an intensity threshold can be applied to create a mask. Using this mask, the plug-in ‘particle descriptor 1u’ can create a Rose diagram to visually present particle orientations. This information is also available in spreadsheet format, if changes in particle properties (such as angle or translation) wish to be assessed. Of interest maybe to, a) assess if the placement method creates a random or flattened orientation of particles, and b) to compare pre-test and post-test changes.

4.13 Synthesis

- The PLIF technique uses a sheet of laser light which passes through a box shaped permeameter filled with optically matched glass particles and hydrocarbon oil as the fluid. Fluorescent dye in the oil causes the fluid to fluoresce while the glass particles appear as dark shadows. A camera captures images at regular intervals throughout the test, which involves stepping up the hydraulic gradient in stages until the test is commenced.
- To allow the glass and oil material interactions to be directly compared to soil and water materials used in embankment dams, the Kozeny-Carmen equation determined the scaling factor which resulted in the up-scaling of the glass particles by 4 times.
- Glass was crushed to create particles of appropriate sizes, and a method was developed to clean and prepare the glass particles following and prior to each successive test.
- The permeameter apparatus underwent several modifications, but a fully functioning apparatus was developed.

- A re-circulation system was developed that allowed for the flow rate and piezometric response to be measured, and so the hydraulic head could be controlled.
- A range of PSDs were chosen for testing, including several replicated materials from Skempton and Brogan (1994) and Fannin and Moffat (2006)
- The testing procedure is outlined, including a summary of how one may wish to use image processing to assess results.

Chapter 5: Results from PSD analysis and physical testing

5.1 Introduction

The results in this section include a PSD analysis to assess the theoretical stability or instability of each sample. This includes the Kenney and Lau (1985), Kezdi (1979), Burenkova (1993) and Wan and Fell (2008) approaches. In addition, the uniformity coefficient ($C_u = D_{60}/D_{10}$) is included, as Istomina (1957) determined values where suffusion occurs. Test data is also presented with the average hydraulic gradient plotted against seepage velocity, with some plots having a velocity correction as explained later in Chapter 7. This data is correlated with a step by step analysis of observations made from gathered images. Theoretical critical hydraulic gradients (i_c) are compared to observed critical gradients (i_{cr}), and the Skempton and Brogan (1994) alpha factor (α) is calculated. A selection of images is presented to accompany the average hydraulic gradient vs. velocity plots and written explanations. Interpretations and a discussion of these results are made in Chapter 7. For a description of the material tested and their naming terminology, refer to Chapter 4.9. The reader will be referred to the Video Appendix in a few instances, which can be found on the attached CD.

5.2 Uniform PSD Tests

To check the validity of this testing method using glass-oil mixtures, two PSDs were tested. The first, a distribution of particle sizes between 4.75 mm and 6.7 mm, was to check that laminar flow according to Darcy's Law (Darcy 1856) was validated. The second, a uniform distribution of particles between 0.425 mm and 0.710 mm, was to confirm whether the calculated Terzaghi critical hydraulic gradient (i_c) (Terzaghi 1925) for materials with no top stress, was valid. The results from these tests follow.

5.2.1 G100CF Test

The G100CF specimen consists of a PSD with particles passing the 6.7 mm sieve and caught in the 4.75 mm sieve (coarser fraction). The distribution of particle sizes within this range is assumed to be even, or uniform. The sample had a porosity of $n = 0.372$.

The Burenkova (1993) analysis showed this PSD to be stable (Figure 5.1), as does the Wan and Fell (2008) approach (Figure 5.2) for determining stability. The uniformity coefficient $C_u = D_{60}/D_{10}$ is 1.20

which suggests the sample is self-filtering according to Istomina (1957), and the filter ratio (Kezdi 1979) (assuming an even distribution of particles between 4.75 mm and 6.7 mm) $(D'_{15}/d'_{85})_{max}$ is 1.06, which is well below the limit of 4-5, suggesting a stable PSD. A summary of PSD analysis data is presented in Table 5.1. A Kenney and Lau (1985) analysis could not be carried out on this sample, due to the uniformity of the PSD. The theoretical critical hydraulic gradient according to Terzaghi (1925) is $i_c = 0.772$.

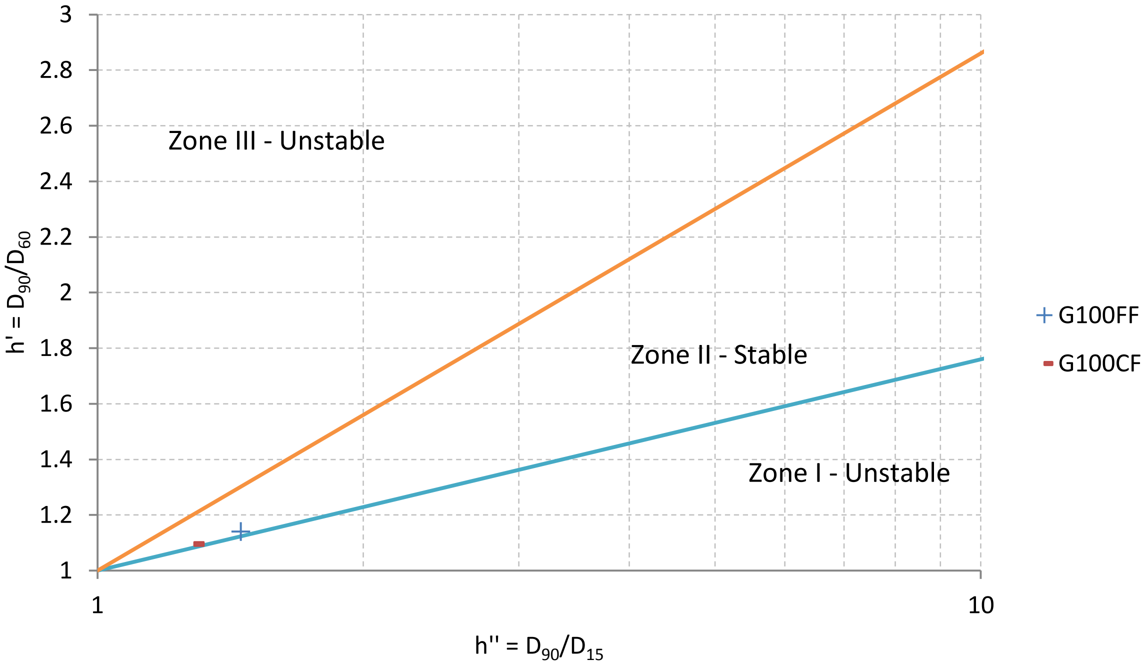

Figure 5.1: Burenkova (1993) plot for predicting stability of G100CF and G100FF.

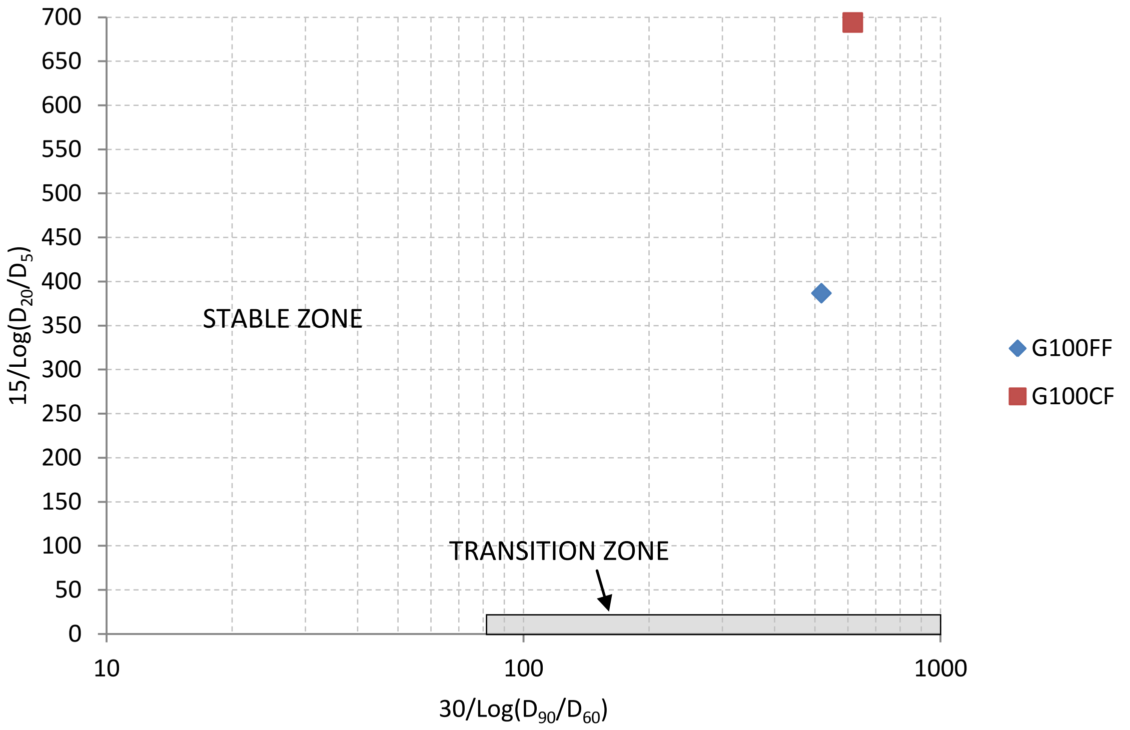

Figure 5.2: Wan and Fell (2008) approach to stability analysis for the G100FF and G100CF materials.

In order to increase the flow rate as the test progressed, the head was increased in increments as discussed in Chapter 4. The head was increased in 1 cm increments between 38 cm (above table height) and 65 cm, then in 2 cm increments from 65 cm to 81 cm. After this point images were no longer collected, and the head was raised in 12 cm increments from 81 cm to 115 cm. The whole range corresponded to hydraulic gradients between 0.01 and 0.086.

Table 5.1: Summary PSD analysis for G100CF.

	G100CF
Kenny and Lau	n/a
Kezdi, $(D'_{15}/d'_{85})_{min}$	1.048
Kezdi, $(D'_{15}/d'_{85})_{max}$	1.058
Burenkova	Stable
Wan and Fell	Stable Zone
$C_u = (D_{60}/D_{10})$	1.2 (self filtering)

Pre-test images are shown in Figure 5.3. These images show the high volume of void space and random orientation of particles. The whole 2D slice is captured in these images.

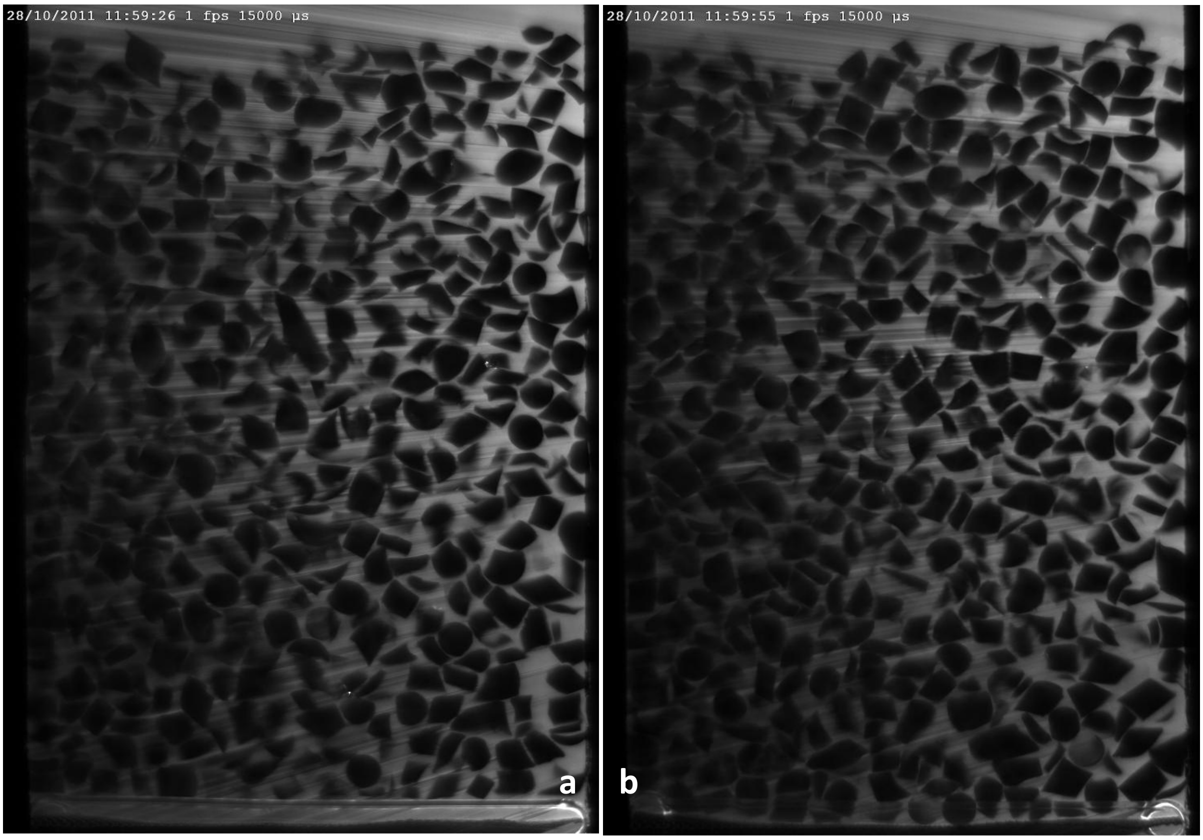

Figure 5.3a-b: Pre test slices of the G100CF sample: a) 1 cm and; b) 2 cm from front wall.

Flow velocity vs. average hydraulic gradient data is shown in Figure 5.4. In this test, the following stages of development were observed.

a) From i_{av} = 0.026 to 0.39 there is a linear relationship between average hydraulic gradient (i_{av}) and flow velocity according to Darcy's Law. No change in particle structure was observed during this time. The computed permeability was k = 2.08 cm/s.
b) Between i_{av} = 0.39 to 0.48 there is no increase in flow velocity with increasing gradient. During this time, these are small translational and rotational movements of some particles. No further movements were seen after this point.
c) From i_{av} = 0.48 to 0.64 the linear relationship continues at a similar gradient as seen previously, with a permeability k = 2.03 cm/s. No change to the particle structure occurs during this time. The test was concluded at this point due to the limitation of the pump in supplying a higher flow, hence the theoretical hydraulic gradient (i_c) was not reached.

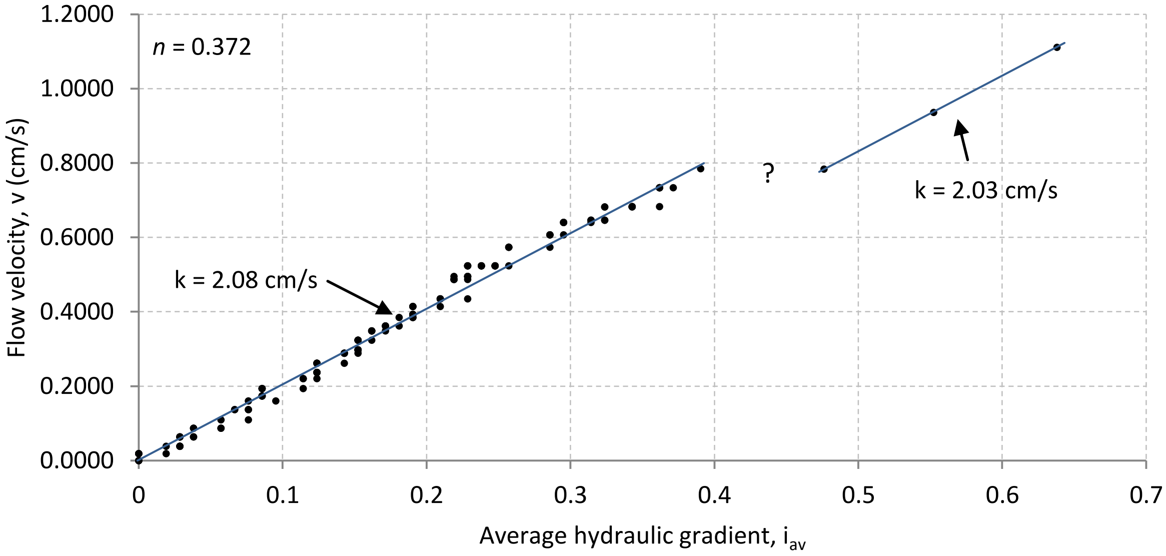

Figure 5.4: Average hydraulic gradient vs. flow velocity (corrected) in the G100CF test.

5.2.2 G100FF Tests

Two tests were run using a narrow gradation of fine particles passing the 0.710 mm sieve and retained on the 0.425 mm sieve (finer fraction). The first test had a 'loose' compaction (G100FF - loose) achieved using the slurry placement method, and the second test being 'compact' (G100FF - compact), achieved by tamping the first sample under saturation after the initial test had been concluded. The Kenney and Lau (1985) analysis was not possible on these uniform samples.

The Kezdi (1979) analysis was used to determine $(D'_{15}/d'_{85})_{max}$ = 1.09 (assuming a uniform particle size between 0.425 mm and 0.710 mm), which is below the recommended limits of 4-5 for stable filters. The Burenkova (1993) analysis showed this PSD to be stable (Figure 5.1), as does the Wan and Fell (2008) approach (Figure 5.2) for determining stability. The uniformity coefficient C_u is 1.31, and according to Istomina (1957), this result suggests suffusion will not occur. A summary of the PSD analysis results is shown in Table 5.2.

In these tests, the head was increased in 2 cm increments, resulting in increments in average hydraulic gradient (i_{av}) between 0.186 and 0.014. As the head was raised in uniform increments, the increments in i_{av} became smaller, likely due to frictional losses in the system.

Table 5.2: Summary PSD analysis for G100FF.

	G100FF
Kenny and Lau	n/a
Kezdi, $(D'_{15}/d'_{85})_{min}$	1.068
Kezdi, $(D'_{15}/d'_{85})_{max}$	1.092
Burenkova	Stable
Wan and Fell	Stable Zone
$C_u = (D_{60}/D_{10})$	1.31 (self filtering)

5.2.2.1 G100FF - loose test

The G100FF - loose sample had a porosity of n = 0.496, and a weight of 1034.46 g. The Terzaghi theoretical critical gradient (Terzaghi 1925), i_c was 0.62.

An image (Figure 5.5) taken prior to commencing the test shows the particles to be uniform in size and packing. Note that the light is quickly attenuated in this sample of fine particles, and that the entire sample is captured in this image.

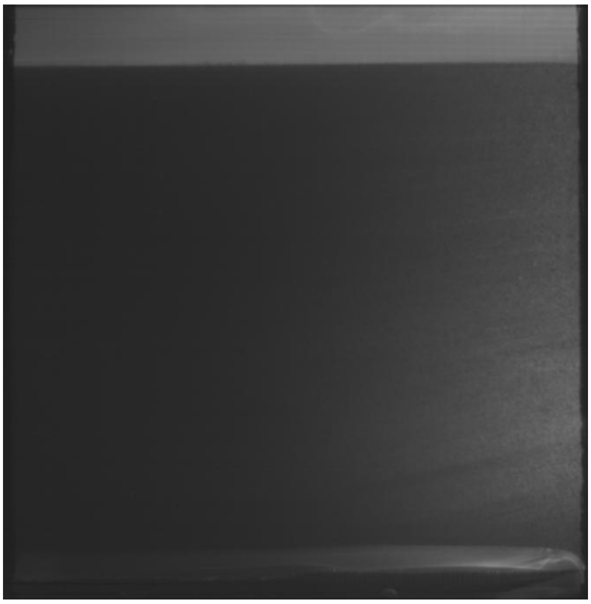

Figure 5.5: Pre-test Image of G100FF - loose sample.

In the test (Figure 5.6) the following stages of development were observed.

a) Up until i_{av} = 0.56, there is laminar flow according to Darcy's Law and the permeability is k = 0.015 cm/s.
b) At i_{av} = 0.56 the sample 'heaves' and global fluidisation occurs (Figure 5.7). The average hydraulic gradient dramatically reduces while the flow velocity is greatly increased. Test

images capture the fluidised sample with a changing preferential flow path of less dense particles, shown by the slightly lighter areas of the image in Figure 5.7. During fluidisation of the sample, these flow paths quickly move and change as the sample 'boiled'. Also note that the top of the sample cannot be seen, showing that the height of the sample has increased as the sample has fluidised and become less dense. The alpha factor, $\alpha = 1.005$.

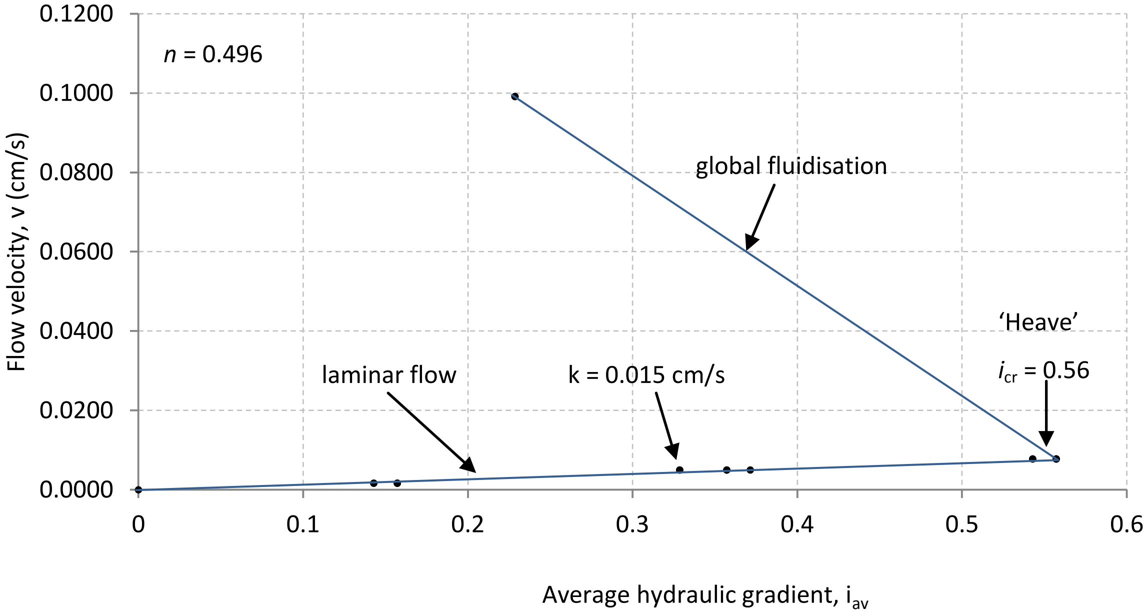

Figure 5.6: Average hydraulic gradient vs. flow velocity (corrected) for the G100FF - loose test.

Figure 5.7: 'Fluidised' G100FF - loose sample. Note lighter areas where surges of oil are flowing, therefore having a lower density of particles.

5.2.2.2 G100FF - compact test

The G100CF - compact sample had a porosity of *n* = 0.448, and a weight of 1034.46 g. The Terzaghi (1925) theoretical critical gradient, $i_c = 0.68$.

In the test (Figure 5.8) the following stages of development were observed.

a) Up until $i_{av} = 0.710$, there is laminar flow according to Darcy's Law and the permeability *k* = 0.013 cm/s.

b) At $i_{av} = 0.710$ the sample 'heaves' and global fluidisation occurs. Similar to the 'loose' test, the average hydraulic gradient dramatically reduces while the flow velocity is greatly increased. The alpha factor (α) = 1.046.

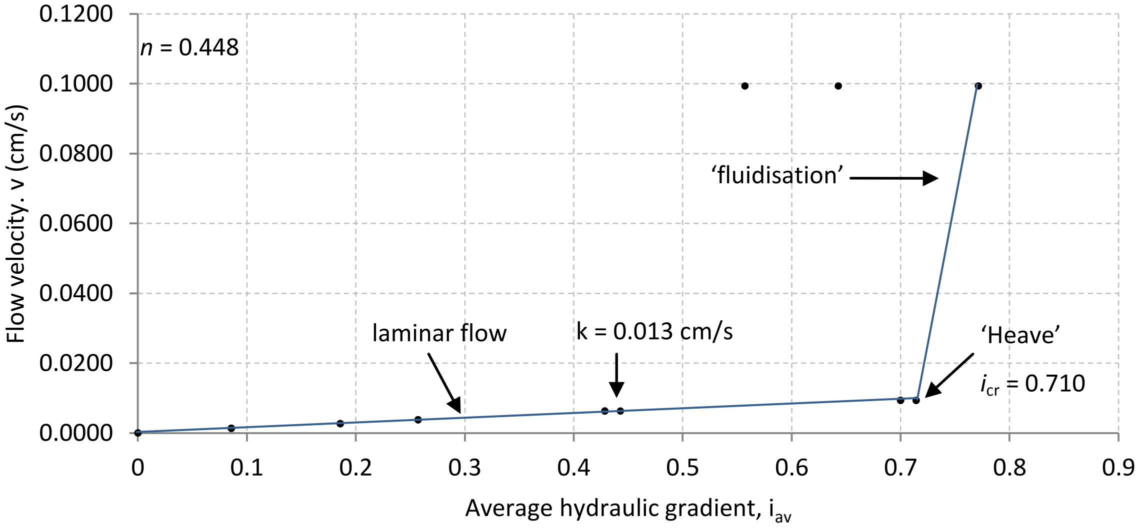

Figure 5.8: Average hydraulic gradient vs. flow velocity (corrected) for the uniform G100FF - compact test.

5.3 G22FF and G40FF Tests

The G22FF and G40FF tests represent simply, a clast supported material and a matrix supported material respectively. The coarse fraction consisted of particles passing the 6.7 mm sieve and caught in the 4.75 mm sieve, as used in the earlier G100CF validation test. The finer fraction consisted of particles passing the 0.710 mm sieve and retained on the 0.425 mm sieve, also used in the earlier G100FF tests. An assumption is made that there is an even distribution of particles between these sieve sizes.

The Kenny and Lau (1985) method for stability is plotted in Figure 5.9 for both the G22FF and G40FF tests. The plot shows the 'stable' and 'unstable' zones according to Kenney and Lau (1985), and also the H=15 boundary for stability, according to Kezdi (1979), where a PSD is unstable if it plots below these boundaries. Using both the Kenny and Lau and Kezdi approaches, both the G22FF and G40FF finer faction samples are classed as unstable. In combining these two approaches, this method for stability analysis was proposed by Li and Fannin (2008). Using the Burenkova (1993) approach, both samples should be 'unstable' (Figure 5.10). In contrast, the Wan and Fell (2008) approach suggests both G22FF and G40FF are stable (Figure 5.11). A summary of PSD analysis results are shown in Table 5.3.

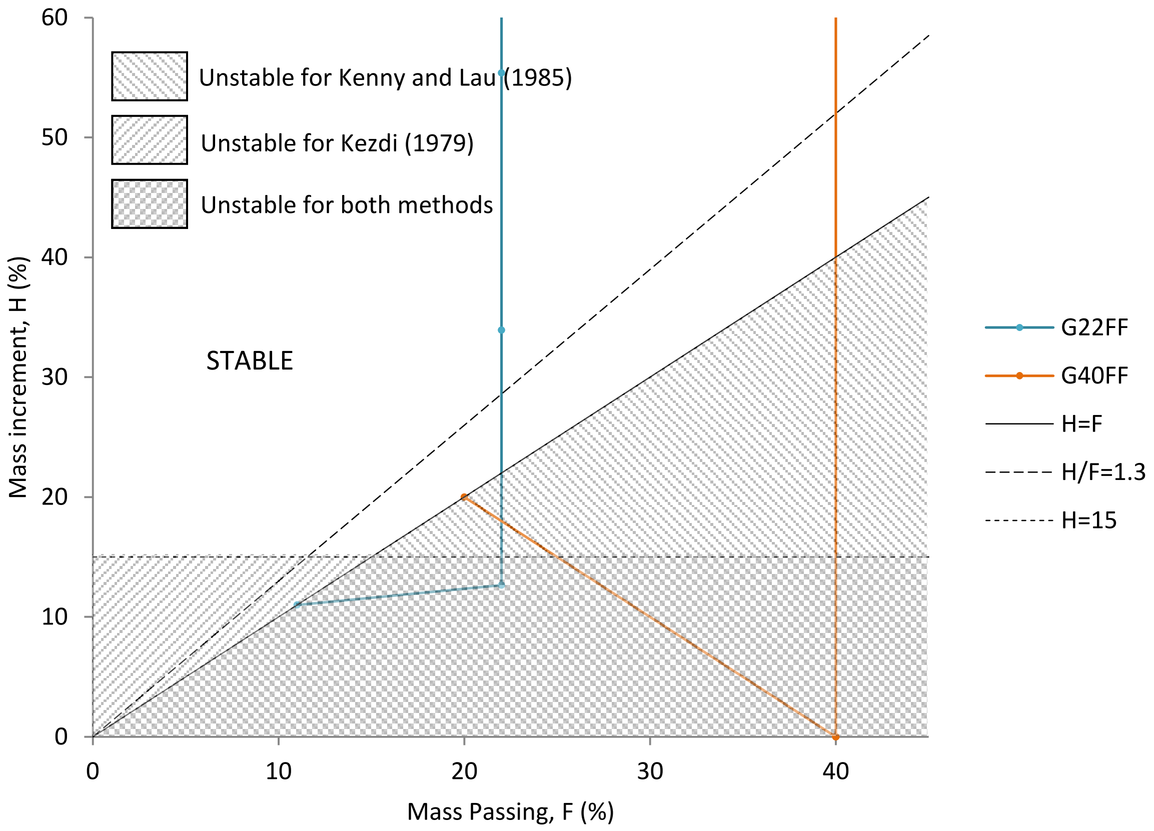

Figure 5.9: Kenney and Lau (1985) method for stability analysis on G22FF and G40FF samples. Also shown on graph is the Kezdi (1979) boundary for stability.

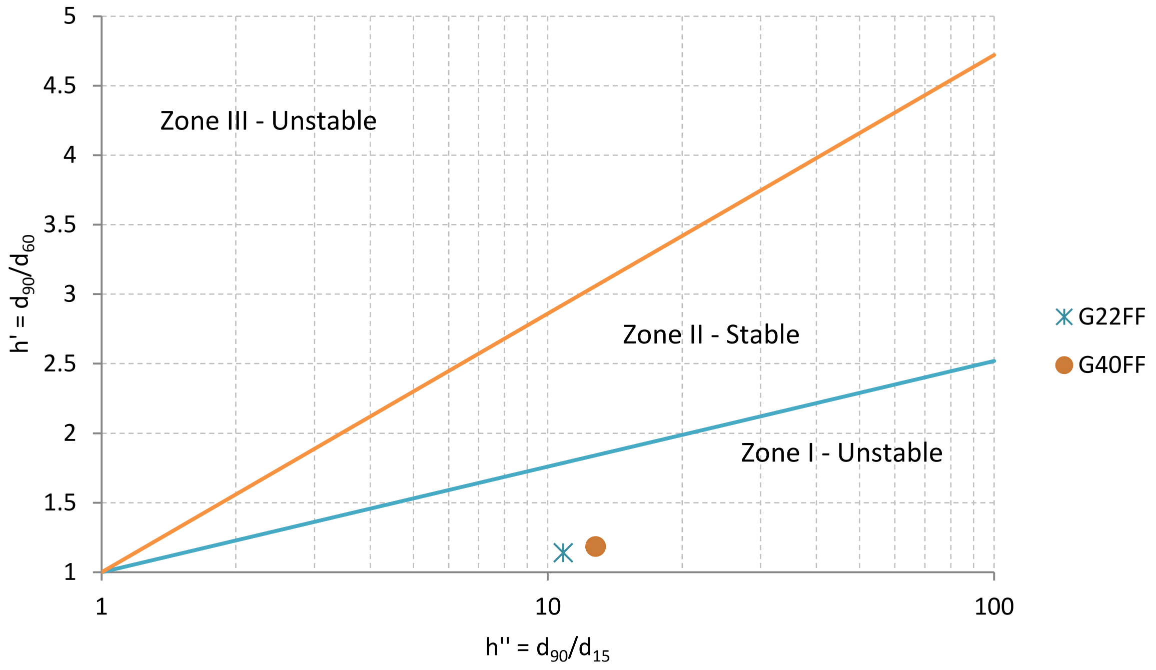

Figure 5.10: Burenkova (1993) plot for predicting stability of G22FF and G40FF.

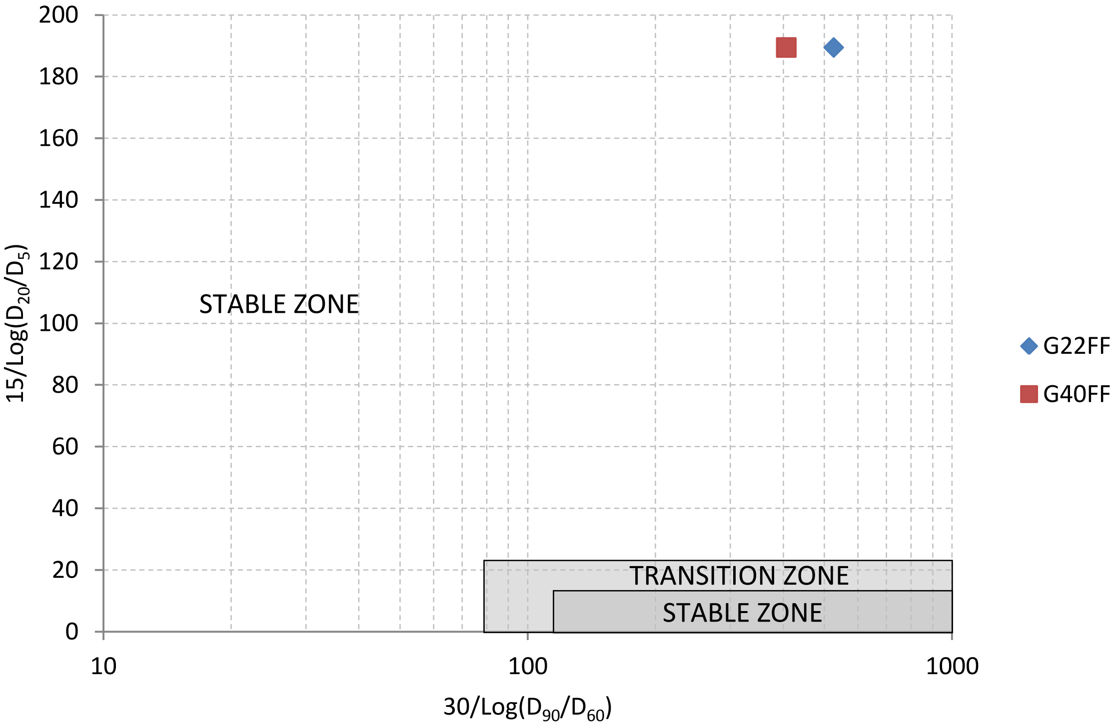

Figure 5.11: Wan and Fell (2008) approach to stability analysis for G22FF and G40FF tests.

Table 5.3: Summary PSD analysis and theoretical critical hydraulic gradient values for G22FF and G40FF materials.

	G22FF	**G40FF**
Kenny and Lau, $(H/F)_{min}$	0.57 (unstable)	0 (unstable)
Kezdi, $(D'_{15}/d'_{85})_{min}$	7.56	7.56
Kezdi, $(D'_{15}/d'_{85})_{max}$	7.56	7.56
Burenkova	Unstable	Unstable
Wan and Fell	Stable	Stable
$C_u = (D_{60}/D_{10})$	9.5 (self filtering)	10.8 (not self filtering)
i_c	0.856	0.89

5.3.1 G22FF Test

The G22FF PSD was tested twice (G22FF-1 and G22FF-2), but only the second test results are presented here. The G22FF-2 specimen was a gap graded and highly unstable sample with $(H/F)_{min}$= 0.58. The sample had a porosity of n = 0.304. The $(D'_{15}/d'_{85})_{max}$ was 7.56, which is above the recommended value of 4-5 for stable filters (Kezdi 1979). The total dry weight of the sample was 2100 g and the theoretical i_c = 0.856.

Images of the sample prior to test initiation show void spaces in the sample, confirming that there were not sufficient fine particles to fill the voids between the coarser fraction. In scanning the laser across the sample, it was confirmed that the sample was clast supported, in that almost every coarser grained particle was connected to another coarser grained particle. The images in Figure 5.12 show several 2D slices through the sample at 1 cm, 2 cm, 3 cm and 4 cm from the front of the permeameter. In some images it appears that part of the sample is matrix supported. This occurs as the laser has intersected the matrix between the coarser fraction, but not at the coarse-grained contact points.

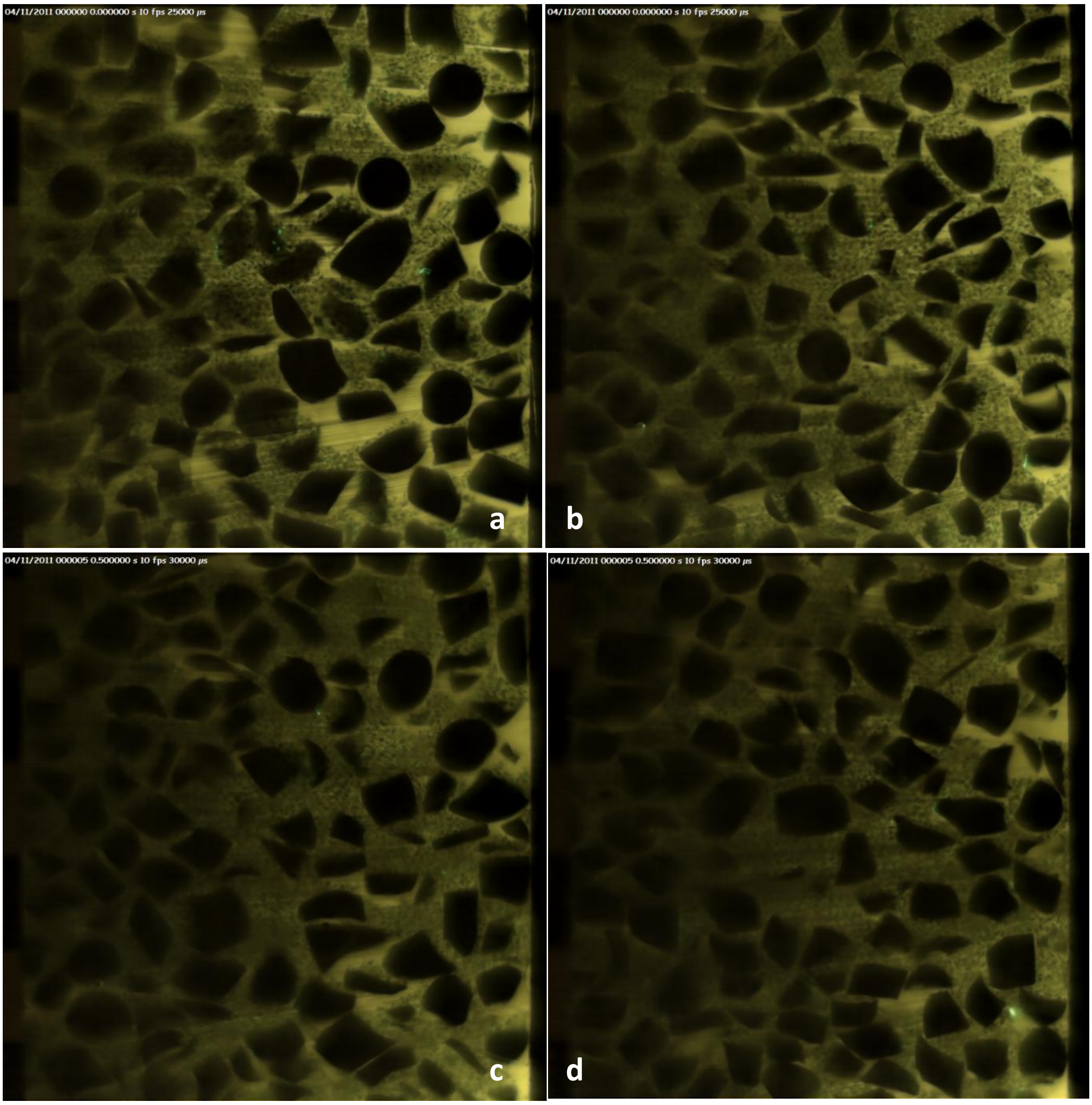

Figure 5.12a-d: Slices through the G22FF-2 sample prior to testing commenced. Images a-d are from 1 cm, 2 cm, 3 cm and 4 cm from the front of the apparatus respectively.

During the test (Figure 5.13) the following stages of development were observed.

a) From $i_{av} = 0$ to 0.152 there was laminar flow with increasing hydraulic gradient. Test images (Figure 5.14) showed minor movements of the finer particles in void spaces as upward flow is applied. White circles are used to highlight areas of interest for Figure 5.14 and in subsequent images. The permeability was constant up to this point, with $k = 0.328$ cm/s.

b) At $i_{av} = 0.152$ the gradient, k, between i_{av} vs. v increased to a permeability $k = 0.7$ cm/s. This increase coincided with a slight rearrangement of the finer particles, more commonly along the permeameter edges, with increasing head. Fines instantly reacted to the increased flow velocity, and then stabilised within approximately 40 seconds.

c) At i_{av} = 0.238 there was significant 'dancing-like' movement in voids along the glass edges, and a moderate amount of washout of the fine material. After approximately 170 seconds, the sample stabilised and only occasional minor movements of the fines occurred. Figure 5.15 (a) and (b) shows this change across the 170 seconds.

d) At i_{av} = 0.257 there was 'dancing' and general upward suffusing of particles within void spaces throughout the sample, not just near the side walls.

e) At i_{av} = 0.305 the general upward suffusing continued, taking 210 seconds to stabilise after the raise in head.

f) At i_{av} = 0.353 there was violent piping of fines and an increase in flow velocity at a constant gradient. When this stage was reached the permeability *k* was 0.7 cm/s, an increase of more than two times the initial laminar permeability.

In this test the critical hydraulic gradient was interpreted to occur at i_{cr} = 0.257 due to the slight, general movement of fines throughout the material. Therefore, the alpha value is α = 0.30.

Post test slices (Figure 5.16a to Figure 5.16d) show the greatest amount of fines that washed out were along the glass walls (Figure 5.16a), with a reduction in washout towards the centre of the sample (Figure 5.16d).

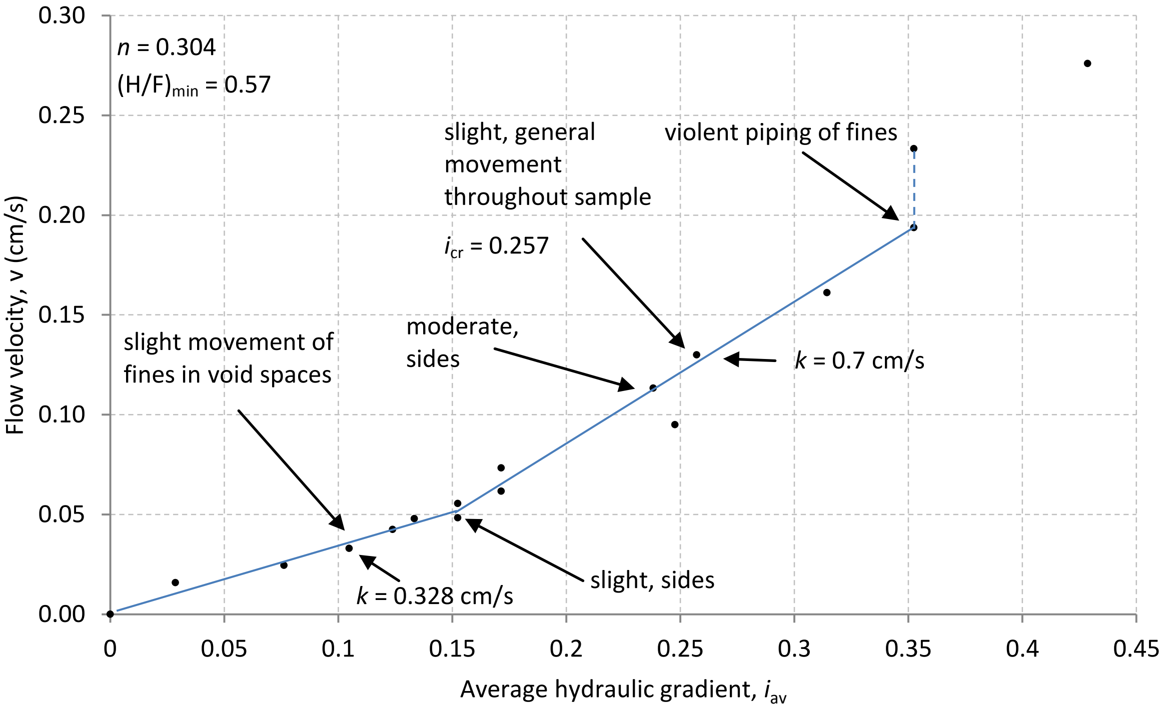

Figure 5.13: Average hydraulic gradient vs. flow velocity in the G22FF-2 test.

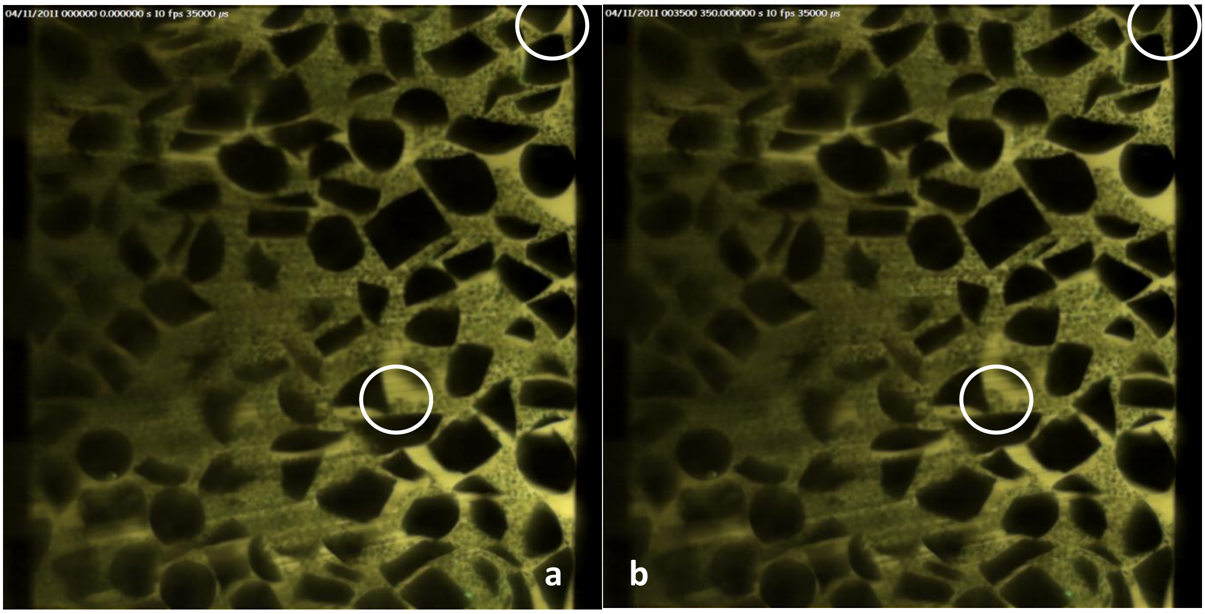

Figure 5.14a-b: Changes in the G22FF-2 sample between i_{av} = 0 (a) to 0.152 (b). White circles showing some of the areas with minor change.

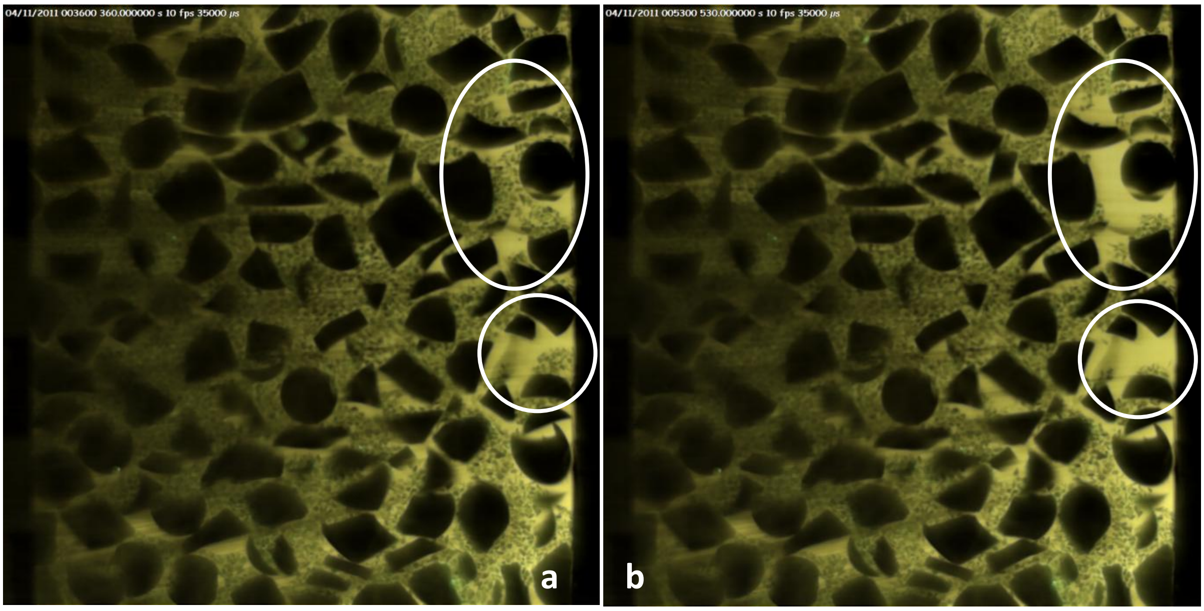

Figure 5.15a-b: At i_{av} = 0.238 there is a washout of fines (outlined in white circles) mainly along the right hand glass wall, before particles stabilise again. a) shows the G22FF-2 sample just before the onset, and b) 170 seconds later.

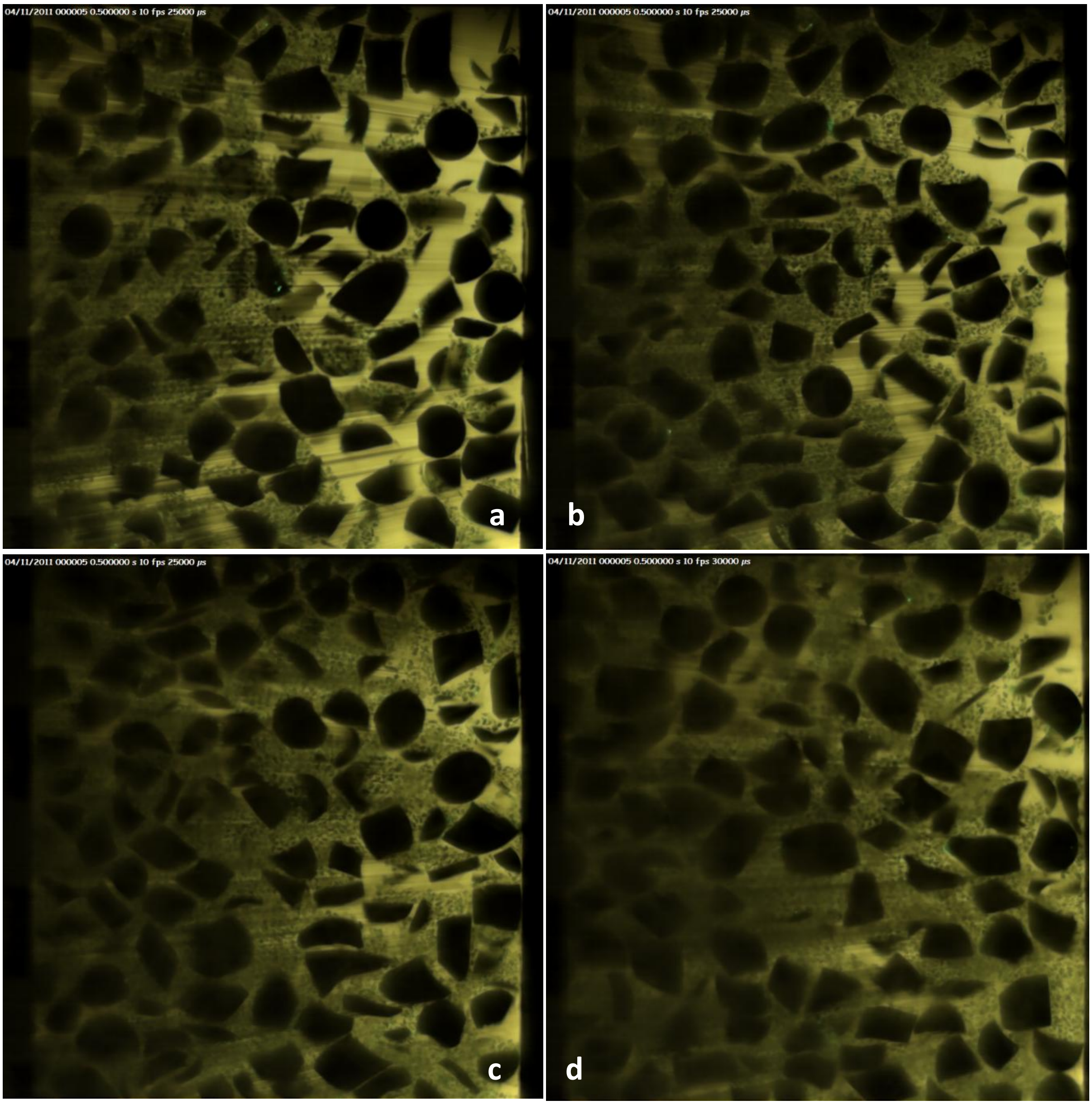

Figure 5.16: Post G22FF-2 test slices at a) 1 cm; b) 2 cm; c) 3 cm and d) 4 cm.

5.3.2 G40FF Tests

The G40FF samples were gap graded and unstable with $(H/F)_{min}$= 0. The material had a porosity of *n* = 0.273. The $(D'_{15}/d'_{85})_{max}$ was 7.56, which is above the recommended value of 4-5 for stable filters. The total dry weight of the sample was 2042.5 g and the theoretical critical hydraulic gradient was i_c = 0.89.

This sample was tested three times (G40FF-1, G40FF-2 and G40FF-3), with the results of G40FF-2 and G40FF-3 shown here. Test G40FF-2 underwent the slurry placement technique, as described in Chapter 4, while for the second test, upon the completion of the G40FF-2 test, the sample was remixed inside the permeameter apparatus until an even distribution of the PSD was thought to be obtained from a visual inspection, and then retested. Remixing the sample was only trialled once here throughout experiments, and was only done so with this PSD due to it being matrix supported with only two particles sizes, hence uniformity of the sample could be replicated with reasonable certainty. As the sample was matrix supported, the Terzaghi (1925) i_c was calculated to predict when failure might occur. The theoretical value for all G40FF tests was $i_c = 0.89$. Only images from G40FF-2 are presented here.

Images of the sample prior to test initiation show the sample to be matrix supported with no major void spaces (apart from those between the finer fraction) (Figure 5.17a-d). These images confirm that the sample was matrix supported, as the coarser fraction is floating in the finer fraction. Scanning the laser across the sample also confirms that the coarser particles were not supporting the structure of the sample, but rather the finer fraction was. The images in Figure 5.17a-d show a declining image quality with distance from the front of the apparatus. Images beyond 30 mm become quite blurry, particularly on the left hand side, at the furthest point from the laser source, making particle boundaries difficult to differentiate.

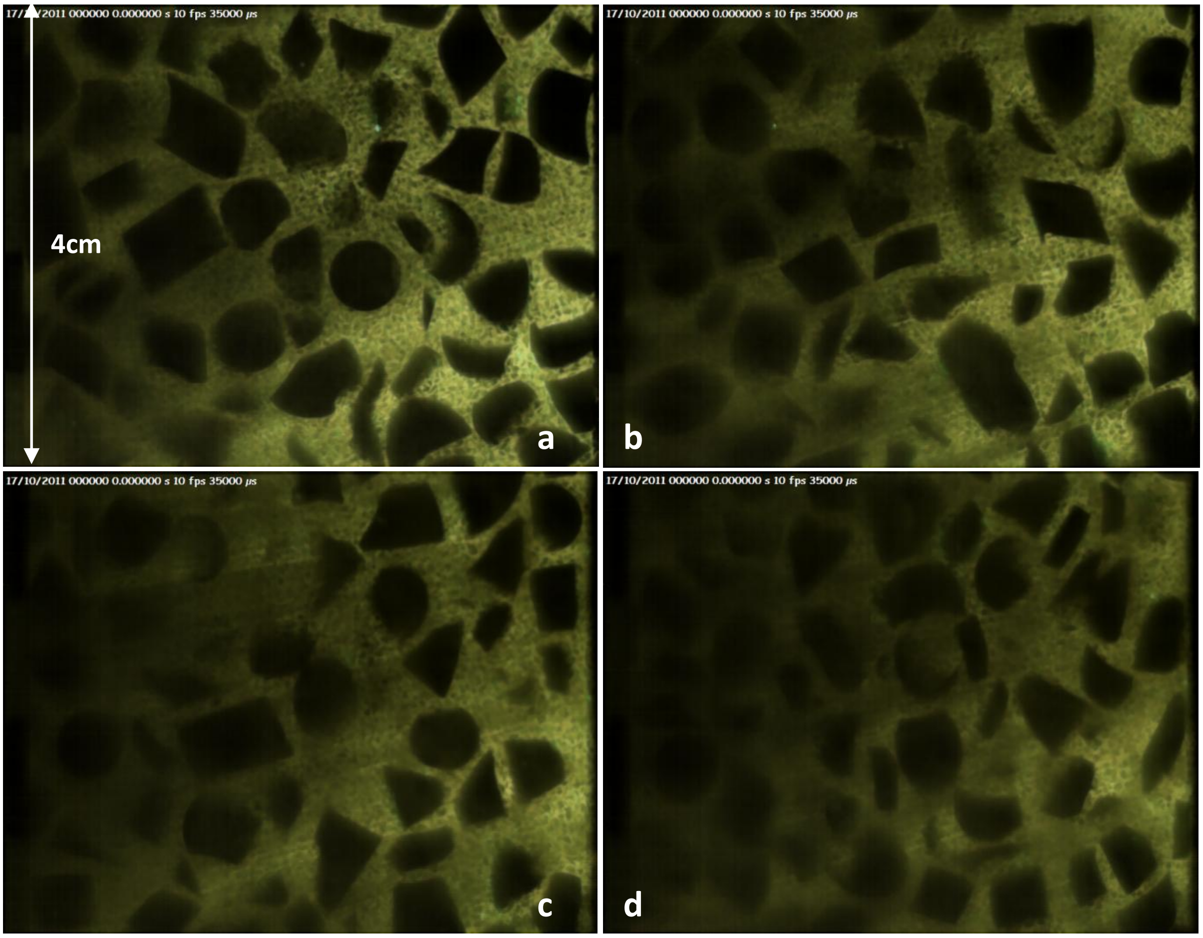

Figure 5.17a-d: Pre-test slices of G40FF-2 sample at a) 5 mm; b) 10 mm; c) 15 mm and; d) 20 mm from front wall.

In G40FF-1 (Figure 5.18), failure occurred within the sample, and the following stages of development were observed.

a) From i_{av} = 0 to 0.56 there was laminar flow according to Darcy's Law (1856). No movement of fines was observed. The permeability between these hydraulic gradients was k = 0.013 cm/s.

b) At i_{av} = 0.56 piping failure rapidly occurred towards the back right of the sample, approximately 2 cm in from the glass walls. Piping of fines was localised to this pipe, which increased in size as piping continued. Immediately after piping development, the permeability had nearly doubled to k = 0.22 cm/s. As the pipe developed and increased in size, flow velocity and permeability increased while the average hydraulic gradient, i_{av} decreased. Fines were deposited at the top of the sample marking the mechanism of suffosion. The alpha value α = 0.629.

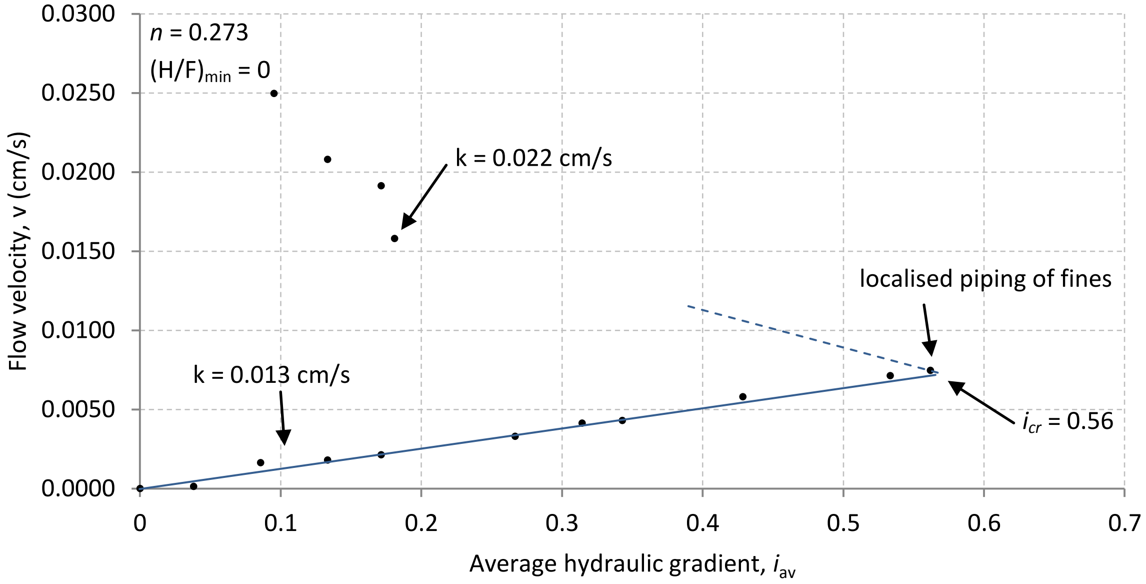

Figure 5.18: Average hydraulic gradient vs. flow velocity (corrected) in G40FF-2 test - failure within sample.

In G40FF-3 (Figure 5.19), failure occurred along the permeameter wall, and the following stages of development were observed.

a) From i_{av} = 0 to 0.35, there was laminar flow according to Darcy's Law. No movement of fines was observed. The permeability between these hydraulic gradients was k = 0.021 cm/s.

b) At i_{av} = 0.35 piping failure rapidly occurred along the front left corner of the permeameter marking the critical hydraulic gradient in this test. Fines were rapidly eroded along the glass walls of the apparatus to a point where a localised area had a permeability high enough to tolerate the increased flow rate without eroding any additional sample. With this new flow path, the volume of flow through the remainder of the sample was likely to be decreased. Fines were deposited on top of the specimen, showing that suffosion occurred. The alpha value (α) was 0.39.

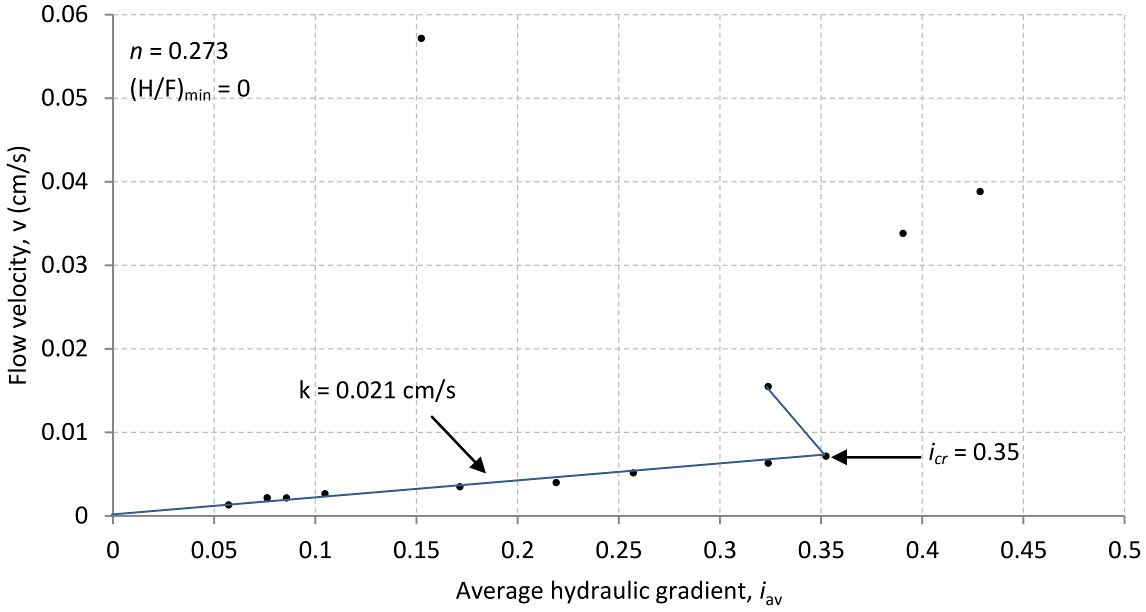

Figure 5.19: Average hydraulic gradient vs. flow velocity (corrected) in G40FF-3 - failure along glass wall.

5.3.3 UBC 22% and 40% finer fraction tests

Tests carried out at UBC (K. Crawford-Flett & R. J. Fannin, Pers. com) using their larger permeameter included 22% finer fraction, 40% finer fraction and 100% finer fraction tests using glass beads and water. Four tests were undertaken using the 22% finer fraction sample, using top stresses of 0 kPa (GB22-0), 50 kPa (GB22-50) and 100 kPa (GB22-100). Results from these tests are summarised in Table 5.4 and compared with the corresponding G22FF tests carried out at UC. The UBC 40% finer fraction test (40%FF) is summarised in

Table 5.5 and compared to the equivalent G40FF test from UC, and the UBC 100% finer fraction test (100%FF) is compared to the G100FF test, in Table 5.6. The 40%FF and 100%FF tests were carried out using no top stress, like the G40FF and G100FF tests.

Table 5.4: UBC vs. UC summary test data for GB22-0, GB22-50, GB22-100 and G22FF tests.

	UBC				**UC**	
Sample	GB22-0	GB22-50	GB22-50a	GB22-100	G22FF-1	G22FF-2
Top Stress/Surcharge, kPa	0	50	50A	100	0	0
Porosity, *n*	0.26	0.27	0.28	0.23	0.307	0.304
D_{15} mm	0.161	0.161	0.161	0.161	0.6	0.6
$C_u = (D_{60}/D_{10})$	9.8	9.8	9.8	9.8	9.5	9.5
Permeability, *k* cm/s	0.048	0.067	0.065	0.038	n/a	0.328
$(D'_{15}/d'_{85})_{min}$	7.46	7.46	7.46	7.46	7.56	7.56
Stability Index $(H/F)_{min}$	0	0	0	0	0.57	0.57
i_{cr} in test	0.3-0.35	0.3-0.4	0.2-0.25	0.9	n/a	0.26
Stability	suffusion	suffusion	suffusion	suffusion	suffusion	suffusion

Table 5.5: UBC vs. UC summary test data for G40FF tests.

	UBC	**UC**		
Sample	40% FF	G40FF-1	G40FF-2	G40FF-3
Top Stress/Surcharge, kPa	0	0	0	0
Porosity, *n*	0.26	0.273	0.273	0.273
D_{15} mm	0.1425	0.5	0.5	0.5
$C_u = (D_{60}/D_{10})$	10.13	10.8	10.8	10.8
Permeability, *k* cm/s	0.018	n/a	0.013	0.021
$(D'_{15}/d'_{85})_{min}$	7.46	7.56	7.56	7.56
Stability Index $(H/F)_{min}$	0	0	0	0
i_{cr} in test	1	0.52	0.56	0.34
Stability	suffosion	suffosion	suffosion	suffosion

Table 5.6: UBC vs. UC summary test data for 100%FF and G100FF tests.

	UBC	**UC**	
Sample	100% FF	G100FF - loose	G100FF - compact
Top Stress/Surcharge, kPa	0	0	0
Porosity, *n*	0.26	0.496	0.448
D_{15}, mm	0.129	0.468	0.468
$C_u = (D_{60}/D_{10})$	1.24	1.31	1.31
Permeability, *k* cm/s	0.012	0.015	0.032
$(D'_{15}/d'_{85})_{min}$	1.06	1.09	1.09
Stability Index $(H/F)_{min}$	E	E	E
i_{cr} in test	0.905-0.95	0.56	0.71
Stability	fluidisation (global)	fluidisation (global)	fluidisation (global)

5.4 Skempton and Brogan (1994) Replications

Results from replicated Skempton and Brogan (1994) samples A, B and D are presented in this section. The corresponding glass PSDs have been named GS&B-A, GS&B-B and GS&B-D.

An analysis to evaluate the likely stability of each PSD was undertaken prior to testing each material. The Kenney and Lau (1985) approach (Figure 5.20) shows GS&B-A as 'unstable', GS&B-B falls just within the 'unstable' zone, and GS&B-D as 'stable'. Applying the Kezdi (1979) approach, all three PSDs have values beyond the recommended value of 4-5 for stable filters. GS&B-D had the lowest $(D'_{15}/d'_{85})_{max}$ value of 7.15, while GS&B-A had the highest value with $(D'_{15}/d'_{85})_{max}$ of 14.91. The Burenkova (1993) formula suggests that all GS&B-A and GS&B-B and GS&B-D are unstable, while GS&B-D is close to being within the 'stable area' as shown in Figure 5.21. Plotting the samples using the Wan and Fell (2008) method for analysis (Figure 5.22), GS&B-A falls right on the boundary of the 'unstable zone' and 'transition zone', while GS&B-B is in the 'transition zone' and GS&B-D in the 'stable zone'. Finally, applying the Istomina (1957) boundaries to the uniformity coefficient, C_u, GS&B-A is not self filtering, while GS&B-B and GS&B-D are self filtering. Void ratio and porosity values for each sample are presented in Table 5.7, along with a summary of the above analyses.

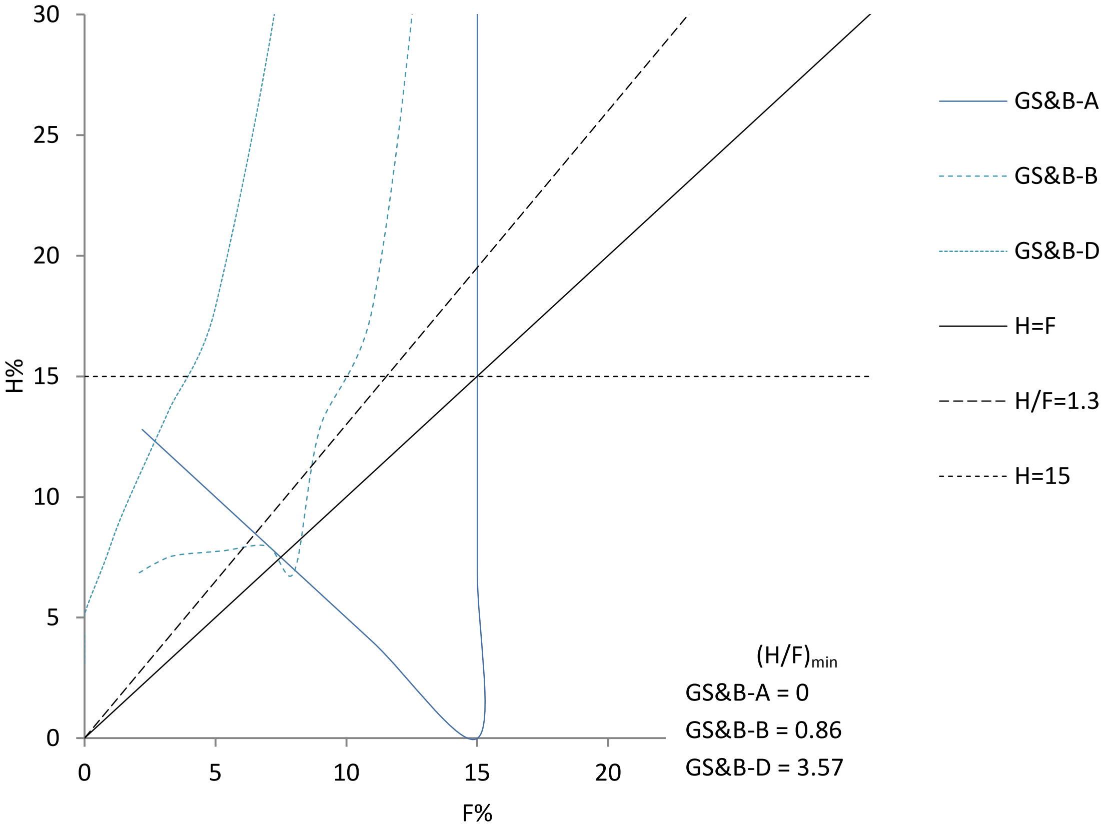

Figure 5.20: Kenney and Lau (1985) diagrams for GS&B-A, GS&B-B and GS&B-D materials.

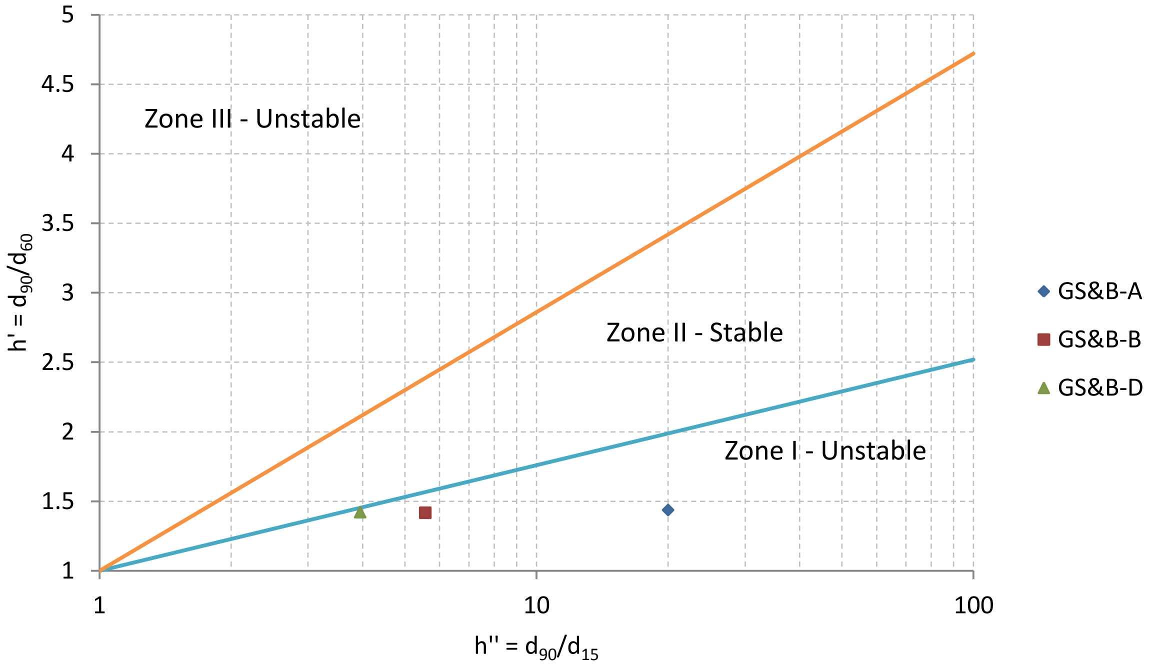

Figure 5.21: Burenkova (1993) plot showing predicted stability of GS&B-A, GS&B-B and GS&B-D materials.

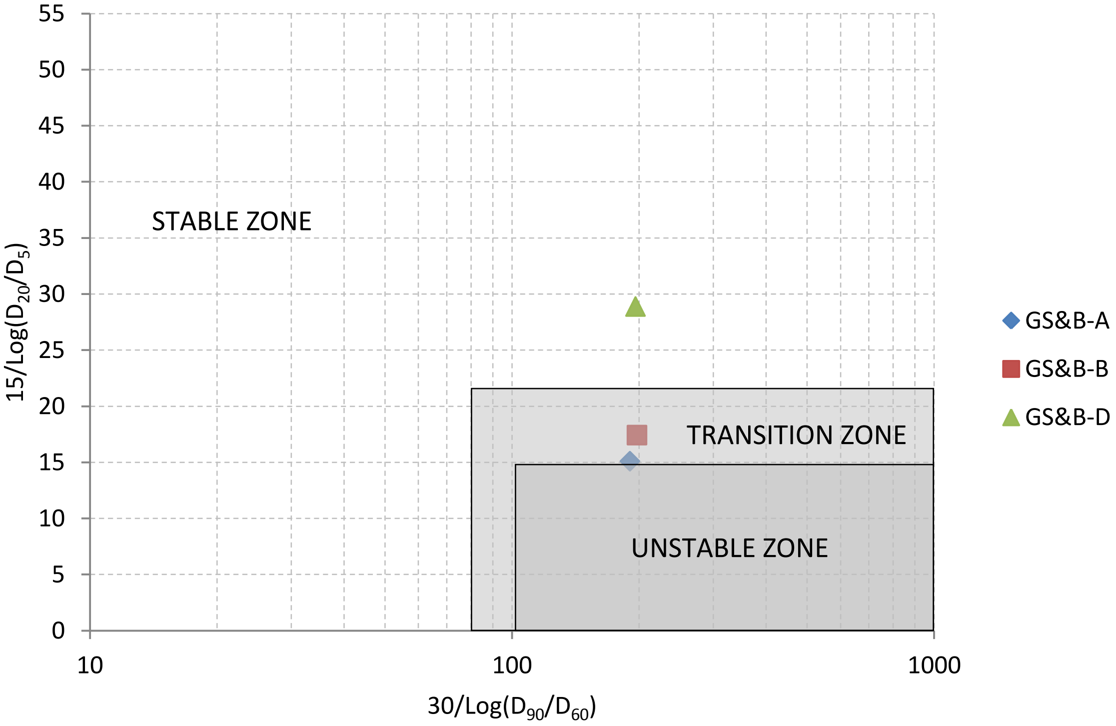

Figure 5.22: Wan and Fell (2008) approach to stability analysis for GS&B-A, GS&B-B and GS&B-D materials.

Table 5.7: Summary PSD analysis and theoretical critical hydraulic gradient for GS&B-A, GS&B-B and GS&B-D materials.

	GS&B-A	**GS&B-B**	**GS&B-D**
Kenny and Lau, $(H/F)_{min}$	0 (unstable)	0.86 (unstable/boundary)	3.57 (stable)
Kezdi, $(D'_{15}/d'_{85})_{min}$	1.15	1.19	1.13
Kezdi, $(D'_{15}/d'_{85})_{max}$	14.91	9.61	7.15
Burenkova	Unstable	Unstable	Unstable
Wan and Fell	Transition Zone	Stable Zone	Stable Zone
$C_u = (D_{60}/D_{10})$	19.13 (transition condition)	8.05 (self filtering)	4.03 (self filtering)
i_c	0.898	0.873	0.875

Table 5.8: Void ratio and porosity of GS&B-A, GS&B-B and GS&B-B materials.

	Void Ratio, e	Porosity, *n*
GS&B-A	0.37	0.27
GS&B-B	0.41	0.29
GS&B-D	0.41	0.29

5.4.1 GS&B-A

Sample GS&B-A was a gap-graded, highly unstable sandy gravel with $(H/F)_{min} = 0$. The sample had a porosity $n = 0.27$. The $(D'_{15}/d'_{85})_{max}$ was 14.91, and the uniformity coefficient, C_u $(D_{60}/D_{10}) = 19.13$, indicating the sample was not self filtering. The total dry weight of the sample was 2197.04 g and the theoretical critical hydraulic gradient was $i_c = 0.898$.

Pre-test slices (Figure 5.23) show that there were open voids present throughout the sample, however there was a higher proportion along the edges of the permeameter. There also appears to have been a band of open void space along the width of the specimen, approximately 3-4 cm from the bottom.

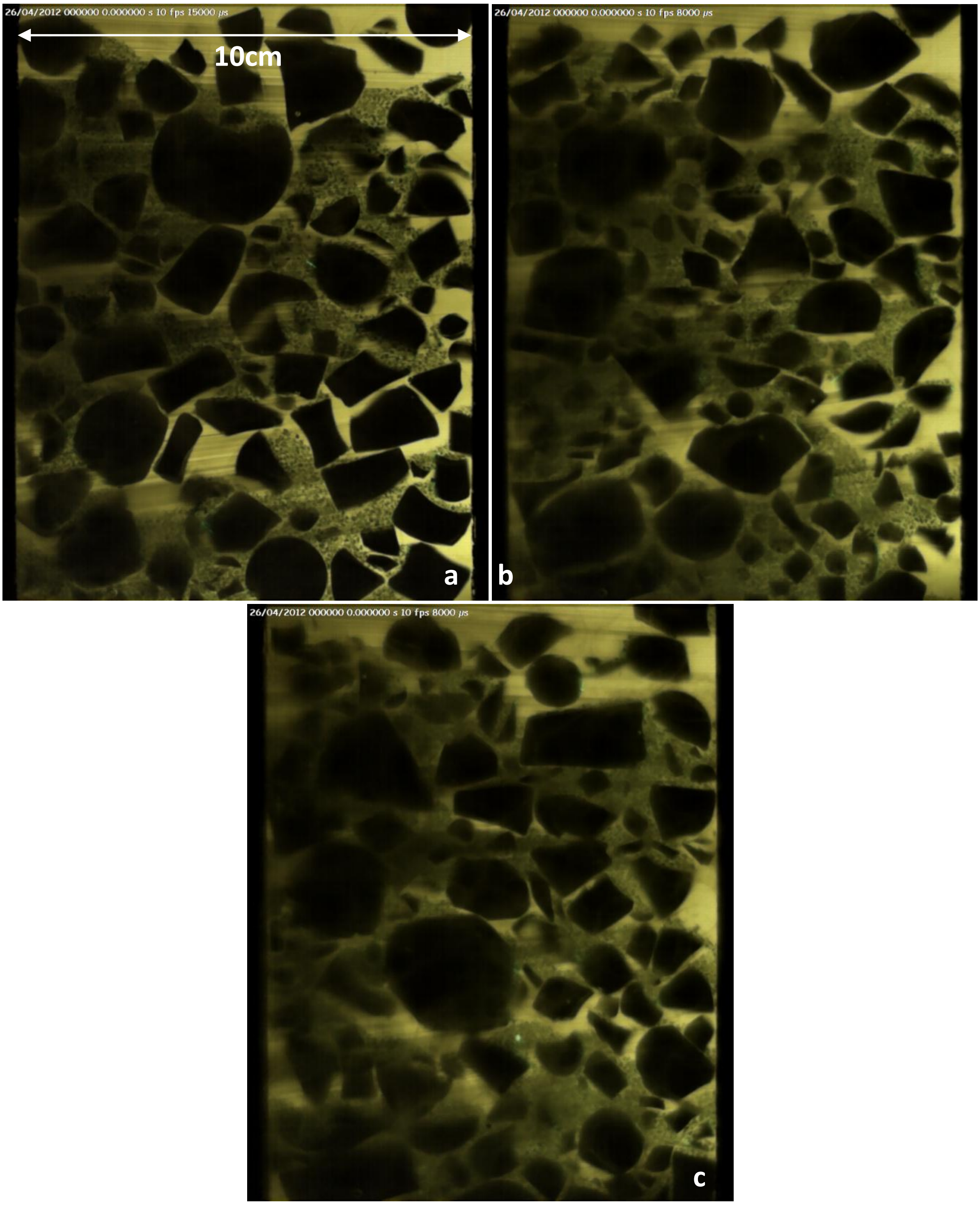

Figure 5.23a-c: Pre test slices of sample GS&B-A at a) 1 cm; b) 2 cm and; c) 3 cm from front of apparatus.

In the test (Figure 5.24) the following stages of development were observed.

a) At i_{av} = 0.153 there was a slight movement of fines in void spaces, both along the glass edges and within the sample upon first applying gradient. Particles stabilised after approximately 30 seconds. The permeability was constant up to the point where k = 0.26 cm/s. Figure 5.25a-b shows the change in structure from i_{av} = 0 to 0.153.

b) At i_{av} = 0.23 there was a break in laminar flow, with an increase in i_{av} vs. v slope.

c) At i_{av} = 0.248 to 0.286, fines began to slowly move upwards through the sample, and 'dancing-like' movements were seen in some voids. At i_{av} = 0.276 the permeability k = 1.6 cm/s (Figure 5.26).

d) At i_{av} = 0.286 strong general piping initiated throughout the sample and fines migrated up through the sample, while gravel particles remained undisturbed. There was an increase in flow velocity gradient against hydraulic gradient marking an increased permeability k = 3.29 cm/s (Figure 5.27).

e) Up to i_{av} = 0.381 strong general piping continued without the initiation of 'violent piping'.

Given that i_{cr} = 0.248, the alpha value, α = 0.276.

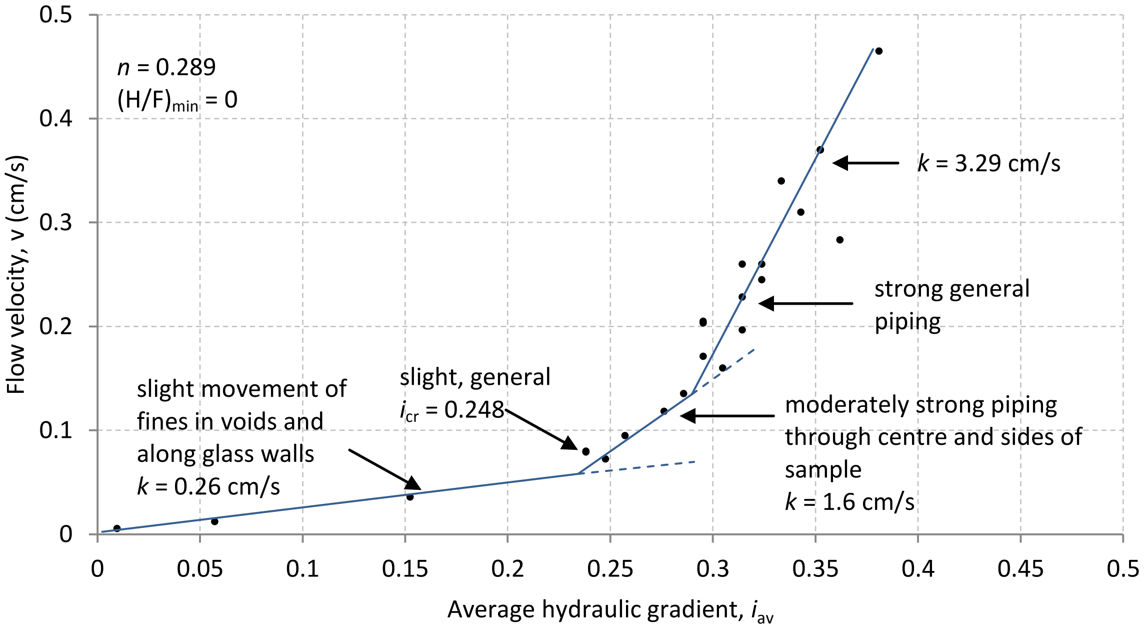

Figure 5.24: Average hydraulic gradient vs. flow velocity for GS&B–A.

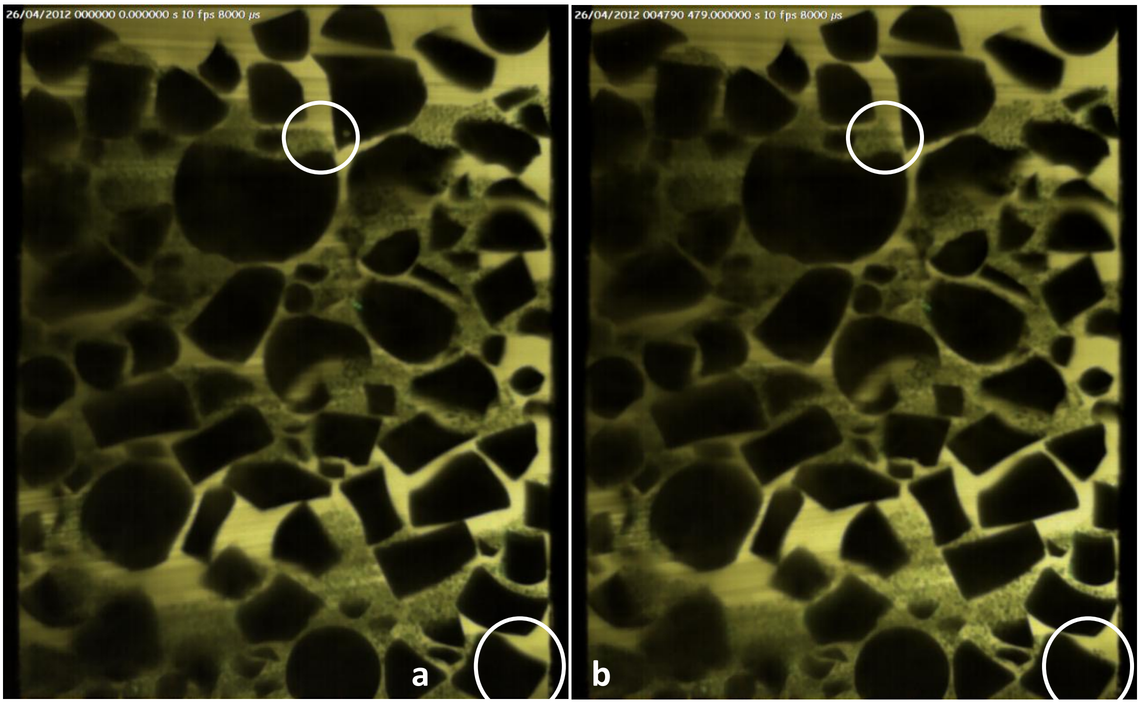

Figure 5.25a-b: Change in particle structure of Glass S&B-A between a) i_{av} = 0 and; b) i_{av} = 0.153. Note some changes highlighted with white circles where fines have migrated away.

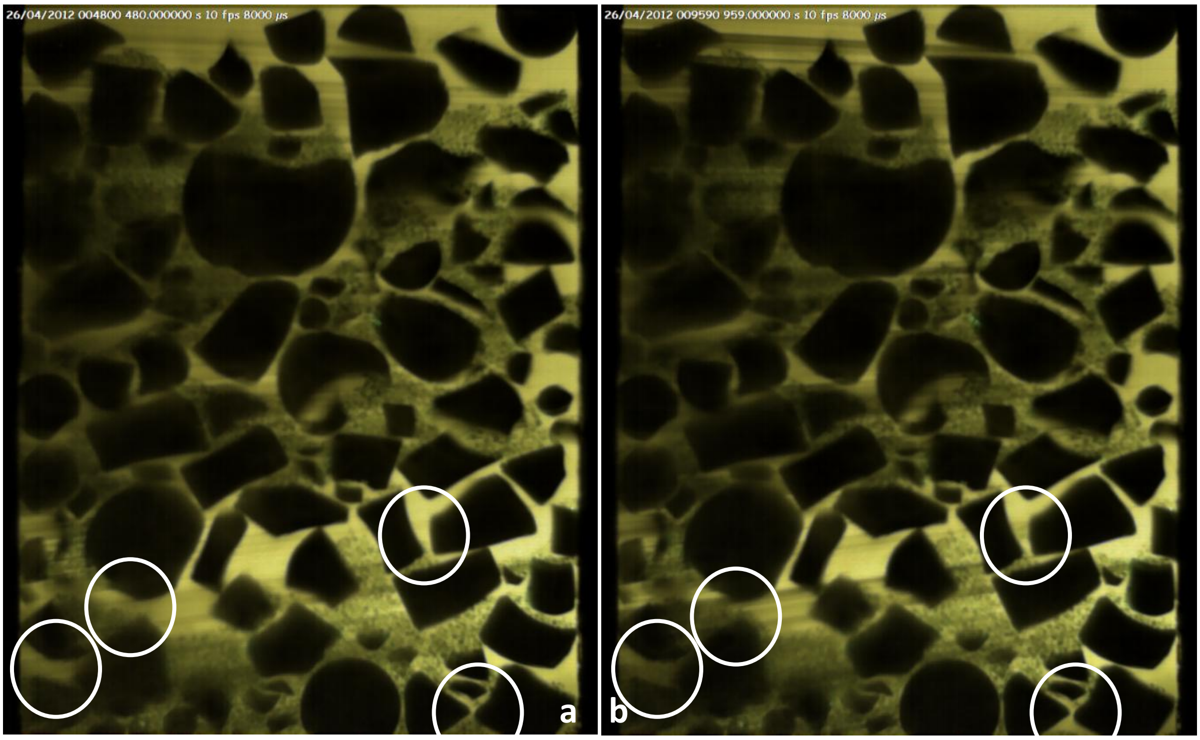

Figure 5.26a-b: Chances in particle structure of Glass S&B-A between a) i_{av} = 0.248 and; i_{av} =0.286. Note some changes highlighted with white circles.

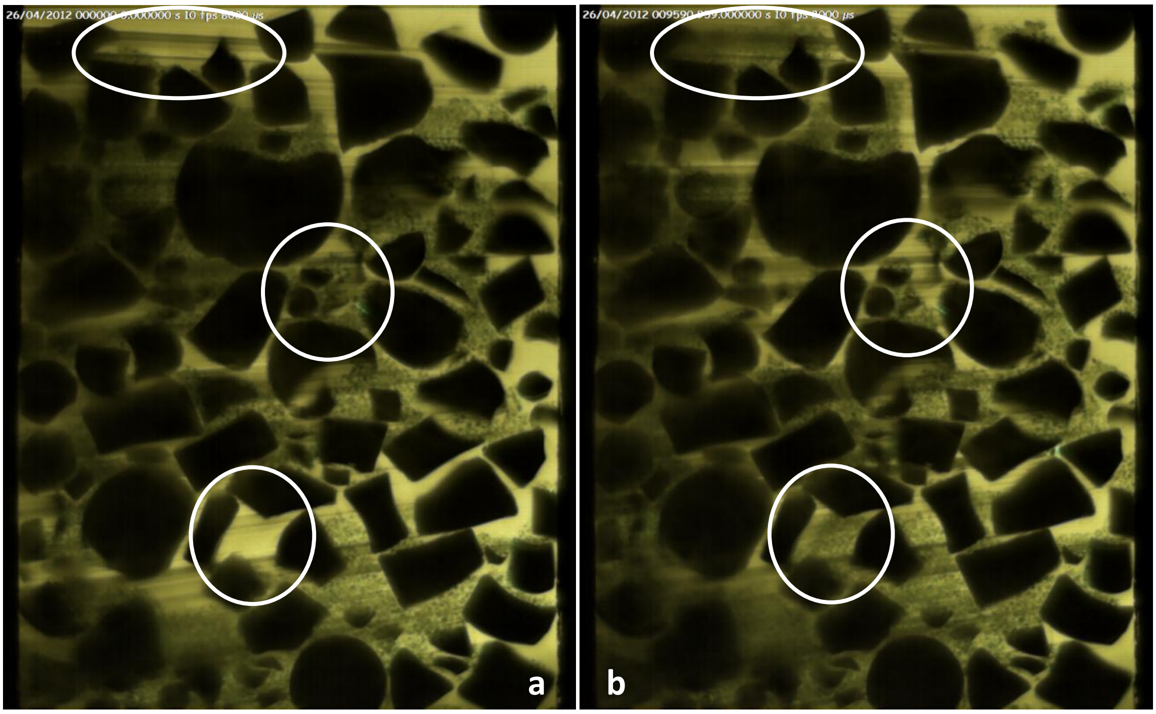

Figure 5.27a-b: Change in particle structure of GS&B-A between a) i_{av} = 0.286 and; b) i_{av} = 0.381, with a selection of changes highlighted in white where fines have migrated away.

5.4.2 GS&B-B

GS&B - B has a $(H/F)_{min}$ = 0.86, a $(D'_{15}/d'_{85})_{max}$ of 9.61, and a uniformity coefficient C_u (D_{60}/D_{10}) = 8.05. The sample was loosely packed, which can be seen in Figure 5.28, as there are void spaces throughout the sample. The porosity of the material was n = 0.289. This sample appears to lie just within the boundary of stability, and depending on the packing density, could have the potential to be unstable. The theoretical critical hydraulic gradient was i_c = 0.873.

In the test (Figure 5.29), the following was observed.

a) From i_{av} = 0.1 to 0.157 there was a slight movement of fine particles in some void spaces of the sample (Figure 5.30). The permeability was k = 1.0 cm/s.
b) From i_{av} = 0.229 to 0.5 there was an increase in gradient between i_{av} and v. At i_{av} = 0.229 there was an increase in the amount of fine particles moving in localised void spaces. At i_{av} = 0.3 a slight migration of fines initiated throughout voids in the sample, which increased at i_{av} = 0.386. The permeability during this time was k = 1.46 cm/s.
c) At i_{av} = 0.5 some of the coarser fraction made small readjustments in their structure, inside void areas. Finer particles continued to move also. These movements only occurred where void spaces were present, however. In other parts of the sample where there were few

voids, there was no noticeable particle movement, and these sections appeared stable (Figure 5.31).

d) At i_{av} = 0.621 to 0.879 the flow velocity became high, resulting in the oil becoming airated due to limitations in the equipment, which resulted in decreased image quality (Figure 5.32). At this hydraulic gradient, there was a continued movement of the some of the coarser fraction while fine fraction also continued to migrate upwards where possible. The permeability reduced to k = 0.72 cm/s, likely due to the intrusion of air bubbles.

e) At i_{av} = 1.014 the sample heaved (Figure 5.33).

Given the i_{cr} = 0.3, the alpha value is, α = 0.394.

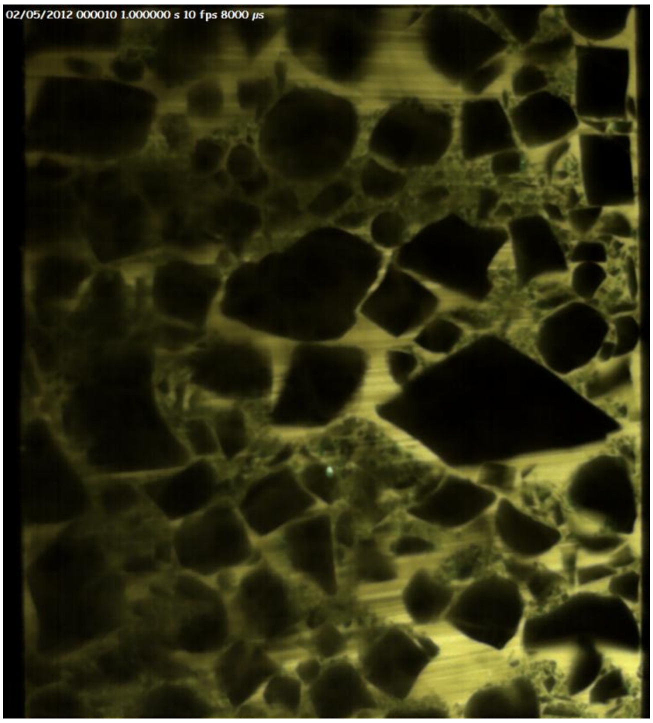

Figure 5.28: GS&B-B sample at beginning of test.

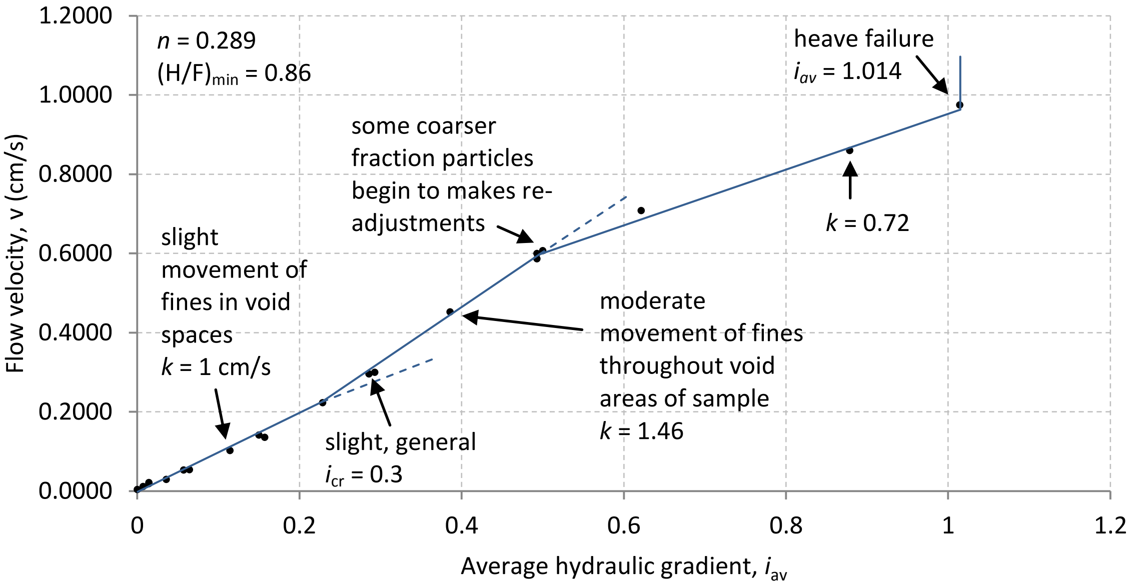

Figure 5.29: Average hydraulic gradient vs. flow velocity for GS&B-B.

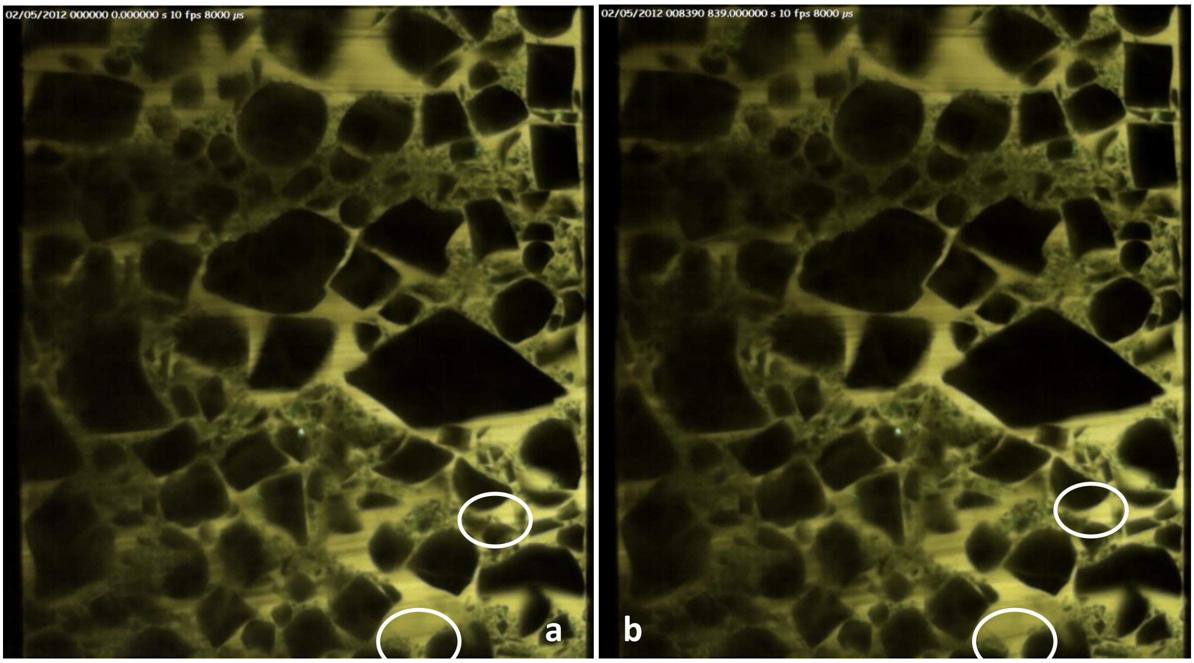

Figure 5.30: Minor changes in material structure in GS&B-B between a) i_{av} = 0.1 and b) i_{av} = 0.157 (some changes highlighted in white circles).

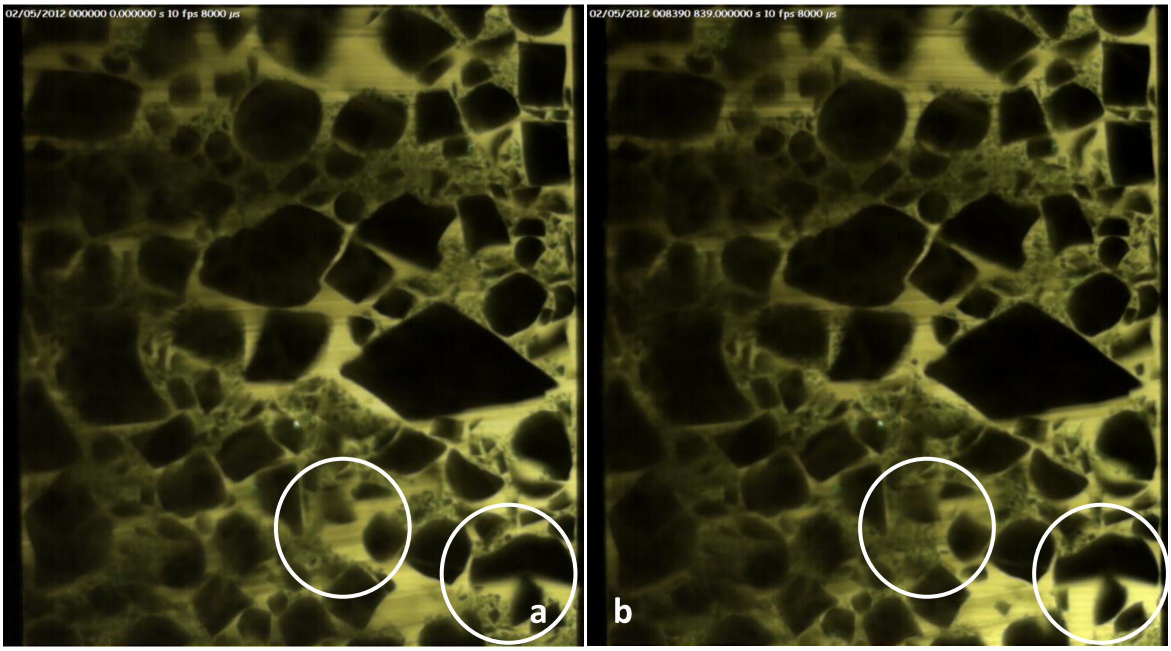

Figure 5.31: Changes in GS&B-B between a) $i_{av} = 0.229$ and; b) $i_{av} = 0.5$.

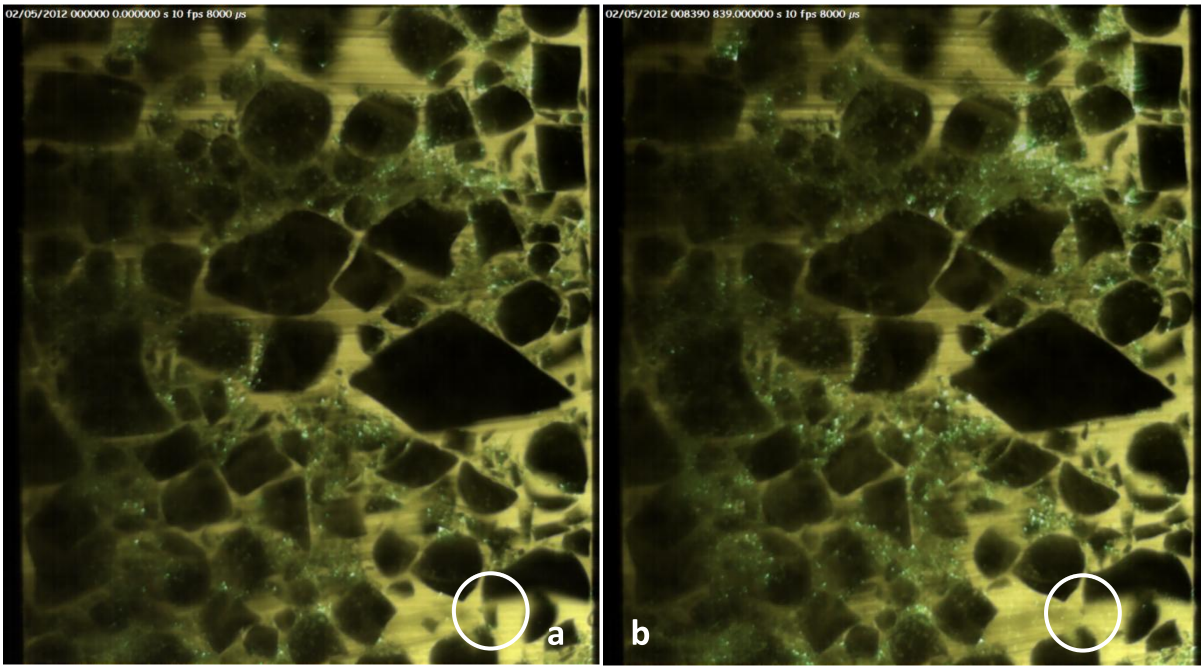

Figure 5.32: GS&B-B between a) $i_{av} = 0.621$ and; b) $i_{av} = 0.879$. Note air bubbles in oil degrading image quality.

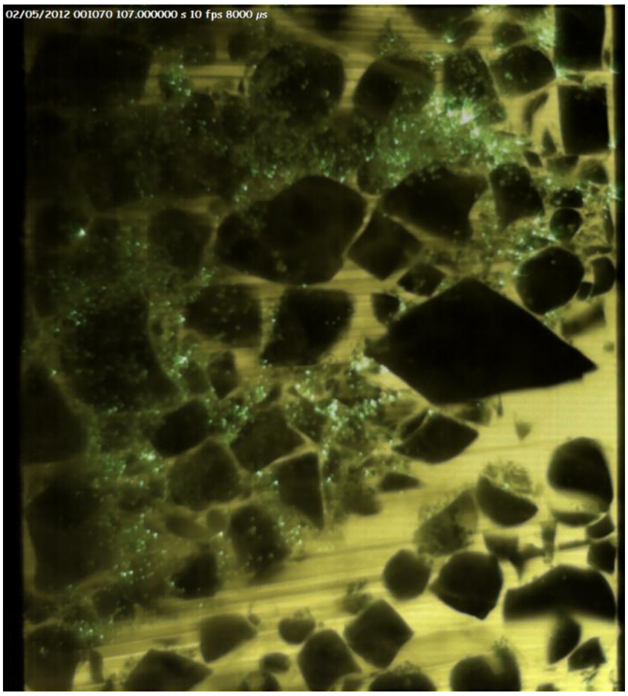

Figure 5.33: GS&B-B at i_{av} = 1.014 when the sample failed by 'heave'. 'Gap' in material shows where upper portion of sample has heaved.

5.4.3 GS&B-D

Sample GS&B-D was a well graded material with a $(H/F)_{min}$ = 3.57, a uniformity coefficient C_u (D_{60}/D_{10}) = 3.86 (self filtering), a $(D'_{15}/d'_{85})_{max}$ of 7.15 and a porosity of n = 0.289, all of which suggest that this sample would be stable. Test results confirmed this. Unfortunately the flow rate values in this test do not represent the true flow velocities within the material, as this test was carried out using a rotameter calibration that was later discovered to be underestimated. However, the calibration applied was close to linear, so the absolute flow velocity values can be used to show changes occurring within the material. The theoretical critical hydraulic gradient was i_c = 0.875.

The following observations were made during the test (Figure 5.34).

a) Up until i_{av} = 1.16, there were small translational and/or rotational movements in some of the finer grains in void spaces, generally underlying larger grains, where the upward flow presses smaller grains into the overlying larger grains. The specimen appeared very stable up to this point. During this time the permeability k = 0.147 cm/s.
b) Upon the next head rise to i_{av} = 1.33, the entire sample experienced an upward translation, or heave, of approximately 1 mm (Figure 5.35). The permeability during this time was k = 0.212 cm/s.

c) Up until i_{av} = 1.63, each subsequent raise in head lifted the entire specimen slightly higher, and it rose to a height of 6.8 mm above the steel frame compared to where it started.

d) At i_{av} = 1.63 the specimen lifts up to the top of the apparatus and particles fell from the base of the sample as turbulent flow under the sample initiated (Figure 5.36).

Given the critical hydraulic gradient, i_{cr} = 1.33, the alpha value was α = 1.52.

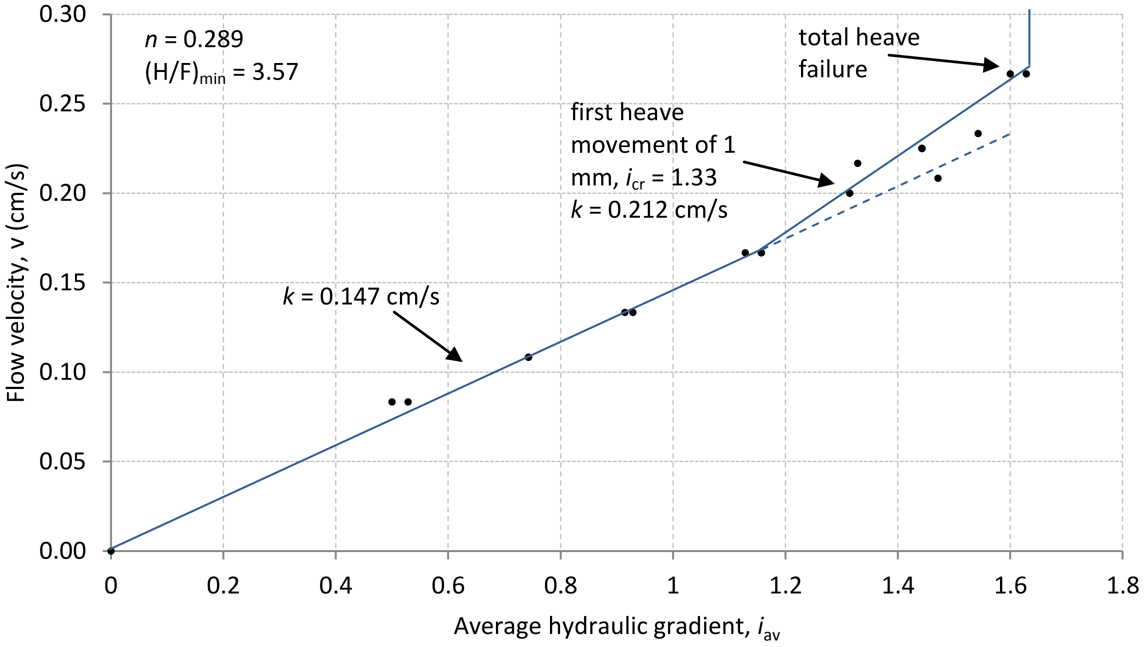

Figure 5.34: Average hydraulic gradient vs. flow velocity for GS&B–D.

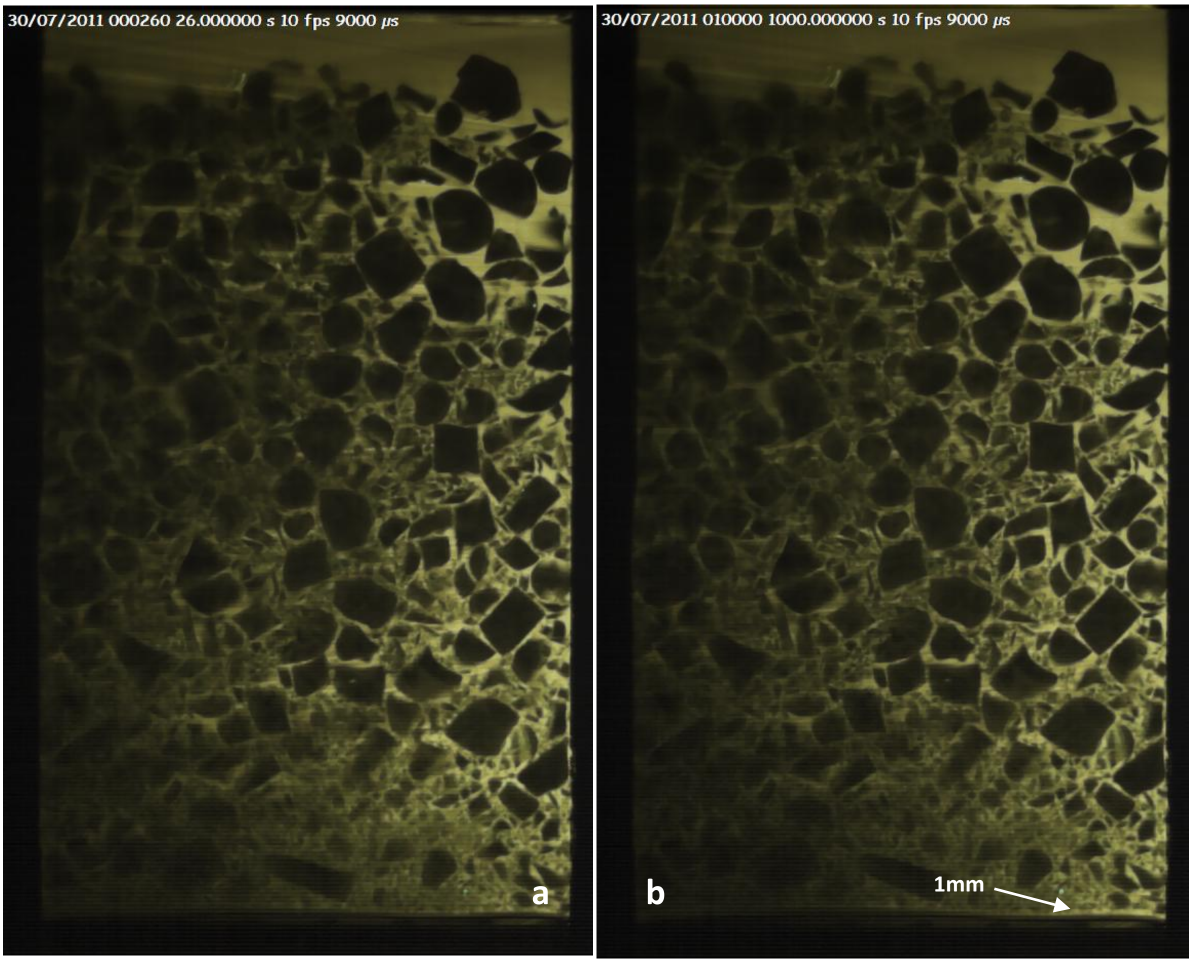

Figure 5.35: GS&B-D at, a) i_{av} =0.5 and; b) i_{av} = 1.33 when 'heave' first observed.

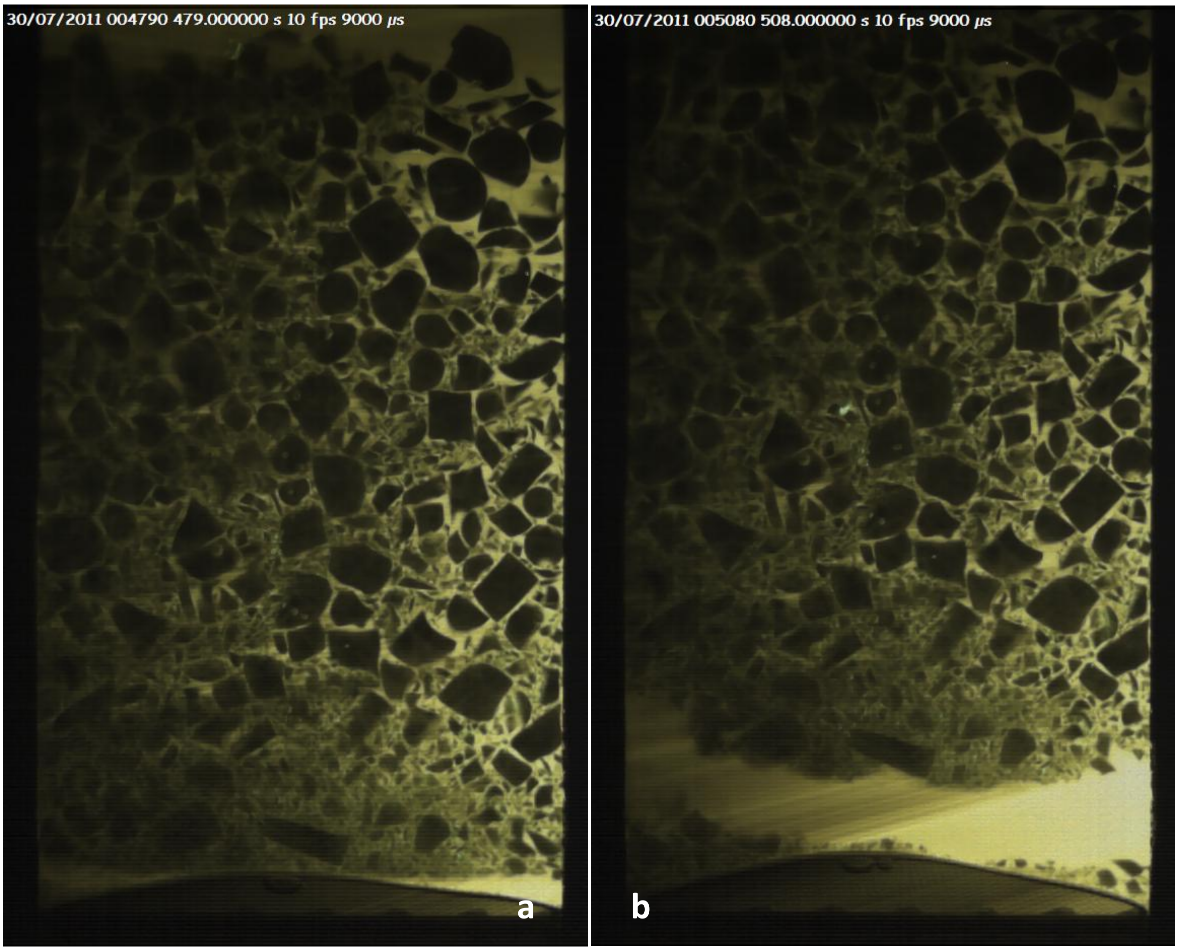

Figure 5.36: GS&B-D at a) i_{av} = 1.54 and; b) i_{av} = 1.63.

5.5 Skempton and Brogan Hybrid

Following tests on GS&B-A and GS&B-B samples, it was decided to create a 'hybrid' sample that would lie between the "A" and "B" PSD. The PSD of this GS&B-Hybrid sample is shown in Figure 5.37. Using the Kenney and Lau (1985) (Figure 5.38), Kezdi (1979), Burenkova (1993) (Figure 5.39) and Wan and Fell (2008) (Figure 5.40) analysis methods, the sample appears to be 'unstable', and the Istomina (1957) boundaries on the uniformity coefficient, C_u suggests the sample is not self filtering. A summary of the PSD analysis is shown in Table 5.9.

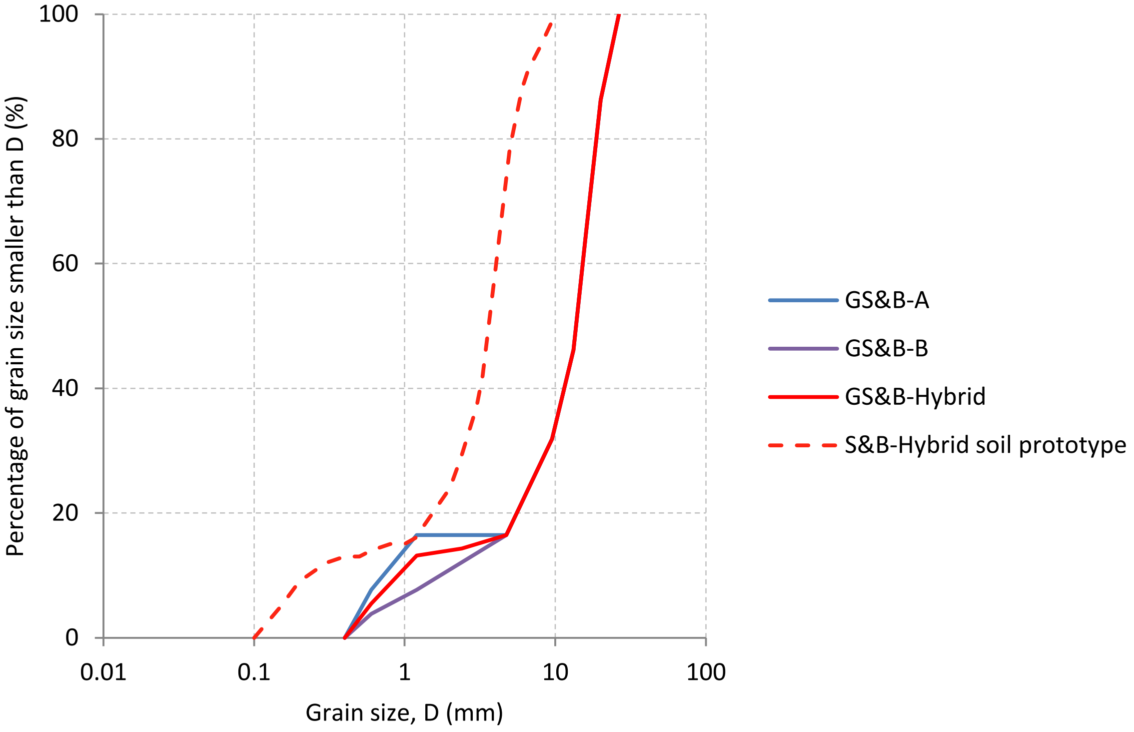

Figure 5.37: PSD of GS&B-Hybrid. Also shown is a 'prototype' soil PSD, in which the glass PSD is modelling.

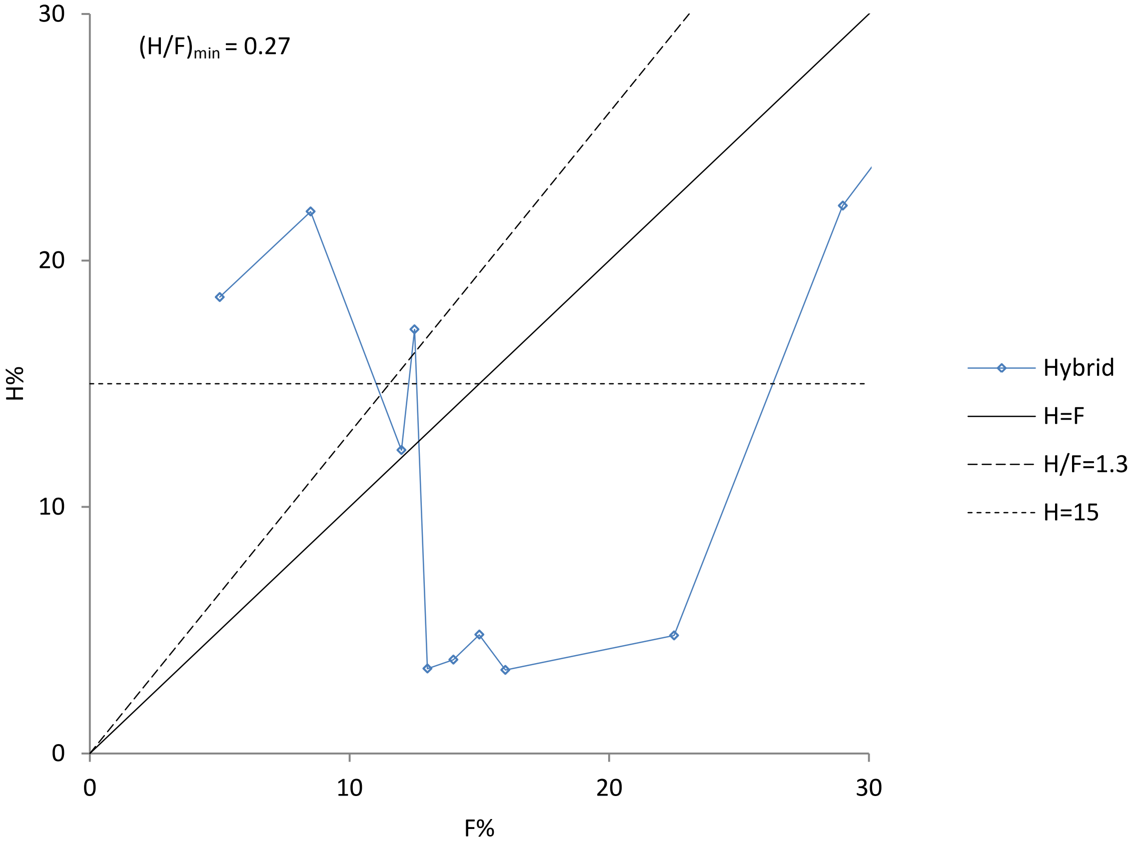

Figure 5.38: Kenny and Lau Analysis for GS&B-Hybrid.

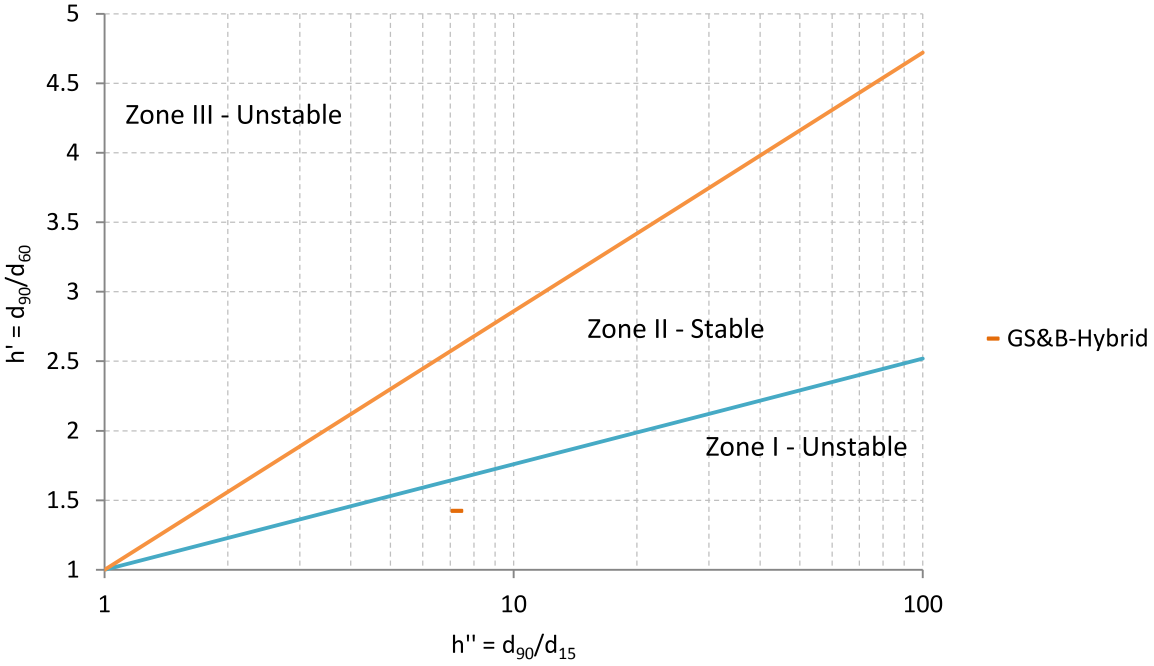

Figure 5.39: Burenkova (1993) plot for predicting stability of GS&B-Hybrid.

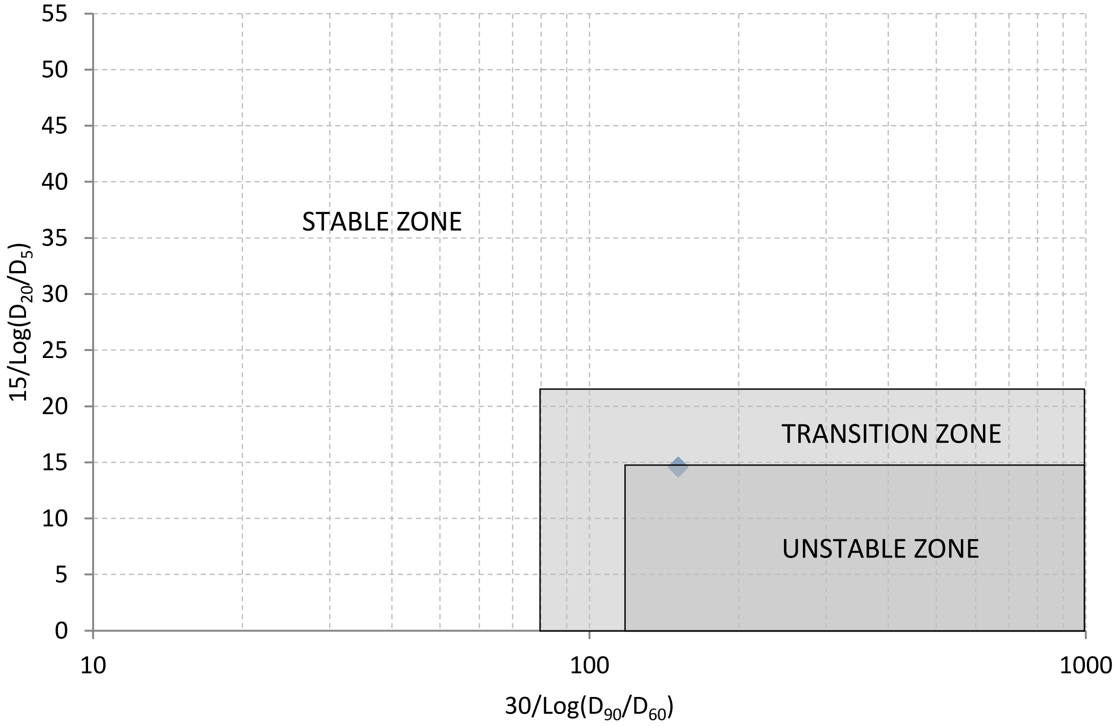

Figure 5.40: Wan and Fell Analysis for GS&B-Hybrid.

Table 5.9: Summary of PSD Analysis for GS&B-Hybrid.

	GS&B-Hybrid
Kenny and Lau, $(H/F)_{min}$	0.27 (unstable)
Kezdi, $(D'_{15}/d'_{85})_{min}$	1.17
Kezdi, $(D'_{15}/d'_{85})_{max}$	9.95
Burenkova	Unstable
Wan and Fell	Unstable Zone
$C_u = (D_{60}/D_{10})$	15.3 (transition condition)
i_c	0.883

Sample GS&B-Hybrid has a uniformity coefficient, C_u (D_{60}/D_{10}) of 16.2, a $(H/F)_{min}$ = 0.27 and a porosity n = 0.282. The maximum filter ratio of the components $(D'_{15}/d'_{85})_{max}$ was 9.95, hence was expected to be 'unstable'. The total dry weight of the sample was 2202.62 g and the theoretical hydraulic gradient was i_c = 0.883.

Pre test slices (Figure 5.41) show all slices to have areas with open void spaces where the fines have not filled the spaces. Typically voids will occur underneath larger particles and along the glass walls of the permeameter.

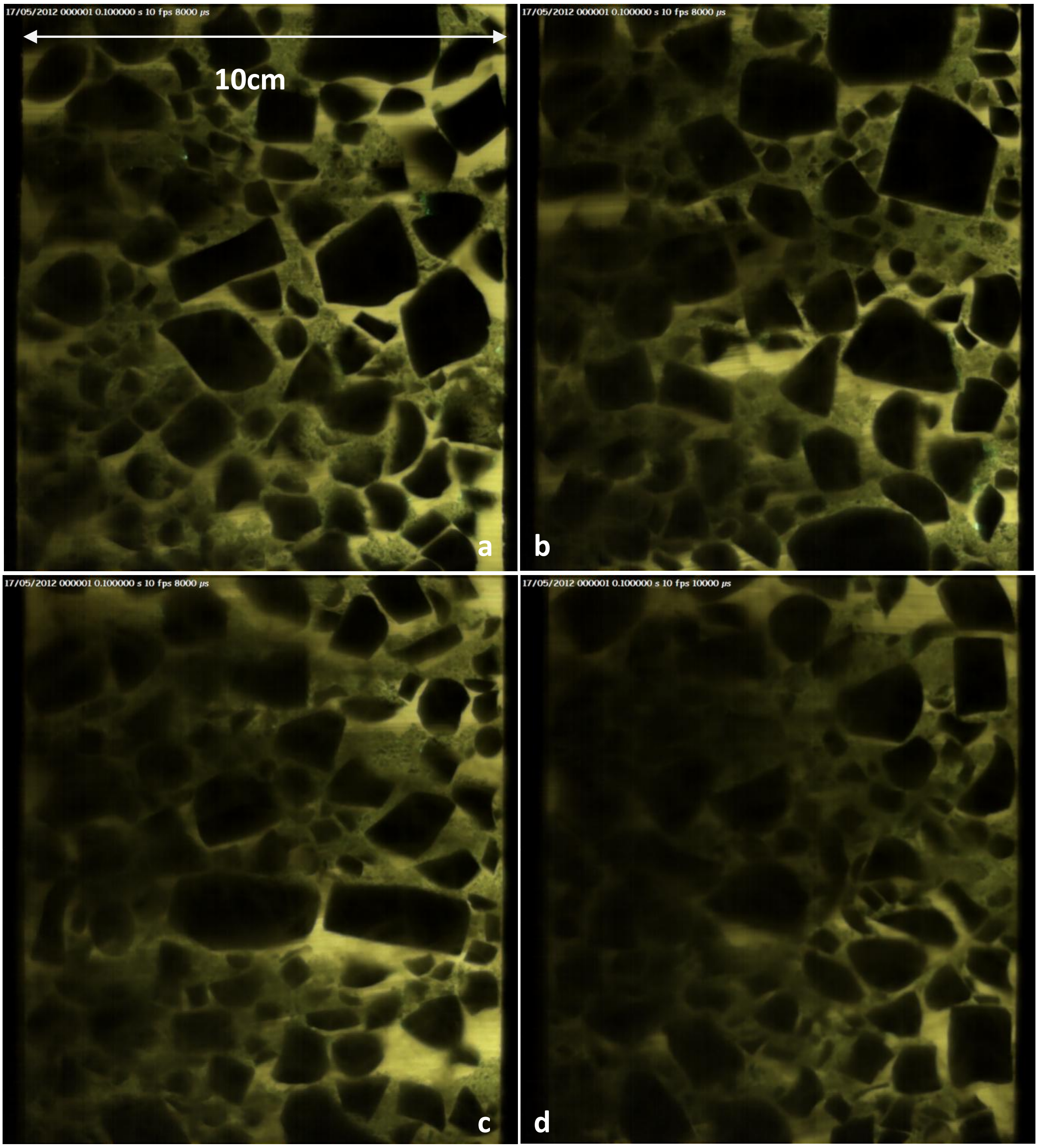

Figure 5.41: Pre test slices of GS&B-Hybrid at a) 1 cm; b) 2 cm; c) 3 cm and; d) 4 cm from front of apparatus.

For this test, a calibration dot target was setup along various points of the apparatus, prior to the placement of the glass material. These dots of known distances allowed a scale to be added to the images, which was also used for scaling during image processing, as described in Chapter 6. Figure 5.42 shows the calibration dots and the first image of the test, both positioned at the same distance of 15 mm from the front of the apparatus.

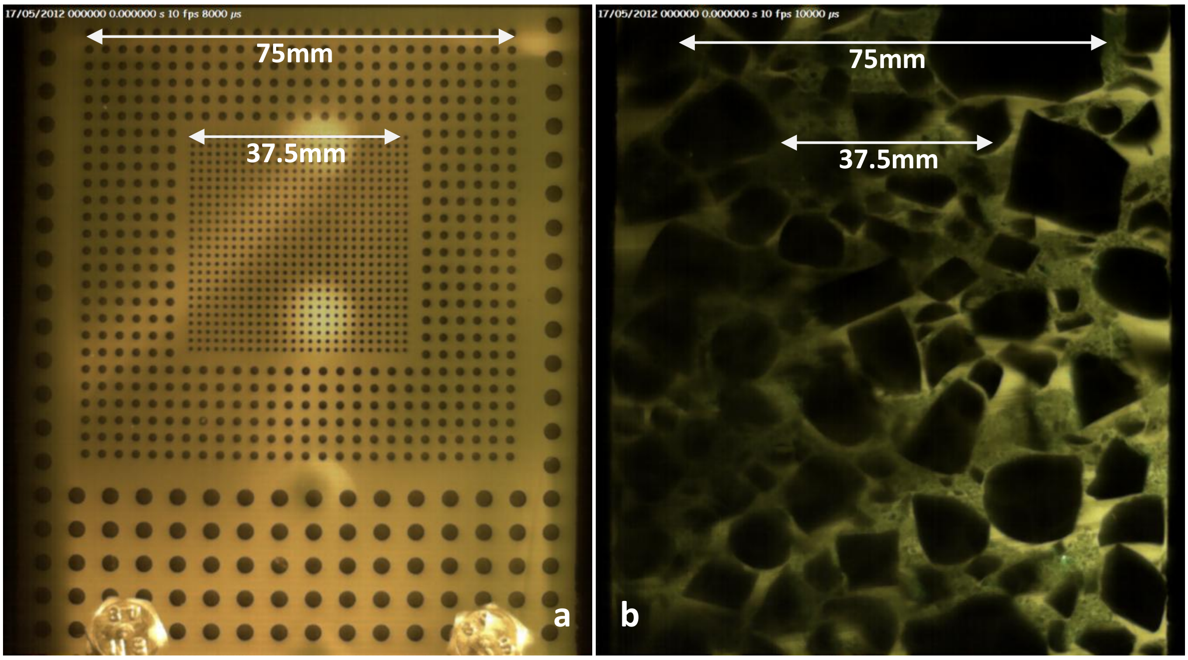

Figure 5.42: a) Calibration dots at 15 mm from front of permeameter, and; b) first test image, at 15 mm from front of permeameter.

In the test (Figure 5.43), the following was observed.

a) From i_{av} = 0 to i_{av} = 0.152 there was approximately laminar flow with a permeability of k = 0.50 cm/s. Small movements in fines were observed along the glass walls from i_{av} = 0.057. Figure 5.44 shows the change in structure during this time.

b) From i_{av} = 0.15 to i_{av} = 0.19 fines began to suffuse through the coarser clasts, leaving new void spaces within the material (Figure 5.45). This occurred throughout all parts of the sample.

c) At i_{av} = 0.19 there was an increase in slope between i_{av} vs. v giving a permeability of k = 1.17 cm/s. Fines continued to move throughout the sample, with some of the smaller, coarse grains making minor movements (Figure 5.46).

d) At i_{av} = 0.33 piping along the centre, front edge of the permeameter initiated, and a mound of fines began accumulating at the surface. Some of the smaller coarse fraction moved in void spaces as fines were 'washed' from the specimen (Figure 5.47). The gradient between i_{av} vs. v increased again and remained approximately linear until the test was terminated at i_{av} = 0.6. The permeability increased to k = 1.47 cm/s.

The critical hydraulic gradient in the test, i_{cr} = 0.15 leads to an alpha value of α = 0.170.

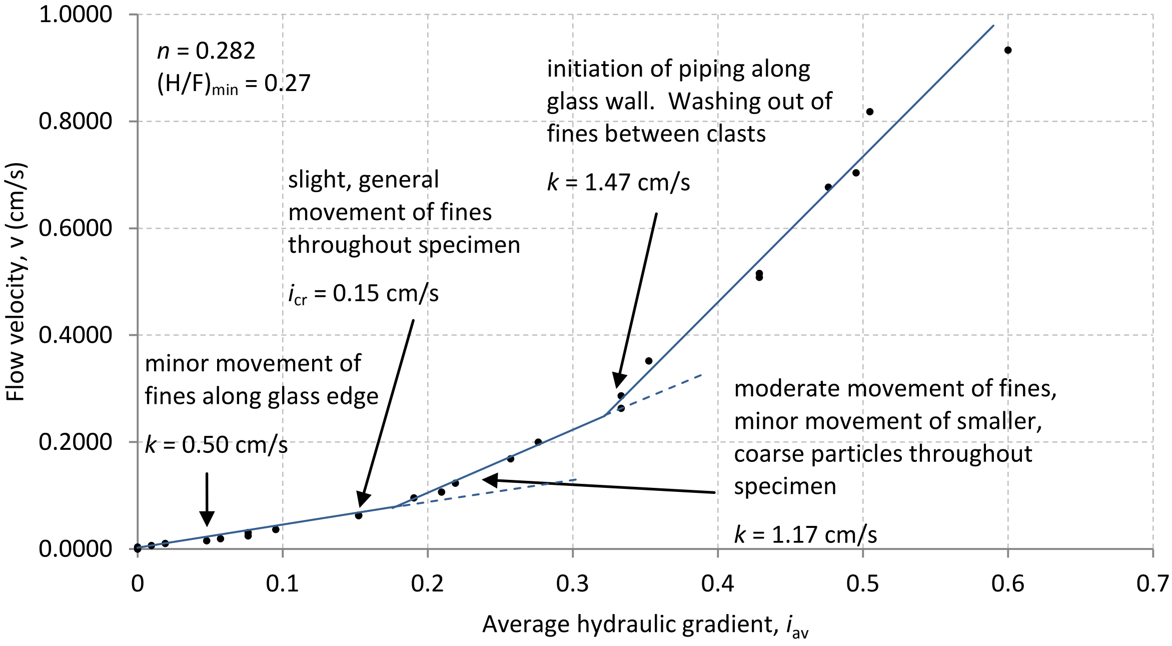

Figure 5.43: Average hydraulic gradient vs. flow velocity for GS&B-Hybrid.

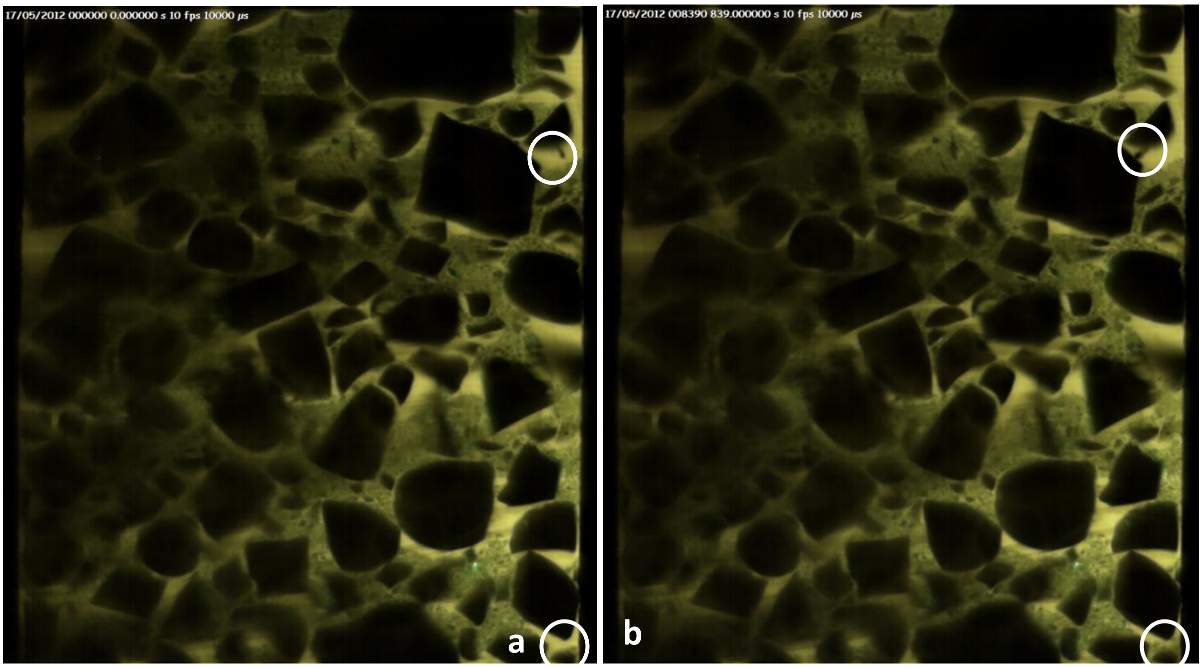

Figure 5.44: GS&B-Hybrid changes in structure between a) i_{av} = 0 and; b) i_{av} = 0.152.

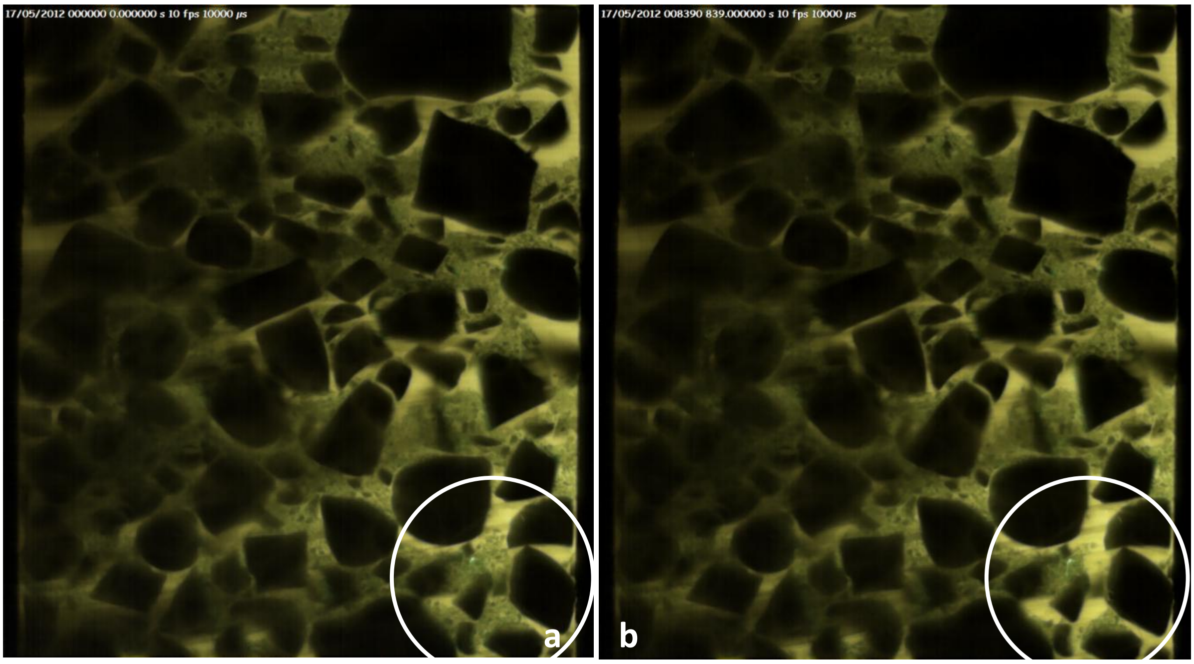

Figure 5.45: GS&B-Hybrid changes in structure between a) i_{av} = 0.152 and; b) i_{av} = 0.19.

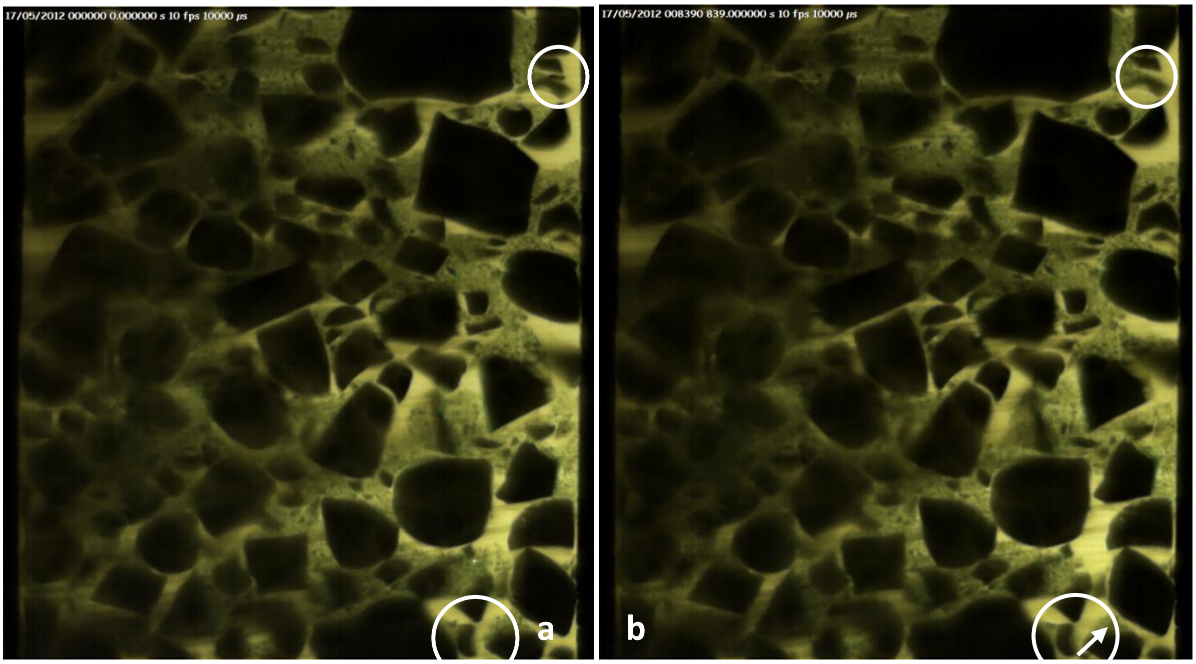

Figure 5.46: Change in particle structure of GS&B-Hybrid between a) i_{av} = 0.19 and; b) i_{av} =0.276.

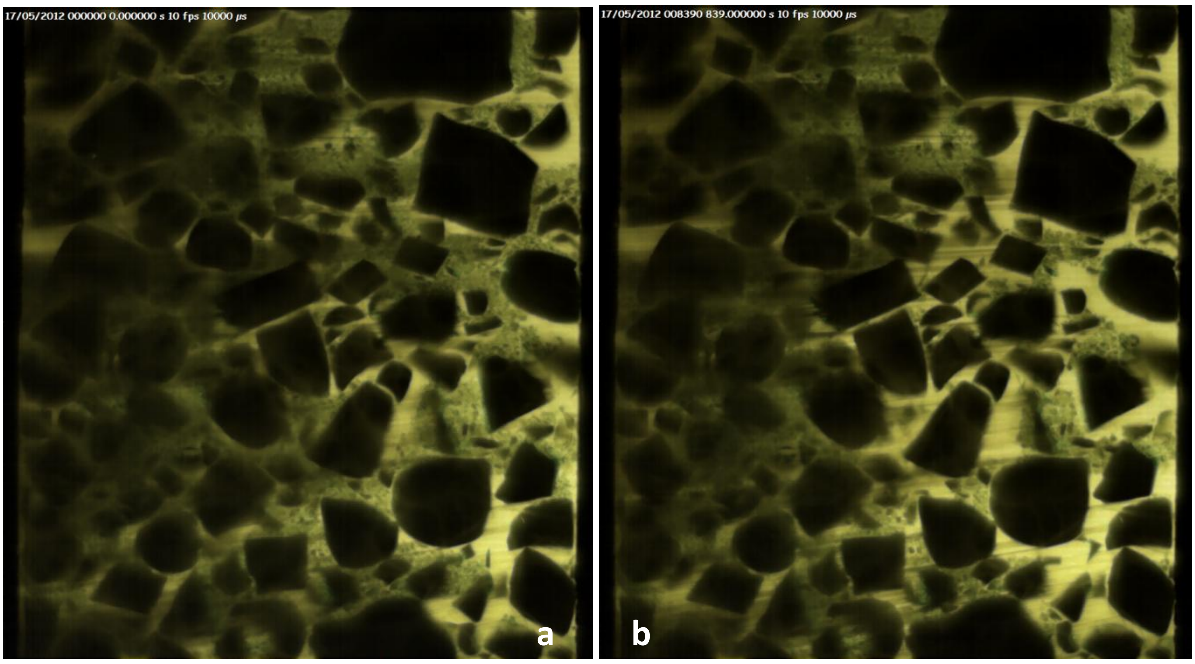

Figure 5.47: Change in structure of GS&B-Hybrid between a) i_{av} = 0.33 and; b) i_{av} = 0.6. Note washing out of fines.

Post-test slices (Figure 5.48) show that close to the glass wall of the permeameter (Figure 5.48a-b) there was a significant amount of washout of fine particles. In general, there was a reduction in washout further away from the front edge, where the pipe initiated.

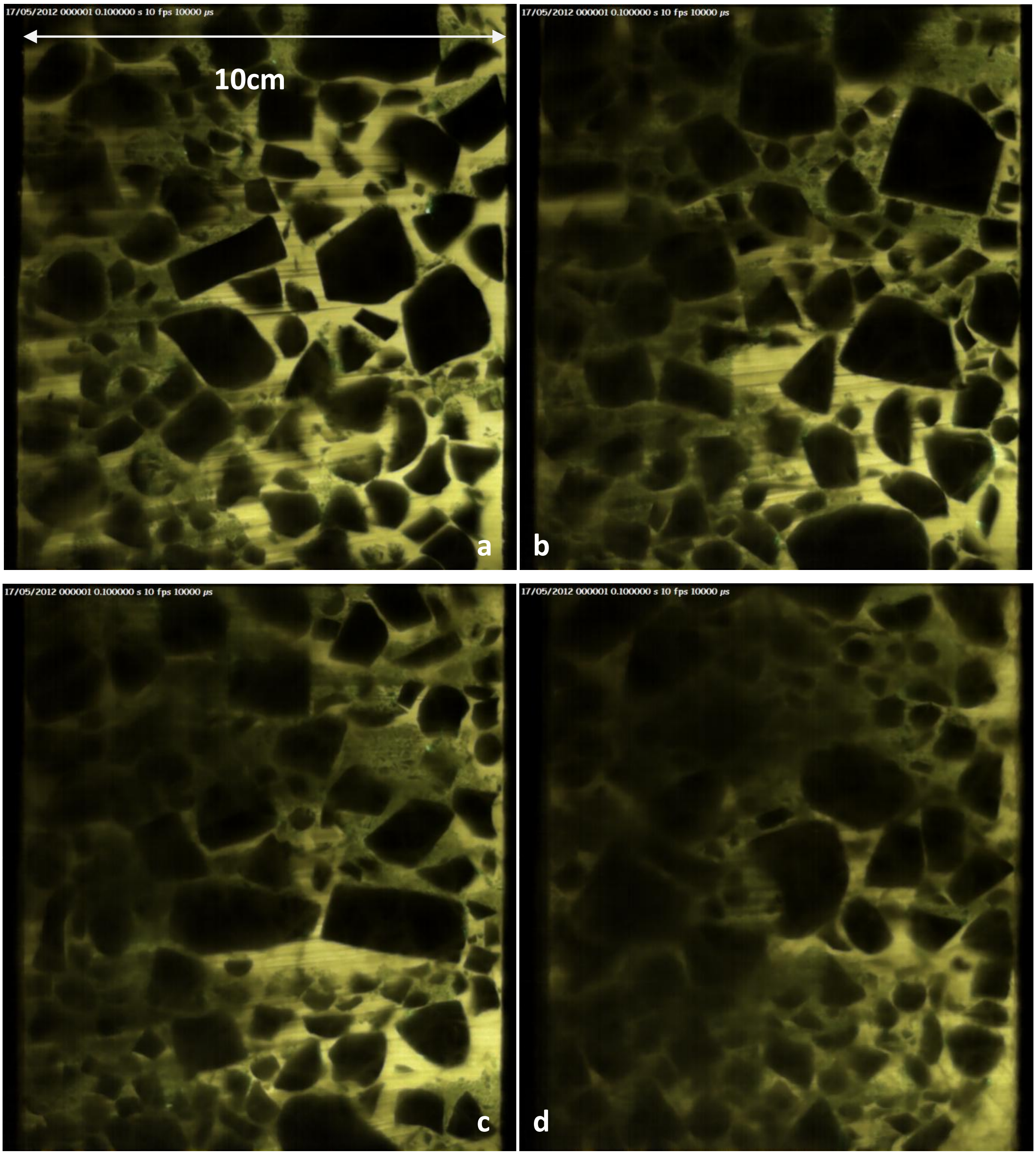

Figure 5.48: Post-test slices of GS&B-Hybrid at a) 1 cm; b) 2 cm; c) 3 cm and; d) 4 cm from front of apparatus.

5.6 Fannin and Moffat (2006) Replication

Results from replicated Fannin and Moffat (2006) sample G4-C are presented in this section. The corresponding glass PSD has been named GF&M-G4C. GF&M-G4C had a uniformity coefficient C_u = 11.67, a $(D'_{15}/d'_{85})_{max}$ = 6.66 and an $(H/F)_{min}$ = 0, which all points towards an unstable specimen. The Kenney and Lau (1985) analysis (Figure 5.49) and Burenkova (1993) analysis (Figure 5.50) gave this material to be unstable. Only the Wan and Fell (2008) approach (Figure 5.51) suggests the material is stable, however due to the sample having a gap grade between 1 mm and 4.72 mm, as shown in Figure 4.45 in Chapter 4.9.5, this approach is not valid (Wan & Fell 2008).

Table 5.10 summarises the PSD analysis results. The porosity was $n = 0.266$, while the sample weight was 2201.65 g. The theoretical hydraulic gradient was $i_c = 0.903$.

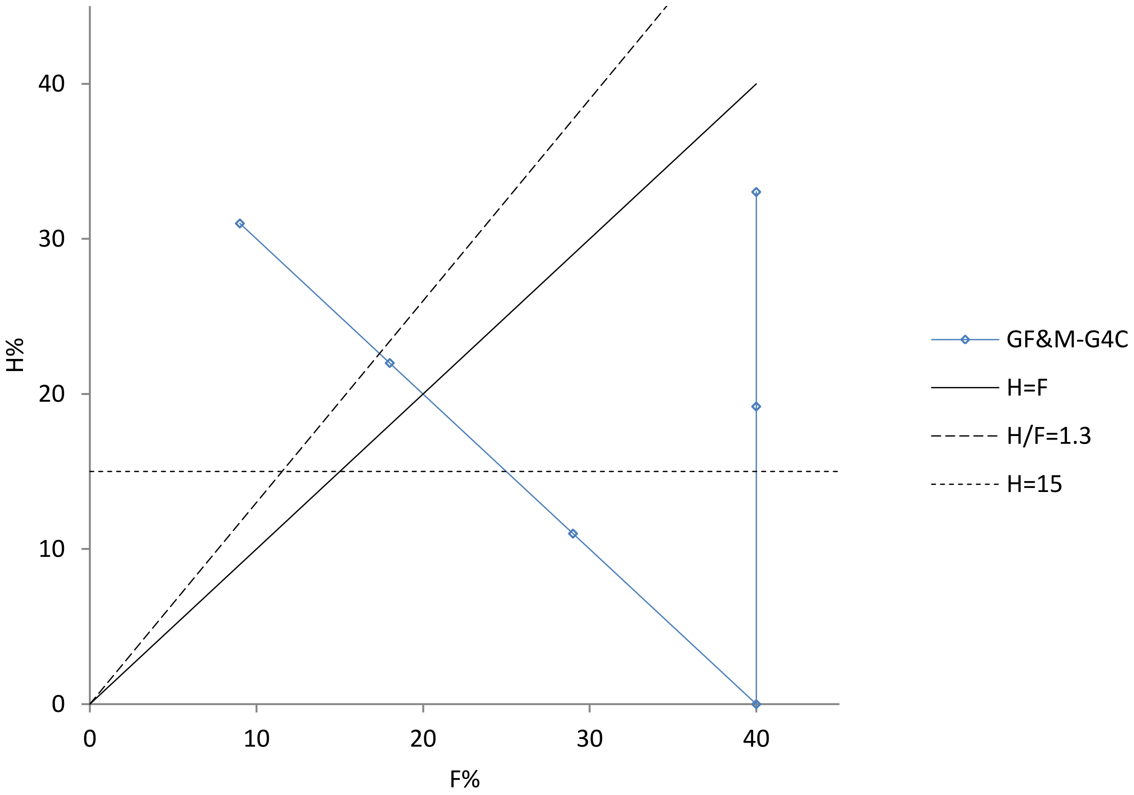

Figure 5.49: Kenney and Lau (1985) plot for GF&M-G4C.

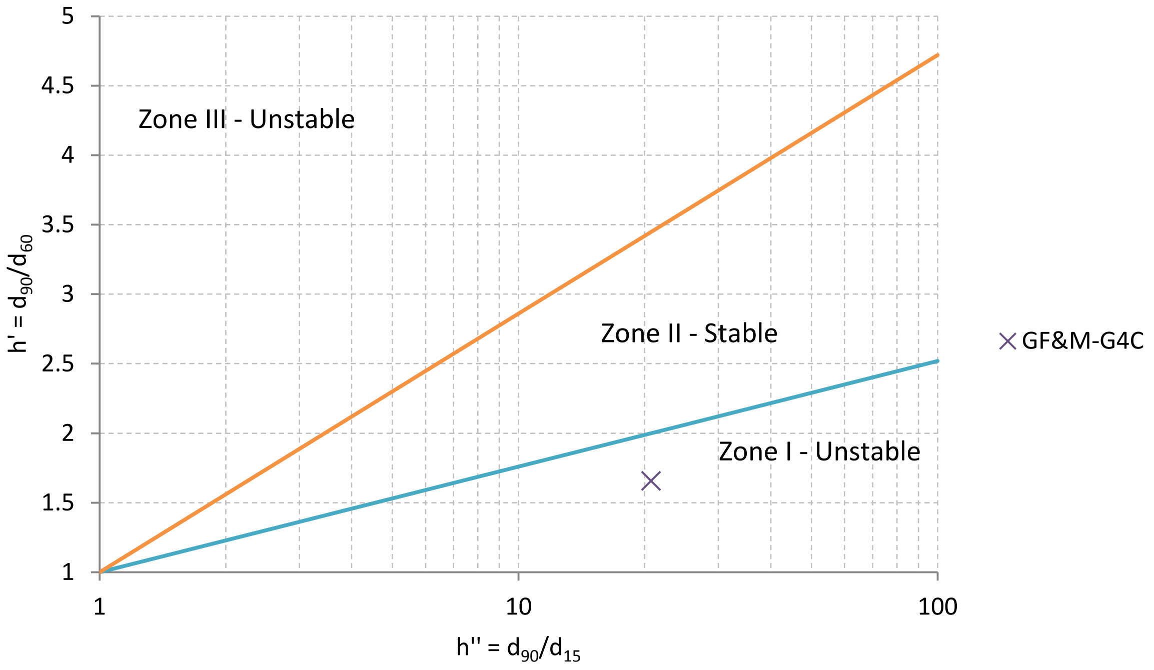

Figure 5.50: Burenkova (1993) plot for predicting stability of GF&M-G4C.

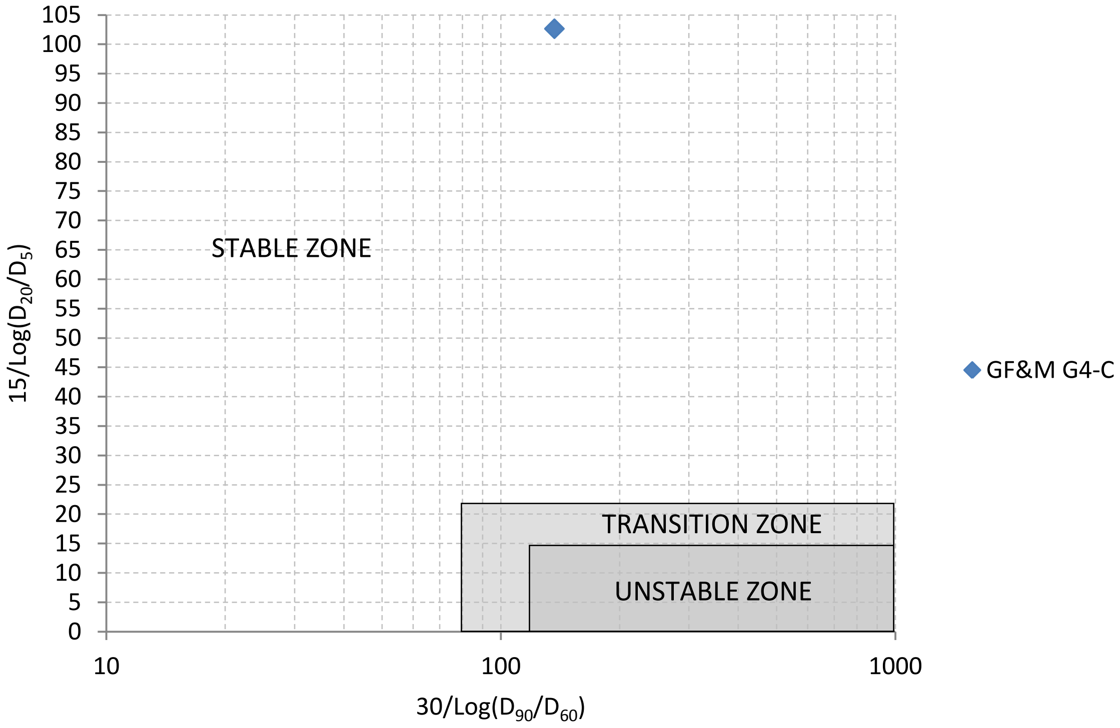

Figure 5.51: Wan and Fell approach to stability analysis for GF&M-G4C.

Table 5.10: Summary of PSD analysis for GF&M-G4C.

	GF&M-G4C
Kenny and Lau, $(H/F)_{min}$	0 (unstable)
Kezdi, $(D'_{15}/d'_{85})_{min}$	1.28
Kezdi, $(D'_{15}/d'_{85})_{max}$	6.66
Burenkova	Unstable
Wan and Fell	Stable Zone
$C_u = (D_{60}/D_{10})$	11.67 (not self filtering)

Observations from the test (Figure 5.52) show.

a) From $i_{av} = 0$ to $i_{av} = 0.40$ there was laminar flow according to Darcy's Law, and no movement of any particles observed. The permeability was $k = 0.023$ cm/s.

b) At $i_{av} = 0.5$ there was a small movement of some fines which moved into small voids, typically between two larger particles (Figure 5.53).

c) From $i_{av} = 0.58$ to $i_{av} = 0.72$ fines near the top of the sample began to move along the glass edges. There was a very slight increase in sample height as fines began to deposit at the top of the specimen, showing suffosion to be occurring (Figure 5.54).

d) Upon the next raise in head, the sample instantaneously failed by piping in the front left corner. In watching the sequence of images in succession as a 'movie', one can see the fines washing out of the sample, resulting in the collapse and consolidation of the coarser particles as the matrix supporting material is removed (ie suffosion). As failure initiated on the left side, the collapse first occurs on this side, but as the wash out of fines progresses over to the right side, it too collapses down. The fines are deposited at the top of the specimen in a mound. The sequence described here is shown in Video Appendix A, where the clip shows one hundred seconds of real time video footage over ten seconds.

Given the critical hydraulic gradient $i_{cr} = 0.72$, the alpha value was 0.798.

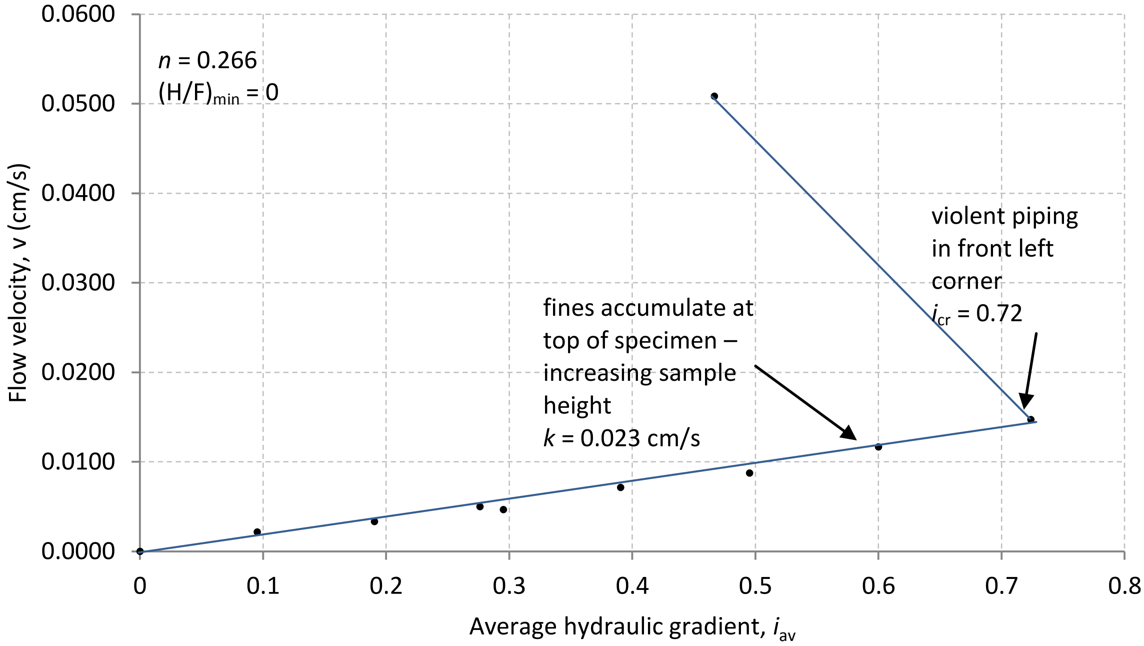

Figure 5.52: Average hydraulic gradient vs. flow velocity for GF&M-G4C.

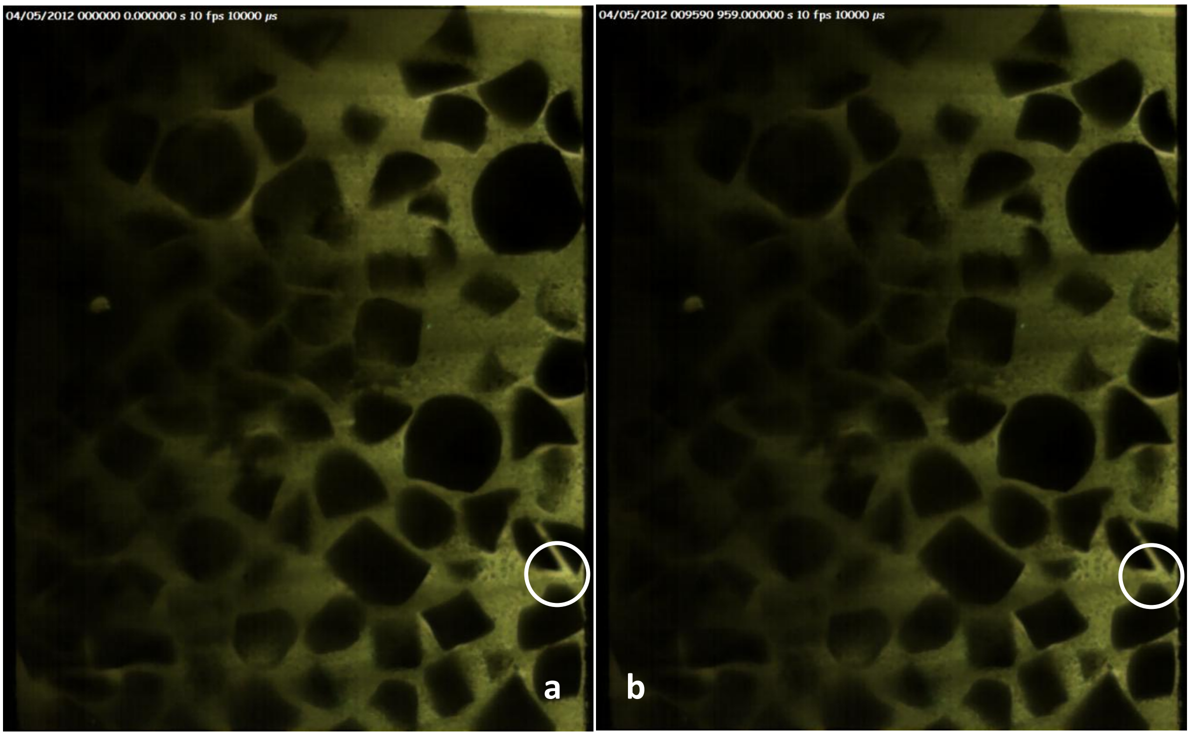

Figure 5.53: GF&M-G4C at a) i_{av} = 0 and; b) i_{av} = 0.5.

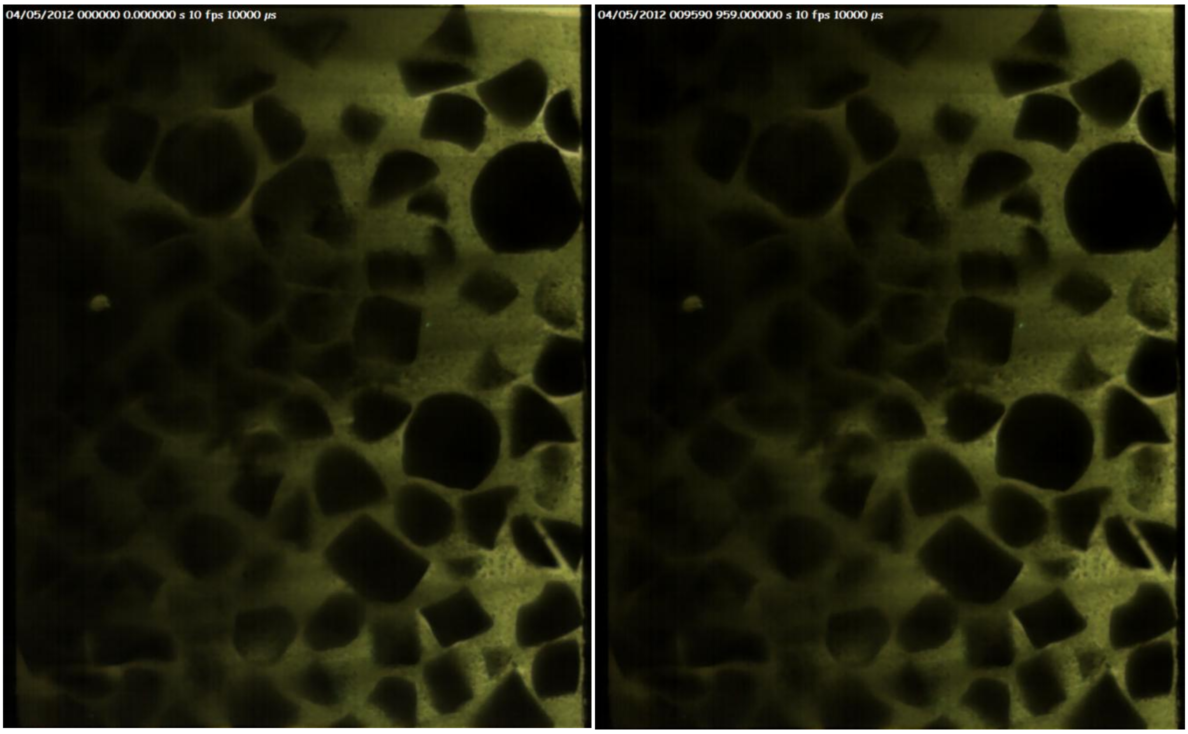

Figure 5.54: GF&M-G4C at a) i_{av} = 0.58 and; b) i_{av} = 0.72.

5.7 Long Tail Test

The Glass Long Tail specimen (PSD plotted in Figure 4.47 in Chapter 4.9.6) had a low fines content and a resulting high permeability. With an $(H/F)_{min}$ = 0.79 and a $(D'_{15}/d'_{85})_{max}$ = 8.01, both the Kenney and Lau (1985) (Figure 5.55), Burenkova (1993) (Figure 5.56) and Kezdi analyses suggested the sample was unstable. The specimen plotted in the stable zone using the Wan and Fell (2008) method (Figure 5.57) and the C_u (D_{60}/D_{10}) = 1.95, suggesting the suffusion would not occur (Istomina 1957). A summary of the PSD analysis is shown in Table 5.11.

The test sample weighed 1991.96 g, had a porosity or n = 0.384 and had a theoretical hydraulic gradient i_c = 0.758.

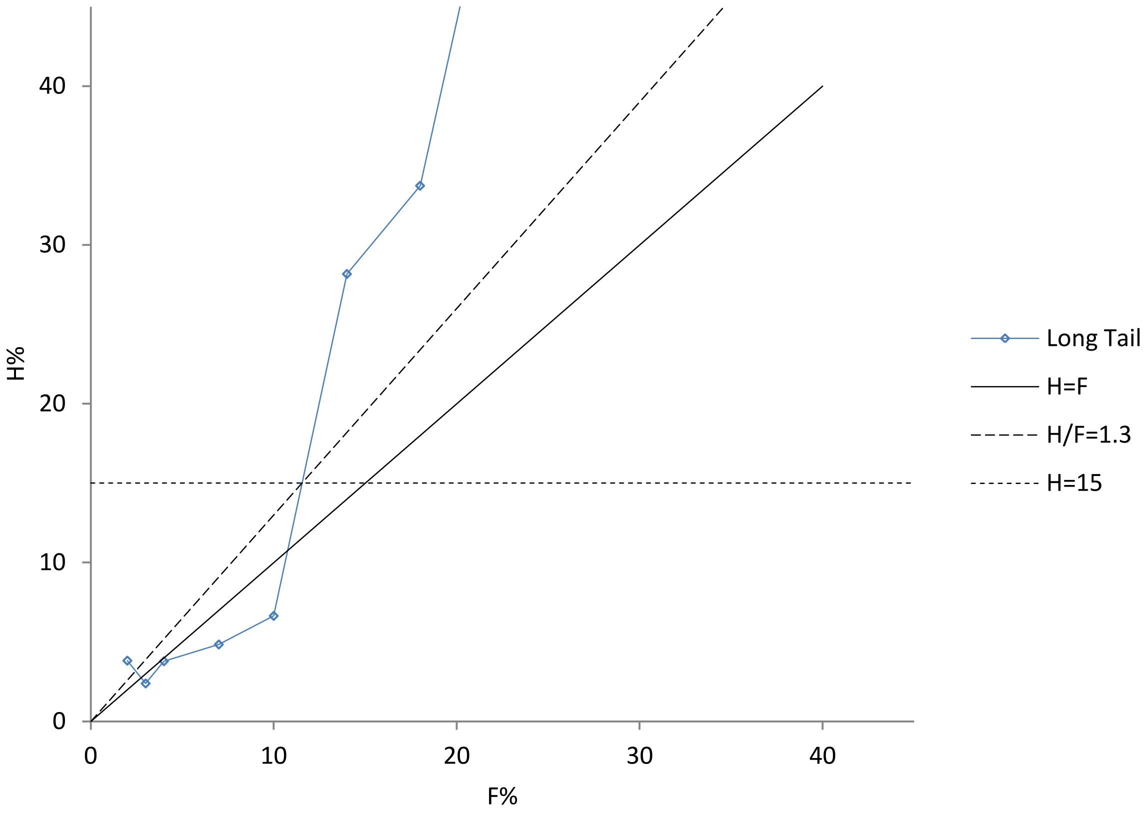

Figure 5.55: Kenney and Lau (1985) analysis for Glass Long Tail specimen.

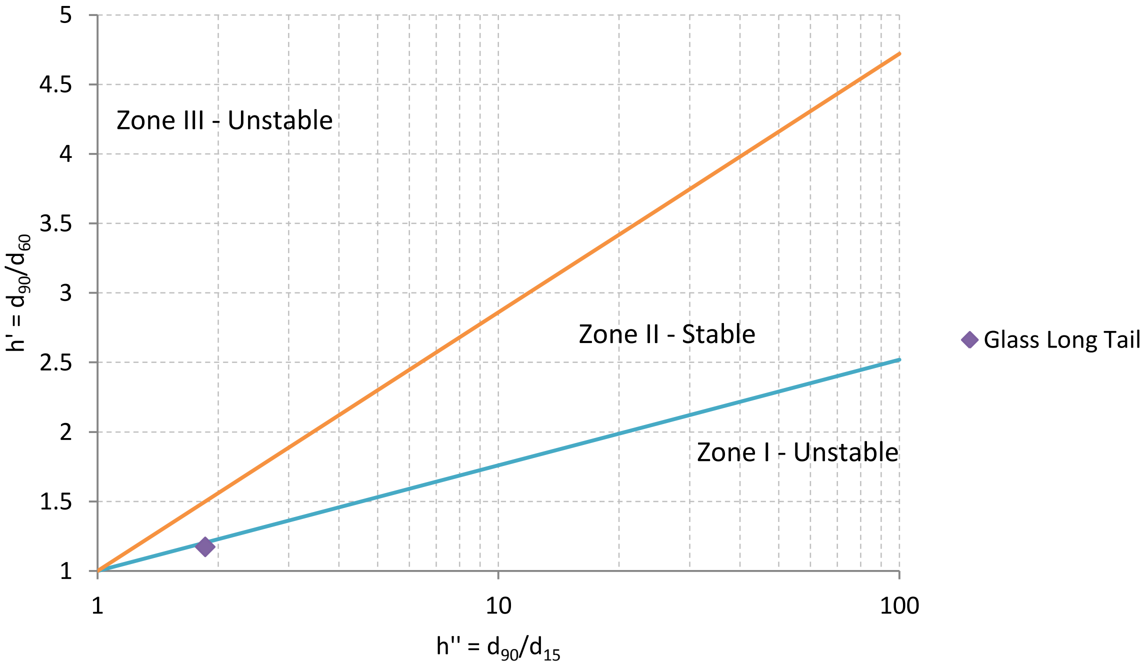

Figure 5.56: Burenkova (1993) plot for stability analysis of Glass Long Tail.

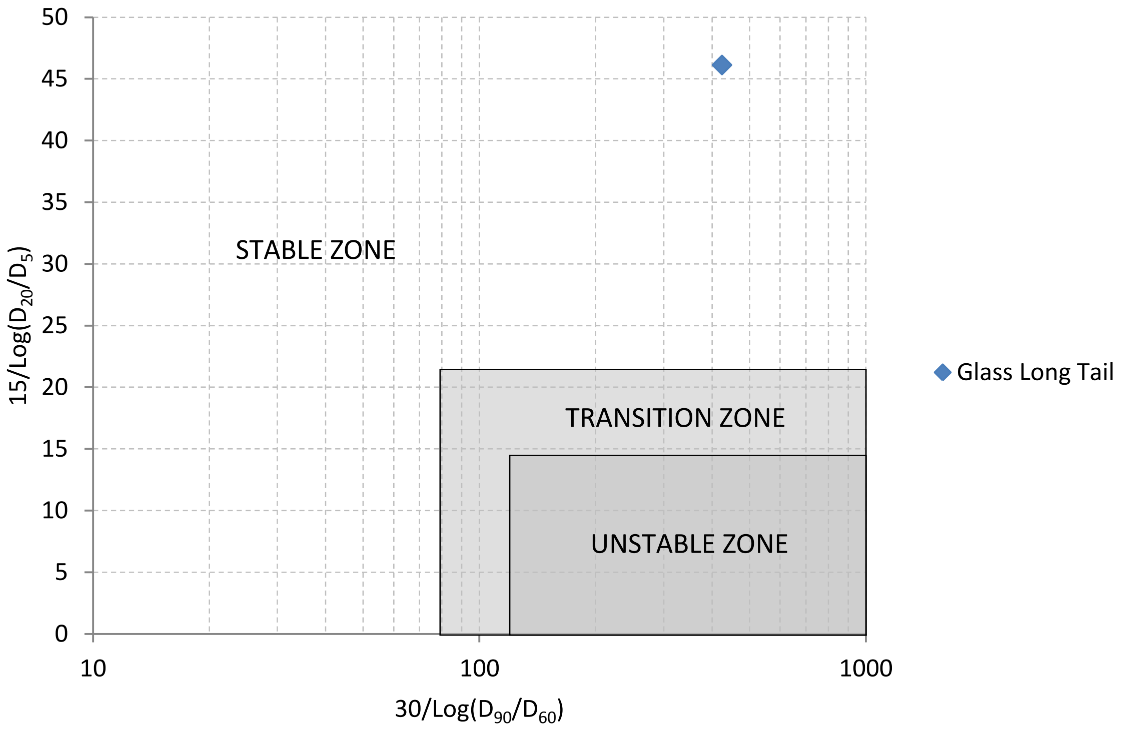

Figure 5.57: Wan and Fell (2008) approach to stability analysis for Glass Long Tail specimen.

Table 5.11: Summary PSD analysis for Glass Long Tail specimen.

	Glass Long Tail
Kenny and Lau, $(H/F)_{min}$	0.79 (unstable)
Kezdi, $(D'_{15}/d'_{85})_{min}$	1.09
Kezdi, $(D'_{15}/d'_{85})_{max}$	8.01
Burenkova	Unstable
Wan and Fell	Stable Zone
$C_u = (D_{60}/D_{10})$	1.95 (self filtering)

Images in this test were collected at 10 frames per second across various short segments. A 10 mm extension tube was added to the lens to focus on a small frame of interest with dimensions of 55 mm x 60mm. The aim of this was to gather 'close up' images at a high frame rate, with the intension of using them for a detailed imaged analysis.

In the test (Figure 5.58), the following observations were made.

a) From i_{av} 0 to 0.029 there is laminar flow according to Darcy's Law, and the permeability was k = 4.23 cm/s. No movement in any particles was observed during this time.

b) At i_{av} = 0.029 there was a change in slope between flow velocity vs. average hydraulic gradient, resulting in a permeability k = 8.73 cm/s.

c) At i_{av} = 0.14, small movements were observed in the finer fraction (Figure 5.59). The test was terminated at i_{av} = 0.162 due to limitations in the pumping capacity.

With a critical hydraulic gradient i_{cr} = 0.14 in the test, the alpha value α = 0.185.

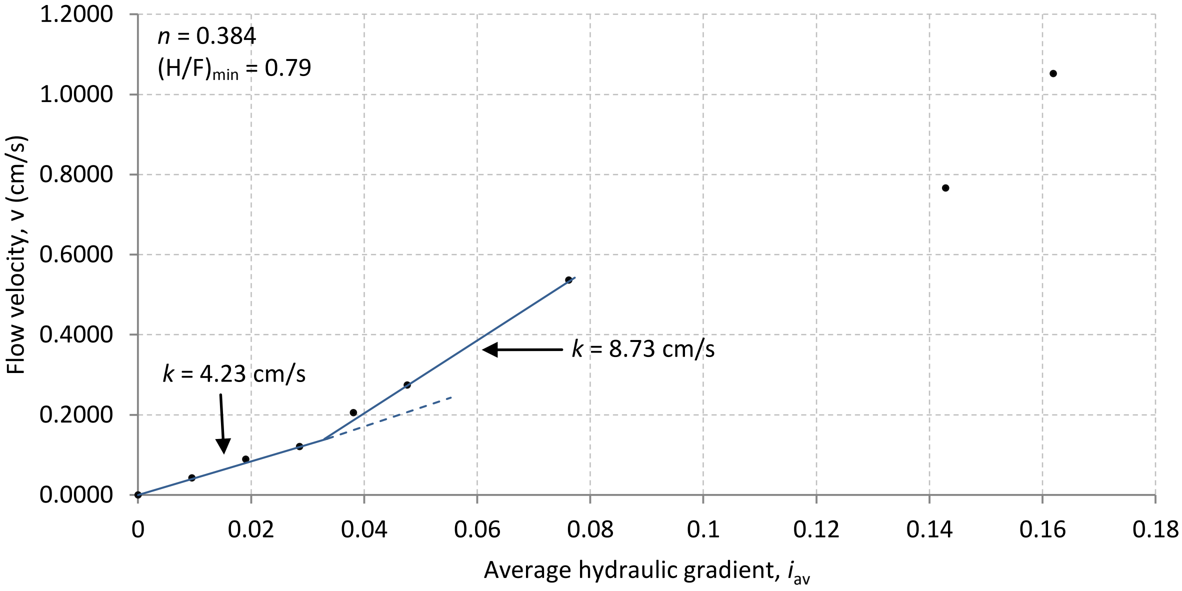

Figure 5.58: Average hydraulic gradient vs. flow velocity for Glass Long Tail test.

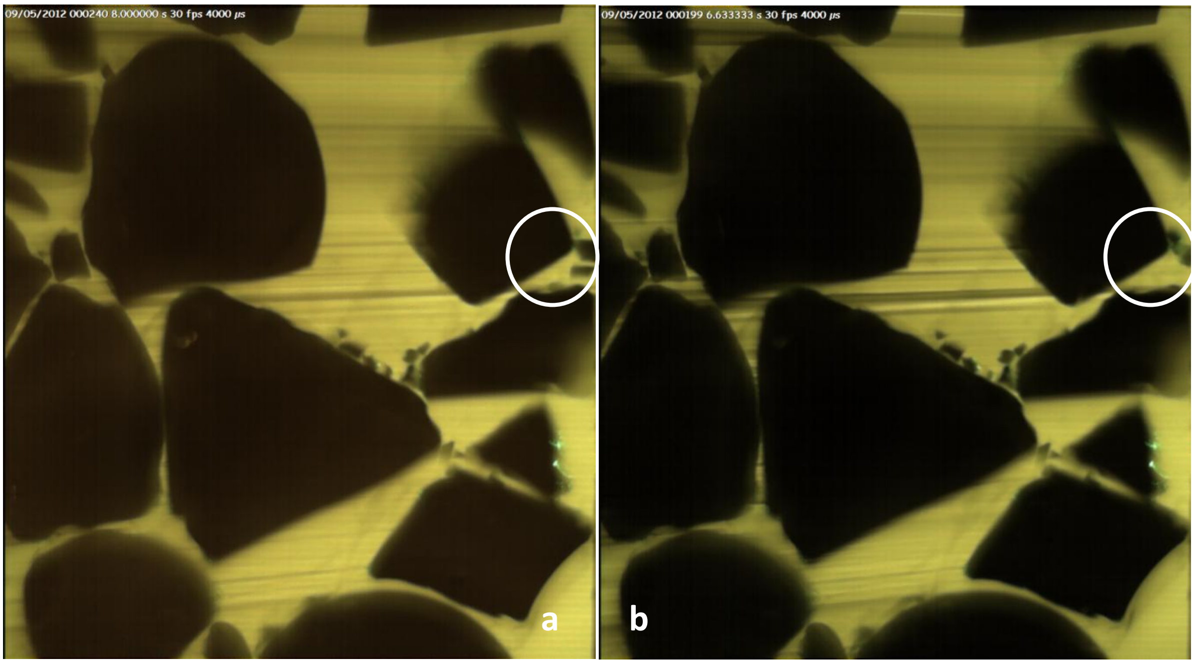

Figure 5.59: Glass Long Tail test at, a) i_{av} = 0 and; b) i_{av} = 0.143.

5.8 Results from preliminary testing – pipe formation

The development of the testing apparatus and methodology took many months, in which time various trial PSDs were tested. As these tests were undertaken during the development phase when equipment and procedures had not been fully developed, their results have not been included in the main body of this thesis. However, during this time, some interesting image sequences were captured which have useful qualitative aspects. One of these sequences is discussed here.

In a preliminary test on a gap-graded material, similar to GS&B-A, the illuminated 2D slice intersected the location where piping was developing. A short clip is shown in Video Appendix B. This ten second clip shows 100 seconds in real time. In the clip, fines have already washed out from an area in the bottom right side. At the top left of the material, fines begin to migrate upwards and 'backward' erosion develops lower down into the specimen. This occurs rapidly with the formation of the well developed pipe taking place over a matter of seconds.

5.9 Synthesis

- Tests on samples with a narrow particle range (G100CF and G100FF) proved that Darcy's Law (1856) for laminar flow exists in the glass and oil mixtures.
- The gap-graded GS&B-A and GS&B-Hybrid materials were the two most unstable having the lowest critical hydraulic gradients.
- Failures of materials included both piping and heave, with heave failure generally occurring in the more stable and less permeable materials.
- Five different methods were used to predict the stability of the tested materials, being those by Kenney and Lau (1985), Kezdi (1979), Burenkova (1993), Wan and Fell (2008) and Istomina (1957). The effectiveness of these methods is discussed in Chapter 7.
- Captured images were able to show visible changes in the material structure over the duration of a test, which could be related to changes in the measured flow and hydraulic gradient data.

Chapter 6: Image analysis using Image-Pro and ImageJ

In this chapter, examples of how Image-Pro and ImageJ can be used in the study of internal erosion are presented. Image analysis is undertaken on one test sample only, being GS&B-Hybrid, to show how one might like to process images obtained during transparent soil internal erosion tests in this thesis.

6.1 Pre-test vs. Post-test comparisons

The first part of this analysis looks at the difference between the pre-test and post-test images. In the GS&B-Hybrid test, images were captured at 1 cm, 2 cm, 3 cm and 5 cm from the front of the apparatus, before, and after testing.

In this analysis, the images were converted to 8-bit black and white, and then flattening and sharpening filters were used to improve the image quality. Only the right half (5cm) of the images was analysed, due to the deteriorating image quality on the left making it difficult to analyse using this method (Figure 6.1). A scale was added to each image based on a calibration target, as shown in Chapter 5.5. For each slice, the coarse fraction area and 'open void' areas were determined by applying a mask across certain shade bands. This allowed for the darker, coarse sized particles to be 'highlighted', therefore allowing an area to be calculated (Figure 6.1b). A separate mask was then applied to highlight the area of 'open voids' (Figure 6.1c). Open voids, referred to in this thesis, are not small voids between fines, but large areas where fines are absent. These may occur in a clast supported specimen where the fines have washed out, for example. Using these calculated areas, parameters such as void ratio and porosity can be determined. As the frame dimensions are known, the area of the coarser fraction and open voids can be subtracted from the frame area, giving an area of fine particles and 'small voids' between the particles. Adding the coarser fraction area to the finer fraction and small voids will give an over estimate of the total solid area. These values are presented in Table 6.1.

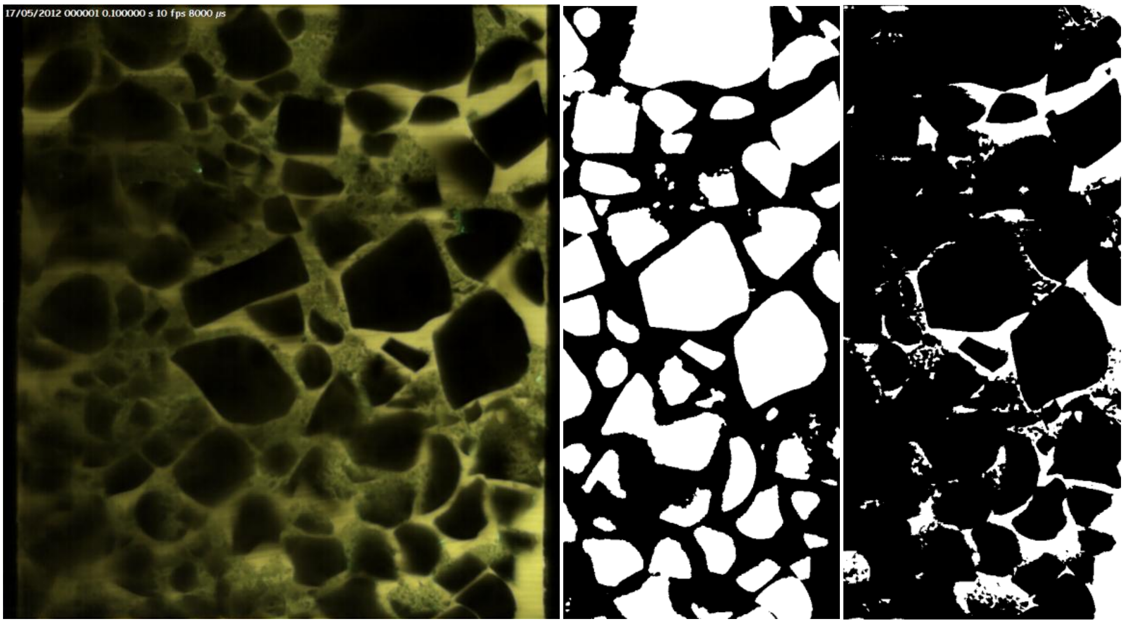

Figure 6.1: *An example of 'masks' created from a) an unprocessed image, to highlight; b) the coarser fraction (in white), and; c) open void space (in white).*

Table 6.1: Calculated and measured parameters from image processing of GS&B-Hybrid.

	Averages	
	Pre-test (area, mm^2)	Post-test (area, mm^2)
Frame area, Vt	5829.013	5860.509
Coarser fraction area	3175.422	2920.326
Open void area, Vv	674.060	1108.361
Finer fraction + small void Area	1979.531	1831.822
Total solid area Vs, + small voids	5154.954	4752.148
Coarser fraction open void ratio	0.215	0.368
Calculated void ratio, e (total solids + small voids)	0.133	0.246
Measured void ratio, e	0.392	0.392
Open void porosity	0.117	0.191
Measured porosity	0.282	0.282
Porosity of finer fraction (Measured porosity – open void porosity)	0.165	0.091

In making void ratio and porosity calculations, it is assumed that the 2D image is representative of the 3D structure. Of course there will be variations throughout the specimen, however it is hoped that by averaging values across four 2D slices, representative values will be obtained.

The process of choosing an intensity range to create a mask of the coarser fraction area and the open void area, known as thresholds, has some constraints. Firstly, it was not possible to create a mask of the finer fraction. This was in part due to the laser sheet width, being approximately 2 mm, while particle sizes were as small as 0.4 mm. These finer fraction particles create an intensity shade in between that of an open void and a larger particle. Secondly, the edges of the larger particles also have an intensity shade that is in between an open void and a solid particle, due the rounded or spherical nature of parts of the particle shape. This results in an underestimate of the coarse fraction size. Thirdly, as light becomes dissipated as it travels through the specimen, the intensity shades furthest away from the laser source are darker than those close to the laser source. As a result, the intensity shade range does not always include some void spaces at points furthest away from the laser source. If one was to increase the intensity shade range to include all voids, the result would be that some of the finer fraction, which has a medium shade between the open void and coarse particle shade, would become included in the mask area, and the open void area would therefore be overestimated.

To test this rationale, an attempt to calculate the void ratio using image processing was undertaken and compared to the 'measured' void ratio, which was calculated prior to the test commenced by weighing the sample and measuring the occupied volume (Table 6.2). To do this, the smallest grain sizes that were included in the 'coarser fraction' mask area were measured. Typically, most grain sizes in this coarser fraction mask were 2 mm in diameter or larger, which agrees with theory, as the laser sheet that intersects the specimen is 2 mm in width. On the PSD curve of the specimen (Figure 5.37), the percentage of fines smaller than 2 mm was found to be 13.9%. Assuming that there was a uniform placement of the PSD, and by knowing the area occupied by the coarser fraction, a theoretical total solid volume (Vs) could be calculated. This calculation was made simply using the following equation:

$$Vs = coarser\ fraction\ area\ \times\ 13.9\%(coarser\ fraction\ area) \tag{6.1}$$

Knowing Vs allowed the total volume of void space (Vv) to be calculated given that the image frame size (Vt) was known, therefore allowing the void ratio (Vv/Vs) and porosity (Vv/Vt) to be calculated. These calculations were then compared to the measured void ratio and porosity. The findings in Table 6.2 show that across the 4 pre-test slices, calculated void ratios were 10.8% to 28.5% above the measured, and the porosity was 5.1% to 12.2% above that measured.

The results show that unfortunately, unless image processing can be improved to better segregate the three areas of coarse particles, open voids and fines + small voids, or the testing equipment is upgraded to produce a stronger laser light and thinner sheet of light, then the images cannot be relied on to calculate accurate void ratio or porosity values.

Table 6.2: Calculations of void ratio and porosity using pre-test slice images for GS&B-Hybrid.

Image e and Φ calculations from Pre-test slices				
	Distance from front of permeameter			
	1cm	2cm	3cm	5cm
Frame area (mm^2), Vt	5596.297	5704.430	5906.358	6108.969
Coarser fraction area (mm^2)	2899.135	3305.605	3067.884	3429.065
Total solids area (mm^2), Vs	3336.173	3803.919	3530.361	3945.989
FF Area (mm^2)	437.039	498.313	462.477	516.925
Total void area (mm^2), Vv	2260.123	1900.511	2375.997	2162.979
Void ratio, e	0.677	0.500	0.673	0.548
Porosity, Φ	0.404	0.333	0.402	0.354
Measured void ratio, e	0.392			
Measured porosity, Φ	0.282			
Difference, e	0.285	0.108	0.281	0.156
Difference, Φ	0.122	0.051	0.120	0.072

6.2 Assessment of particle orientation

A benefit of image processing is its ability to determine parameters using individual particles. By applying shade thresholds to isolate a group of particles from the background, image software can calculate such things as particle area, perimeter, angle, form factor, roundness, aspect ratio and solidity, to name a few. In the GS&B-Hybrid test, image processing was used to assess if particles had a random orientation from placement, by creating Rose Diagrams of the long axis of each particle. Rose Diagrams were also created for post-test slices, to assess if there was a particle movement during testing. To carry out this processing, ImageJ was used.

Pre-test and post-test images were converted to 8 bit greyscale and then filtered using the ‘pseudo flat-field’ filter, so that an intensity threshold could be applied to highlight the coarser fraction and create a mask. An example is shown in Figure 6.2. The plug-in ‘shape descriptor 1u’ was then used to create Rose Diagrams of the particle orientation. One downfall with this method is that some particles are joined together, which often has significant effects on the rose diagram shape. Using ImageJ, particles cannot be split and separated, as they can in Image Pro. A solution is to split the particles in ImagePro and export the mask to ImageJ for processing.

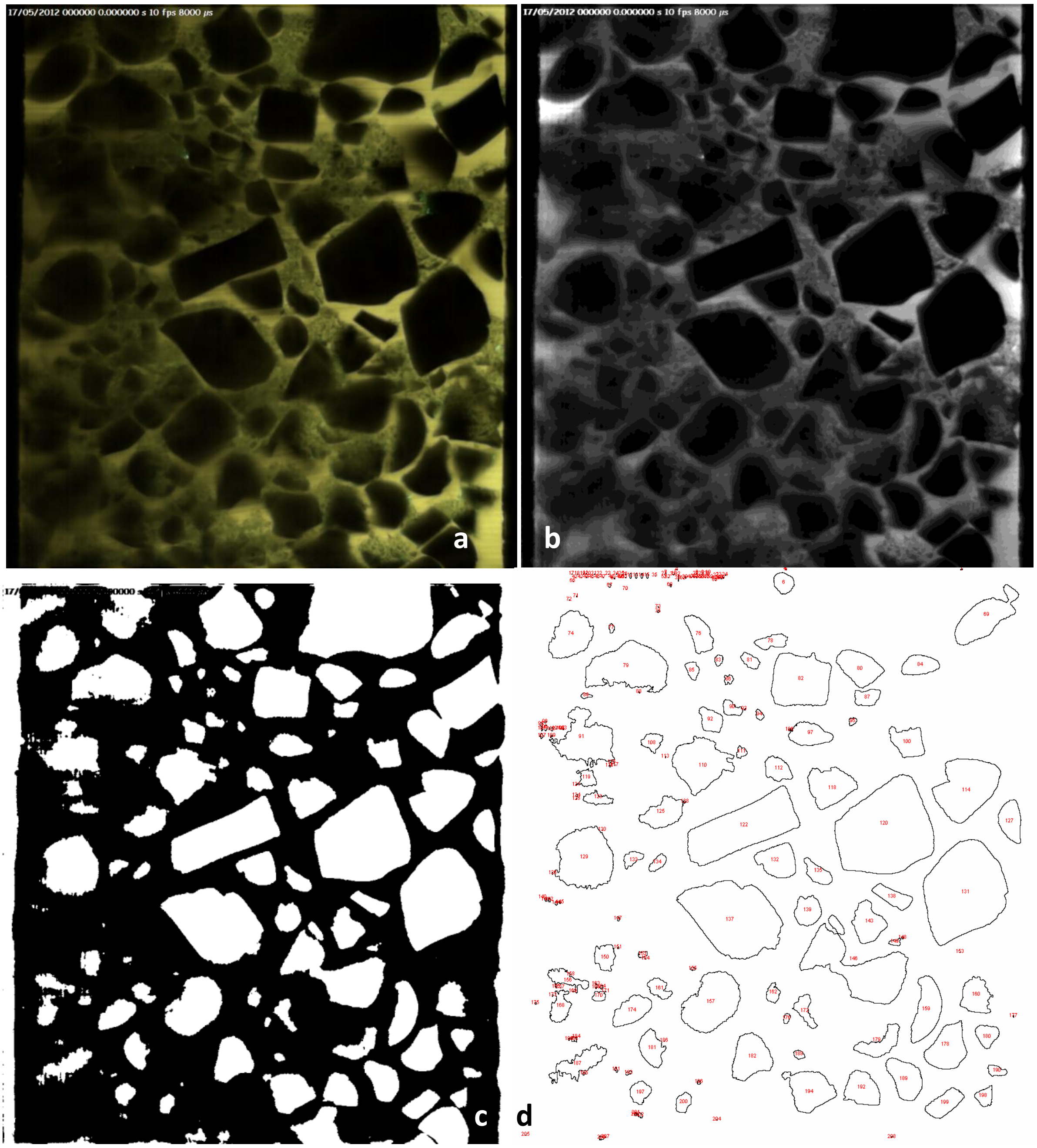

Figure 6.2: Image processing in ImageJ for GS&B-Hybrid, pretest 1 cm, showing a) unprocessed slice; b) image with pseudo flatfield filter; c) coarser fraction mask, and; d) particle outlines, with boundary particles excluded.

The drawback of comparing pre-test data with post-test data, using a manual placement of the laser, is that the slice being analysed is never exactly identical. Despite care being taken during to align the laser sheet as accurately to each marker point before and after a test, it only takes a very small variation in positioning for the acquired images to vary considerably. This constraint is shown in Figure 6.3 – Figure 6.10, as in the GS&B-Hybrid test, no rearrangement of the coarser fraction was observed during testing. The Rose Diagrams in these figures clearly show a particle arrangement of a slightly different slice.

One trend to come from the Rose Diagrams is that there are no major particles with the long axis in the vertical plane. This shows that there is a slight tendency for particles to fall toward the horizontal during placement (actual major orientation is slightly at a diagonal – around 30°-40° to the horizontal). The author notes that for Rose Diagrams to produce robust results, a large amount of particles are required. In this demonstration, up to 120 particles were included in the calculations.

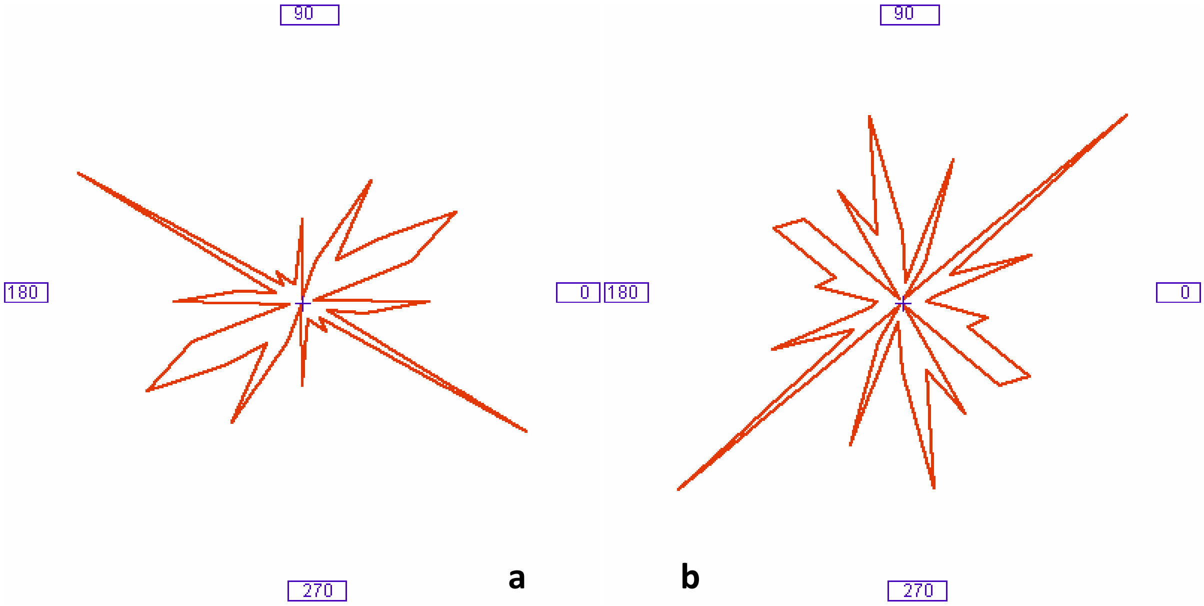

Figure 6.3: Rose diagrams showing long axis particle orientation for 1 cm slices of GS&B-Hybrid for a) pre-test and; b) post-test. '0' points towards the vertical.

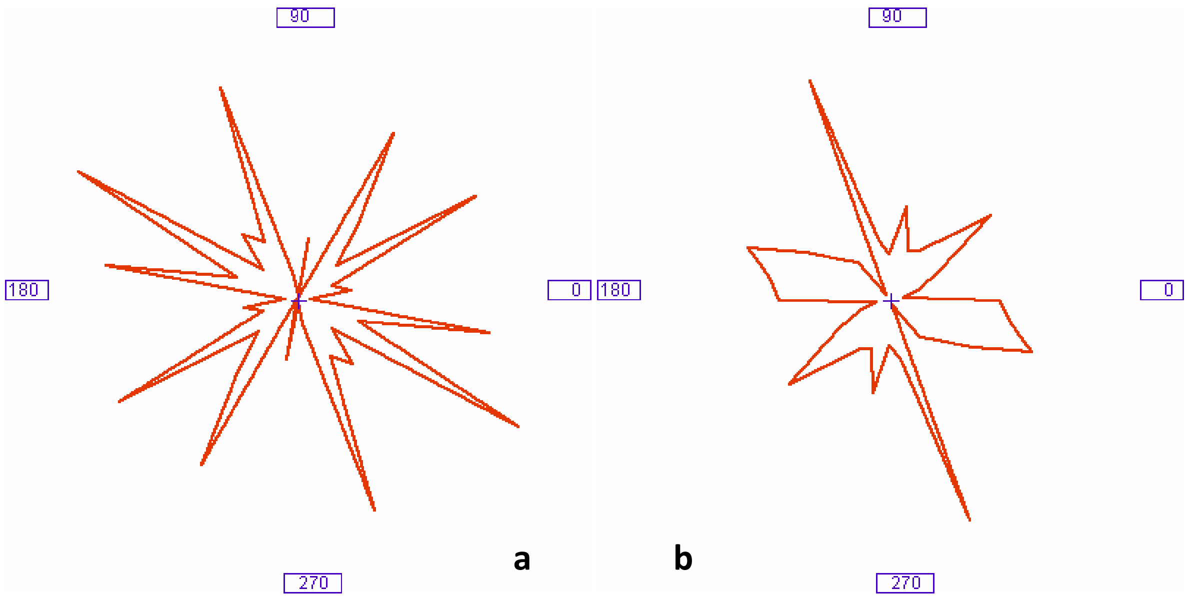

Figure 6.4: Rose diagrams showing long axis particle orientation for 2 cm slices of GS&B-Hybrid for a) pre-test and; b) post-test. '0' points towards the vertical.

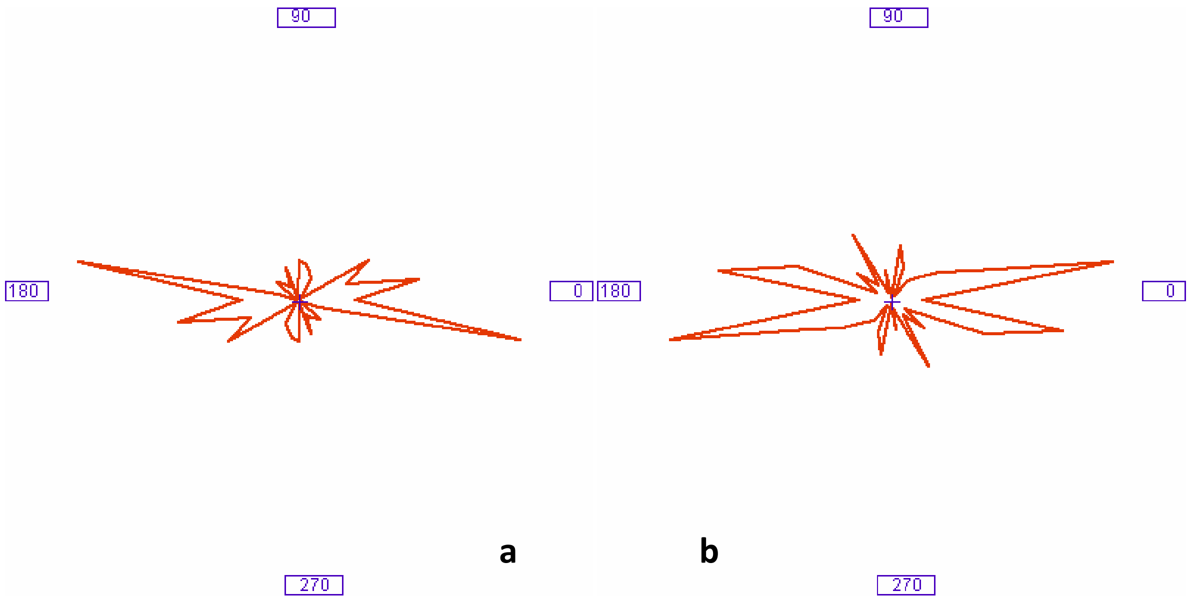

Figure 6.5: Rose diagrams showing long axis particle orientation for 3 cm slices of GS&B-Hybrid for a) pre-test and; b) post-test. '0' points towards the vertical.

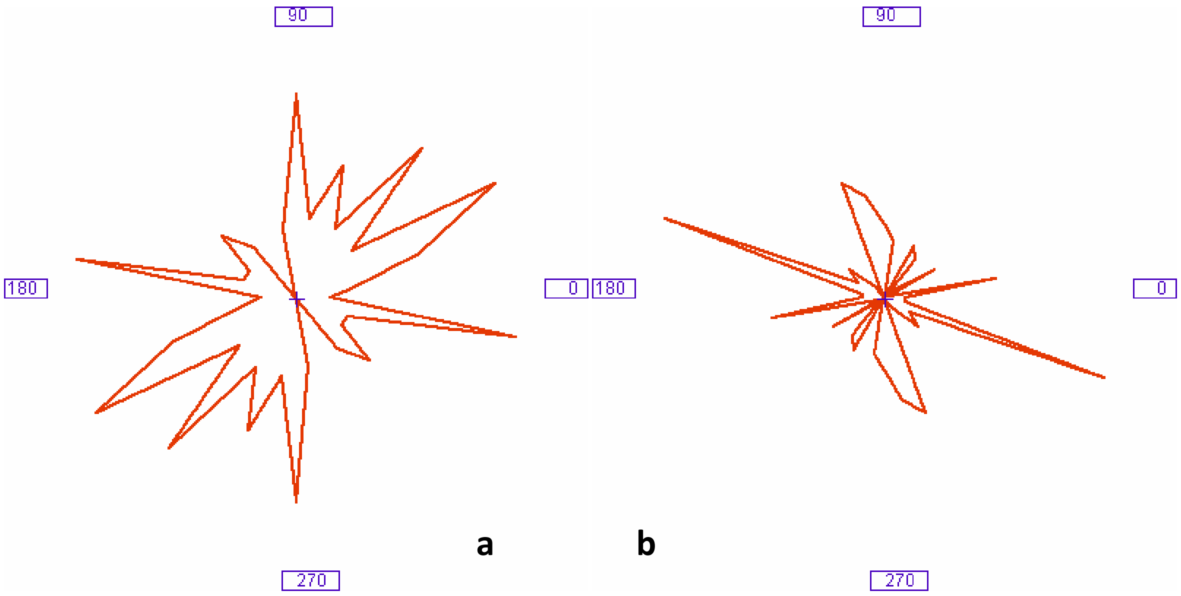

Figure 6.6: Rose diagrams showing long axis particle orientation for 5 cm slices of GS&B-Hybrid for a) pre-test and; b) post-test. '0' points towards the vertical.

6.3 'Phase' Analysis

For the second part of the analysis, the test was split into 6 phases of internal erosion development (Figure 6.7), being:

1. Beginning of test, $i_{av} = 0$.
2. When a minor movement of fines was observed along the glass edge at $i_{av} = 0.095$.
3. When a slight movement of fines was observed throughout the specimen (typically within open void spaces) at $i_{av} = 0.19$.
4. When a moderate amount of fines are suffusing, and small movements of the smaller of the coarse fraction occurs, at $i_{av} = 0.276$.
5. Shortly after piping initiates along the glass wall at $i_{av} = 0.35$.
6. At the end of the test when piping and wash out of fines is well developed, at $i_{av} = 0.48$.

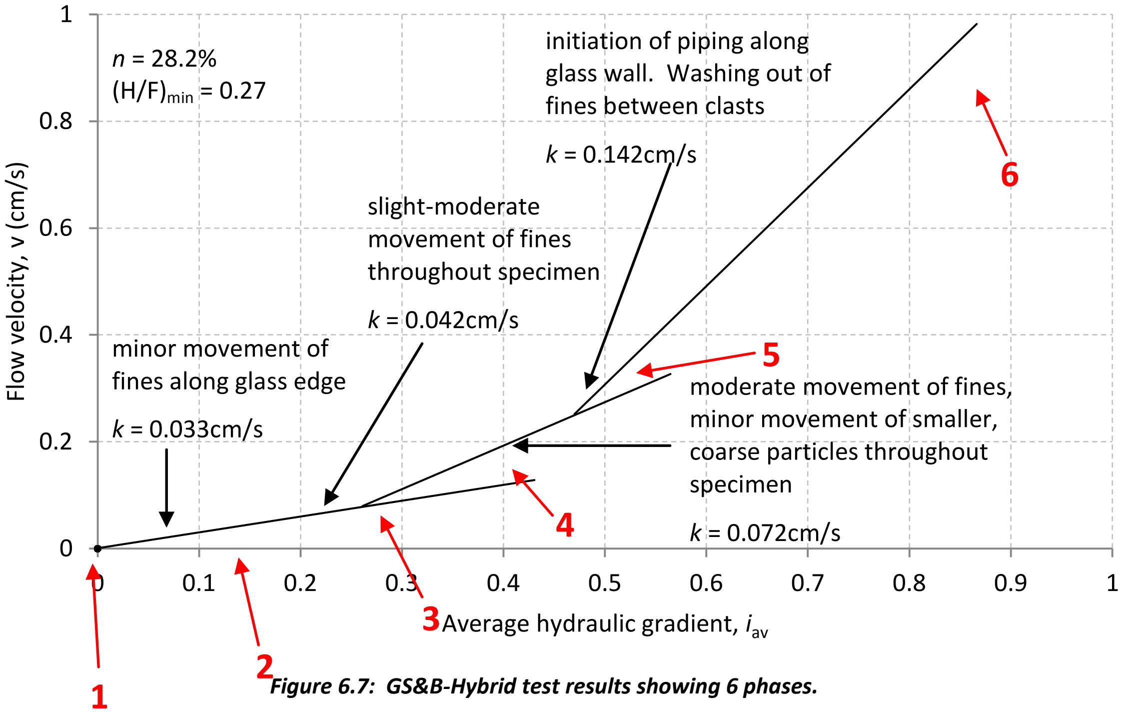

Figure 6.7: GS&B-Hybrid test results showing 6 phases.

One single image from each phase was selected for image processing. Due to the light dissipating throughout the sample, the left side was much darker than the right side. An attempt to flatten the light using filtering was made to help with the image processing process. Although some degree of flattening was achieved, the contrast across the image was still too great. For this reason, it was decided to process the brighter half of the specimen, closest to the laser source, which was then divided into 3 sections. Section 1 is the lower third, section 2 is the middle third, and section 3 is the top third (Figure 6.8). A filter to sharpen the images was also applied.

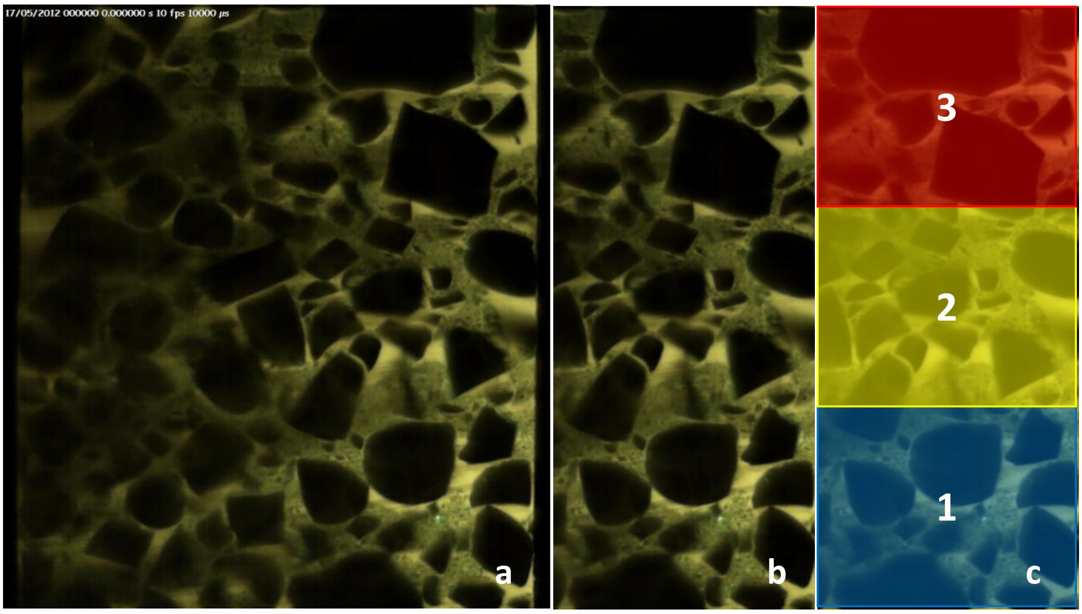

Figure 6.8: a) Original image; b) Right hand half of image for processing; c) Division of sections 1-3.

Using calibration dot images that were taken at the same distance from the front glass wall as the illuminated slice, a scale was added to the acquired images. This allowed the image to be divided into equal slices of known area, and for the particle sizes and void volumes to be calculated.

For each section of the slice, all images for each phase were opened. First a mask was applied to each image to calculate the area of the coarser fraction, which were particles larger than 2 mm. This data was then exported to Excel (Microsoft). A mask was then applied to calculate the area of open void space (Figure 6.9), which illuminates the brightest in the images. This data was also exported to Excel (Microsoft). Theoretically, the remaining volume consists of a combination of the finer particles and the small void spaces between them. Unfortunately the fine particles were too small to be accurately measured using this processing method.

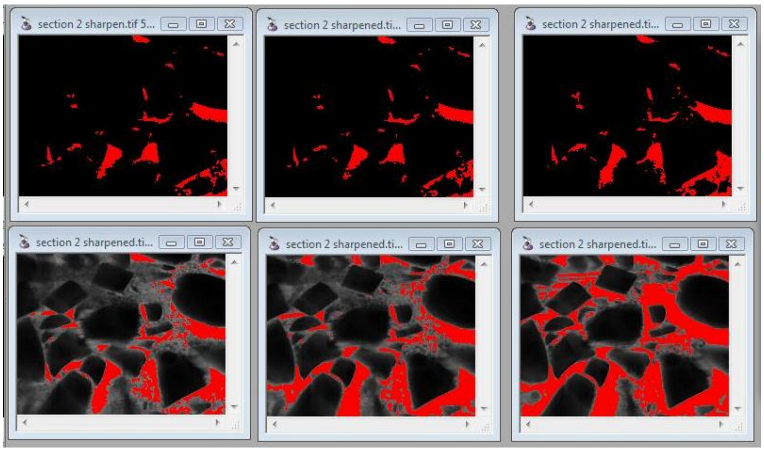

Figure 6.9: Example of applying a mask to images in order to calculate the 'open void' area.

Table 6.3: Area of open voids as a percentage of frame area, across sections 1, 2 and 3, in GS&B-Hybrid test.

	Section		
Phase	1	2	3
1	3.63	5.94	7.98
2	3.74	6.02	7.98
3	7.22	5.48	11.06
4	8.02	3.63	11.70
5	11.64	4.28	13.92
6	14.85	15.95	16.27
% Increase	11.22	10.01	8.28
Ratio increase	4.09	2.69	2.04

Table 6.3 shows the area of open voids per section over the 6 phases of the test. This was then plotted in Figure 6.10. An analysis of this graph is given below.

a) In phase 1 and 2, Section 1 has the lowest area of open void space, while section 3 has the highest area.
b) By phase 3, Section 1 has increased the volume of open voids, while section 2 has a decreased volume. This shows fines moving out of section 1, and into section 2. Section 3 also has an increasing open void volume, showing it too is losing fines.
c) Phase 4 shows the trend in phase 3 developing even more. Phase 2 continues to gain fines, while phases 1 and 3 lose fines.
d) Phase 4 shows a break in trend for section 2, where it begins a slight net gain in open void space (net loss of fines). Sections 1 and 3 shows an accelerated increase in open void volume.
e) In phase 5, sections 1 and 3 show a steady increase in open void space, while section 2 shows a rapid loss of fines as the open void space volume rapidly increases.
f) At the end of the test in phase 6, all three zones finish with a similar amount of open void space volume, with section 1 having the least volume and section 3 having the greatest amount of open void volume. Section 1 showed an increase of 4.09 times, section 2 showed a 2.69 fold increase, and section 3 had a 2.04 fold increase in open void space (Table 6.3).

An analysis and discussion of these results is given in Chapter 7.4.

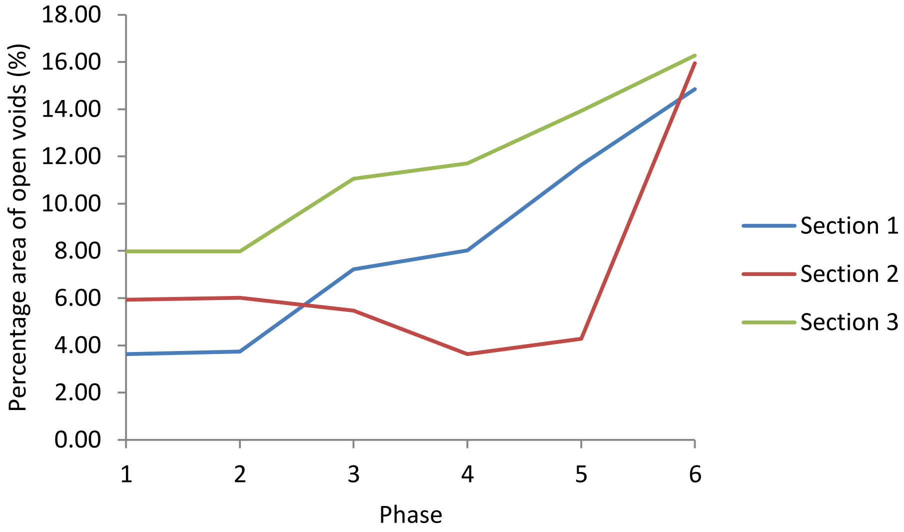

Figure 6.10: Area occupied by 'open voids', as a percentage of frame area for sections 1, 2 and 3 across 6 phases in the GS&B-Hybrid test.

6.4 Synthesis

- A method for comparing pre-test and post-test images was proposed. This firstly involved the application of filters to improve image quality and the removal of a portion of the image frame where image quality was too poor for processing. A scale was applied to the frame, and the masks were applied to highlight the portion of 'open voids' and 'coarser particles'. By carrying this out across several slices of the filter sample before and after the test, changes between the void ratio and porosity could be calculated and compared to the values 'measured' before the test. Using this method, the porosity and void ratio was overestimated. Improvements in image processing of testing equipment are required to obtain more accurate results.
- An assessment of particle orientation was carried out to assess if there were changes in the general particle orientation following a test. Unfortunately since the laser could not be positioned at the exact same positions before and after a test the results cannot be directly compared. Furthermore, for a more robust comparison of particle orientations, a greater amount of particles should be analysed than was used in this analysis.
- A 'Phase' analysis looked at images from various points throughout a test and calculated the change in area that 'open' voids occupied. This aimed to quantitatively characterise the changes that occur as finer particles migrate throughout a material. This method was successful in measuring changes in 'open void' space between the bottom, middle and top sections of the filter material.

Chapter 7: Analysis and Discussion

In this section, results from Chapter 5 are discussed and interpretations made. For each test discussed, the reader will be referred to the relevant section in Chapter 5.

7.1 G100CF Test

Results from this test are presented in Chapter 5.2.1. The linear relationship up until the hydraulic gradient of i_{av} = 0.39 shows that Darcy's Law for laminar flow (Darcy 1856) is valid for the glass and oil materials. Between average hydraulic gradients of i_{av} = 0.48 to 0.64 the head was increased in significantly larger increments than the earlier lifts, and the time between lifts was also reduced. This was done towards the end of the test in an attempt to gain data at the upper limits of the pumping capacity.

It is interesting to note that between i_{av} = 0.39 to 0.48 there was no increase in flow velocity with increasing average hydraulic gradient, which coincided with the only particle movements observed in the images throughout this test. A possible cause of this may be due to a blockage in the material caused by the minor structural rearrangement, reducing the permeability and increasing the average hydraulic gradient across the specimen, for the same flow velocity.

In some tests, particularly earlier tests, the trend line of i_{av} vs. v crosses the flow velocity axis above the zero point, whereas in reality, at zero hydraulic gradient there is a zero flow velocity. This occurrence is likely due to two reasons. Firstly, in earlier tests the starting height of the header tank was above the height required to impose flow through the permeameter, therefore flow velocities at very low hydraulic gradients were not recorded. Secondly, the method of collecting a quantity of oil over an amount of time, typically 5 minutes in the early stages of the test, is thought to impose a large degree of error, as even across 5 minutes, only a small volume of oil was collected into a 1L measuring cylinder. Therefore, for such a small quantity of oil, the cylinder was too large to be accurate. Due to this error, some i_{av} vs. v plots have been corrected by raising the horizontal axis to where the trend line crosses the vertical axis. If this correction was applied to graphs, it has been noted in the titles.

7.2 G100FF Tests

The G100FF tests (presented in Chapter 5.2.2) were undertaken to determine whether the Terzaghi (1925) theoretical critical hydraulic gradient for upward flow through soil was valid in the glass-oil mixtures. In the G100FF – loose test, heave occurred at i_{cr} = 0.56 and was calculated to occur at i_c = 0.62. In the G100FF – compact test, heave occurred at i_{av} = 0.710 and was calculated to occur at i_c = 0.679. These tests gave alpha values, as specified by Skempton and Brogan (1994), of α = 1.005 and α = 1.046 for loose and compact tests, respectively. These values, being close to 1.0, show that the observed critical hydraulic gradient occurred only slightly above the theoretical critical hydraulic gradient, which validates that Terzaghi (1925) theoretical critical gradient calculations are valid for the glass-oil mixtures under zero top stress, as explained in Chapter 3.12.

Interestingly, the measured permeability in the G100FF-loose test being k = 0.015 cm/s, was less than half that of the G100FF-compact test, which has a permeability of k = 0.032 cm/s. This result was not predicted given that the compact specimen had a lower porosity of n = 0.448 compared to the loose specimen with porosity n = 0.496, hence the fluid flowing through the compact specimen should not be able to flow with greater ease.

The trend line in the plot of i_{av} vs. v was corrected so that it crossed the zero point for reasons outlined in Section 7.1.1.

7.3 G22FF-2 Test

The G22FF-2 test results are presented in Chapter 5.2.2.1. Using the graph (Figure 5.13) and the annotated notes based on collected images, it then becomes subjective as to when the critical hydraulic gradient, i_c occurs. An increase in permeability and a slight movement of fines along the permeameter sides is observed to occur at i_{av} = 0.152, while the first slight movements in void spaces were observed to occur from i_{av} = 0 onwards. Other noteworthy occurrences were the initiation of 'moderate' movements along the sides, slight general movements of fines throughout the sample, and finally violent piping of fines. Choosing the i_{cr} value is clearly a subjective process which needs careful consideration. In this thesis, the reported critical hydraulic gradient i_{cr} occurs when there are slight movements of fines occurring throughout the sample, reported as 'slight, general' in annotated graphs. As flow conditions along the permeameter walls are not considered to be representative of those throughout the bulk of the specimen, any movement in fines along the walls is considered to be premature in relation to the critical hydraulic gradient. Furthermore, minor movements of fine particles in open void spaces are not considered to be 'suffusion'. For suffusion to occur, the fine particles need to be able to move out from the cavity they occupy, and through the specimens' skeleton. Initial movements of fines typically observed could be best described as a 'twitch' or a momentary translational or rotational movement.

The i_{cr} = 0.257 occurred at a value less than that predicted by the Terzaghi (1925) theoretical value, described by the alpha value of α = 0.30. This value shows that the material became internally unstable at 30% of the hydraulic gradient required for heave to occur. This phenomenon can be attributed to the coarser fraction predominantly taking the overburden load, while the finer fraction is left under relatively low stress and is therefore able to migrate from the material. This occurrence is known as segregation piping (Skempton & Brogan 1994).

7.4 G40FF Tests

In both the G40FF-2 and G40FF-3 tests (results in Chapter 5.3.2) it was clear that the materials were in fact matrix-supported. This was determined by images showing that the coarser fraction was 'floating' in a matrix of fines, and also by the behaviour of the materials in the tests. In the tests, there was laminar flow and no movement of fines visible at observed scale until piping initiated, as there were no 'open void' or cavity spaces. It is possible that there were movements of particles smaller than could be detected.

These samples possessed laminar flow until sudden failure (Figure 5.18 and Figure 5.19), as observed in the G100FF tests (Figure 5.6 and Figure 5.8). This was expected, given that the fines content was of the same size range, and that both materials were matrix supported. One difference in the way the G100FF failed compared to the G40FF samples, was that the G40FF specimens failed by localised piping, rather than global heave. Furthermore, the G40FF samples did not 'fluidise', like the G100FF test. This is likely due to the 60% coarser fraction particles present in the G40FF specimens which are too heavy given the upward flow velocity, to 'fluidise' like the G100FF fine particles. Even though the entire specimen was unable to heave and therefore fluidise, the fluid may have found a weaker part of the specimen which allowed for a more localised heave, in which a pipe then formed.

Interestingly, the tests failed at considerably lower average hydraulic gradients than were predicted using the Terzaghi (1925) calculation of i_c = 0.89. The G40FF-2 and G40FF-3 tests failed with i_{cr} = 0.56 and i_{cr} = 0.35, giving alpha values of α = 0.629 and α = 0.393 respectively. In both G40FF-2 and G40FF-3 tests the materials failed close to the permeameter walls, so failure was thought to have occurred prematurely. Given this earlier than expected failure, void spaces or cavities within the specimen acted as a key factor to these materials failing, as they would have provided pathways for preferential flow to develop, therefore increasing localised flow velocities which could carry fines from the bulk material.

7.5 UBC 22FF, 40FF and 100FF Tests

Collaborations with UBC enabled the transparent soil test methodology in this thesis to be refined, and also allowed results (in Chapter 5.3.3) from their glass bead tests to be compared to corresponding test materials in this thesis. By enabling these two sets of data to be compared, it has not only allowed the PLIF technique and use of the transparent soil permeameter used in this thesis to be verified, but has also allowed data about the macro behaviour (UBC) to be compared to data about the micro (UC) mechanisms that occur during internal erosion.

In comparing the UBC 22FF-0 test with the G22FF-1 and G22FF-2 tests, of which all had no applied top stress, several similarities and differences can be noted. Firstly, the UBC 22FF-0 test material had a lower porosity, which may be an attribute of the spherical glass beads, compared to the angular beads used in the UC tests. The D_{15} values are similar, being 0.161 for GB22-0 and 0.6 for G22FF, which scales to 0.15 once having applied a scaling factor of 4 to the UC test materials, while the uniformity coefficient C_u values and $(D'_{15}/d'_{85})_{min}$ value are also very similar, being 9.8 for GB22-0 and 9.5 for G22FF.

In the UBC 40%FF and G40FF tests, which also did not use a top stress, porosity values are slightly higher in the angular UC glass-oil mixtures with $n = 0.273$, and $n = 0.26$ for the 40%FF material. The D_{15} value of the UBC material ($D_{15} = 0.1425$) is similar once the scaling factor of 4 has been applied to the UC glass material ($D_{15} = 0.5$; scales to $D_{15} = 0.125$), and C_u values are similar, being $C_u = 10.1$ for the UBC 40%FF material, and $C_u = 10.8$ for the G40FF material. The permeabilities are also very similar with the UBC 40%FF having a $k = 0.018$ cm/s, and the G40FF materials having k values between 0.013 and 0.021 for G40FF-2 and G40FF-3 tests respectively. $(D'_{15}/d'_{85})_{min}$ values are almost identical being 7.46 for 40%FF and 7.56 for G40FF materials, and all tests experienced suffosion. In all three G40FF tests the critical gradient was $i_{cr} = 0.34$ to 0.56, two to three times lower than that experienced in the UBC 40FF test which had a $i_{cr} = 1$. The theoretical i_c for the G40FF tests was 0.89, hence the G40FF tests appear to have failed prematurely shown by alpha factors of 0.629 and 0.39 for G40FF-2 and G40GG-3 respectively, which is a strong possibility given that they failed along glass walls. This reinforces the need to obtain uniform packing along permeameter walls, which is often a difficult task to achieve.

The 100%FF test carried out at UBC had porosity *n* = 0.260, approximately half that of the G100FF tests of *n* = 0.496 and 0.448 for loose and compact specimens respectively, while D_{15} and C_u values were similar. Permeabilities between the UBC 100%FF test (*k* = 0.012 cm/s) and the UC G100FF-loose test (*k* = 0.015 cm/s) were very similar, while the UC G100FF-compact test has a permeability of *k* = 0.032 cm/s which is more than double that experienced by UBC. $(D'_{15}/d'_{85})_{min}$ values are similar being 1.06 for the UBC 100%FF material and 1.09 for the UC G100FF material, which all 'fluidised' upon failure. While the UBC 100%FF test failed at approximately its calculated i_c of 0.91(i.e. at i_{cr} between 0.905 and 0.95) the G100FF-loose and G100FF-compact tests failed slightly before the calculated i_c values of 0.62 (at i_{cr} = 0.56) and 0.679 (at i_{cr} = 0.71) respectively.

Despite there being a few minor differences in observed parameters, there is strong evidence to show that the glass-water materials used at UBC behaved very similar to the glass-oil materials used at UC. The differences in i_c and i_{cr} are most likely due to the premature failure caused by an inconsistent packing of particles along the glass walls, and also due to the larger particles compared to the permeameter size causing larger voids along the glass walls in the UC G100FF tests.

Comparisons between these tests have shown that the glass PSDs at UC create D_{15}, C_u and $(D'_{15}/d'_{85})_{min}$ values similar to those of spherical glass beads used at UBC. Slight discrepancies are likely due to the differences in particle shape. Despite some UC tests failing prematurely, both test types showed the same failure mechanisms. Based on these comparisons, there is strong evidence that the methodology and glass-oil testing materials used in this thesis are capable of recreating similar results to glass-water materials, as used at UBC.

7.6 GS&B-A Test

Three Skempton and Brogan (1994) PSDs were replicated, with some slight modifications (Chapter 4) and tested using the transparent soil permeameter designed in this thesis. The basic design between the two permeameters was similar in that they were both upward flow tests with no top stress. The Skempton and Brogan (1994) tests on soils that were stable, on the boundary of stability, and unstable, made for a sound basis to compare results to the replicated glass materials, and to test the validity of using the PLIF technique in the transparent soil permeameter.

Test results from S&B-A are shown in Figure 7.1, while a comparison between Skempton and Brogan (1994) test properties and GS&B test properties are shown in Table 7.1. The full description of GS&B-A results can be found in Chapter 5.4.1.

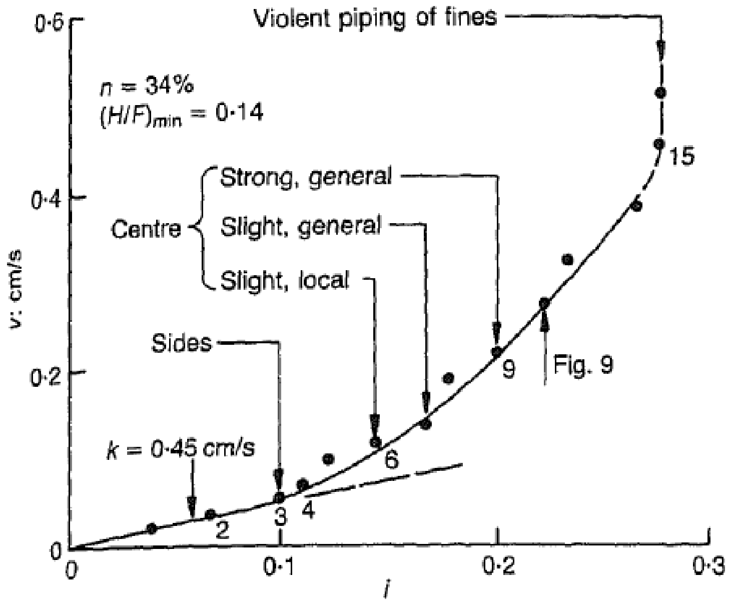

Figure 7.1: Test results from S&B-A (Skempton & Brogan 1994).

Table 7.1: Comparison of properties between Skempton and Brogan (1994) samples and GS&B samples.

	S&B-A	GS&B-A	S&B-B	GS&B-B	S&B-D	GS&B-D
Porosity, *n*	0.34	0.27	0.37	0.29	0.365	0.29
D_{15}: mm	0.6	1.1	0.9	3.9	1.6	5.8
C_u	24	19.13	10	8.05	4.5	4.03
Permeability *k* *: cm/s	0.45	0.261	0.84	1	1.8	0.147**
D'_{15}/d'_{85}	11	n/a	3.9	n/a	3.2	n/a
(D'_{15}/d'_{85}) **	13.14	14.91	15.17	9.61	6.04	7.15
Stability Index $(H/F)_{min}$	0.14	0	0.98	0.86	2.8	3.57
Theoretical i_c	1.09	0.898	1.04	0.873	1.05	0.875
Test i_{cr}	0.2	0.25	0.34	0.3	1	1.33
Alpha factor, α	0.18	0.27	0.34	0.34	0.95	1.52

* In GS&B tests, calculated during laminar flow

** Not actual permeability due to measurement and calculation errors

One of the first things to note is that S&B-A has a higher porosity of *n* = 0.34, compared to the GS&B-A specimen, which had a porosity of *n* = 0.27 (Table 7.1). This is likely due to a mixture of the upper and lower tails of the PSD being cut off, particle shape and surface friction. The glass particles have angular corners compared to natural materials, with a sub-rounded shape. It is also likely that the glass having a low surface friction, combined with the oil which also acts to reduce the friction between particles, promoted a denser packing of particles. The difference in porosities may explain the difference in permeability, which for S&B-A was *k* = 0.45cm/s, and for GS&B-A was *k* = 0.261, as materials with lower porosities can generally expect to have lower permeabilities due to the decreases void space limiting the ease in which fluid can move between particles.

The difference between the $(H/F)_{min}$, being 0.14 for S&B-A and 0 for GS&B-A (Table 7.1), is attributable to the slight difference in the manufactured PSD, due to the exclusion of upper and lower tails. The modification of the PSD is also the cause for the difference in the uniformity coefficient C_u between the two samples (Table 7.1), being 24 for S&B-A and 19.13 for GS&B-A. Furthermore, in scaling up the glass PSD by a factor of 4, one would expect the D_{15} value of the GS&B-A sample (1.1 mm) to be four times larger than that of the S&B-A sample (0.6 mm), which would sum to 2.4 mm. However, with a portion of the upper and lower tails being excluded from the glass PSDs, the GS&B PSDs become stretched, as shown in Figure 4.40, Figure 4.41 and Figure 4.42. In the S&B-A specimen, the gap grade is at 15% by weight finer than D, and the reported D_{15} is 0.6 mm, which lies in the middle of the gap-grade. However, by excluding a portion of the upper and lower tail, the gap grade is raised to 16.5% by weight finer than D, hence the D_{15} value lies on the smaller side of the gap grade, as shown in Figure 7.2.

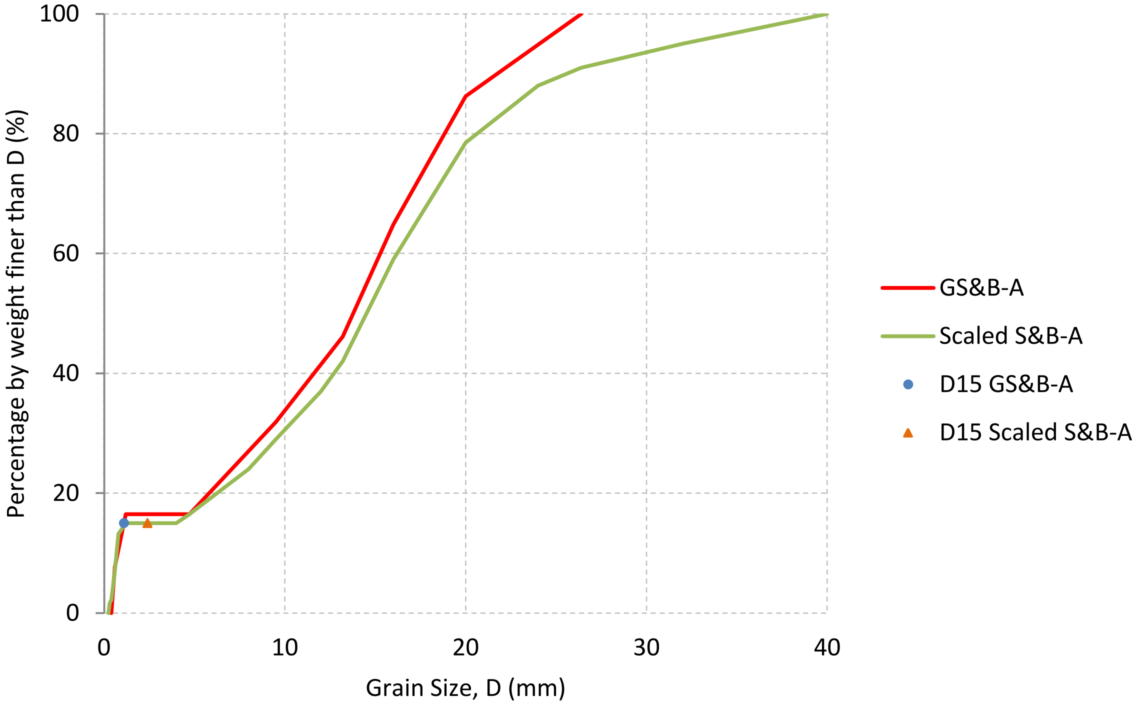

Figure 7.2: GS&B-A PSD and a scaled PSD of Skempton and Brogan (1994) 'A' (Scaled S&B-A) showing D_{15} values.

Skempton and Brogan (1994) report the filter ratio of the sand and gravel components D'_{15}/d'_{85}, being the 15% grain size of the gravel component, divided by the 85% grain size of the sand component. In this thesis, however, given that the materials are constructed from a range of particle sizes rather than from two components, the Kezdi (1979) method for analysis has been used, where the $(D'_{15}/d'_{85})_{max}$ values are reported, as described in Chapter 2.10. Therefore, in order to make direct comparisons, the Kezdi (1979) analysis was applied to Skempton and Brogan (1994) test materials, with results in Table 7.1. Comparing the $(D'_{15}/d'_{85})_{max}$ values shows that the S&B-A material had a lower value of 13.14, compared to the GS&B-A value of 14.91. This suggests that by altering the PSD for the glass replication, the material became more unstable than the S&B-A material. However, both materials were well outside the limits of 4-5 for stable filters (Kezdi 1979). These values are confirmed by the instability experienced with both materials.

Despite the differences, the behaviour of the two S&B-A and GS&B-A specimens was similar. In both tests, fines were first noticed to migrate along the side walls of the permeameters, followed by general movement within the specimen, increasing until violent piping of fines initiated. In S&B-A, violent piping initiated at i_{cr} = 0.2, while in GS&B-A strong piping occurred at i_{cr} = 0.32. Skempton and Brogan (1994) make a note that in S&B-A, the calculated critical hydraulic gradient i_c was 1.09, while in the test violent piping initiated at i_{cr} = 0.20. The theory for this is described in Chapter 3.12, but in summary it states that for piping to occur, the effective stress σ' must be zero, therefore the pore pressure u is equal to the total vertical stress σ, because $\sigma' = \sigma - u$. However, in this case, it is likely that the framework of the coarser fraction is taking a majority of the overburden stress, therefore allowing the finer fraction to move under a hydraulic gradient required for migration in horizontal flow when gravity plays little part. Assuming this, an alpha factor α can be calculated to describe when internal instability can be expected as $i_{\mathrm{c}} = \alpha i_{\mathrm{cr}}$. Images from tests verify that fine particles are not carrying overburden load in most cases. In the S&B-A test, the α value was 0.18, while in the GS&B-A test, α = 0.27, showing that internal instability occurred at 18% and 27% of the hydraulic gradient required for heave failure respectively, according to the observation by Skempton and Brogan (1994).

In general, despite some minor differences in the tested PSD between S&B-A and GS&B-A, the two tested materials gave similar results. In this test, the GS&B-A specimen showed that the glass and hydrocarbon oil mixture behaves similarly to the Skempton and Brogan (1994) soil-water material used in their 'A' sample.

7.7 GS&B-B Test

Results from this test are shown in Chapter 5.4.2, while a summary and comparison of results with S&B-B are shown in Table 7.1. The GS&B-B specimen had a lower porosity (at *n* = 0.27) than the replicated GS&B specimen (at n = 0.37) (Table 7.1), again probably due to the properties of oil and glass causing a lower surface friction. The D_{15} value of the GS&B-B material is only a fraction larger than expected after scaling the particles by a factor of 4, unlike the GS&B-A sample. The uniformity coefficient C_u of the GS&B-B specimen (at 0.9, which scales to 3.6) is slightly smaller than that of the S&B-B specimen (at 3.9), which can be attributed to the tails of the PSD being modified. The stability index $(H/F)_{min}$ of both S&B-B and GS&B-B samples are similar at 0.98 and 0.86 respectively, and both sit close to the boundary of stability, according to Kenney and Lau (1985).

The S&B-B material had a slightly lower permeability at k = 0.84 cm/s compared to GS&B-B with a permeability of k = 1.0 cm/s, which was not expected given that GS&B-B had the lower porosity of n = 0.29 compared to S&B-B with n = 0.39. At i_{av} = 0.5 the permeability reduced from k = 1.46 to k = 0.72 which coincided with a rearrangement of some coarser particles, but it also coincided with aeration of the oil. Air bubbles strongly affect the permeability as they reduce the level of saturation. A soil with a higher degree of saturation will have a higher permeability, and in the case of certain sands, the permeability has been see to increase by three times with an increase in saturation from 80-100% (Chapuis & Aubertin 2003). It is unknown how much of the reduction in permeability was caused by the aeration compared to the structural rearrangement, but it is expected the aeration would account for a larger portion of the change due to the reduced saturation.

Despite both the S&B-B and GS&B-B tests experiencing a similar critical hydraulic gradient (i_{cr}) for the initiation of suffusion, and an identical alpha value of α = 0.34 (Table 7.1), the tests experienced different behaviour. In the S&B-B test (Figure 7.3), the specimen experienced an increasing movement of fines, before piping initiated at approximately i_{cr} = 0.34. In the GS&B-B test, the amount of fines migration increased with hydraulic gradient, however the specimen failed by heave at a hydraulic gradient of approximately i_{cr} = 1. The GS&B-B test (Figure 5.29) showed an increase in the slope of the line between i_{av} vs. v, indicating an increase in permeability from k = 1 cm/s until i_{av} = 0.229 to k = 1.46 cm/s after i_{av} = 0.229, as in the S&B-B test, however at i_{av} = 0.5 the slope reduced again so that the permeability was k = 0.72 cm/s. This change in slope occurred in unison with observed movements in the coarser fraction, which appeared to cause the specimen to stabilise. The test finally failed by heave at a hydraulic gradient of i_{av} = 1.014. This result is interesting as the PSD in question is one in which sits just within the ‘unstable zone’ of the Kenney and Lau (1985) boundary of stability and instability, confirming the method’s prediction.

The S&B-B material has a D'_{15}/d'_{85} value of 3.9, which rests right on the boundary of stability according to the Kezdi (1979) criterion. However, when considering the $(D'_{15}/d'_{85})_{max}$, S&B-B has a value of 15.17, which suggests the material to be internally unstable, according to Kezdi. The D'_{15}/d'_{85} was not calculated for GS&B-B as the sample was made up by weighing out particles of appropriate grain sizes, rather than using specific soils like in Skempton and Brogan (1994). However the $(D'_{15}/d'_{85})_{max}$ was calculated to be 9.61, suggesting the material is also internally unstable, but potentially less so then S&B-B. Test results showed that in the GS&B-B test, although the material initially behaved unstably, piping failure could not be induced. The calculation of the $(D'_{15}/d'_{85})_{max}$ for GS&B-B implies that not all of the particles can be self-filtered, which was observed in the GS&B-B test where fines were able to migrate. The conclusion of this test is that the GS&B-B material is unstable, as observed by the migration of fines, however also possesses some qualities of a stable filter, in that piping could not be induced.

When comparing the S&B-A and GS&B-A tests, both behaved very similarly in terms of the qualitative observations and qualitative data as expected with ‘unstable’ materials. However, it is interesting to see that the GS&B-B material initially appeared to be following the same path of the S&B-B test, before experiencing a rearrangement in particle structure at the point where the S&B-B material failed, before stabilising. It may be that in the laboratory, materials on the boundary of stability and instability may behave in a stable or unstable manner from test to test. Factors affecting the stability for these marginal materials could simply be attributed to minor defects in the specimen caused during sample placement.

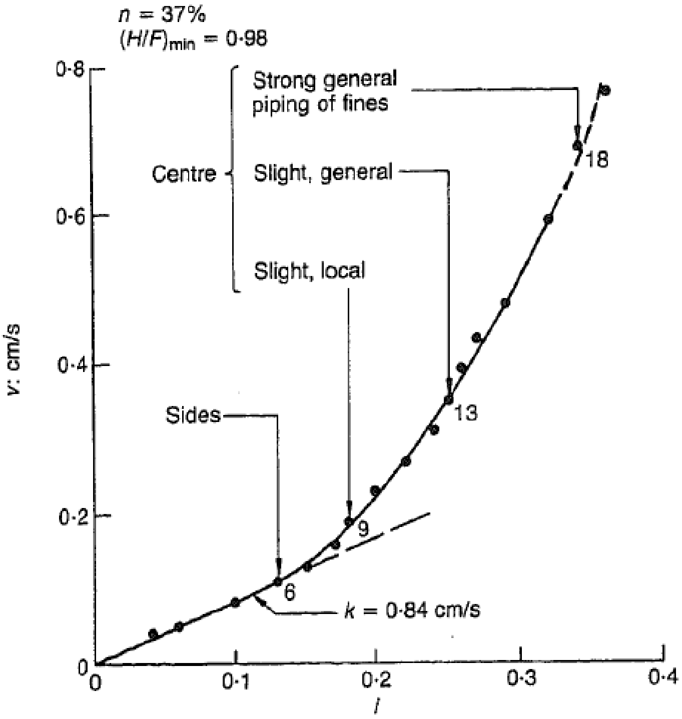

Figure 7.3: Test results from S&B-B (Skempton & Brogan 1994).

7.8 GS&B-D

Results from this test are presented in Chapter 5.4.3. As with previous glass specimens, the GS&B-D material has a lower porosity (at n = 0.29) than the S&B-D material (at n = 0.369), likely due to the low glass surface friction and oil. The D_{15} value for the GS&B-D material was 1.6 mm which scales to 6.4 mm, which is slightly higher than that of S&B-D with a D_{15} = 5.8 mm. The stability index $(H/F)_{min}$ was slightly higher for the GS&B-D material at 3.57 compared to the S&B-D material at 2.8, but considering the S&B-D PSD was slightly modified, this was to be expected.

Skempton and Brogan (1994) did not publish the test results from the S&B-D test due to its close similarities to their 'C' sample, herein named S&B-C (Figure 7.4). Comparing the S&B-C and GS&B-D tests did show the specimens to behave slightly differently. While the S&B-C sample exhibited only a slight movement of fines before strong piping initiated at i_{av} = 1.0, the GS&B-D material showed a slight movement of fines before the sample heaved at i_{av} = 1.33. The two materials did behave similarly however, in that in both tests only slight movements of fines were observed before failure occurred. Due to this slight movement and method of failure, the GS&B-D sample is deemed to be stable, in agreement with Skempton and Brogan (1994). The lower porosity of GS&B-D may explain why piping failure could not be triggered, as there may not have been sufficient void space required to create a preferential flow path.

The theoretical i_c for the S&B-D was 1.05, which was in close agreement with the observed value of i_{cr} = 1.0, giving an alpha factor, α = 0.95. In contrast, the GS&B-D test had a i_c = 0.875 and i_{cr} = 1.33, giving an alpha factor of α = 1.52, showing that failure occurred at a hydraulic gradient 52% higher than predicted. This may have occurred due to friction of glass particles against the permeameter walls, resisting the upward heave movement.

In GS&B-D, the ability of the fines to make small movements may be attributed to the calculated $(D'_{15}/d'_{85})_{max}$ value of 7.15. Skempton and Brogan (1994) calculate their S&B-C and S&B-D materials to have D'_{15}/d'_{85} values of 3.2, which suggests the materials are self filtering (Kezdi 1979), whereas the Kezdi (1979) analysis undertaken in this thesis shows that $(D'_{15}/d'_{85})_{max}$ = 6.04, suggesting not all the material is self-filtering. Attributes of both these D'_{15}/d'_{85} and $(D'_{15}/d'_{85})_{max}$ values were observed in the GS&B-D test, in that fines were observed to migrate, as suggested by the $(D'_{15}/d'_{85})_{max}$ value of 7.15, while the Skempton and Brogan (1994) calculation of D'_{15}/d'_{85} = 3.2 comparing the overall sand and gravel components suggests the overall material to be self-filtering, as seen in this test. Based on these results, it has become apparent that calculations of the D'_{15}/d'_{85} between the major components within a specimen, and the $(D'_{15}/d'_{85})_{max}$ can both be beneficial in predicting the likely behaviour of a filter material.

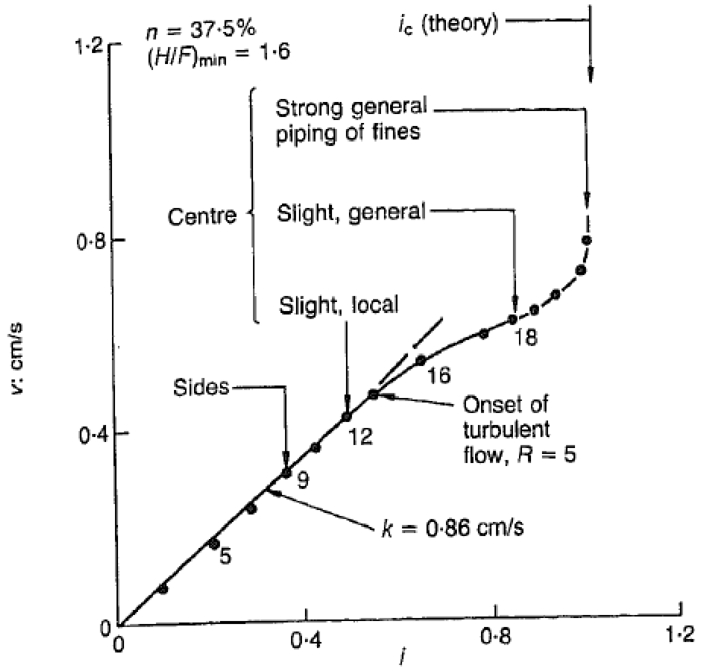

Figure 7.4: Test results from S&B-C (Skempton & Brogan 1994).

The rotameter was found to produce differing calibration curves from test to test. Initially this was not realised. Therefore, many of the preliminary tests that were carried out using the calibration curve applied to them created flow velocities that were not accurate. Unfortunately the GS&B-D test was one of these tests, which were not re-run using the updated manual method to measure flow rate, and the extremely low permeability value of k = 0.147 cm/s for the GS&B-D sample shows this, when compared to k = 1.8 cm/s for S&B-D (Table 7.1). However, the hydraulic gradient values are correct, and the applied calibration curve is linear, hence velocity values still show the fundamental fluid behaviour.

7.9 GS&B-Hybrid Test

The PSD analysis (Chapter 5.5) on the GS&B-Hybrid specimen showed that it was likely to be unstable. From a very low hydraulic gradient (i_{av} = 0.057), fines were observed moving within the material, confirming that this PSD was in fact unstable. Interestingly, this specimen showed a movement in fine materials, albeit along the glass edge, at a lower hydraulic gradient then observed in the GS&B-A material, which was deemed to be slightly more stable, based on less extreme values in $(D'_{15}/d'_{85})_{max}$ (being 14.91 for GS&B-A and 9.95 for GS&B-Hybrid) and $(H/F)_{min}$ (being 0 for GS&B-A and 0.27 for GS&B-Hybrid). The C_u values being 19.13 for GS&B-A and 15.3 for GS&B-Hybrid are both within the ‘transition’ range according to Istomina (1957), but despite the GS&B-Hybrid material having a lower C_u, proved to be more unstable.

The i_c of the GS&B-Hybrid was 0.88, while the observed i_{cr} was 0.15, giving an alpha factor of α = 0.170, which is less than that of GS&B-A and GS&B-B, which had values of α = 0.27 and 0.34 respectively. Based on these alpha values and results from the PSD analysis, the GS&B-Hybrid material showed more internal instability than the GS&B-A test material, which was not expected. By eliminating the gap-grade present in the GS&B-A PSD, it was assumed that the GS&B-Hybrid material would have experienced an increased internal stability. Repeating this test would help confirm whether this material is in fact more internally stable than GS&B-A, or if the test in this thesis failed prematurely.

7.10 GF&M-G4C Test

After replicating Skempton and Brogan (1994) tests in the transparent soil permeameter, it was decided to compare a test material by Fannin and Moffat (2006), where they impose an axial load onto the specimen to create conditions more likely to be found inside an embankment dam. The GS&B tests showed that the transparent soil permeameter and glass-oil mixtures were capable of producing results similar to those carried out using soil-water combinations, thereby validating the method.

In the Fannin and Moffat (2006) G4-C tests, of which there were two (G4-C(1) and G4-C(2)), no seepage induced loss of fines was observed until average hydraulic gradients, i_{av} = 9.1 and 8. When these gradients were reached, a significant loss of fines was induced which resulted from piping through the length of the specimen. The GF&M-G4C specimen behaved in a similar way, with laminar flow occurring until violent piping was suddenly induced at i_{cr} = 0.72. In the GF&M-G4C test, fine particles were observed to move in void spaces initially, and then in the upper part of the specimen, accumulate a thin layer of fines. However, this movement and accumulation of fines was only occurring at the top of the specimen and not in the mid or lower sections. This erosion of fines is not thought to be representative of behaviour of the specimen under the implied conditions. The initiation of piping at i_{cr} = 0.72 is therefore considered to be the critical hydraulic gradient. The theoretical critical hydraulic gradient was i_c = 0.9, giving an alpha value of α = 0.80. It is possible that this value occurred prematurely due to the movement of fines at the top of the specimen. This led to piping and was initiated from the process of backward erosion.

In the G4-C test, the i_{cr} is significantly higher than that observed in the GF&M-G4C test. The higher i_{cr} value is mainly due to the 25 kPa vertical stress applied to the specimen, while the mesh screens above and below the specimen may have a small influence, as they act to hold particles in place and compress the sample. Despite the differences in the testing apparatus and conditions applied to the two materials, they both exhibited similar behaviour during testing, in that almost no movement of fines was observed before piping was triggered. This similarity is encouraging when considering the use and plausibility of the transparent soil permeameter in the assessment of internal erosion.

Interestingly, despite the significant difference in stresses applied to the two tests, they both had very similar permeabilities, with the F&M-G4C material having a k = 0.022 cm/s and the GFM-G4C material having a k = 0.023 cm/s, implying that applied stress has little or no affect on the permeability. The similar permeabilities are clearly a function of similar porosities, where F&M-G4C having an n = 0.24 and GF&M-G4C having an n = 0.266. The slightly lower value in the F&M-G4C material is likely due to the applied top stress which would act to compress the material, and also due to the spherical round beads which may have allowed for a more compressed specimen compared to the UC angular particles, thereby reducing pore space.

In Li and Fannin (2012), a hydromechanical envelope is presented which expands on the alpha factor to include the effects of effective stress as well as upward flow stress. Their formula that defines the hydromechanical envelope for heave of an internally stable soil is given by:

$$i = 2(\frac{\sigma_{vm}}{\gamma_w \Delta z} + \frac{0.5\gamma'}{\gamma_w}) \tag{7.1}$$

while the hydromechanical envelope for the initiation of internally instability is given by:

$$i = \frac{\alpha}{1 - 0.5\alpha}(\frac{\sigma_{vm}}{\gamma_w \Delta z} + \frac{0.5\gamma'}{\gamma_w}) \tag{7.2}$$

where σ_{vm} is the mean vertical effective stress. In these equations, the alpha factor α should not change with increasing effective stress, however with an increased effective stress the critical hydraulic gradient will be increased. This equation can therefore explain why the F&MG4-C had critical hydraulic gradient values of i_{cr} = 9.1 and 8 when a top stress of 25 kPa was applied, compared to the GFM-G4C material which failed at i_{cr} = 0.72 with no top stress.

Fannin and Moffat (2006) did not supply alpha factors, but were calculated using Equation 7.2 by the author of this thesis. For values of i_{cr} = 9.1 and 8, alpha values were calculated to be α = 0.30 and 0.27 respectively. These values are considerably lower than that calculated for the UC GF&MG4-C, being α = 0.8. This could be a function of the spherical ballotini glass beads used by Fannin and Moffat (2006) compared to the UC angular glass particles used in this thesis, whereby angular particles at this fine scale may resist internal erosion processes more than spherical particles.

Table 7.2: Comparison of properties between F&MG4-C and GF&M-G4C samples.

	F&MG4-C	GF&M-G4C
Porosity, *n*	0.24	0.266
C_u (D_{60}/D_{10})	14.5	11.67
Permeability *k*: cm/s *	0.022	0.023
$(D'_{15}/d'_{85})_{max}$	7.4	6.66
Theoretical i_c	n/a	0.903
Test i_{cr}	9.1 & 8**	0.72
Alpha factor, α	0.27 & 0.30**	0.8

* In F&MG4-C, average *k* between i = 0.1 and 0.2; In GF&M-G4C test, calculated during laminar flow.

** G4-C(1) and G4-C(2)

7.11 Glass Long Tail Test

The attempt to create a ‘long tailed’ PSD was difficult given the narrow range of particle sizes that the current transparent soil permeameter test can operate with. The resulting PSD which tried to mimic the shape of a moraine till (Figure 4.47) had 7% of particles smaller than 9.5 mm. This very low content of finer particles is obvious in Figure 5.59 which shows a skeleton of coarse grains and few fines.

For this test, the 10 mm extension tube was used between the camera and camera lens to try and gather close up images of the particles, while the frame rate was increased from 1 fps to 10 fps to gather greater resolution. Instead of capturing images across the entire test duration, shorter segments were collected at various points throughout the test, with the aim of capturing images at ‘interesting points’. Unfortunately, with such a low content of fine particles, and the resulting high permeability of the material, the test was not able to produce images of suffusion, suffosion or piping for example. However, the technique of obtaining close up images at a high frame rate proved to be successful. The frame rate of 10 fps could also be increased if one wished to gain even more resolution in image data, however by increasing the frame rate.

If a broadly graded soil is to be tested using this method, the permeameter size will need to be increased to allow a greater range of particle sizes to be included. Furthermore, a narrower laser sheet of light would allow for smaller particles to be included and seen in test images.

7.12 Other results from preliminary testing – pipe formation

Video Appendix B showing the formation of a pipe gives a good visual and qualitative understanding of how backward erosion initiates and develops. From the video clip, one can see that the fines at the top of the material erode away first, making space for fines lower down to migrate away. As the material is removed from a localised area, fine particles are free to migrate upwards under the flow of fluid, which progresses to the base of the specimen. The location of the pipe was positioned where open voids existed, which reinforces the fact that inconsistencies in particle packing can have a significant impact on the stability of a filter material.

7.13 Discussion of PSD analysis

Table 7.3 shows the glass materials tested with the summary of results from PSD analyses. The Kenney and Lau (1985) approach was the best in predicting whether a material was going to be stable, or unstable using the boundary H/F = 1. This approach successfully predicted the stability of all eight materials evaluated in Table 7.3.

The Burenkova (1993) approach proved successful in predicting the stability for 7/8 materials. It unsuccessfully predicted the stability of GS&B-D, however this material plotted very close to the boundary of stability. Using this method for prediction it is therefore worth noting that materials plotting slightly on the unstable side of the boundary, may exhibit stable behaviour.

The Kezdi (1979) approach of splitting the PSD curve to determine the $(D'_{15}/d'_{85})_{max}$ was also successful in most instances. However this approach is based on whether particles within a material can physically move between voids, and is therefore on the conservative side. This was evident in the GS&B-D test where fine particles were observed to make some movements, however the overall material was deemed stable. Li and Fannin (2008) found that the Kezdi (1979) approach was more accurate in predicting the internal stability of gap-graded soils than the Kenney and Lau (1985) approach.

Considering its simplicity, the Istomina (1957) boundaries that were set for the uniformity coefficient were able to predict 5/8 stabilities, assuming that values in the 'transition condition' range were not able to self filter. This method was not successful in predicting the gap-graded GS&B-A material, and so care should be taken when considering this approach for gap-graded materials, although it did successfully predict the gap-graded GF&M-G4C material.

The Wan and Fell (2008) approach was the least successful in predicting stabilities with 1/8, however the authors do note that it is best suited to broadly graded materials, whereas all materials tested in this research were more narrowly graded. It is therefore confirmed that this approach is not suited to narrowly or gap-graded materials.

Table 7.3: Comparison of methods for evaluating stability of each PSD. The observed stability of the tested material is noted in brackets below the named specimen, while the coloured boxes show the predicted stability. Green shaded boxes = stable, orange = boundary between stability and instability (transition zone), and red = unstable.

	G22FF (unstable)	G40FF (unstable)	GS&B-A (unstable)	GS&B-B (unstable)	GS&B-D (stable)	GS&B-Hybrid (unstable)	GF&M-G4C (unstable)	G Long Tail (unstable)	Correct predictions
Kenny and Lau, $(H/F)_{min}$	🟥 0.57	🟥 0	🟥 0	🟥 0.86	🟩 3.57	🟥 0.27	🟥 0	🟥 0.79	8/8
Kezdi, $(D'_{15}/d'_{85})_{min}$	🟥 7.56	🟥 7.56	🟩 1.15	🟩 1.19	🟩 1.13	🟩 1.17	🟩 1.28	🟩 1.09	3/8
Kezdi, $(D'_{15}/d'_{85})_{max}$	🟥 7.56	🟥 7.56	🟥 14.91	🟥 9.61	🟥 7.15	🟥 9.95	🟥 6.66	🟥 8.01	6/8
Burenkova	🟥 Unstable	🟥 Unstable	🟥 Unstable	🟥 Unstable	🟥 Unstable	🟥 Unstable	🟥 Unstable	🟥 Unstable	7/8
Wan and Fell	🟩 Stable	🟩 Stable	🟧 Transition Zone	🟩 Stable Zone	🟩 Stable Zone	🟥 Unstable Zone	🟩 Stable Zone	🟩 Stable Zone	1/8
Istomina, $C_u = (D_{60}/D_{10})$	🟩 9.5	🟧 10.8*	🟧 19.13*	🟩 8.05	🟩 4.03	🟧 15.3 *	🟧 11.67*	🟩 1.95	5/8

* ‘Transition zone’ by authors classification, categorised as ‘unstable’ in this assessment.

7.14 Limitations and Improvements in Apparatus and Procedure

The ATSM D 2434-68 standard (2006) states that permeameters should be cylindrical to help obtain an even flow through the sample, while eliminating irregularities that can occur in particle packing in permeameters with corners. The 'box' shaped permeameter creates four corners which can make even particle packing difficult, and can create unwanted void spaces in which preferential flow paths can develop. Furthermore, with the oil inlet being centred in the middle of the apparatus, flow may take a central route through the sample. A dissipation filter underneath the steel frame is placed in an attempt to reduce this effect, however an even flow may not be obtained in the corners of the apparatus.

The recording instrumentation on this apparatus was basic and required manual recording, which created low resolution data compared to electronic, automated and continuous types of instrumentation. Throughout a test, data was collected at regular intervals, typically point every one minute, while images were being captured. This involved reading the rotameter value and four or five standpipe piezometer heights, which would take a combined time of approximately 20 seconds. In addition to this, a measured volume of oil was collected for each lift in head height, which typically occurred every 6 minutes. The measured volume was collected 2-4 minutes after the head increase to allow for the flow to stabilise. When critical gradients were nearing, or when a significant change was occurring in the particle structure, flow rates and hydraulic gradients could fluctuate dramatically over short periods of time. With this type of measurement, often these changes were not well documented, or would be 'smoothed' or averaged out.

Under the ATSM D 2434 - 68 standard (ATSM 2006) for permeability testing, the permeameter diameter must be 8 to 12 times the diameter of the largest particle, and the largest particles should not exceed 19 mm. The transparent soil permeameter used for this testing does not meet these requirements due to limitations in the resources required to upscale the apparatus. For example, a larger permeameter would require a larger pump, hoses and rotameter to circulate the higher volume of oil, a larger header tank and storage reservoir, and a greater volume of oil and amount of crushed glass, which with the available resources was not feasible. The objectives of this research were also to assess the feasibility of this test method before a more sophisticated apparatus is constructed. Furthermore, with particles being too large for the permeameter, large voids along rigid walls are likely to occur and create premature failure.

As individual particles become smaller, they become increasingly more difficult to detect with the camera and naked eye. Particles that pass the number 40 sieve (smaller than 0.425 mm) were excluded from PSDs as: a) they are difficult to detect with the camera and; b) they reduce the clarity of the overall image. Despite the oil and glass having an almost identical refractive index, testing has shown that PSDs with a higher proportion of finer particles result in an increasingly 'cloudy' or blurred appearance. The cause of this is likely a result of a combination of the small difference in refractive index between the oil and glass, impurities in the oil and on the glass particle surfaces, and from damaged glass, such as particles with fractures and highly chipped edges, which cause refraction and reflection of light. With the absence of particles smaller than 0.425 mm, the mechanics of the samples may behave differently to those had the finer particles not been removed, despite the overall proportion of these particles sizes being relatively small.

Due to the restriction in maximum sized particles that could be used in the apparatus, the upper tails of mimicked PSDs sometimes had to be excluded. This therefore slightly changed the overall PSD of the transparent soil. Increasing the size of the permeameter would allow unmodified replications of soil samples to be tested.

Due to the method used to create the glass particles, the particle shapes were mainly angular. The author notes that soil particles used in embankment dams tend to be of a more rounded to sub-angular nature, however some confidence for the use of angular particles comes from Sherard et al. (1984a) following laboratory testing, suggests that angular particles can be used in place of rounded particles, and the same filter design criterion applied.

Effort was made to remove air bubbles from the oil within the system as they deteriorate the clarity of the images by reflecting light, and also affect the permeability (as explained in Section 7.7). In the preparation of each sample the slurry mixtures were placed in vacuum desiccators to remove the majority of air bubbles entrained in the oil, however it was not feasible to carry this out on the entirety of the oil in the reservoir. Efforts were also made to remove larger air bubbles in the hoses and rotameter prior to placing the sample in the apparatus. Despite these efforts however, 'micro' air bubbles could still be seen within the sample, and on occasion larger air bubbles were forced into the apparatus from the inlet hoses. The oil recirculation system caused air to become entrained into the oil, particularly at high flow rates. Oil pumping into the header tank was forced up through the reservoir where it broke the surface and entrained air. The orange light filter in front of the camera lens was quite successful in eliminating the reflected light that resulted from these air bubbles, however larger bubbles are still visible in some images.

Light entering the permeameter became increasingly dissipated as it travelled through the glass-oil mixture. As a result, it became increasingly difficult to distinguish particles further from the light source. It also created problems with image processing, outlined later. One possible solution to this problem would be to implement a second laser which would generate a second sheet of light, entering the apparatus from the opposite side. A system to mount the two laser line generators would need to be developed so that the generated light was in the same plane. If this device was equipped on a roller system, the illuminated slice could be easily moved across the test specimen. This system could allow for the exact same slice to be illuminated before and after a test, if the device has a measurement scale.

For reasons described earlier, perfect optical transparency was not obtained. This is obvious when comparing pre-test and post-test slices where the image clarity decreases with depth into the material. The best images come from the very front of the apparatus, however the objective of this test method was to provide a view inside the material where edge affects are significantly reduced. Good image quality was obtained to a depth of approximately 5 cm from the front of the permeameter, with images at greater depth becoming increasingly unclear.

Due to the transparent soil not having any applied top stress, the conditions were not representative of those experienced inside an embankment dam. However, the results can be compared to other physical testing research, namely Skempton and Brogan (1994), who also test soils with no top stress. Results also can be directly compared to those currently being carried out at UBC where experimentation is being conducted with glass beads, water and no vertical stress. That research is aimed to better understand the mechanisms occurring during internal erosion. Transparent soil tests carried out in this thesis showed that the behaviour of materials with no top stress were similar to tests with top stress carried out by Fannin and Moffat (2006), however instabilities occurred at lower hydraulic gradients when no top stress was applied.

It may be instructive for future tests to include a top stress. This would require a re-design of the permeameter in order to take the load. A permeable filter or ball bearings could also be rested over the test specimen to attempt to restrict the migration of fines from the top of the specimen, and to apply some top stress.

The camera used for capturing the images had a minimum frame rate of 10 frames per second and has an internal memory of 8 GB, which then had to be downloaded to a computer. It was decided to save one in every ten images, resulting in a saved frame rate of 1 frame per second. At this rate the download time took approximately 10 minutes, during which time oil kept flowing through the sample at a flow rate governed by the head which was left unchanged from the last raise in height. This resulted in 'blackout' periods when no image data was recorded. In most instances this method worked well as test materials tended to stabilise within 6 minutes. However, when the critical gradient was nearing, or had been surpassed, some samples were still in a 'dynamic' condition when image recording ceased, and the material continued to exhibit unstable behaviour.

The saved frame rate of 1 frame per second was chosen as it allowed a balance between the degree of resolution (i.e. number of frames per second) and the amount of time it takes to download the images. If a higher frame rate was chosen, there would have been a longer 'blackout' periods. The dilemma is that one wishes to capture high resolution data (high frame rate) when instabilities are observed, but also wishes to have minimal 'blackout' time.

Laser light exiting the 'line generator' lens has a width of two millimetres which diverges and increases in width with distance from the lens. This creates an optical issue when particles or portions of particles smaller than this are intersected by the light. When a 'large' particle is intersected (the whole width of the laser light intersects the particle) the image received by the camera is clear, with well defined boundaries (Figure 7.5). However, for particles that are too small to intersect the entirety of the laser 'sheet', the particle boundaries become increasingly undefined and blurry (Figure 7.5). The limitation in this is therefore not only that particles smaller than the laser sheet thickness are not as well defined as those that are significantly larger, but also for the extremities of some particles that partially intersect the light (Figure 7.5). Despite some particles having slightly 'blurry' boundaries, the particles can generally still be visually identified. In the instances when they cannot be identified, their presence within the material is important as they affect the behaviour of the 'soil'. This creates problems for image processing, described in later in this Chapter.

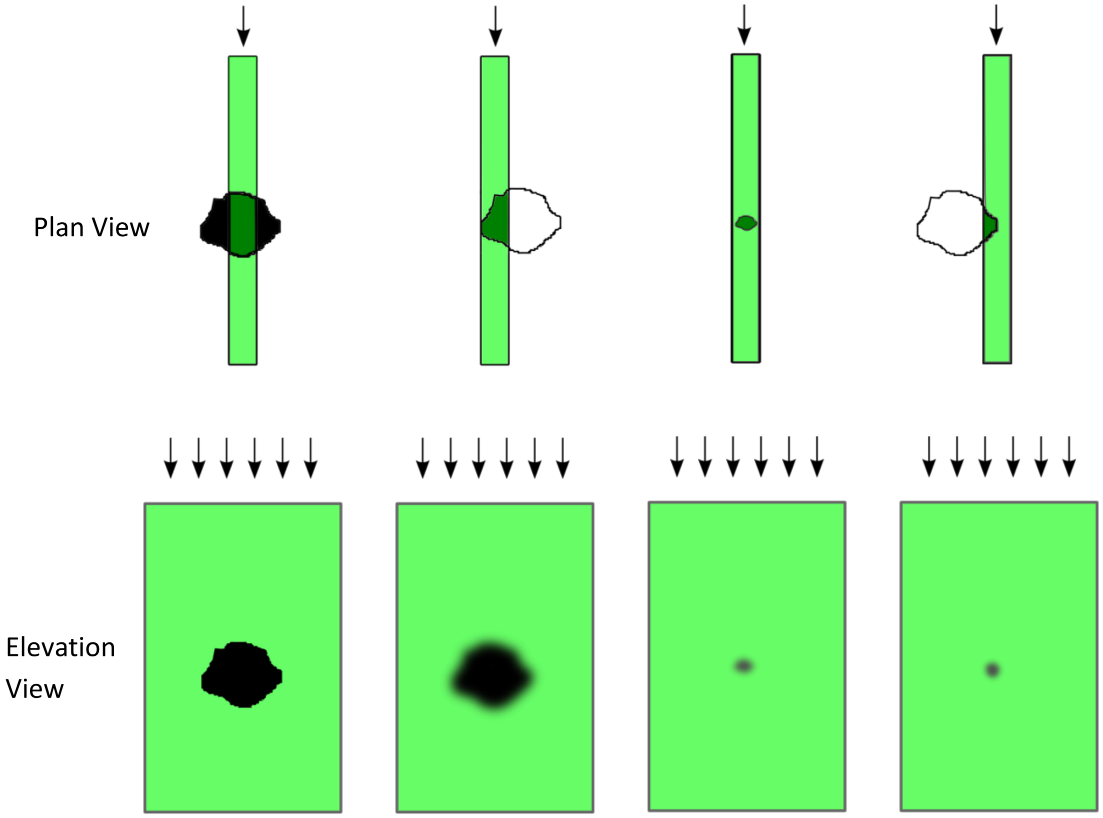

Figure 7.5: Light-particle interaction between laser sheet and glass particles of varying sizes.

A limitation in the testing procedure described in this thesis, is that the laser is set in the one location for the duration of the test. The laser is not moved so that images from a single slice within the test specimen can be directly compared with one another, to view the changes in soil structure. It is also important that the camera or laser is not moved or bumped so image processing can be carried out. The drawback of this technique is that often the part of the specimen where internal erosion mechanisms first initiate and develop, does not occur within the illuminated slice. A variation in the technique may be to focus on obtaining qualitative information about the development of internal erosion mechanisms. This could be done by manually scanning the laser through the test specimen during a test, to find the location where instability or an interesting mechanism is taking place. The laser sheet of light could then be left in that position, while the camera lens is focused and an image sequence is gathered of the developing mechanism. The drawback of this technique is that the mechanism will not be recorded from its initiation, and there would be no images within the slice of interest prior to the change in particle structure.

7.15 Discussion of Image Analysis

As mentioned earlier, the width of the laser line creates issues with defining particle boundaries. A blurred boundary makes it difficult to apply a mask to particles, therefore making calculations of particle area within a frame difficult to determine. This problem is also not helped by the light across the frame becoming attenuated. For these reasons, calculations of coarse fraction area, open void area, and finer fraction area are not accurate as shown in Table 6.2. This means that image calculations of void ratio and porosity cannot be carried out with any certainty.

Despite these downfalls, the area of open void space can be calculated with reasonable certainty. The changes in open void space can then be calculated, and compared with one another across a test, as was done in Chapter 6. From the results in Chapter 6.3, the graph was produced (Figure 6.10) showing the changes in open void space during a test. The analysis of this test is given below:

- The increasing volume in open void space from section 1 up to section 3 is possibly due to the compaction of the sample from overburden stress. It may also occur when placing the sample, if fines fall through the sample toward the bottom.
- Between phases 2 and 4, sections 1 and 3 have an increasing area of open voids, representing the net loss of fines. Section 2 however, shows a net gain in fines. For this to occur, one of two things needs to happen. Either, a) no fines are leaving section 2, or b) there are more fines entering section 2 than leaving. One can see that the latter must be true, as the volume increase of open void space in section 1, compared to the volume decrease in open void space does not match. Therefore, section 2 is gaining more fines than it is losing at this point.
- Following phase 5, section 2 shows that the initiation of piping results in a large net loss in fines at a greater rate than sections 1 and 3. This will occur due to the fact that section 2 has more fines to lose at this point.

In carrying out image processing it was noted that the light from the laser sheet ‘flickered’, or increased and decreased in strength from time to time. With this occurrence the same shade intensity could not be applied to all the images being processed, as some open void space may have been excluded if it coincided in a drop in light strength. This reinforces the need for a quality laser and components, if this method of analysis is to be used. Furthermore, with the intensity threshold having to be manually selected, continuity between images is difficult and subjective based on the operator. It also makes image processing time consuming, as the images cannot be processed in a ‘batch’, or all at once, but rather one by one.

Chapter 8: Conclusions and Recommendations

8.1 Conclusions on stability analyses:

- The Kenney and Lau (1985) approach to stability analysis proved to be the most accurate and reliable method for the materials tested in this thesis.
- The Kezdi (1979) methodology gives a conservative gauge for stability, but was accurate in predicting the stability of most materials.
- The Burenkova (1993) approach performed well in predicting stability in most instances.
- The limits prescribed by Istomina (1957) for predicting suffusion, based on the uniformity coefficient C_u, were surprisingly accurate given its simplicity.
- The Wan and Fell (2008) approach scored poorly in predicting the stability of materials in this thesis, however this was expected given their narrow and gap-grades. This approach should only be applied to broadly graded soils, as proven and prescribed by Wan and Fell (2008).

8.2 Laboratory tests have led to the following conclusions:

- The Terzaghi (1925) calculation of critical hydraulic gradient is applicable to calculating theoretical critical hydraulic gradients in glass-oil mixtures used in this thesis.
- Materials that exhibit internal instability before the theoretical critical hydraulic gradient can be described by segregation piping (Skempton & Brogan 1994) where the coarse grains are carrying most of the overburden stress, therefore allowing the finer fraction to migrate. This can be described using an alpha factor, α.
- The PLIF technique and transparent soil permeameter were able to recreate similar results as those obtained by Skempton and Brogan (1994).
- Borosilicate glass (Duran by Scott) particles scaled up by a factor of 4 combined with Immersion hydrocarbon oil can produce behaviour similar to that of coheshionless soil-water combinations.
- Permeabilities obtained from tests using up-scaled glass and oil were very similar to those published by Skempton and Brogan (1994) for soil and water mixtures, and also similar to those by Fannin and Moffat (2006) who used glass beads and water.
- The PLIF technique was successful in capturing images from inside a test specimen, where edge effects are assumed to be minimal.

- Results in this thesis showed that similar fundamental behaviour of materials can occur in laboratory tests with a top stress (Fannin & Moffat 2006), or with no top stress.
- Subtle changes in the shape of the PSD can significant effects on the internal stability of materials, as shown by GS&B-A, GS&B-B and GS&B-Hybrid tests.

8.3 Image processing using Image Pro and ImageJ software led to the following conclusions:

- Image processing is a labour intensive exercise, but was able to produce valuable outputs.
- Image analysis was capable of turning qualitative results (images) into measurable qualitative results.
- Image processing would become easier and more accurate with an improved apparatus, as described below.

8.4 To improve the quality of results, the following are recommended:

- Use of a more powerful laser to gain better transmission of light through the sample and to obtain consistent light intensity, or;
- Use two lasers, one on each side of the permeameter, to gain a more even transmission of light through the sample.
- Use a line generator (lens) than is capable of producing a thinner sheet of light.
- Apply a top stress to the specimen to better mimic conditions inside a dam.
- Increase the side of the permeameter to allow a greater range of particles to be tested, specifically broadly graded and moraine till soils.
- Implement automated pressure transducers to measure the hydraulic gradient. This will give better resolution and accuracy of test data.
- Investigate a better way to accurately measure the flow rate, which would preferably be automated.

Bibliography

ATSM 2006. Standard Test Method for Permeability of Granular Soils (Constant Head). West Conshokocken, PA, USA, ATSM International.

Baumann T, Werth CJ 2004. Visualization and modeling of polystyrol colloid transport in a silicon micromodel. Vadose Zone Journal 3(2): 434-443.

Benson B 2011. Internal Erosion Meta-stable Behaviour at Tekapo Canal. In: Wilshere D ed. Internal Erosion of Embankment Dams and their Foundations.

Bertram GE 1940. An Experimental Investigation of Protective Filters, Graduate School of Engineering, Harvard University, Cambridge, Mass., 1-21.

Bonelli S, Marot D 2008. On the modelling of internal soil erosion. The 12th International Conference of International Association for Computer Methods and Advances in Geomechanics (IACMAG) India.

Burenkova VV 1993. Assessment of suffosion in non-cohesive and graded soils. In: Brauns, Helbaum, Schuler ed. Filters in Geotechnical and Hydraulic Engineering. Balkema, Rotterdam. Pp. 357-360.

Carrier DW 2003. Goodbye, Hazen; Hello, Kozeny-Carmen. Journal of Geotechnical and Geoenvironmental Engineering 129(11): 1054-1056.

Chapuis RP 1992. Similarity of internal stability criteria for granular soils. Canadian Geotechnical Journal 29: 711-713.

Chapuis RP, Aubertin M 2003. On the use of the Kozeny-Carmen equation to predict the hydraulic conductivity of soil. Canadian Geotechnical Journal 40(3): 616-628

Chapuis RP, Constant A, Baass KA 1996. Migration of fines in 0-20 mm crushed base during placement, compaction, and seepage under laboratory conditions. Canadian Geotechnical Journal 33(1): 168-176.

Cistin J 1955. Problems of Deformation of some Mechanic Filters (in Czech). Vodohospodarski Chasopis No. 2.

Cyganiewicz J, Sills G, Fell R, Davidson R, Foster M, Vroman N 2008. Seepage and Piping Toolbox - Overview. The Sustainability of Experience - Investing in the Human Factor.

Darcy H 1856. Les fontaines publiques de la ville de Dijon. Paris, Vietor Dalmont.

Fannin RJ 2008. Karl Terzaghi: from throry to practice in geotechnical filter design. Journal of Geotechnical and Geoenvironmental Engineering 134: 267-276.

Fannin RJ, Moffat R 2006. Observations on internal stability of cohesionless soils. Geotechnique 56(No. 7): 497-500.

Fell R, Wan CF 2004. Methods for Estimating the Probability of Failure of Embankment Dams by Internal Erosion and Piping: Piping Through the Embankment. UNICIV REPORT No. R-436 JANUARY 2005.

Fell R, MacGregor P, Stapledon D 2005. Geotechnical engineering of embankment dams. Rotterdam ; Brookfield, Balkema. ix, 675 p. p.

Fell R, Foster M, Davidson R, Cyganiewicz J, Sills G, Vroman N 2008. Seepage and Piping Toolbox - Initiation of Internal Erosion. The Sustainability of Experience - Investing in the Human Factor (USSD).

Foster M, Fell R 1999. A Framework for estimating the probability of failure of embankment dams by piping using the event tree methods. UNICIV Report No. R377.

Foster M, Fell R 2001a. Assessing Embankment Dam Filters That Do Not Satisfy Design Criteria. Journal of Geotechnical and Geoenvironmental Engineering 127(5): 398-407.

Foster M, Fell R 2001b. Assessing embankment dam filters that do not satisfy design criteria. Journal of Geotechnical and Geoenvironmental Engineering May: 398-407.

Foster M, Fell R, Spannagle M 2000. The stastics of embankment dam failures and accidents. Canadian Geotechnical Journal 37: 1000-1024.

Foster M, & Fell, R. 1999. Filter Testing for Dams - No Erosion and Continuing Erosion Boundaries. Proc., 8th Australia New Zealand Conference on Geomechanics, Hobart: 503-511.

Garner SJ, Sobkowicz JC 2002. Internal instability in gap-graded cores and filters. Proc. 2002 annual CDA conference. Pp. 1-10.

Garner SJ, Fannin RJ 2010. Understanding internal erosion: a decade of research following a sinkhole event. International Journal on Hydropower and dams 17(3): 93-98.

Hazen A 1892. Some physical properties of sands and gravels, with spacial reference to their use in filtration. 24th Annual Rep., Massachusetts State Board of Health Pub. Doc. No. 34: 539-556.

Hillis SF, Truscott EG 1983. Magat Dams: Design of internal filters and drains. Canadian Geotechnical Journal 20: 491-501.

ICOLD 1994. Embankment dams granular filters and dams. Bulletin 95.

ICOLD 2008. Dams & The World's water. Paris, France, ICOLD.

Istomina VS 1957. Filtration Stability of Soils (in Russian). Gostroizdat, Moscow, Leningrad.

Karpoff KP 1955. The use of laboratory tests to develop design criteria for protective filters. Proc., ATSM 55: 1183-1198.

Kenney TC, Lau D 1984. Stability of particle grading of compact granular filters Publication 84-06.

Kenney TC, Lau D 1985. Internal stability of granular filters. Canadian Geotechnical Journal 22: 215-225.

Kenney TC, Lau D 1986. Internal stability of granular filters: Reply. Canadian Geotechnical Journal 23: 420-423.

Kenney TC, Lau D, Clute G 1983. Filter tests on 235 mm diameter specimens of granular materials. Publication 84-07.

Kenney TC, Chahal R, Chiu GI, Ofoegbu GN, Ume CA 1985. Controlling constriction sizes of granular filters. Canadian Geotechnical Journal 22: 32-43.

Kenny TC, & Lau, D. 1985. Internal stability of granular filters. Canadian Geotechnical Journal 22: 215-225.

Kezdi A 1979. Soil Physics - Selected Topics. Amsterdam, Elsevier Scientific Publishing Co.

Kovacs G 1981. Seepage Hydraulics - Volume 10 of developments in water science. Illustrated ed. Amsterdam, The Netherlands, Elsevier.

Lafleur J 1984. Filter testing of broadly graded coheshionless tills. Canadian Geotechnical Journal 61: 634-643.

Lafleur J, Wendling G, Tetreault M 1986. Filtration of broadly graded soils by woven geotextiles. Proc. IIIrd Int. Conf. on Geotextiles. Pp. 657-662.

Lafleur J, Mlynarek J, Rollin AL 1989. Filtration of Broadly Graded Cohesionless Soils. Journal of Geotechnical Engineering 115(12): 1747-1768.

Li M, Fannin RJ 2008. Comparison of two criteria for internal stability of granular soil. Canadian Geotechnical Journal 45: 1313-1309.

Li M, Fannin RJ 2012. A theoretical envelope for internal instability of cohesionless soil. Geotechnique 62(1): 77-80.

Locke MR, Intraratna B 1999. Critical Review of Filter Design Methods for Dams. Proc., 8th Australia New Zealand Conference on Geomechanics, Hobart: 513-519.

Lowe J 1988. Seepage analysis, in advanced dam engineering, for design, construction and rehabilitation. Jansen RB ed. New York, Van Nostrand Rheinhold.

Ltd WFI no date. WF26010/20635 Falling Head/Constant Head Permeability Cells. Berks, England.

Mahmood A, Mitchell JK 1974. Fabric-Property Relationships in Fine Granular Materials. Clays and Clay Minerals 22: 397-408.

Milligan V 1986. Internal stability of granular filters: Discussion. Canadian Geotechnical Journal 23: 414-418.

Moffat R, Fannin RJ 2011. A hydromechanical relation governing internal stability of cohesionless soil. Canadian Geotechnical Journal 48: 413-424.

Moffat R, Fannin RJ, Garner SJ 2011. Spatial and temporal progression of internal erosion in cohesionless soil. Canadian Geotechnical Journal 48: 399-412.

Moffat RA, Fannin RJ 2006. A Large Permeameter for Study of Internal Stability in Cohesionless Soils. Geotechnical Testing Journal 29(4): 273-279.

Okita Y, Nishigaki M 1993. Filtration processes observed with γ-ray density meter. Filters in Geotechnical and Hydraulic Engineering.

Ramos FD, Locke M ed. 2000. Design of granular filters: Guidelines and recommendations for laboratory testing, Balkema, Rotterdam.

Regazzoni P-L, Marot D 2011. Investigation to interface erosion rate by Jet Erosion Test and statistical analysis. European Journal of Environmental and Civil Engineering 15(8): 1167-1185.

Richards KS, Reddy KR 2007. Critical appraisal of piping phenomena in earth dams. Bulletin of Engineering Geology and the Environment 66(381-402).

Rönnqvist H 2010. Predicting Surfacing Internal Erosion in Moraine Core Dams. Unpublished thesis, KTH. TRITA-LWR Lic Thesis 2050.

Rosenbrand E 2011. Investigation into quantitative visualisation of suffusion. Unpublished thesis, Delft University of Technology, The Netherlands.

Sanvitali N 2010. An experimental study on saturated granular flows and its application to the physical modelling of debris flows. Unpublished thesis, University of Padua, Italy.

Sherard JL 1979. Sinkholes in dams of coarse, broadly graded soils. Proceedings of the 13th International Commission in Large Dams (ICOLD), New Dehli, India 2: 25-34.

Sherard JL, Dunnigan LP 1985. Filters and Leakage Control in Embankment Dams. Volpe RL, Kelly WE ed, ASCE.

Sherard JL, Dunnigan LP 1989. Critical Filters for Impervious Soils. Journal of Geotechnical Engineering 115(7): 927-947.

Sherard JL, Dunnigan LP, Talbot JR 1984a. Basic Properties of Sand and Gravel Filters. Journal of Geotechnical Engineering 110(6): 684-700.

Sherard JL, Dunnigan LP, Talbot JR 1984b. Filters for Silts and Clays. Journal of Geotechnical Engineering 110(6): 701-718.

Sherard JL, Woodward RJ, Gizienski SF, Clevenger WA 1963. Earth and Earth-Rock Dams. New York, Wiley.

Skempton AW, Brogan JM 1994. Experiments on piping in sandy gravels. Geotechnique 44(3): 449-460.

Sobkowicz JC, Byrne PM, Leroueil S, Garner SJ 2000. The effect of dissolved and free air on the pore pressures within the core of the WAC Bennett Dam. Proceedings 53rd Canadian Geotechnical Conference.

Stewart RA, Garner SJ 2002. Performance and Safety of WAC Bennett Dam - A Seven Year Update. Proceedings, 53rd Canadian Geotechnical Conference. Pp. pp. 97-106.

Taylor DW 1948. Fundamentals of Soil Mechanics. New York, John Wiley & Sons, Inc.

Terzaghi K 1922. Der Grundbruch an Staveverken und Seine Verbutung. Die Wasser-Kraft 17: 445-449.

Terzaghi K 1925. Erdbaumechanik. Vienna: Deuticke.

Terzaghi K 1939. Soil Mechanics: A New Chapter in Engineering Practice. Journal Instn. Civil Engineers 12: 106-142.

Terzaghi K, Peck RB, Mesri G 1996. Soil Mechanics in Engineering Practice (Third Edition), Wiley and Sons, Inc.

Thomas HH, . 1976. The Engineering of Large Dams. London, Wiley and Sons Ltd.

Tomlinson SS, Vaid YP 2000. Seepage forces and confining pressure effects on piping erosion. Canadian Geotechnical Journal 37: 1-13.

USACE 1953. Filter Experiments and Design Criteria. Technical Memorandum No. 3-360.

USBR 1987. "Filters." Chapter 5, Design standards No. 13 - Embankment Dams. Denver.

Vaughan PR, Soares HF 1982. Design of Filters for Clay Cores of Dams. Journal of Geotechnical Engineering 108, No. GT1(January): 17-31.

Wan CF 2006. Experimental investigation of piping erosion and suffusion of soils in embankment dams and their foundations. PhD Thesis, The University of New South Wales, Sydney, Australia.

Wan CF, Fell R 2002. Investigation of internal erosion and piping of soils in embankment dams by the slot erosion test and hole erosion test. UNICIV Report No. R-412, ISBN: 85841 379 5.

Wan CF, Fell R 2004a. Experimental investigation of internal instability of soils in embankment dams and their foundations. UNICIV REPORT No. R-429 OCTOBER 2004.

Wan CF, Fell R 2004b. Investigation of Rate of Erosion of Soils in Embankment Dams. Journal of Geotechnical and Geoenvironmental Engineering April: 373-380.

Wan CF, Fell R 2008. Assessing the Potential of Internal Instability and Suffusion in Embankment Dams and Their Foundations. Journal of Geotechnical and Geoenvironmental Engineering March: 401-407.

Appendix

Appendix A – Cargille data sheet on Immersion Liquid 5095

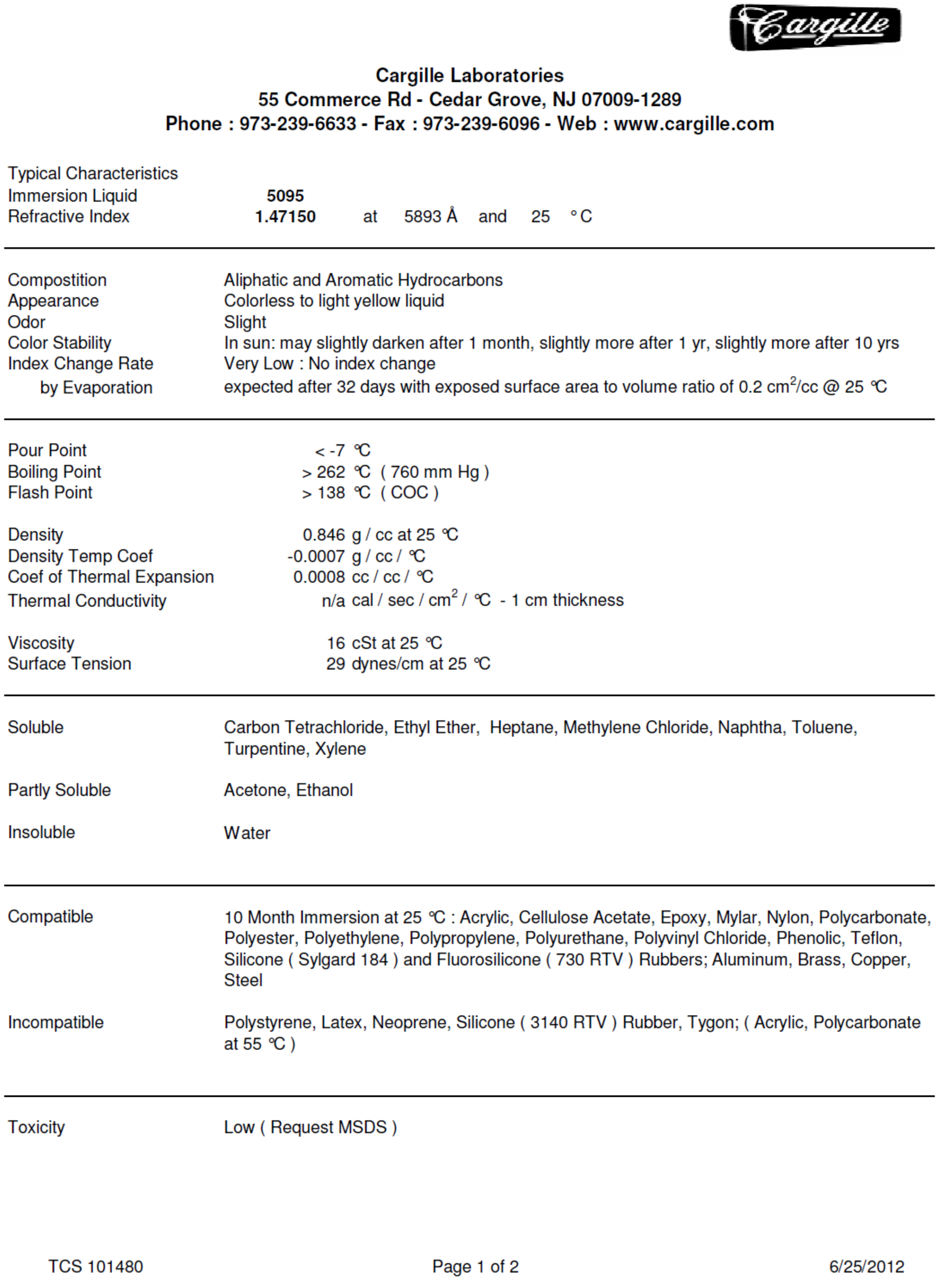

Cargille Laboratories
55 Commerce Rd - Cedar Grove, NJ 07009-1289
Phone : 973-239-6633 - Fax : 973-239-6096 - Web : www.cargille.com

Typical Characteristics					
Immersion Liquid	**5095**				
Refractive Index	**1.47150**	at	5893 Å	and	25 °C

Compostition	Aliphatic and Aromatic Hydrocarbons
Appearance	Colorless to light yellow liquid
Odor	Slight
Color Stability	In sun: may slightly darken after 1 month, slightly more after 1 yr, slightly more after 10 yrs
Index Change Rate by Evaporation	Very Low : No index change expected after 32 days with exposed surface area to volume ratio of 0.2 cm^2/cc @ 25 °C

Pour Point	< -7 °C
Boiling Point	> 262 °C (760 mm Hg)
Flash Point	> 138 °C (COC)
Density	0.846 g / cc at 25 °C
Density Temp Coef	-0.0007 g / cc / °C
Coef of Thermal Expansion	0.0008 cc / cc / °C
Thermal Conductivity	n/a cal / sec / cm^2 / °C - 1 cm thickness
Viscosity	16 cSt at 25 °C
Surface Tension	29 dynes/cm at 25 °C

Soluble	Carbon Tetrachloride, Ethyl Ether, Heptane, Methylene Chloride, Naphtha, Toluene, Turpentine, Xylene
Partly Soluble	Acetone, Ethanol
Insoluble	Water

Compatible	10 Month Immersion at 25 °C : Acrylic, Cellulose Acetate, Epoxy, Mylar, Nylon, Polycarbonate, Polyester, Polyethylene, Polypropylene, Polyurethane, Polyvinyl Chloride, Phenolic, Teflon, Silicone (Sylgard 184) and Fluorosilicone (730 RTV) Rubbers; Aluminum, Brass, Copper, Steel
Incompatible	Polystyrene, Latex, Neoprene, Silicone (3140 RTV) Rubber, Tygon; (Acrylic, Polycarbonate at 55 °C)

Toxicity	Low (Request MSDS)

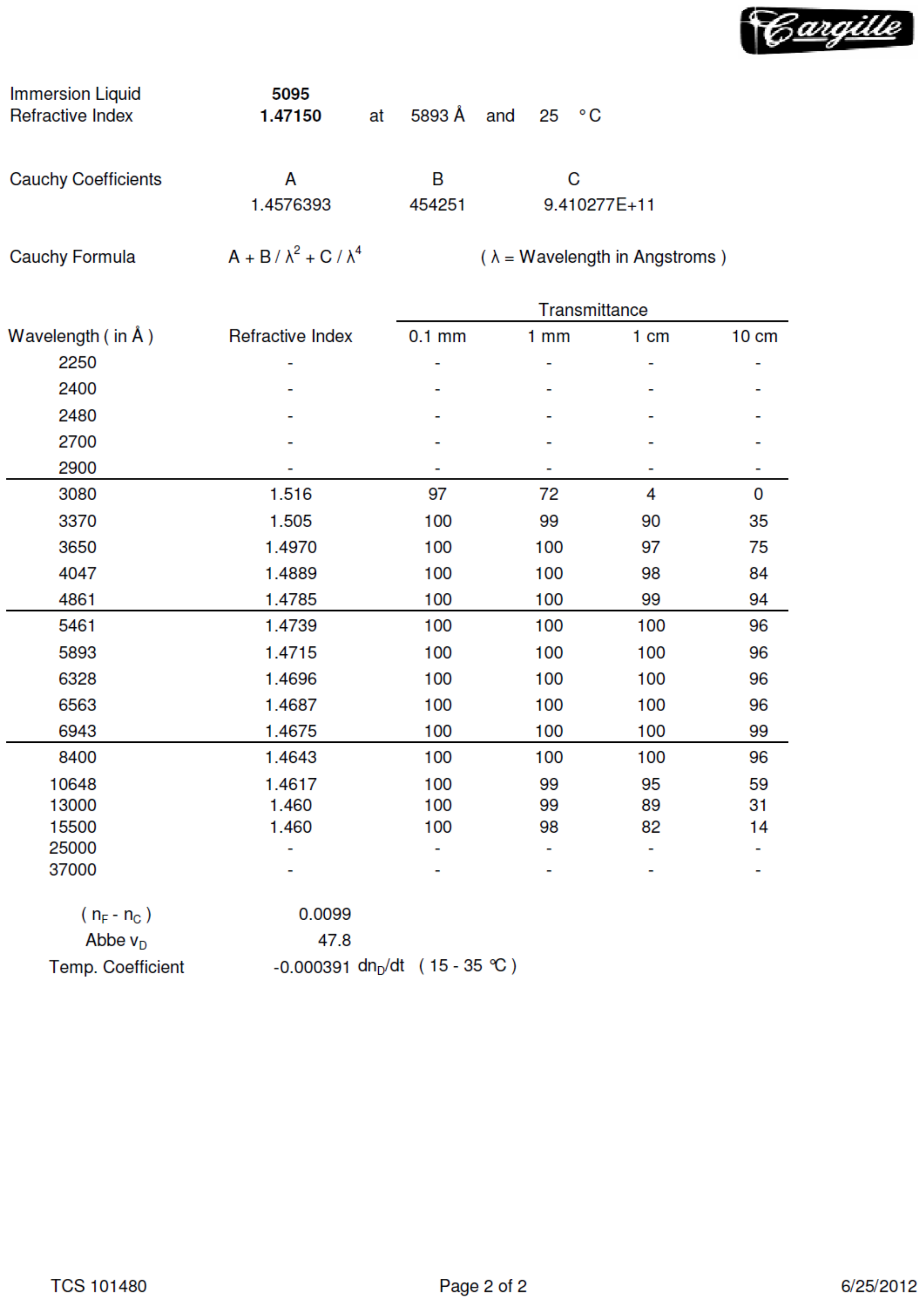

Cargille

Immersion Liquid **5095**
Refractive Index **1.47150** at 5893 Å and 25 °C

Cauchy Coefficients	A	B	C
	1.4576393	454251	9.410277E+11

Cauchy Formula $A + B / \lambda^2 + C / \lambda^4$ (λ = Wavelength in Angstroms)

Wavelength (in Å)	Refractive Index	Transmittance 0.1 mm	1 mm	1 cm	10 cm
2250	-	-	-	-	-
2400	-	-	-	-	-
2480	-	-	-	-	-
2700	-	-	-	-	-
2900	-	-	-	-	-
3080	1.516	97	72	4	0
3370	1.505	100	99	90	35
3650	1.4970	100	100	97	75
4047	1.4889	100	100	98	84
4861	1.4785	100	100	99	94
5461	1.4739	100	100	100	96
5893	1.4715	100	100	100	96
6328	1.4696	100	100	100	96
6563	1.4687	100	100	100	96
6943	1.4675	100	100	100	99
8400	1.4643	100	100	100	96
10648	1.4617	100	99	95	59
13000	1.460	100	99	89	31
15500	1.460	100	98	82	14
25000	-	-	-	-	-
37000	-	-	-	-	-

$(n_F - n_C)$	0.0099
Abbe v_D	47.8
Temp. Coefficient	-0.000391 dn_D/dt (15 - 35 ℃)

TCS 101480 Page 2 of 2 6/25/2012

Video Appendix A – GFM-G4C (see attached CD)

Video Appendix B – Pipe formation (see attached CD)